

# UNIVERSITÀ DEGLI STUDI DI NAPOLI FEDERICO II

---

UNIVERSITY OF NAPOLI "FEDERICO II"  
POLYTECHNIC AND SCIENCE SCHOOL



PH.D. THESIS

MOLECULAR APPROACH FOR THE STUDY AND DEVELOPMENT OF  
ADVANCED MATERIAL, WITH HIGH MECHANICAL RESISTANCE, AND  
SELF-HEALING PROPERTIES.

*Supervisor:*

***Prof.***

**Claudio De Rosa**

***Prof.***

**Finizia Auriemma**

*Candidate:*

**Mauro Milazzo**

PH.D. SCHOOL IN CHEMICAL SCIENCES - 34TH CYCLE

ACADEMIC YEAR 2020-2021

*Show Them No Fear.*

*Show Them No Pain.*

## ABSTRACT

This Ph.D. project aimed to design a thermoset-based material that exhibits self-healing properties. The thermoset resins used as matrices are commercial grades with high modulus and high chemical and thermal resistance that are already utilized in several sectors, including the automotive and construction industry. However, thermosets are usually brittle materials. As such, they are prone to cracking, causing penetration of detrimental agents inside the structure and consequent early deterioration and failure. Finding an easy way to achieve self-healing material readily applicable in the industrial process it was crucial. The synthesis and the curing of thermoset resins are characterized by complex mechanism reactions that engrave on the kinetics and the final properties of the material, depending on composition, chemistry, curing condition, presence of hardener, and additives.

To address the complexity of these curable systems, research activities were first focused on the characterization of sets of some commercial resin. The thermal, structural, and thermomechanical characterization of Phenolic (phenol-formaldehyde) and Melamine (melamine-formaldehyde) based resins are reported in Chapter III. In particular, the curing behavior of a set of novolac-type phenol-formaldehyde (PF) resins and a set of melamine-based resin, containing hexamethylolmelamine or MF oligomeric resin, using hexamethylenetetramine as a hardener, has been investigated. A method based on numerical descriptors extracted from the rheological data has been proposed in order to tag the different types of resins on the basis of the curing kinetics.

Self-healing tests have been performed on mixtures of a commercial fast curable phenol-formaldehyde novolac-type resins and polyamide 12 (PA12). In Chapter IV, it has been shown that the components are partially miscible and realize good adhesion at the interfaces. Viscoelastic and morphological studies have been performed on the repaired specimens in order to evaluate the efficiency of the self-healing process in the restoration. In particular, thermomechanical analysis has

revealed that the mixtures with PA12 content higher than 20 %wt are inherently able to restore their integrity. Since PA12 keeps crystallizing in the cured samples before and after healing, it is suggested that the healing process is triggered by heating at temperatures higher than the melting temperature of the PA12 component through the diffusion of the melt towards the fracture and the establishment of new interactions of the amide groups with the hydroxyl groups of PF resin, followed by successive crystallization of PA12 upon cooling. It has been shown that this mechanism is general as it allows achieving efficient welding regardless of the temperature adopted for curing the mixtures and also for other types of PF resins having different curing behavior.

Model mixtures of PF resin and PA12 in absence of the hardener have been also studied. Whereas investigation of the structure and thermal properties confirm the good compatibility of the two components, FTIR analysis provides direct evidence of the formation of hydrogen bonds even though the possible formation of covalent bonds at PF/PA12 interface.

Finally, a simple procedure is set up, that allows using a PF/PA12 blend with high PA12 content as masterbatch, to obtain efficient self-healing materials by mixing with HAP resin or melamine-based resins. It is demonstrated that with the use of the masterbatch, the desired self-healing performances may be achieved using a lower amount of PA12 component.

# SUMMARY

Abstract .....	I
Chapter I: Introduction .....	7
1.1 Introduction .....	7
1.2 Problem Statement .....	8
2.1.1 Different Self-healing mechanism.....	11
1.3 Phenolic Resins .....	12
1.4 Melamine Resin .....	15
1.5 Bismaleimide Resins .....	17
1.6 Scope of the Study .....	18
Chapter II: Experimental.....	20
2.1 Thermal Analysis .....	20
2.1.1 Differential Scanning Calorimetry - DSC .....	20
2.1.2 Thermogravimetric Analysis - TGA .....	20
2.3 Maldi-TOF .....	22
2.4 Structural Characterization - WAXS.....	22
2.5 Curing and Compression molding.....	22
2.6 Nuclear Magnetic Resonance - NMR .....	23
2.7 Infrared Spectroscopy - IR .....	23
2.8 Rheology and DMTA measurements .....	23
2.8.1 Rheology .....	24
2.8.2 Dynamic Mechanical Thermal Analysis - DMTA .....	25
2.9 Scanning electron microscopy - SEM .....	28

Chapter III: Characterization.....	29
3.1 Phenol-formaldehyde resins.....	29
3.2 Melamine based resins .....	37
3.3 Bismaleimide resins .....	43
3.4 Rheology of resins – curing behavior.....	45
3.4 Characterization of samples cured by compression molding.....	56
3.4.1 Thermal stability of the specimens.....	56
3.4.2 Viscoelastic properties of the specimens.....	60
Chapter IV: self-healing system.....	70
4.1 The self-healing system: PF resin/PA12 blends.....	70
4.1.1 Analysis of the PA12 sample .....	70
4.1.2 Analysis of the HAP resin/PA12 blends .....	73
4.2 Self-healing tests .....	82
4.2.1 DMTA and SEM analysis .....	82
4.2.2 Curing temperature.....	88
4.2.3 Study of other resin/PA12 systems .....	93
4.3 Novolac (HMTA free)-polyamide blends: the study of the compatibilization.....	98
4.4 Novolac-polyamide blend as masterbatch.....	106
Chapter V: Self-healing Composites.....	116
5.1 Composite material .....	116
5.2 Characterization of the Rubber Samples .....	118
5.2.1 Infrared spectroscopy .....	120

5.2.2	Solution Nuclear Magnetic Resonance analysis.....	122
5.2.3	DSC and WAXS.....	127
5.2.4	Thermogravimetric Analysis.....	133
5.2.5	Dynamical Mechanical Thermal Analysis of the Rubber Samples.	135
5.3.1	Characterization of PAN fibers .....	138
5.3.2	HAP-based composites with PAN .....	140
5.4	HAP/PA12/PAN/Rubbers Composites .....	142
5.4.1	Composite with PA12 as a healing agent.....	143
5.4.2	Differential Scanning Calorimetry .....	144
5.4.3	Thermogravimetric Analysis.....	145
5.4.4	Composite prepared using the masterbatch B03070C as a healing agent	151
5.4.5	Thermogravimetric Analysis of “C” composites .....	152
5.4.6	Comparison of the thermomechanical behavior of “D” and “C” composites.....	155
	Conclusions.....	157
	Bibliography.....	161
	Appendix A3.0.....	173
	Appendix A3.1 .....	173
	Appendix A3.2.....	178
	Appendix A3.3 .....	187
	Appendix A4.0.....	194
	Appendix A4.1 .....	195
	Appendix A4.2.....	196

Appendix A5.0.....199

# CHAPTER I: INTRODUCTION

## 1.1 Introduction

Thermosetting polymers are a specific class of polymers that form irreversible chemical networks that tend to grow in three dimensions through the process of hardening, also called curing, of a soft solid or viscous liquid prepolymer. During the curing process, the functional groups of monomers and/or oligomers, mixed with or without a curing agent, also called hardener, react to form covalent bonds which give to the thermoset a strong and rigid structure and an infusible and insoluble three-dimensional polymer network. Thermosets generally are used for all those applications that require high performance as rigidity, high modulus, chemical, and mechanical resistance. Thanks to these properties, thermosetting polymers find application in a variety of fields which include automotive, aircraft, civil engineering, building industry, adhesive, electronics, especially as binders in compounds<sup>1,2</sup>. Thermosets are also highly used in advanced applications, especially in the aerospace<sup>3</sup> and military industries due to the multiplicity of composite materials that can be produced through the inclusion of carbon and glass fibers<sup>4</sup>, which induce reinforcement.

Thermosets show generally higher mechanical strength than thermoplastic materials and are also better suited to high-temperature applications up to the decomposition temperature since they keep their shape as strong covalent bonds between polymer chains cannot be broken easily<sup>3,5,6</sup>. The downside is that they cannot be melted and reshaped after curing. This usually prevents recycling for the same purpose. Downcycling is instead feasible, using them as fillers of thermoplastic resins after milling<sup>7,8</sup>.

The high crosslink density of a thermoset polymer gives higher resistance to thermal and chemical attacks. Mechanical strength and hardness also improve with crosslink density, although at the expense of brittleness<sup>1,9,10</sup>.

Thermoset polymers have replaced most conventional engineering and structural materials due to their considerable physical and mechanical properties. Improvement of the thermal properties of thermosets is recognized as the most important issue to further improve their performances even at high temperatures and thus broaden their application profile. The thermal properties of thermosets in the aspects of thermal cure characteristics, glass transition temperature, thermal stability, flame retardancy, thermal expansion coefficient, and thermal conductivity are still being studied<sup>11</sup>. The thermal properties of thermosets have further enhanced through structural or compositional modifications of precursors, incorporation of inorganic moieties such as phosphorus, nitrogen, silicon, and boron, the addition of nano-fillers or micro-fillers in mono or hybrid form, surface modifications of additives especially fillers, and blending of thermosets with other polymers or modifiers<sup>1,12</sup>.

## 1.2 Problem Statement

In the common material, small external or internal damages generally result in non-reparable flaws which may easily cause the subsequent decrease in performances, and/or a decrease in lifetime, durability, and reliability up to complete failure. All the materials are susceptible to damage induced by radiation, chemicals, thermal, and mechanical factors<sup>13,14</sup>. In order to mitigate the effects that follow the damage, the interest in material with self-healing ability has constantly grown in recent decades. In addition, the use of a self-healing material reduces the waste, just as a direct consequence of the lengthening of the lifetime<sup>15,16</sup>.

Self-healing is a property observed in nature. The most striking example is represented by fresh-water polyps, named Hydra, capable of regenerating a new individual from small pieces of the original polyp by a mechanism (morphallaxis) which involves the transformation of existing body parts or tissues into newly organized structures. The generic principles that govern the healing of Hydra can still be applied to *intrinsic self-healing* polymer materials<sup>17,18</sup>. The healing mechanism of Hydra requires delay time, reorganization of tissue, continuous

signaling, gradients of molecule concentration to provide positional information, adhesion of regenerating cells to the permanent wall, and critical minimum tissue size (Figure 1.1). Analogously, a healing polymer requires damage detection, resting time, reorganization of chains, polymer integrity maintained during healing, and critical damage size.

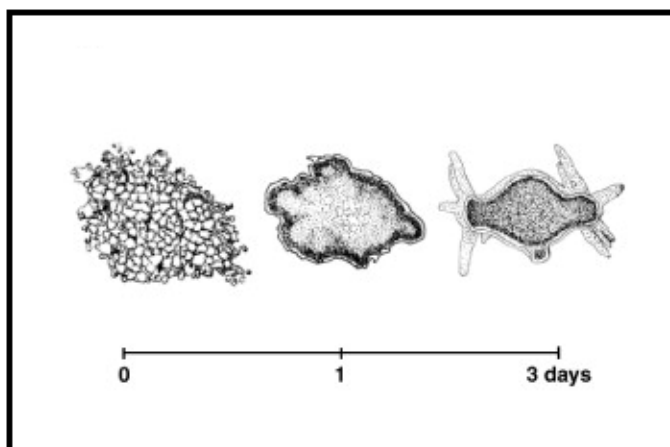


**Figure 1.1:** Hydra, a natural example of intrinsic self-healing mechanism. Regeneration of an intact polyp from a clump of isolated cells<sup>17</sup>.

Despite these similarities with Hydra, self-healing engineering systems have reached a level of development that allows more straightforward conceptual comparisons with the healing mechanisms used by other natural systems. The plants follow a two-step repair process consisting of self-sealing by liquid flooding and self-healing by hardening the released liquid. This two-step model forms the basis for *extrinsic self-healing* approaches where the healing agent (generally liquid) is incorporated into the matrix as discrete entities such as capsules.

Natural systems can still be used as an inspiration to develop intrinsic self-healing systems<sup>16-20</sup>. In the case of intrinsic healing approaches, where the healing capability is intrinsically connected to the (chemically or compositionally tuned) matrix polymer architecture, the two-step process can be translated into a softening step leading to local mobility towards the damage followed by a hardening process

leading to the restoration of the original properties as represented in Figure 1.2 by the recovery of the local viscosity after the healing trigger (temperature) is removed.

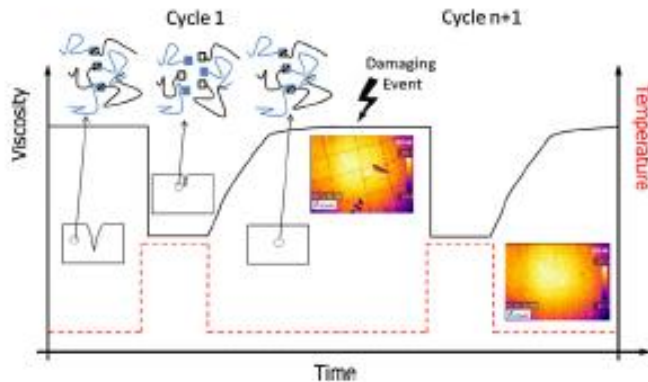


**Figure 1.2:** Schematic intrinsic healing triggered by temperature. The increase in temperature (red dash line) gives a drop in viscosity that allows polymer local mobility. The subsequent decrease in temperature permits the formation of covalent bonds<sup>18</sup>.

Self-healing is thus aimed at restoring a lost functionality (property) of certain material in a specific application in order to extend the service lifetime of the whole system. A schematic way to explain the benefits of using self-healing material is shown in Figure 1.3. In this scheme a generic performance or property of the material (e.g. stiffness, ductility, shape) is plotted versus the time of usage of a generic product. Unlike traditional materials, which after localized damage give a rapid decay of performance (curves a and b), self-healing materials act to mitigate the effect of the local damage in order to fully restore a lost property or functionality (curve c).

Actually, a real self-healing material can only partially restore the property, but it can anyway preserve the structural integrity, safety, and durability of the polymeric components (curve d) obtaining an extension of service life.

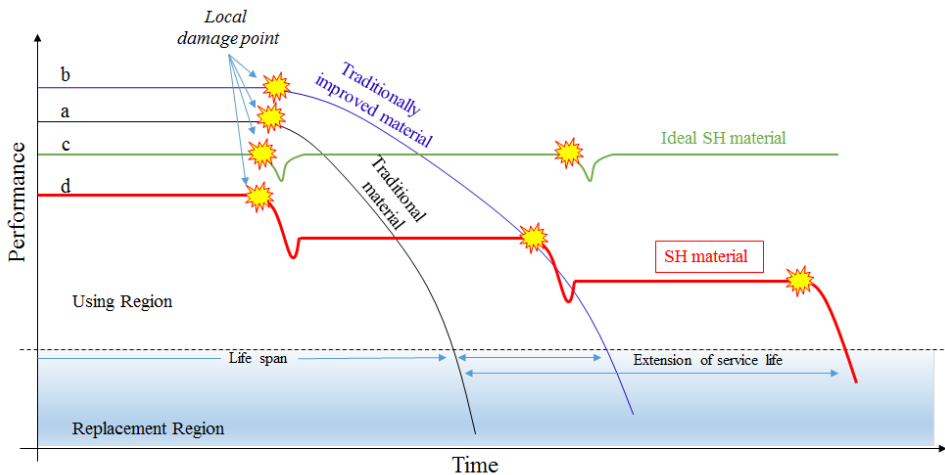


**Figure 1.3:** Lifetime extension of engineered materials by the implementation of self-healing; a) traditional material, b) traditionally improved material, c) ideal self-healing material, d) real self-healing material.

### 2.1.1 Different Self-healing mechanism

Development of self-healing materials or self-healing compounds requires selecting the best mechanism compatible with the desired system. As already mentioned in the previous paragraph, there are two big different families of self-healing mechanisms, the intrinsic self-healing mechanism, and the extrinsic self-healing mechanism.

The **intrinsic mechanism** is based on polymers that are capable of repairing molecular and macroscale damages via a temporary local increase in mobility of the polymeric chains. The recovery mechanism can occur autonomously, or it can be activated by an external stimulus (e.g. temperature, radiation, pressure). Self-healing can be achieved via different mechanisms and processes such as molecular interdiffusion, photo-induced healing, recombination of chain end, formation of reversible bonds, use of living polymer, and addition of nanoparticles. This kind of mechanism is used essentially for thermoplastics<sup>14</sup>.

The **extrinsic mechanism** is the most used for the thermoset-based material, and it is based on the incorporation of low viscosity self-healing agents within a brittle

vessel and the dispersion of the vessels in the polymeric matrix. In this case, the healing process is triggered directly by the damage<sup>18,21</sup>.

The reduced chain mobility due to the cross-linked molecular structure does not allow easy use of the mechanisms seen for thermoplastics. The most common approaches are based on the incorporation of the self-healing agent in a brittle vessel dispersed in the thermoset matrix<sup>21</sup>.

Considering the application, the cost, and the diffusion, three important thermoset resins are here considered: phenolic resins, melamine resins, and bismaleimide resins. All the types of resin are characterized by poor impact resistance which can compromise their durability.

### 1.3 Phenolic Resins

Phenol-formaldehyde resins (PF), also called phenolic resins, are the polycondensation products of the reaction between phenol (P) and formaldehyde (F) and are a category of materials with a three-dimensional network structure<sup>6,22,23</sup>. It was the first synthetic polymer to be developed commercially, since the latest 1910s<sup>22,23</sup>. Today, it has vast and differentiated industrial uses<sup>2</sup>. PF resins exhibit strong water resistance and are used in the wood-based panel industry, mainly in plywood manufacture for outdoor applications. PF resins are widely used in numerous fields because they have low cost, good heat resistance, high chemical, and mechanical strength<sup>6</sup> and the global market is still growing (Figure 1.4). They find applications in numerous fields, including the woodworking industry, molding compounds, foams, foundry, automotive industry for fabrication of friction elements, abrasive materials, paper impregnation, fabrication of laminates, and carbon-carbon composites, coatings, and many others<sup>1,6,24-26</sup>.

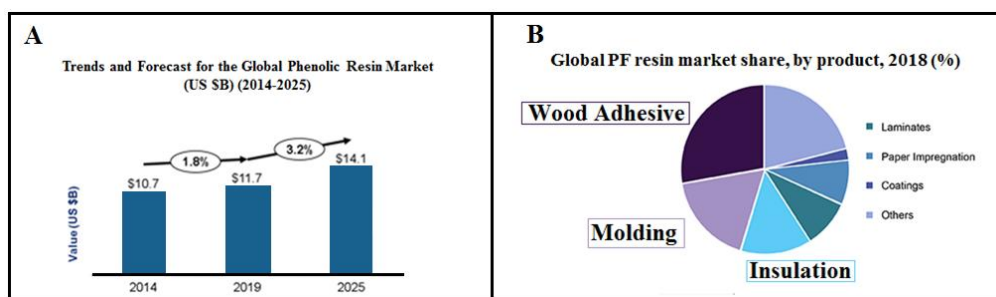


**Figure 1.4:** A) Growth of Global Phenolic Resin Market. B) Global Phenolic Resin Market by product.

Depending on the structure and curing process, two main categories, the cured resol-type and novolac-type phenol-formaldehyde (PF) resins are usually distinguished<sup>6,24,27</sup>. In particular, the reaction of phenols with an excess of formaldehyde (commonly the mol/mol P/F ratio falls between 1:1.1 and 1:3) and in alkaline conditions yields soluble and fusible prepolymers, characterized by methylol groups and moderately branched structures, named resols (Figure 1.5). In general, resols possess good stability at room temperature but undergo polycondensation reactions upon heating and consequent irreversible formation of three-dimensional cross-linked networks. Therefore, the resultant cured resol-type PF resins (thermosets) become infusible and insoluble<sup>6,27</sup>. They are the preferred PF matrix for the fabrication of fiber-reinforced composites<sup>6,24,27</sup>. Cured novolac-type resins, instead, are obtained according to a different strategy involving two steps. In the first step, the reactions of addition and condensation of phenol with formaldehyde are conducted in strongly pH acidic conditions, using an excess of phenol reactant (generally the P:F molar ratio is comprised between 1:0.75 and 1:0.85). This results in the formation of monosubstituted phenols which react to form linear or only slightly branched prepolymers characterized by phenol moieties predominantly connected by methylene bridges (Figure 1.6) and a molecular mass of the order of a few thousand g/mol, named novolacs. Novolacs are thermoplastic polymers, which remain soluble in numerous solvents and can be cured only by the addition of a hardener. In the second step, novolacs are cured by heating in presence

of the hardener, generally, hexamethylenetetramine (HMTA) 5-15% w, to form insoluble and infusible products with a three-dimensional network structure<sup>6,25,28,29</sup>. The curing reaction can occur via benzylamines mechanism and/or via benzoxazine mechanism. The kind of mechanism of cross-linking and the subsequent three-dimensional network depends on the amount of HMTA, thermal condition, the relative amount of ortho/para linkages, and the molecular weight of the prepolymer<sup>30-32</sup>. Novolacs are the preferred PF resins in the production of molding materials.

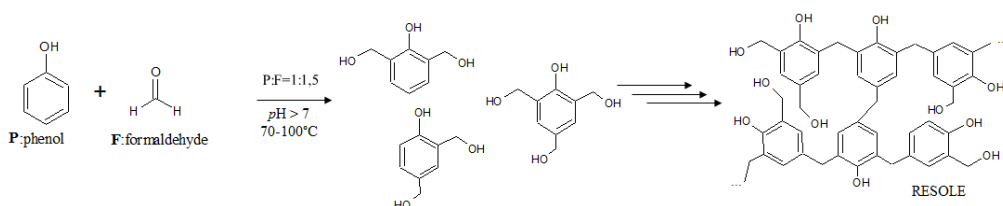


**Figure 1.5:** Synthesis of Resole-type resin. Polycondensation of phenol and formaldehyde in alkaline conditions with defect of phenol.

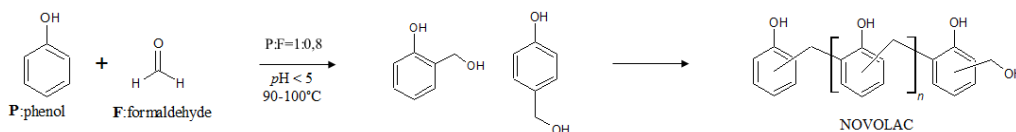


**Figure 1.6:** Synthesis of Novolac-type resin. Polycondensation of phenol and formaldehyde in acidic conditions with defect of formaldehyde.

Although classic unmodified PF resins based on resols and novolacs dominate the resin market, their usage in applications requiring high wear resistance at high temperatures has been hampered due to their limited thermo-oxidative stability and their intrinsic rigid structure, responsible for the brittle behavior. In general, improved thermo-oxidative resistance can be obtained by resorting to chemical modifications:

- i) etherification of the hydroxyl group of the phenolic ring with an alcohol such as methanol or butanol<sup>24</sup>;
- ii) esterification with phosphoric and/or boric acids<sup>24,33</sup> or with phosphorus oxyhalides; modification with phenyl borate compounds;

- iii) addition of silicon compounds<sup>34,35</sup>;
- iv) replacement of the methylene linking groups with heteroatoms such as Si (for instance by reaction with p-silylphenols;
- v) adding thermoplastic phenolic resins such as polyhydroxystyrene<sup>36</sup>, or  $\alpha$ -methyl hydroxystyrene<sup>37</sup>;
- vi) Blending with nitrile and/or acrylic rubbers, or other synthetic or natural rubbers is also an efficient route to improve the properties of PF resins<sup>38,39</sup>.

All these modifications change the kinetic of curing as well as modify the final properties of the material.

## 1.4 Melamine Resin

Melamine-based resins (MF) resins are hard, very durable, and versatile thermosetting aminoplast. They are used for the manufacture of good fire and heat resistance objects<sup>40</sup>.

MF resins are obtained by polycondensation reactions between melamine and formaldehyde<sup>41</sup>, the reaction occurs in acid, neutral, or alkaline conditions (Figure 1.7). It can only occur under pressure in hot conditions and cannot be driven by the addition of an acid catalyst<sup>41</sup>.

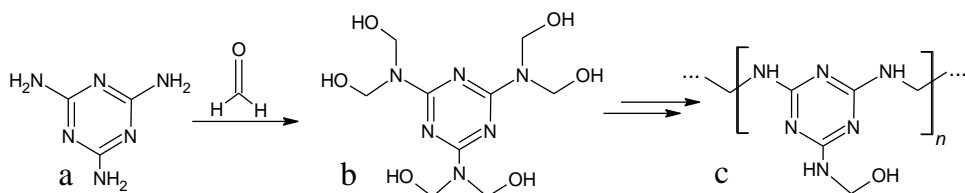


Figure 1.7: Synthesis of MF resin, polycondensation reaction between melamine (a) and formaldehyde to give hexahydroxymethylolmelamine (b) and then the MF resin (c).

Melamine-formaldehyde (MF) and melamine-urea-formaldehyde (MUF) resins are among the most used adhesives for exterior wood-based panels and the production and bonding of low- and high-pressure decorative laminates and overlay sheets.

Their benefits are the significantly higher water and moisture resistance, despite the higher price and slightly lower reactivity<sup>40</sup>, high thermal stability due to the triazine ring which starts thermal degradation at 400 °C<sup>42</sup>, the scratch resistance, the abrasion resistance, and the flame retardant property<sup>43</sup>.

The polycondensation mechanism starts with the attack of the formaldehyde to the amino groups of the melamine forming, under idealized conditions, the hexahydroxymethylol derivative<sup>44</sup> named hexa-hydroxymethylolmelamine (HMM) (Figure 1.7b). Of course, during the first step of the condensation reaction, a series of nine distinct methylol melamine can be produced<sup>45</sup>. Upon heating in the presence of an acid, this or similar hydroxy-methylated species undergoes further condensation and crosslinking (Figure 1.7c), The second step of condensation reaction leads to the formation of many different oligomers containing methylene and methylene ether bridges<sup>46</sup>. The ratio of formation of the two types of bridges depends on the pH of the reaction medium, pH values above 9 produce mainly ether bridges<sup>47</sup>.

MF resins can be cured by heating, which induces polycondensation with water release. The crosslinking can be carried out to a limited degree to give resins. The temperature control during curing reaction is crucial, at a temperature range of 140–160 °C, reversible demethylolation is competitive with the crosslinking reaction, instead, at a temperature higher than 160 °C, the crosslinking reaction dominates<sup>42</sup>. The melamine-formaldehyde resins and melamine-formaldehyde "monomer" (HMM) can be both cured by treatment with a polyols. The principal use of melamine resin is as the main constituent of high-pressure laminates, such as Formica, and laminate flooring. Melamine-resin tile wall panels can also be used as whiteboards, molding compounds, coatings, and adhesives<sup>46,48</sup>.

The HMM monomer and/or the MF resin can be used as a hardener for PF resin obtaining a Melamine based PF resin<sup>49</sup>.

## 1.5 Bismaleimide Resins

Bismaleimide (BMI) resins are a very big family of addition-type polyimides used in high-performance structural composites that require higher temperature use and increased toughness. They find applications in high-performance structural composites and adhesives for aircraft, and aerospace and defense applications where temperatures beyond 150–180 °C are experienced<sup>24</sup>. BMI resins have usually glass transition temperatures higher than 260°C and a continuous-use temperature of 200–230°C<sup>50</sup>. The final properties depend on the crosslink density of the cured material and the nature of the alkyl/aryl group in the reappointing unit. This group indicated with R in Figure 1.8, could be chain extenders such as diamines, a bulky aromatic group as a fluorenyl cardo group, or long chain compounds such as the R group with 36 carbon atoms C<sub>36</sub> of Figure 1.9<sup>51</sup>.

Monomers are usually synthesized from maleic anhydride and an aromatic diamine and the bismaleamic acid formed is cyclo-dehydrated to a bismaleimide resin<sup>52,53</sup>. The double bond of the maleimide is very reactive due to the electron-withdrawing nature of the carbonyl groups. The curing mechanism is based on chain-extension reactions due to amine addition (nucleophilic addition) or homopolymerization (Figure 1.8)<sup>54</sup>.

When bismaleimides are heated to 210 °C, they polymerize by an addition mechanism with the consequent formation of a cross-linked network<sup>54</sup>.

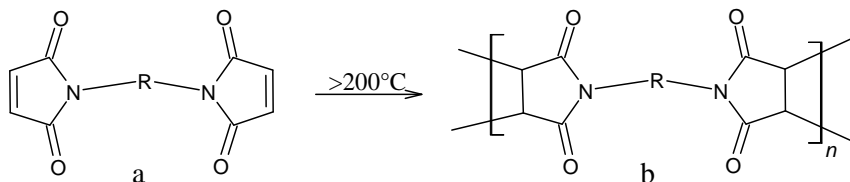


**Figure 1.8:** Curing reaction of a generic monomer (a) to bismaleimide crosslinked resin (b). The final properties are controlled by the chemical nature of the group R.

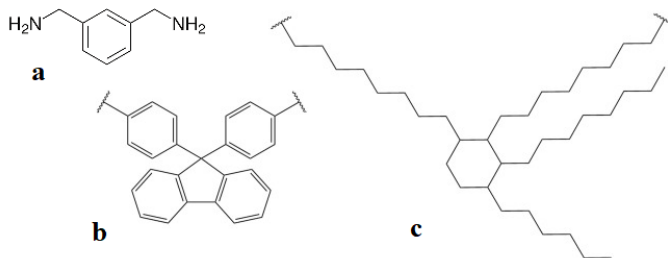


**Figure 1.9:** Examples of typical R groups used in BMI resins. Xylylene-diamine (a), fluorenyl cardo group (b), and long-chain  $C_{36}$  (c)<sup>51</sup>.

As it is already discussed for other thermosets, thermoplastic polymers are used as modifiers in order to tailor the desired characteristic. Examples of thermoplastics that have been tested in BMI resins include poly(ether-ketone)s, poly(ether-sulfone)s, and polyetherimides<sup>51,55,56</sup>.

BMI resins can be also blended with other high-performance thermosets to obtain materials that combine their high performances at elevated temperatures with the advantages offered by the secondary system. Typical systems used in these materials are epoxy resins, cyanate esters, and benzoxazine<sup>51</sup>.

## 1.6 Scope of the Study

The aim of this project is the synthesis of innovative thermosetting resins with intrinsic self-healing properties. The objective is to develop PF-based resins with self-healing properties. As described before, self-healing polymers possess the ability to heal in response to damage wherever and whenever it occurs in the material. This allows preserving the structural integrity, safety, and durability of the polymeric components. The second objective is to improve the performance of the final self-healing resins by using fillers that improve the mechanical strength and/or the dissipative properties, obtaining composite materials that exhibit self-healing properties.

The thesis is organized into 5 chapters. After the present introductory chapter, Chapter II is dedicated to the description of all the experimental procedures and

techniques employed in this work. The commercial grades of the three types of thermoset resins have been described and characterized in Chapter III. A new method based on rheological data that define the cross-linking efficiency of a homogeneous set of thermosetting resins is described in Chapter III. The method is useful for industrial or scientific applications and allows us to select the best thermosetting matrix for the self-healing system. In Chapter IV, the occurrence of the self-healing phenomenon and the possible variables that influence the self-healing process such as composition, curing temperature, type of matrix were explored. To improve the efficiency of the system, the possibility of using a compatibilized mixture as a masterbatch was also studied. In Chapter V, the occurrence of the self-healing phenomenon in composite materials using HAP resin as binder, PAN fiber, and rubber has been studied.

The main conclusions of this work are presented in Chapter VI.

## CHAPTER II: EXPERIMENTAL

### 2.1 Thermal Analysis

#### 2.1.1 Differential Scanning Calorimetry - DSC

The thermal characterization was carried out by Differential Scanning Calorimetry (DSC) by using a Mettler-Toledo DSC822 calorimeter, equipped with an intracooler system (lower allowed temperature is  $-70^{\circ}\text{C}$ ) and a Mettler-Toledo DSC1 apparatus, equipped with a liquid nitrogen cooling system for measurements at temperatures lower than  $-70^{\circ}\text{C}$  (minimum allowed temperature is  $-140^{\circ}\text{C}$ ).

- DSC measurements were performed on 3 — 10 mg of the sample placed in an aluminum pan. The samples were heated/cooled, in a specific temperature range at scanning (when not otherwise stated) of  $10^{\circ}\text{C}/\text{min}$ , in a nitrogen atmosphere (flow rate of  $50\text{ mL}/\text{min}$ ). The samples were scanned in the temperature range  $0 — 350^{\circ}\text{C}$  or  $0 — 200^{\circ}\text{C}$  at  $10^{\circ}\text{C}/\text{min}$  scanning rate, depending on the kind of material.

The main information deduced from DSC measurements for thermoset samples are the crosslinking temperature ( $T_{\text{CL}}$ ), which is identified with the endothermic or exothermic peaks occurring at temperatures higher than  $130^{\circ}\text{C}$  (usually  $\sim 150^{\circ}\text{C}$ ), the softening temperature ( $T_s$ ), which is identified with the broad endothermic peak at temperatures higher than  $50^{\circ}\text{C}$ .

#### 2.1.2 Thermogravimetric Analysis - TGA

Thermogravimetric (TGA) measurements were performed using a Perkin Elmer Thermogravimetric (TGA) measurements were performed using a Perkin Elmer Thermogravimetric Analyzer TGA 4000.

Small amount (6 — 10 mg) of the samples was set in a ceramic pan and heated from 30 °C to 900 °C with a rate of 10 °C/min, under a dry air atmosphere with a flow rate of 20 mL/min.

The weight loss of the sample is recorded as a function of the temperature, which is related to the volatile content (including dehydration and chemical reactions involving mass variation). TGA can be used to evaluate the thermal stability of a material. In the desired temperature range, if a species is thermally stable, there will be no observed mass change. Negligible mass loss corresponds to little or no slope in the TGA trace. TGA also gives the upper use temperature of a material. Beyond this temperature, the material will begin to degrade.

Two parameters have been selected to evaluate the thermal behavior of the samples: the temperature at which the weight of the sample is reduced to 95% ( $T_{95\%}$ ) of the initial weight and the temperature of maximum weight loss  $T_d$ , corresponding to the inflection point of the TGA curve or to the peak position of the corresponding first derivate. Samples undergoing gradual weight loss show multiple  $T_d$ . This step-wise thermal degradation occurs, especially for composite materials.

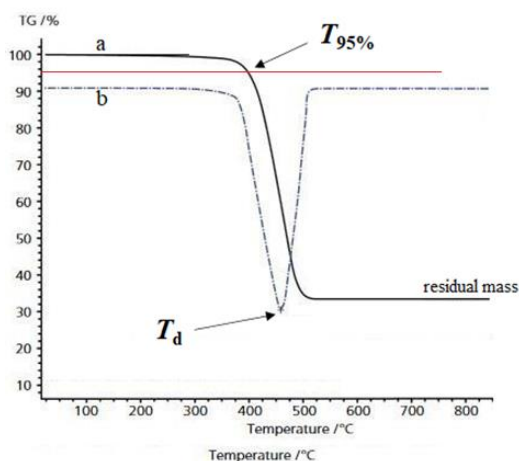


**Figure 2.1:** Typical TGA curve (a) and its first derivate (b). On this graph, it can easily be read the values of  $T_{95\%}$ ,  $T_d$ , and the residual mass due to the inorganic materials if present.

## 2.3 Maldi-TOF

Matrix-assisted laser desorption/ionization (MALDI) mass spectrometry (MS) experiments were performed on a 5800 MALDI-TOF-TOF ABSciex equipped with a nitrogen laser (337 nm) (AB SCIEX, Milan, Italy). MS spectra were acquired in reflector positive mode, by using a mass ( $m/z$ ) range of 100–4000 Da. Laser power was set to 3500 V for MS spectra acquisition. Each spectrum represents the sum of 5000 laser pulses from randomly chosen spots per sample position. The data were reported as monoisotopic masses.

This technique has been used to evaluate the molecular weight of the oligomers and to obtain more details about the repeating unit of the uncured resins

## 2.4 Structural Characterization - WAXS

The structural characterization was performed by Wide Angle X-ray Scattering (WAXS). X-ray powder diffraction profiles were obtained with Ni filtered CuK $\alpha$  radiation using an automatic diffractometer X-Pert by Panalytical. This technique was used essentially for the phase analysis in the raw materials (filler identification and identification of the crystalline phases of crystallizable polymers).

## 2.5 Curing and Compression molding

Specimens of rectangular basal shape (dimensions 50 x 10 mm<sup>2</sup>) and thickness of 1.5-2.0 mm were cured in isothermal conditions in a press equipped with heating/cooling plates, under similar conditions, under the constant pressure of  $\approx$ 400 kPa, and identical compression molding time ( $t_{cm}$ ). The curing temperatures in the press, named compression molding temperature ( $T_{cm}$ ), were selected in between the peak temperature of the curing exotherm measured in the DSC thermograms  $T_{CL}$  (150-160 °C), and a temperature  $\approx$ 50-60°C higher than  $T_{CL}$  ( $T_{CL} + 50-60$  °C). At the end of the isothermal treatment, the samples were cooled down to room temperature,

by fluxing cold water in the refrigerating system of the press-plates (average cooling rate of  $\approx 20\text{-}30^\circ\text{C}/\text{min}$ ).

In the case of mixing or grinding of materials as-prepared or cured, the mill IKA Labortechnik A10, Janke & Kunkel, 180W was used at 20'000 RPM in three steps of 30 seconds.

## 2.6 Nuclear Magnetic Resonance - NMR

$^1\text{H}$  and  $^{13}\text{C}$  solution nuclear magnetic resonance spectra (NMR) were recorded using a Bruker 400 spectrometer on 15 mg of sample dissolved in 500 $\mu\text{L}$  of deuterated chloroform ( $\text{CDCl}_3$ ) or deuterated dimethyl-sulphoxide ( $\text{d}_6\text{-DMSO}$ ), depending on the solubility of the polymer.

## 2.7 Infrared Spectroscopy - IR

Fourier Transform Infrared spectroscopy (FTIR) measurements were carried out using a Nicolet Continuum FT-IR – ThermoScientific spectrometer equipped with a Universal ATR (attenuated total reflectance), using 64 accumulations and a resolution of  $4\text{ cm}^{-1}$ , in transmission mode, and using 128 accumulation and resolution of  $4\text{ cm}^{-1}$ , in reflectance mode with Zinc Sulfur (ZnS) single crystal. The range of measurements is the *mid-infrared*, ( $4,000\text{--}500\text{ cm}^{-1}$ ) which is generally used to study the fundamental vibrations and associated rotational–vibrational structure.

## 2.8 Rheology and DMTA measurements

The kinetic analysis of the curing process is an essential step for the control of the manufacturing process of thermoset. The material, initially liquid, at the end of the process will be solid: viscosity is the most relevant property that changes during the process. As the complex modulus  $\eta^*$  corresponds to the ratio of the complex modulus  $G^*$  and frequency  $\omega$ , the kinetic analysis of the cross-linking reactions may

be performed measuring the variation of the storage  $G'$  and loss  $G''$  moduli ( $G^* = G' + iG''$ ) through use of a rheometer during the curing process at a constant frequency and as a function of temperature. On the other hand, the effect of curing process on the sample may be analyzed through the measure of the storage and loss modulus of a cured thermoset by performing dynamic mechanical thermal analysis<sup>57</sup>.

### 2.8.1 Rheology

The rheological curing behavior was measured employing an Advanced Rheometric Expansion System (ARES) by TA Instrument, equipped with a Force Rebalance Transducer (FRT). Parallel plates of 8 mm diameter with a gap thickness of about 1mm were used. A convection oven guarantees the temperature control with an accuracy of  $\pm 0.1^\circ\text{C}$ . All tests are performed at a frequency of 1rad/s and an imposed strain of 0.5%.

As shown in Figure 2.2, after an "induction time" during which both storage modulus ( $G'$ ) and loss modulus ( $G''$ ) decreases and achieve a minimum, they start increasing, with an abrupt change in slope. Then, at a given temperature they cross each other and the increase of  $G'$  and  $G''$  slow down up to achieve a plateau. When they reach the plateau, the reaction is considered concluded.

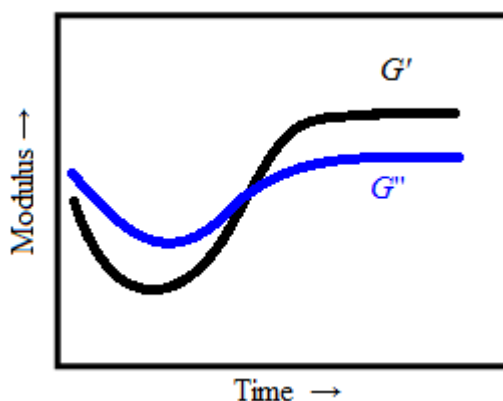


**Figure 2.2:** Evolution with time of storage modulus  $G'$  and loss modulus  $G''$  during a curing reaction in isothermal conditions.

At the beginning, for the uncured resins, the loss modulus is higher than the storage modulus, indicating that the system behaves as a liquid. After the inception of the cross-linking reactions, the storage modulus becomes higher than the loss modulus and the resins has a solid-like behavior.

The degree of curing is usually defined equation:

$$\alpha = \frac{G'(t) - G'_{min}}{G'_{max} - G'_{min}} \quad (1)$$

The degree of curing starts from zero (at the beginning of the reaction) and grows until one (the end of the reaction). The slope of the  $G'$  curve changes with time and shows a maximum at about half of the reaction.

Measurements were conducted in two steps: a temperature ramp at a heating rate of 5°C/min from 100-120°C up to the curing temperature ( $T_r$ ), followed by a time sweep test under isothermal conditions at  $T_r$ . The value of the curing temperature  $T_r$  was selected close to the peak temperature of the curing reactions,  $T_{CL}$ , extracted from DSC analysis.

The isothermal evolution at  $T_r$  was followed for at least 500 s in order to reach a plateau or a quasi-plateau region of the storage modulus  $G'$  and/or stopping the experiment when a threshold value for the torque, equal to  $\approx 75\%$  of the full-scale (200 g cm), was reached or for a time longer than 4000 seconds.

### 2.8.2 Dynamic Mechanical Thermal Analysis - DMTA

Dynamic Mechanical Thermal Analysis (DMTA) or DMA is a technique where a small periodic deformation is applied to a sample, and it is used for the evaluation of the viscoelastic properties of polymers and the response of the material to stress as a function of temperature and frequency of deformation. The change of modulus with temperature allows for the evaluation of relaxation phenomena occurring during heating, such as glass transition ( $T_g$ ) and other molecular relaxations. The glass

transition temperature is evaluated by the onset of a large drop (a decade or more) of the storage modulus ( $G'$ ), the maximum of the loss modulus ( $G''$ ) or the maximum of the  $\tan \delta$ , also called loss factor, which is defined as the ratio of  $G''$  to  $G'$  (Figure 2.4).

The choice of the geometry and the dimension of the specimen depends on the nature of the analyzed samples. In particular, for the bending test, there are two kinds of geometry: single cantilever, which is preferable for stiff samples, and dual cantilever, which is preferable for semiflexible samples (Figure 2.3).

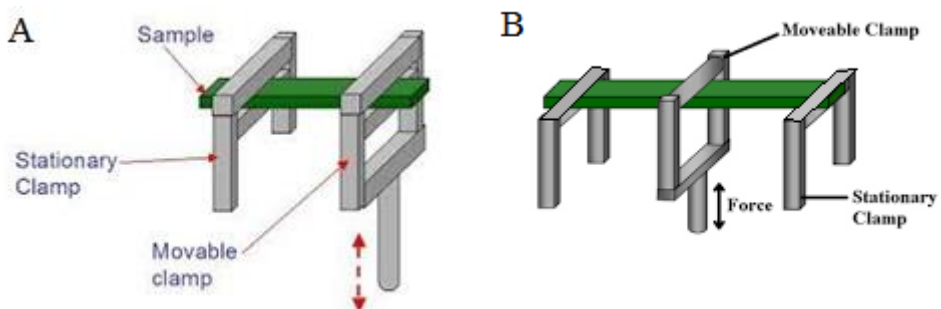


**Figure 2.3:** different geometry used in DMTA measurements in bending mode. A) single cantilever, preferred for stiff specimens; B) Dual cantilever, preferred for semiflexible specimens.

The  $\tan \delta$  (loss or damping factor) is the dissipation of energy in material under cyclic load and indicates the ability of a material to absorb energy. It varies with the state of the material, its temperature, and with frequency<sup>58,59</sup>.

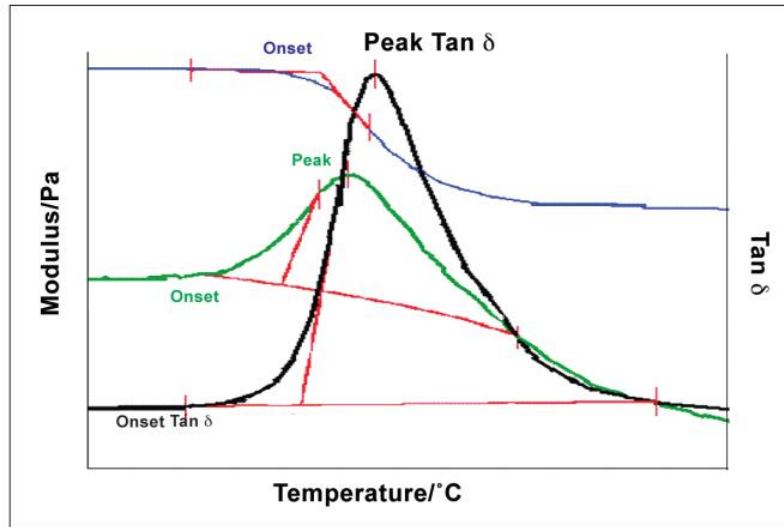


**Figure 2.4:** Evolution of storage modulus  $G'$  (blue line), loss modulus  $G''$  (green line), and the  $\tan \delta$  (black line) during a thermal scan. The glass transition can be evaluated by the drop in the storage modulus, the peak in the loss modulus, or the peak in the  $\tan \delta$ .

The viscoelastic properties of the analyzed samples (crosslinked samples, thermoplastics, and elastomers) were studied by Dynamic Mechanical Thermal Analysis (DMTA) with a TTDMA dynamic mechanical analyzer by Triton, in single cantilever or dual cantilever bending mode, imposing a frequency of 1Hz and a displacement amplitude of 0.02mm, while heating the sample at a rate of 5°C/min in the following temperature ranges:

- Thermoset samples: range temperature is from 25 °C to 350 °C with a single cantilever.
- Elastomeric samples: range temperature is from -100 °C to 200 °C with a dual cantilever.
- Thermoplastic samples: from 0°C to 320°C with a single cantilever.
- Compound samples: from -100 °C to 320 °C with a single cantilever.

## 2.9 Scanning electron microscopy - SEM

Scanning electron microscopy (SEM) images have been collected using a Nova Nano FEG-SEM 450 of FEI-ThermoFisher Scientific in high vacuum conditions. SEM creates a topographic image of a sample by scanning its surface with a low-energy beam of electrons (typically from 1 to 30 keV). The incident electron beam is scanned in a raster pattern across the surface of the sample, and the backscattered or the secondary electrons emitted are detected.

This technique was used to perform morphological analysis of the bulk interior of thermoset specimens and to check the self-healing mechanism.

## CHAPTER III: CHARACTERIZATION

In this chapter, the three different types of thermoset resins presented in Chapter I have been characterized, namely phenol-formaldehyde resins, melamine-based resins, and bismaleimide resins. All of these resins have the ability to disperse and incorporate the healing agent.

### 3.1 Phenol-formaldehyde resins

The analyzed phenol-formaldehyde (PF) resins are commercial grades of the novolac-type resins and the main characteristics are shown in Table 3.1.

They are characterized by different modifications of a base phenol/formaldehyde resin with a statistical (ortho/para) substitution at aromatic rings (Figure 3.1) and contain from 0 to 15 wt % of the cross-linking agent HMTA.

The samples Ph00, Ph01, and Ph02 are classic random ortho/para PF resin of novolac-type (Figure 3.1).

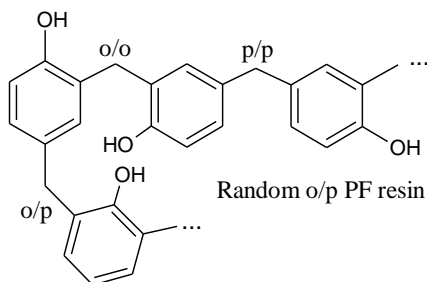


**Figure 3.1:** Structure of random ortho/para novolac-type phenolic resin.

Sample Ph00 does not contain HMTA, so it needs a hardener to give the curing reaction. Sample Ph01 is a PF resin in which the cross-linking agent HMTA is added to the molten polymer to ensure a good dispersion according to the Hexamine Adduct Phenolic (HAP) technology<sup>5</sup>. Sample Ph03 is a PF resin where the methylene bridges are essentially in the ortho position of the phenolic ring (Figure 3.2). This resin can give the curing reaction only in the free para position.

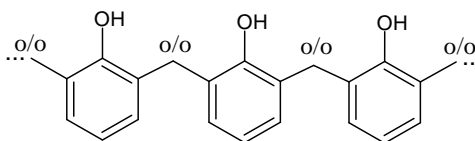


**Figure 3.2:** Structure of ortho novolac-type phenolic resin.

The substitution pattern of the methylene linkages at *ortho*- positions relative to the phenolic hydroxyl group for the sample Ph03 was confirmed by performing ATR-FTIR measurements, using the bands in the spectral range of 700-900  $\text{cm}^{-1}$ . The ATR-FTIR spectra in the relevant wavenumber range of the samples Ph03, the uncured ortho-PF resin containing HMTA, Ph00, the statistical o/p-PF resin that does not contain HMTA, Ph01, the same type of resin but with 10%wt HMTA (HAP resin), and of the neat HMTA are compared in Figure 3.3. The band at  $\approx 820 \text{ cm}^{-1}$  can be assigned to the aromatic ring substitutions at 4 and 2,4 (para and/or para/ortho) positions, whereas the band at  $\approx 750 \text{ cm}^{-1}$  is relative to 2 and 2,6 (ortho and/or ortho/ortho) substitutions (curve c)<sup>60</sup>. These bands are present in the spectra of the HMTA free PF sample (curve c) and the HAP resin (curve b), indicating that both samples are characterized by a statistical *ortho/para* substitution, even though in the case of the HAP resin the band at  $\approx 820 \text{ cm}^{-1}$  overlaps with the band at  $\approx 810 \text{ cm}^{-1}$  of HMTA (curves a). The predominant band of the sample Ph03 containing 6-7 wt% HMTA, instead, occurs at  $\approx 750 \text{ cm}^{-1}$  (curve d), and the contribution samples from HMTA at  $\approx 820 \text{ cm}^{-1}$  is of little or no significance, confirming that it is almost exclusively of ortho type.

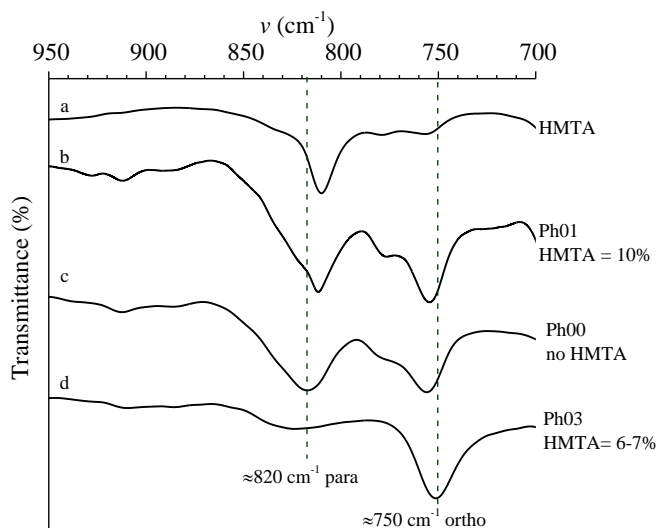


**Figure 3.3:** ATR-FTIR spectra of HMTA (a), the HAP resin Ph01 containing 10wt% HMTA (b), an HMTA free PF resin Ph00 (c), the ortho-PF resin Ph03 characterized by a prevailing ortho substitution pattern at phenolic ring containing 6-7wt% HMTA (d).

The samples PhXy, PhA01, PhA02, PhA03, and PhA04 are PF modified resins by the addition of an alkyl or aralkyl phenol copolymer. In particular, the sample PhXy contains a copolymer resulting by copolymerization of formaldehyde with phenol and 1,3-dimethylbenzene (m-Xylene) (Figure 3.4-A), whereas sample PhA03 contains a copolymer with 1,4-bis(methoxymethyl)benzene (Figure 3.4B).

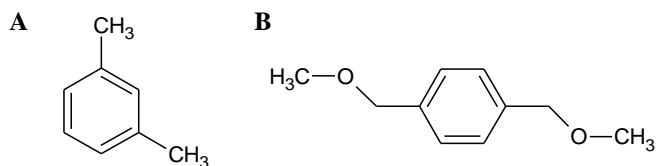


**Figure 3.4:** Comonomer of the samples alkyl or aralkyl PF resins, A) m-xylene (PhXy); B) 1,4-bis(methoxymethyl)benzene (PhA03).

The samples PhGA01, PhGA02, PhGA03, and PhGA04 are PF resins modified by the addition of a different amount of acrylic rubber. The samples PhSi01, PhSi02, PhSi03, and PhSi04 are PF resins modified by the addition of a silicone polymer. In particular, the samples PhSi01 and PhSi02 contains also

octamethylcyclotetrasiloxane (Figure 3.5). Sample Ph14 is a PF resin modified by the addition of a boric component (3% wt); this kind of modification tends to give an ortho-PF resin as confirmed by FT-IR spectroscopy (appendix A3.0). Samples Ph11 and Ph13 are PF resins filled with a polychloroprene elastomer and graphite respectively. Sample Ph12 is a PF resin mixed with benzoxazine; this system can give crosslinking without the addition of a hardener. Finally, the resins Ph15 and Ph16 are two PF resins that contain an additive, covered by industrial secret, which increases the rate of crosslinking reactions.

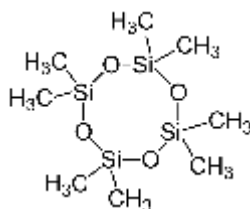


**Figure 3.5:** Silicon-based additive in the samples PhSi01 and PhSi02.

Generally, the chemical modifications regard the presence of different atoms in the bridges or substituents of the phenolic rings. The molecular structures influence the viscoelastic properties and the crosslinking kinetics. The main objective of the chemical modification is to find the molecular basis for tailoring the viscoelastic properties and efficiency of curing.

**Table 3.1** – Main characteristics of the novolac-type PF resins. Concentration of the curing agent HMTA, softening temperature ( $T_s$ ), and crosslinking temperature ( $T_{CL}$ ).

Sample	Type of resin	HMTA	$T_s$ (°C)	$T_{CL}$ (°C)
Ph00	PF resin (random novolac)	no	70	n.d.
Ph01	hexamine adduct phenolic (HAP) resin	10%	72	151
Ph02	PF resin Novolac	9%	72	158
Ph03	ortho PF resin	6-7%	91	154
PhXy	PF resin Xylene copolymer	< 9%	61	151
PhA01	100% alkylbenzene	~10%	>50	161
PhA02	100% aralkyl	~10%	50-60	161
PhA03	High MW PF resin (sub.aryl-alkyl)	10%	50	159
PhA04	PF resin modified with polyvinyl butyral (PVB)	9%	62	156
PhGA01	PF resin with acrylic rubber (15-20%)	~10%	62	154
PhGA02	PF resin (HAP) with acrylic rubber (15-20%)	15%	63	154
PhGA03	PF resin with acrylic rubber (10-20%)	11%	55	155
PhGA04	PF resin with acrylic rubber (13-23%)	11%	74	155
Ph11	PF resin modified 10% chloroprene elastomer	~10%	62	148
Ph12	bisoxazoline + phenoxy resin	no	68	235
Ph13	Graphene modified PF resin	9%	66	151
Ph14	Boron (3%) modified o-PF resin	~10%	91	155
Ph15	Fast cross-linking PF resin (HAP)	15%	83	150
Ph16	Fast cross-linking PF resin	15%	70	149
PhSi01	PF resin with polysiloxane	~10%	67	154
PhSi02	PF resin with polysiloxane (10% wt)	~10%	55	156
PhSi03	PF resin with polysiloxane	7-10%	61	151
PhSi04	PF resin with polysiloxane	15%	58	154

The information about the type of the resin and the HMTA amount reported in Table 3.1 have been extracted from the technical datasheet, whereas the values of softening ( $T_s$ ) and crosslinking ( $T_{CL}$ ) temperatures have been deduced from DSC analysis.

The WAXS profiles and DSC curves of the PF resins of Table 3.1 are reported in Figures 3.6-3.9. The softening ( $T_s$ ) and crosslinking temperatures ( $T_{CL}$ ) are read in correspondence of the endothermic peaks and successive main exothermic peaks, respectively.

The WAXS profiles of all resins show a broad halo centered at  $2\theta \approx 19^\circ$ , due to the amorphous PF resins, which, except for the samples Ph00 and Ph12 that do not contain HMTA, is superimposed by sharp Bragg reflections of HMTA at  $2\theta \approx 18$ , 25, and  $31^\circ$ .

The DSC curves of all resins of Figures 3.6B-3.9B show an endothermic peak in the temperature range from  $50^\circ\text{C}$  to  $91^\circ\text{C}$ , corresponding to the softening of the resins, and an exothermic peak in a temperature range from  $149^\circ\text{C}$  to  $161^\circ\text{C}$ , corresponding to the cross-linking reaction (Figures 3.6B-3.9B). For the samples Ph00, instead, no relevant cross-linking reactions occur due to the absence of any hardener, and only a faint exothermic peak at  $\sim 150^\circ\text{C}$  is present (curve a, Figure 3.6B) due to gas emission, whereas for the sample Ph12, the cross-linking temperature is shifted to  $235^\circ\text{C}$  because HMTA is replaced by benzoxazine as a hardener (curve e, Figure 3.8B). Finally, for the acrylic rubber modified PF resins (Figure 3.7B), the exothermic humps that follow the main cross-linking peaks are due to delayed cross-linking reactions occurring at a higher temperature, probably involving the functional groups of the rubber chains.

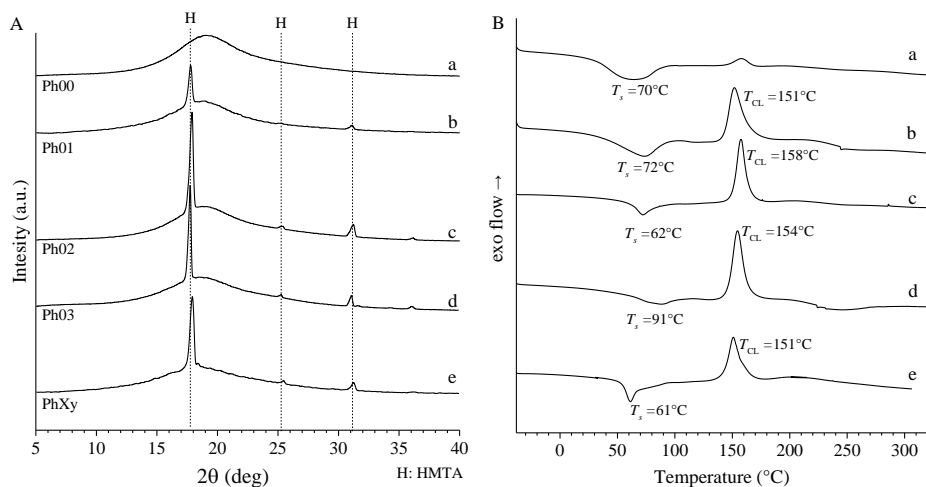


**Figure 3.6:** WAXS (A) and DSC (B) profiles of PF resins Ph00 (a) Ph01 (b), Ph02 (c), Ph03 (d), and PhXy (e). WAXS analysis (A) confirms the presence of HMTA as indicated by the Bragg peaks marked with H, except for the sample Ph00 (A). The DSC curves in B correspond to the first heating thermogram.

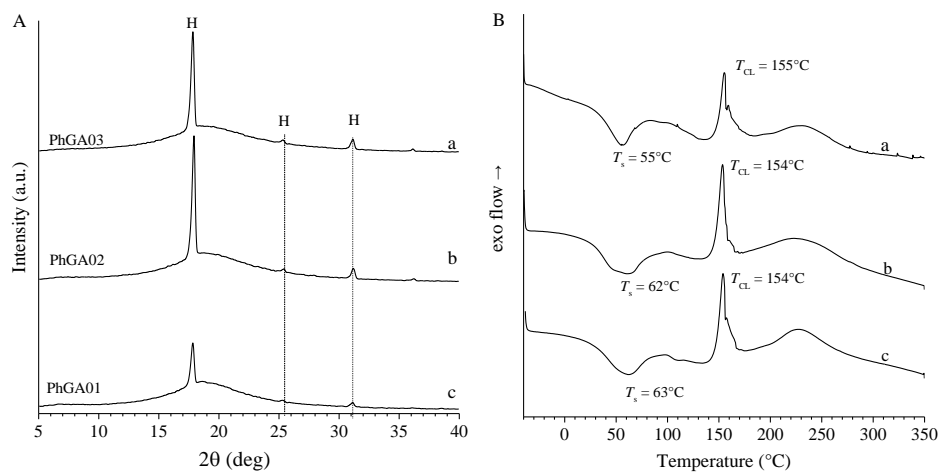


**Figure 3.7:** WAXS (A) and DSC (B) profiles of acrylic rubber modified PF resins PhGA03 (a), PhGA02 (b), and PhGA01 (c). WAXS analysis (A) confirms the presence of HMTA as indicated by the Bragg peaks marked with H (A). The DSC curves in B correspond to the first heating thermogram.

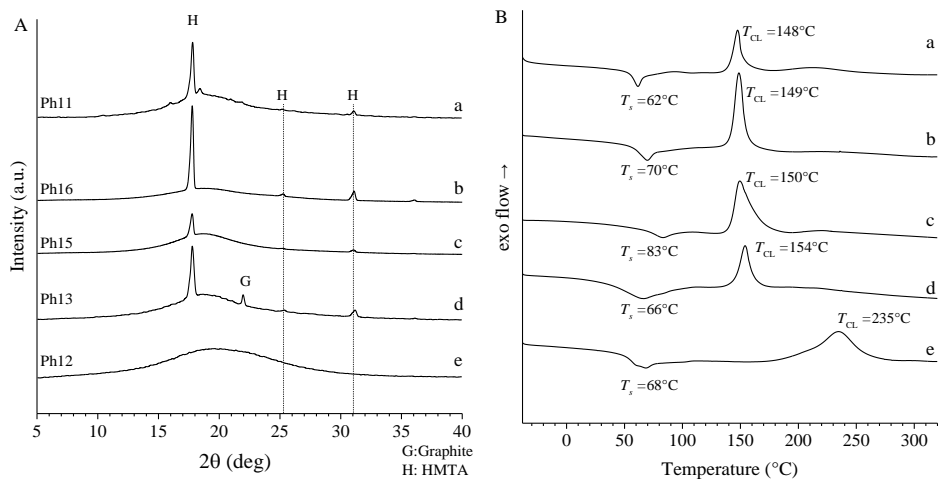


**Figure 3.8:** WAXS (A) and DSC (B) profiles of the samples Ph11 (a), Ph16 (b), Ph15 (c), Ph13 (d) and Ph12 (e). WAXS analysis (A) confirms the presence of HMTA as indicated by the Bragg peaks marked with H, except for sample Ph12 (e), which contains benzoxazine as hardener (A). The DSC curves in B correspond to the first heating thermogram. In A, the sample Ph13 (d) contains graphite, as indicated by the Bragg peak marked with G.

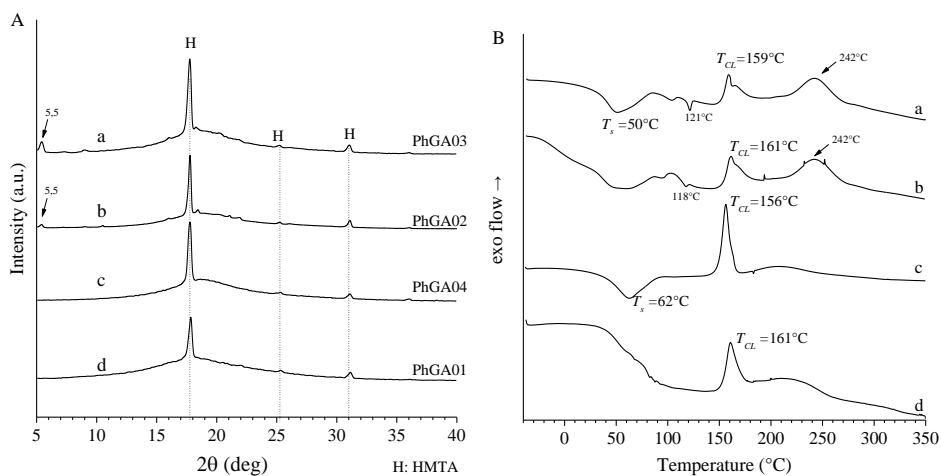


**Figure 3.9:** WAXS (A) and DSC (B) profiles of the samples PhGA03 (a), PhGA02 (b), PhGA04 (c), and PhGA01 (d). WAXS analysis confirm the presence of HMTA (A) as indicated by the Bragg peaks marked with H. The DSC curves in B correspond to the first heating thermogram.

## 3.2 Melamine based resins

The analyzed melamine-based resins are essentially commercial grades of blends between MF resin and PF resin of novolac type (Figure 3.10). They are a homogeneous set of samples that differ in the composition of melamine, PF resin, and hardener.

The main characteristics of samples of the melamine-based resins deduced from the technical datasheet and DSC analysis are shown in Table 3.2. The resins are sorted by melamine relative amount.

The WAXS profiles of all melamine-based resins sorted by melamine relative amount are reported in Figure 3.11. The Bragg peaks at  $2\theta = 6.25, 7.95, 12.45, 20.80, 22.90, 24.67,$  and  $23.13^\circ$  are assigned to the HMM species. These peaks are visible in all samples except for the samples MF01, MF02, and MF03 that do not contain the HMM species but only the MF resin. The Bragg peaks at  $2\theta = 17.90$  and  $31.05^\circ$ , due to HMTA, are detected in the samples MFPh04, MF02, MF04, MFPh01, MFPh08, MFPh09, MFPh10, MF03, MFPh03, and MFPh12.

The DSC curves recorded in the first heating scans of all melamine-based resins, sorted by melamine relative amount, are reported in Figure 3.12. All the resins show softening in the range of temperature from 61 to 71 °C and crosslinking temperature at about 150°C (Figure 3.12). Unlike phenolic resins, for the melamine-based resins, the cross-linking phenomenon is an endothermic process, with exception of samples MF01, MF02, MF03, and MF04. The endothermic or exothermic phenomena depend on the presence of HMTA and/or the presence of MF resin instead of HMM species in the uncured powder resin and on their relative amounts (Figure 3.10).

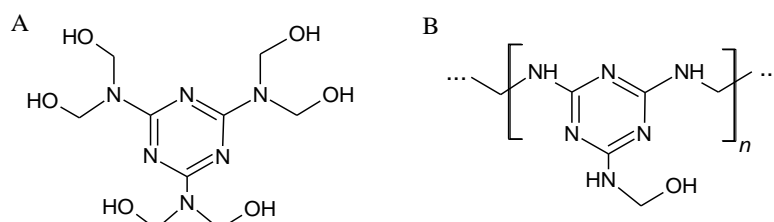


**Figure 3.10:** Melamine components in the melamine based resins:  
A) hexa-hydroxymethylmelamine (HMM), B) MF resin

**Table 3.2** – Main characteristics of the Melamine based resins. The samples containing MF resin are indicated with \*.

Sample	Type of resin	Melamin	HMTA	$T_s$ (°C)	$T_{CL}$ (°C)	DSC CL peak
<b>MFPh04</b>	Melamine mod. PF resin	10%	7,25%	69	149	Endo
<b>MF02</b>	MF resin - PF resin	10%	7,25%	69	155	Exo
<b>MF04</b>	Melamine mod./MF - PF resin	10%	5,5%	69	153	Exo
<b>MFPh05</b>	Melamine mod. PF resin	10%	-	71	150	Endo
<b>MFPh06</b>	Melamine mod. PF resin	25%	-	65	151	Endo
<b>MFPh01</b>	Melamine mod. PF resin	25%	5%	65	145-155	Endo
<b>MFPh07</b>	Melamine mod. PF resin	25%-40%	-	74	149	Endo
<b>MFPh08</b>	Melamine mod. PF resin	25%-40%	3%	73	146	Endo
<b>MFPh09</b>	Melamine mod. PF resin	25%-40%	6%	68	135	Endo
<b>MFPh10</b>	Melamine mod. PF resin	25%-40%	9%	74	135	Endo
<b>MFPh03</b>	Melamine mod. PF resin	40%	3%	67	150	Endo
<b>MF03</b>	MF resin - PF resin	40%	3%	65	145-155	Exo
<b>MFPh02</b>	Melamine mod. PF resin	40%	-	68	149	Endo
<b>MFPh11</b>	Melamine mod. PF resin	45%	-	63	150	Endo
<b>MFPh12</b>	Melamine mod. PF resin	50%	1%	62	149	Endo
<b>MF01</b>	MF resin	100%	-	61	~150	Exo

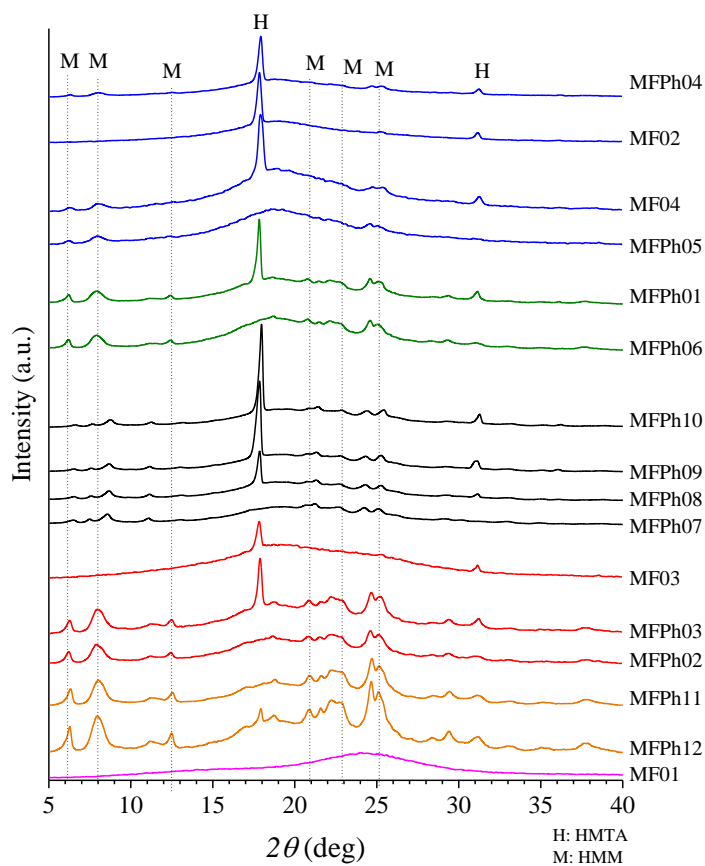


**Figure 3.11:** WAXS profiles of the melamine-based resins of Table 3.2. The letter H indicates Bragg peaks due to HMTA, the letter M indicates Bragg peaks due to HMM. The colors indicate the relative amount of the melamine component: blue = 10% wt, green = 25% wt, black = 25-40%wt, red = 40%wt, orange >40%wt, and magenta = 100% wt.

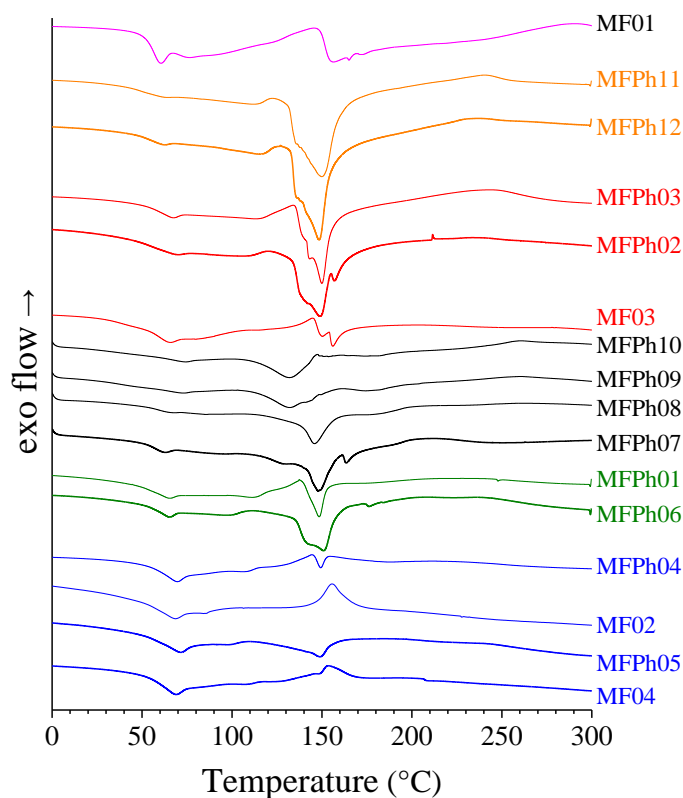


**Figure 3.12:** DSC curves recorded in the first heating scan of melamine based resins with 10% (blue line), 25% (green line), 25-40% (black line), 40% (red line), >40%wt (orange line), and 100%wt (magenta line) of melamine component.

The solution  $^1\text{H-NMR}$  spectrum of the resin MFPh02, reported in figure 3.13 as an example, confirms the presence of the HMM component<sup>61</sup>. The triplet and the doublet centered at 5.50 and 5.02 ppm are due to the hydrogen of the hydroxyl group and the methylene group of HMM, respectively. The integrals of these signals have a ratio of 1:2, consistent with the attribution.

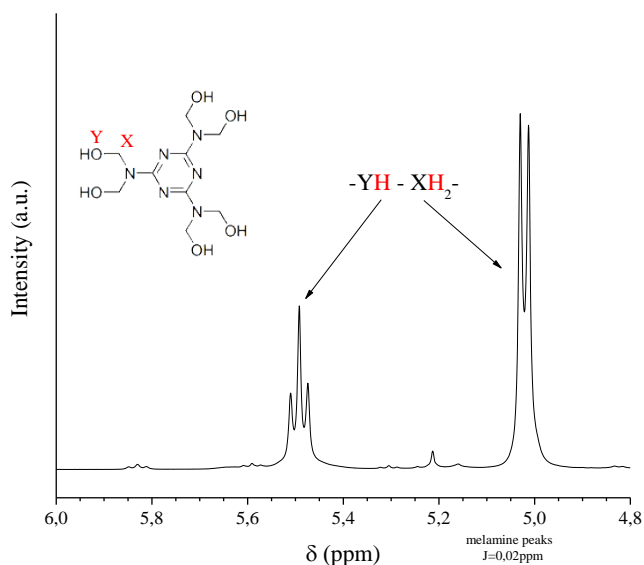


**Figure 3.13:** Solution  $^1\text{H}$ -NMR spectrum of the resin MFPh02 in the ppm range of the melamine component. The doublet at  $\delta=5.02$  ppm and the triplet at  $\delta=5.50$  ppm are due to the hydrogen of hydroxymethyl groups of HMM.

MALDI-TOF analysis has been performed on some samples selected from Table 3.1 and 3.2. As an example, the mass spectra of the PF resin Ph01, the melamine-based resin MFPh02, and the MF resin MF01 are shown in Figures 3.14, 3.15, and 3.16. The predominant peak-to-peak mass increment corresponds to  $\Delta m=106$  Da in Figure 3.14 and Figure 3.15, for the resin Ph01 and MFPh02, and  $\Delta m=223$  Da for the sample MF01 in Figure 3.16. Repeating units compatible with the so-determined  $\Delta m$  values are shown in Figure 3.17, confirming that two resins are of PF and MF type, respectively. Furthermore, the mass spectra of all the samples indicate a number average molecular mass  $M_n$  of 750-1500 Da. The predominance of  $\Delta m$  values of 106 Da for the resin MFPh02 suggests that the MF network is formed only after the curing process.



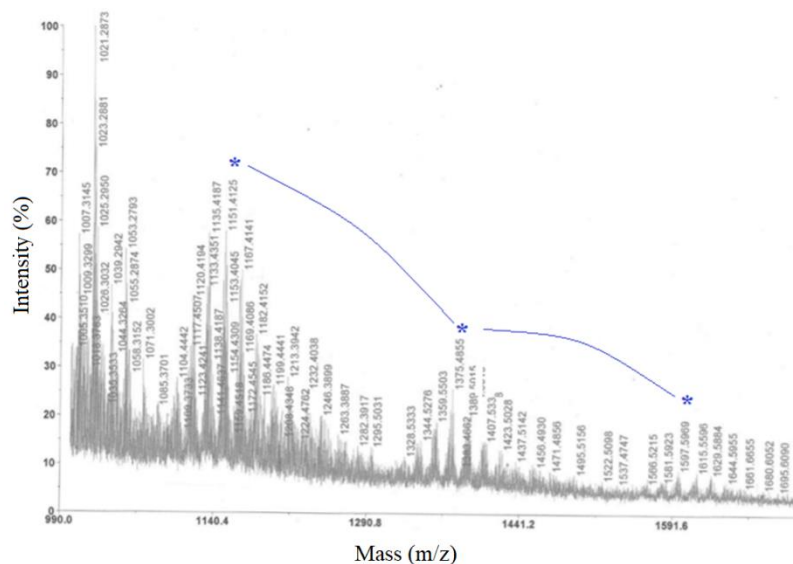


Figure 3.16: MALDI-TOF spectrum of the MF resin MF01. The  $\Delta m = 223\text{Da}$  is compatible with the repeating unit of an MF resin

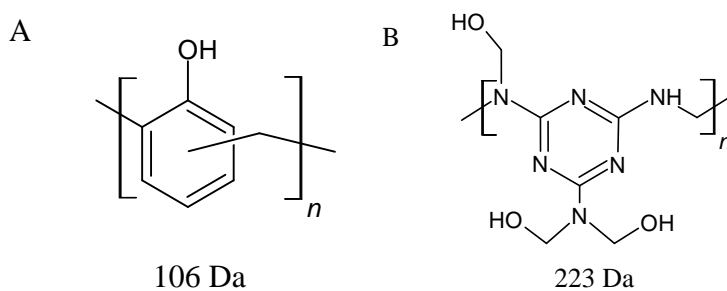


Figure 3.17: Repeating units of the resins Ph01 and MFPh02 (A) and MF01 deduced from MALDI-TOF spectra.

### 3.3 Bismaleimide resins

The here analyzed bismaleimide resins are two commercial grades reported in Table 3.3. The WAXS profiles and the DSC thermograms of the two samples are reported in Figure 3.18. Both samples do not contain hardener and the crosslink occurs at temperatures higher than  $190^{\circ}\text{C}$ .

**Table 3.3** – Main characteristic of the BMI resins

Sample	Type of resin	hardener	$T_s$ (°C)	$T_{CL}$ (°C)
BM-17	Bismaleimide resin	no	80	191
BM-24	Bismaleimide resin	no	72	199

As shown in Figure 3.18-A the resin BM-24 is amorphous as expected, whereas the resin BM-17 shows a number of Bragg peaks probably due to the presence of BMI monomers.

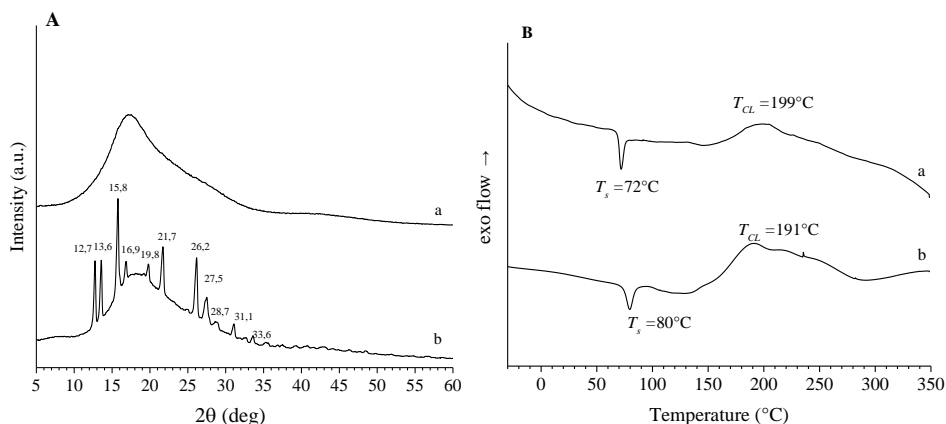


**Figure 3.18:** Resin BM-24 (a) and BM-17 (b). A) WAXS shows the presence of crystalline monomer phase in the sample (b); B) first heating DSC curves

The MALDI-TOF spectrum of the sample BM-24 is shown in Figure 3.19. It is consistent with a number average molecular mass  $M_n$  of 1259 Da and molecular mass of the repeating unit of  $\sim 360$  Da. These data suggest a molecular structure such as that reported in Figure 3.20, and that the sample is a tetramer.

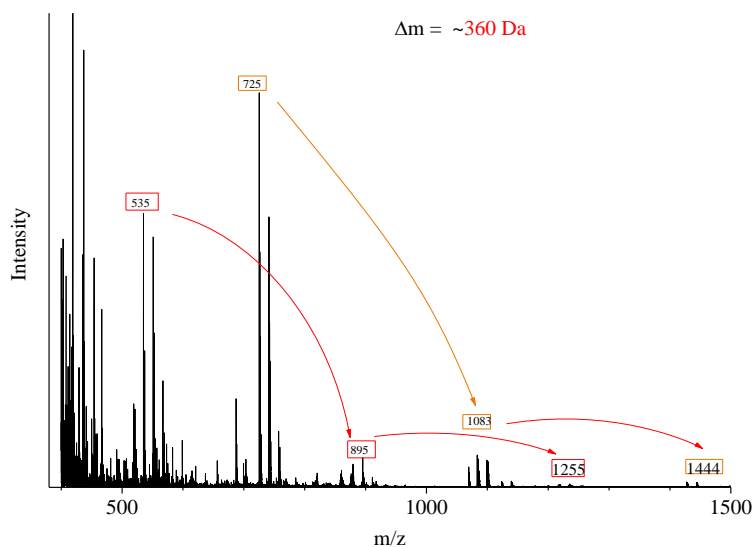


**Figure 3.19:** MALDI-TOF spectrum of the BMI uncured resin BM-24. The  $\Delta m \sim 360\text{Da}$  is compatible with the repeating unit of a BMI resin shown in Figure 3.19.

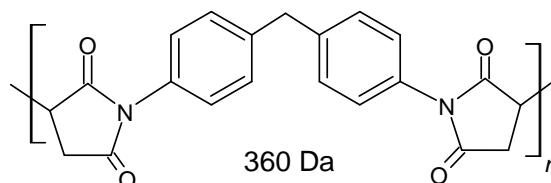


**Figure 3.20:** Repeating unit of the resin BM-24

### 3.4 Rheology of resins – curing behavior

The rheological behavior of the resins during the curing process was followed using the ARES rheometer during a heating step (heating rate  $5^{\circ}\text{C}/\text{min}$ ) from  $100\text{-}120^{\circ}\text{C}$  to the crosslinking temperature  $T_r$ , followed by an isothermal treatment at  $T_r$  for about  $4000\text{ s}$ .

The selected values of the curing temperature ( $T_r$ ) are close to the  $T_{\text{CL}}$  values determined by DSC analysis reported in Tables 3.1, 3.2, and 3.3. Accordingly, the selected curing temperature is  $150^{\circ}\text{C}$  for all the samples, with the exception of the PF resins Ph14 and PhXy, which are isothermally cured at  $160^{\circ}\text{C}$ , and the BMI

resin BM-24, which is isothermally cured at 199 °C. In this way, the cross-linking kinetics may be followed for all the samples adopting nearly equivalent conditions. As an example, the temperature range selected to carry out rheology measurement is shown in Figure 3.21 for the sample Ph01. The rheological measurements were prolonged for at least  $\approx 4000$  s for all the samples, that is up to reach a plateau or a quasi-plateau value for  $G'$  and  $G''$ .

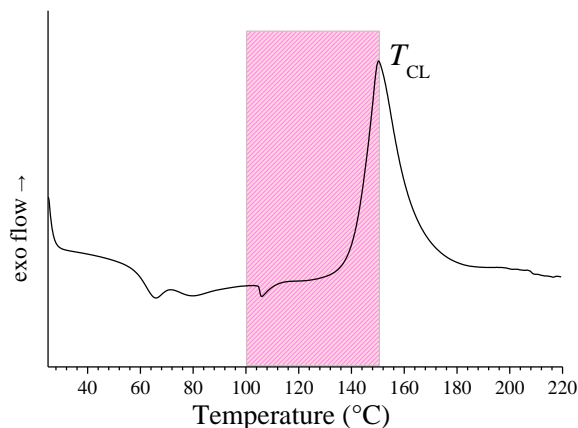


**Figure 3.21:** DSC thermogram recorded in the first heating curve of the sample Ph01, at 10 °C/min. The rectangle indicates the temperature range selected for the rheology measurements.

All the resins show similar rheological behavior. The values of shear storage and loss moduli measured during the heating and isothermal steps of the PF resins Ph01 (HAP) (A) and Ph00 (with 10%wt HMTA) (B), the melamine modified PF resin MFPh02 (C) and the bismaileimide resin BM-24 are reported in Figure 3.21 as a function of time. The samples are cured at 150 (A-C) and 199 °C (D). The temperature profiles are also shown in Figure 3.22. The rheological curves of all other resins of Tables 3.1-3.3 are reported in the appendix A3.1.

In the initial heating stages, the samples have liquid-like behavior, showing values of the loss modulus  $G''$  higher than those of the storage modulus  $G'$ , because they are heated above the softening temperature ( $T_s$ ). No significant crosslinking reactions occur, and both moduli decrease with increasing the temperature. Above

130 °C, both moduli show a steep increase with temperature because of the thermal activation of the cross-linking reactions. In this transition region the values of  $G'$  and  $G''$  are nearly identical, since the liquid-like and solid-like behaviors of the samples are in competition. In the isothermal stage, the storage modulus overcomes the loss modulus, indicating the formation of a rigid network, with a solid-like behavior. During the isotherm, storage and loss moduli keep increasing, due to the increase of the crosslinking density in the partially cross-linked resins, and eventually reach a quasi-plateau value as the crosslinking reactions are completed (Figure 3.22). Since the resin Ph00 is a neat novolac PF resin and has no hardener, 10 wt% HMTA has been added to the pristine sample by mixing the finely ground powders in a vibration mixer. Melamine-based and bismaleimide resins have slow cross-linking kinetics so that the moduli do not reach a plateau value even after one hour of isotherm (Figure 3.22-C, D). The data of Figure 3.22 and appendix A3.1 indicate that different resins having different chemical structures and compositions show different curing rate and final stiffness. Therefore, the different chemical structures strongly affect the curing behavior and the final mechanical properties.

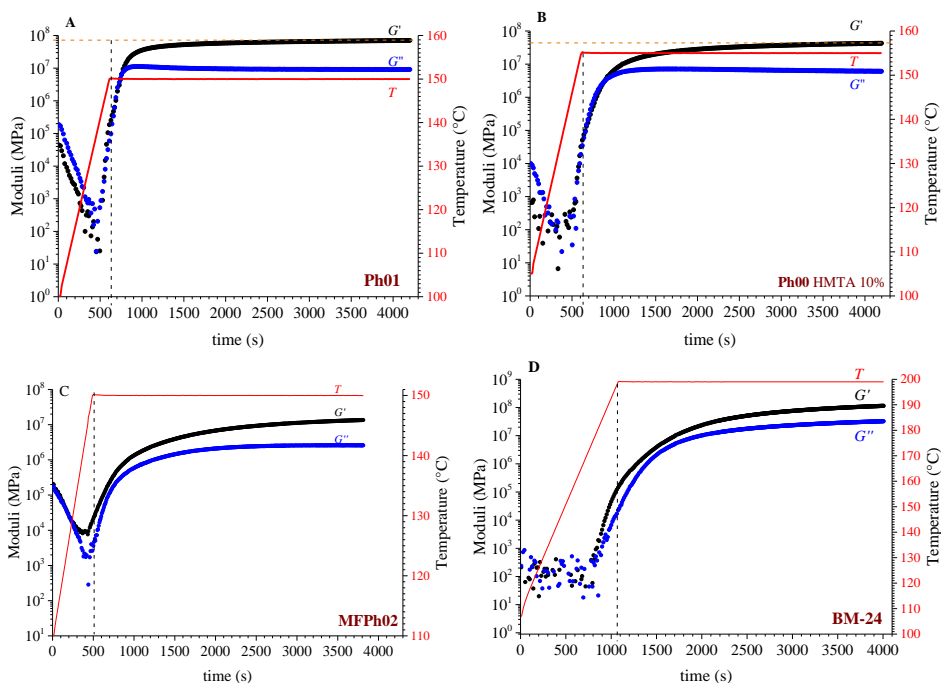


**Figure 3.22:** Storage ( $G'$ ) and loss ( $G''$ ) moduli of the PF resins Ph01 (HAP (A)), Ph00 with 10%wt HMTA (B), the melamine modified PF resin MFPh02 (C) and the bismaileimide resin BM-24 (D), measured during the rheological measurements as a function of time. The samples are heated (at 5 °C/min) from 100 °C up to the cross-linking temperature  $T_r$  of 150 (A-C) and 199 °C (D), and then isothermally cured at  $T_r$ . The solid red lines indicate the temperature profiles (right scale). The dashed vertical line marks the beginning of the isotherm.

Rheological data have been used to extract information about the efficiency of the curing process as a function of the structure and composition of resins. To this aim suitable parameters are extracted from rheological data<sup>62</sup>. These parameters are the “curing ratio” defined as the ratio between the values of the storage modulus  $G'$  after a given time lag  $t_L$  during the isotherm at the temperature  $T_r$  ( $G'_L$ ) and at the beginning ( $G'_i$ ) of the isotherm ( $G'_L/G'_i$ ) and the “maximum curing rate”, calculated as the maximum rate of increase for  $G'$  with time  $(dG'/dt)_{\max}$  during the first  $t_L$  seconds of the isotherm.

The curing ratio ( $G'_L/G'_i$ ) represents a measure of the efficiency of the functional groups in the resin of generating a three-dimensional network by the effect of the heat treatment, already before reaching the isothermal curing step. The lower the

values of the curing ratio, the higher the ability of the resins to reticulate at temperatures lower than the isotherm. Conversely, large values of the curing ratio entail that the major part of the cross-linking reactions occurs during the isothermal treatment at  $T_r$ .

The maximum curing rate  $(dG'/dt)_{\max}$ , instead, measures the rate of the partially cross-linked resins to increase the stiffness by the effect of cross-linking reactions. Therefore, the curing ratio  $(G'_L/G'_i)$  allows measuring the efficiency of a resin to generate a three-dimensional network, regardless of the intrinsic degree of stiffness reached by the resin itself by the effect of reticulation. On the other hand, the value of the maximum curing rate  $(dG'/dt)_{\max}$  indicates how fast, in the early seconds of the isotherm, the partially cross-linked resins transform into a more densely cross-linked network, through the increase of stiffness. In Figure 3.23-A,B, the evaluation of maximum curing rate  $(dG'/dt)_{\max}$  for the resin Ph01 and the values of  $G'_i$  and  $G'_L$  are indicated. The target curing time  $t_L$  is arbitrarily set equal to 500 s.

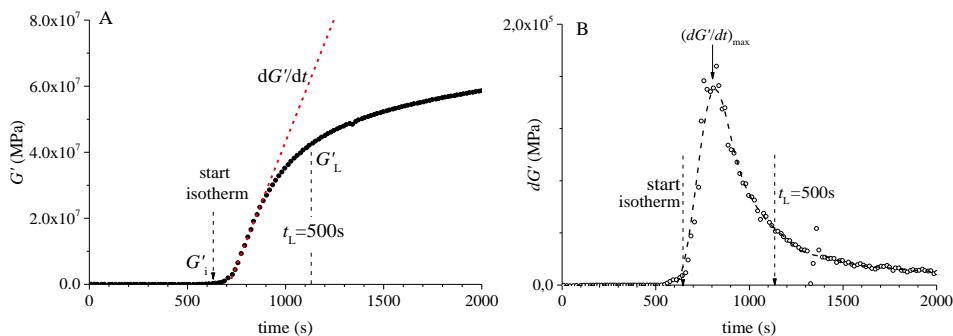


**Figure 3.23:** Evaluation of  $G'_i$ ,  $G'_L$ , and  $dG'/dt$  for the sample Ph01. A: Storage modulus ( $G'$ ) measured during the rheological measurements. The dashed red line indicates the maximum slope during the early stages of the isotherm, comprised between the beginning ( $t=0$ ,  $G'=G'_i$ ) and  $t_L$  ( $G'=G'_L$ ), with  $t_L$  arbitrarily set equal to 500 s (vide infra). B: First derivative of the shear conservative modulus showing a maximum between 0 and  $t_L$ , for the calculation of the maximum curing rate parameter.

The values of these parameters,  $(dG'/dt)_{\max}$  and  $G'_L/G'_i$  are used to construct the diagram named “curing efficiency chart” reported schematically in Figure 3.23. The diagram is centered approximately at the value of the numerical descriptors of a novolac HMTA free resin (sample Ph00) blended with 10% wt of HMTA, so that the

diagram is divided into four quadrants. Four different curing behaviors can be identified depending on the combination of the values of the curing ratio  $G'_L/G'_i$  and the maximum curing rate  $(dG'/dt)_{\max}$ , in comparison with the values of the curing ratio and maximum curing rate of the resin arbitrarily selected as the benchmark. The resins that cross-link efficiently already at the beginning of the isotherm, and quickly approach a higher stiffness, correspond to low values of the curing ratio  $G'_L/G'_i$  and high values of the curing rate  $(dG'/dt)_{\max}$ . They are located in quadrant I of Figure 3.24 and define the class I of curing behavior. The resins that cross-link efficiently (low values of  $G'_L/G'_i$ ) but slowly approach a higher stiffness (low values of  $(dG'/dt)_{\max}$ ) are located in quadrant II of Figure 3.24 and define class II of curing behavior. Resins that cross-link in a less efficient way (showing high values of the curing ratio  $G'_L/G'_i$ ) and slowly approach a higher stiffness (low values of  $(dG'/dt)_{\max}$ ) are placed in part III of the plot of Figure 3.24 and define the class III of curing behavior. Finally, the resins that quickly increase the stiffness (high values of  $(dG'/dt)_{\max}$ ) up to reach high values of the cross-linking density, even though the initial cross-linking density is low (high values of  $G'_L/G'_i$ ) are placed in quadrant IV of Figure 3.24 and define the class IV of curing behavior.

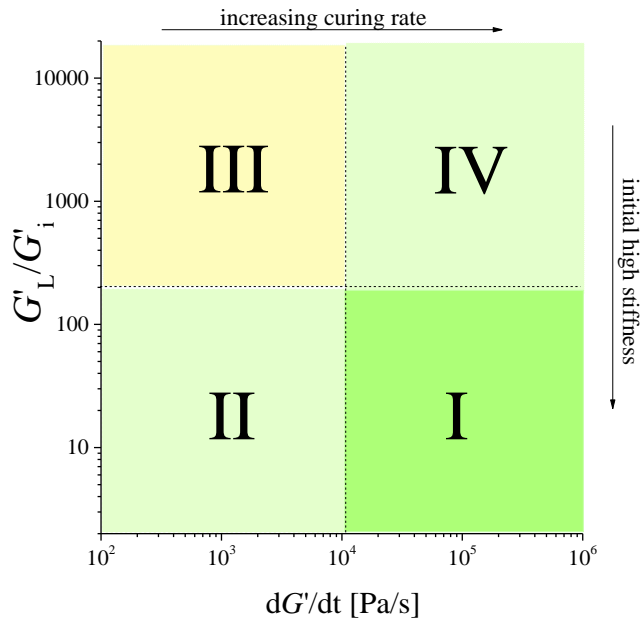


**Figure 3.24:** Correlation diagram of the curing efficiency (curing efficiency chart) of the thermosets analyzed in the present context. For a target curing time  $t_L$  (set to 500 s) the ratio between the storage modulus after  $t_L$  curing time ( $G'_L$ ) and at the beginning of the curing process ( $G'_i$ ) (curing ratio  $G'_L/G'_i$ ) is reported as a function of the maximum increase of the rate of the storage modulus with time, during the early target curing time  $t_L$  of the isotherm, corresponding to the maximum curing rate  $(dG'/dt)_{\max}$ . Four sectors are identified depending on the combination of the values of the curing ratio  $G'_L/G'_i$  and of the maximum curing rate  $(dG'/dt)_{\max}$  in comparison to those of a novolac HMTA free resin (sample Ph00) blended with 10%wt of HMTA, which has been arbitrarily selected as the benchmark. Compared with the benchmark, resins that are already well cured at the beginning of the isotherm and quickly become stiffer during isotherm fall in the region I; resins that are already well cured at the beginning of the isotherm and slowly become stiffer during isotherm fall in the region II; resins that are not well cured at the beginning of the isotherm and slowly become stiffer during isotherm fall in the region III; resins that are not well cured at the beginning of the isotherm and quickly become stiffer during isotherm would fall in the region IV.

The values of the curing ratio  $G'_L/G'_i$  of all PF resins are reported as a function of the maximum curing rate  $(dG'/dt)_{\max}$  in Figure 3.25 and Table 3.4. In Figure 3.25 data relative to the bismaleimide resin BM-24 are also reported. It is apparent that the HAP resin Ph01 is in quadrant I, which means that this resin gives higher crosslinking in a shorter time compared to the PF resin with a similar amount of HMTA. All the acrylic rubber modified PF resins PhGA04, PhGA01, PhGA02, and

PhGA03 are placed in quadrant IV which means they are not well-cured at the beginning of the isotherm and quickly become stiffer.

The unmodified PF resin Ph02, the two fast cross-linking PF resin Ph15 and Ph16, the PF resin modified with 10% of chloroprene elastomer Ph11, and three of the PF resins modified with silicon PhSi01, PhSi02, and PhSi04 cross-link efficiently already before the isotherm and can achieve a higher stiffness (high cross-linking density) in a short time. They belong to the class of resins that slowly become stiffer. They correspond also to the resins that are able to achieve the highest degree of stiffness.

The xylene-modified PF resin PhXy and the PF resin containing graphene Ph13 respectively, cross-links less efficiently and require a longer time to complete the network (quadrant III).

Finally, all the other PF resins are located in quadrant II, indicating that they are already well cured at the beginning of the isotherm and slowly become stiffer.

The values of the curing ratio  $G'_L/G'_i$  and the maximum curing rate  $(dG'/dt)_{max}$  of the bismaleimide (BMI) resin BM-24 are 44 and  $6.5 \times 10^3$ , respectively, and they are plotted in Figure 3.25. This resin is located in quadrant II.

**Table 3.4** – Numerical descriptors deduced from rheology data of PF resins

Sample	Type of resin	HMTA	$(dG'/dt)_{max}$	$G'_L/G'_i$
Ph00	PF resin (random novolac)	10%	$1.0 \times 10^4$	205
Ph01	HAP resin	10%	$1.5 \times 10^5$	101
Ph02	PF resin Novolac	9%	$3.3 \times 10^4$	39
Ph03	ortho PF resin	6-7%	$4.3 \times 10^3$	3.2
PhXy	Xylene modified PF resin	< 9%	$5.1 \times 10^2$	255
PhA01	100% alkylbenzene	~10%	$2.3 \times 10^2$	5.8
PhA02	100% aralkyl	~10%	$2.1 \times 10^3$	7.4
PhA03	High MW PF resin (sub.aryl-alkyl)	10%	$1.1 \times 10^3$	5.6
PhA04	PF resin modified with PVB	9%	$1.4 \times 10^4$	672
PhGA01	PF resin with acrylic rubber (15-20%)	~10%	$3.9 \times 10^4$	350

PhGA02	HAP resin with acrylic rubber (15-20%)	15%	$9.3 \cdot 10^4$	341
PhGA03	PF resin with acrylic rubber (10-20%)	11%	$8.1 \cdot 10^4$	648
PhGA04	PF resin with acrylic rubber (13-23%)	11%	$2.3 \cdot 10^4$	247
Ph11	PF resin mod. 10% chloroprene elastomer	~10%	$5.4 \cdot 10^4$	99
Ph12	bisoxazoline + phenoxy resin	no	$6.7 \cdot 10^2$	1.4
Ph13	Graphene modified PF resin	9%	$8.5 \cdot 10^3$	2463
Ph14	Boron (3%) modified PF resin	~10%	$9.8 \cdot 10^3$	13
Ph15	Fast cross-linking PF resin (HAP)	15%	$2.4 \cdot 10^5$	116
Ph16	Fast cross-linking PF resin	15%	$3.5 \cdot 10^4$	9.4
PhSi01	PF resin with polysiloxane	~10%	$3.3 \cdot 10^4$	152
PhSi02	PF resin with polysiloxane (10%wt)	~10%	$1.3 \cdot 10^4$	57.8
PhSi03	PF resin with polysiloxane	7-10%	$8.6 \cdot 10^3$	46
PhSi04	PF resin with polysiloxane	15%	$1.7 \cdot 10^4$	129

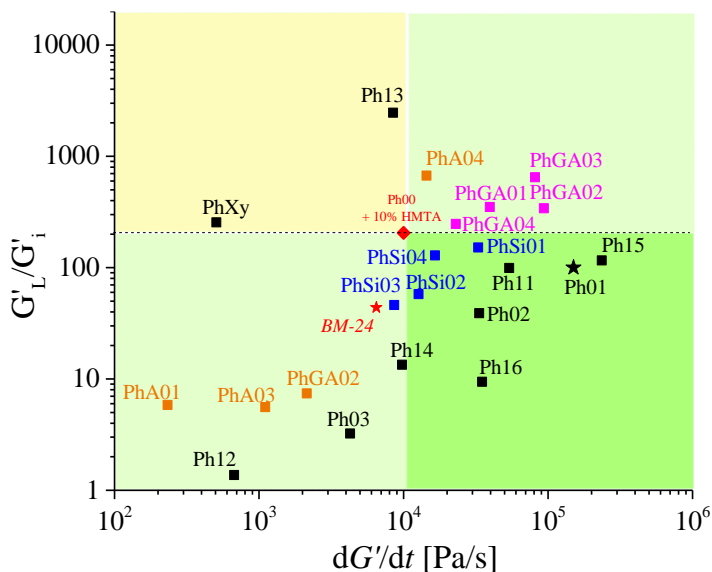


**Figure 3.25:** Curing efficiency chart for the PF resins and bismaleimide resin. The curing performances of a novolac HMTA free resin (sample Ph00) blended with 10%wt of HMTA used as a benchmark is indicated by the red lozenge. The color indicates the type of modifier: black: unmodified resins; orange, aralkyl/aryl modified resins; blue, silicon modified resins; magenta, acrylic modified resins. The HAP resin (quadrant I) is indicated with a black star. The bismaleimide resin (quadrant II) is indicated with a red star.

The values of the curing ratio  $G'_L/G'_i$  and the maximum curing rate  $(dG'/dt)_{\max}$  of all Melamine-based resins are reported in Table 3.5 and plotted in Figure 3.26 as a function of the maximum curing rate  $(dG'/dt)_{\max}$ .

From Figure 3.26, it is evident that the resins with no HMTA, MFPh05, MFPh06, MFPh07, MFPh02, and MFPh11, occupy the quadrant II, that is, they are already well cured at the beginning of the isotherm and slowly become stiffer during isotherm. All the resins with HMM amount between 25%wt and 40%wt, regardless of HMTA amount, namely MFPh08, MFPh09, and MFPh10 fall in the quadrant I, that is, they are already well cured at the beginning of the isotherm and quickly become stiffer during isotherm. In Figure 3.26 the cross-linking kinetics of the melamine resins MFPh05, MFPh06, MFPh02, and MFPh11 not containing HMTA is compared with the cross-linking kinetics of the sample MFPh04, MFPh01, MFPh03, and MFPh12, respectively, with HMTA content of 3-5.5 %, but identical HMM content (10, 25, 40 and 45%wt, respectively). It is apparent that the addition of HMTA results in a remarkable increase in the  $(dG'/dt)_{\max}$  value, and induces only a small increase of the  $G'_L/G'_i$  values. This indicates that whereas the maximum curing rate is controlled by the content of the chemical species used as hardener, the curing ratio is namely dependent on the chemical nature of the polymer matrix and the added compounds.

**Table 3.5** – Numeric descriptors deduced from rheology data of MF-based resins

Sample	Type of resin	Melamin	HMTA	$(dG'/dt)_{\max}$	$G'_L/G'_i$
<b>MFPh04</b>	Melamine mod. PF resin	10%	7,25%	$2.0 \cdot 10^4$	158
<b>MF02</b>	MF resin - PF resin	10%*	7,25%	$6.8 \cdot 10^3$	196
<b>MF04</b>	Melamine mod. PF resin	10%	5,5%	650	13
<b>MFPh05</b>	Melamine mod. PF resin	10%	-	21	12
<b>MFPh06</b>	Melamine mod. PF resin	25%	-	180	99
<b>MFPh01</b>	Melamine mod. PF resin	25%	5%	$1.4 \cdot 10^4$	71
<b>MFPh07</b>	Melamine mod. PF resin	25%-40%	-	709	36

<b>MFPh08</b>	Melamine mod. PF resin	25%-40%	3%	$4.0 \cdot 10^4$	53
<b>MFPh09</b>	Melamine mod. PF resin	25%-40%	6%	$3.7 \cdot 10^4$	75
<b>MFPh10</b>	Melamine mod. PF resin	25%-40%	9%	$3.1 \cdot 10^4$	76
<b>MFPh03</b>	Melamine mod. PF resin	40%	3%	$5.1 \cdot 10^4$	195
<b>MF03</b>	MF resin - PF resin	40%*	3%	$3.3 \cdot 10^3$	291
<b>MFPh02</b>	Melamine mod. PF resin	40%	-	$4.4 \cdot 10^3$	71
<b>MFPh11</b>	Melamine mod. PF resin	45%	-	$8.8 \cdot 10^3$	17
<b>MFPh12</b>	Melamine mod. PF resin	50%	1%	$3.0 \cdot 10^4$	142
<b>MF01</b>	MF resin	100%*	-	$7.2 \cdot 10^4$	8997

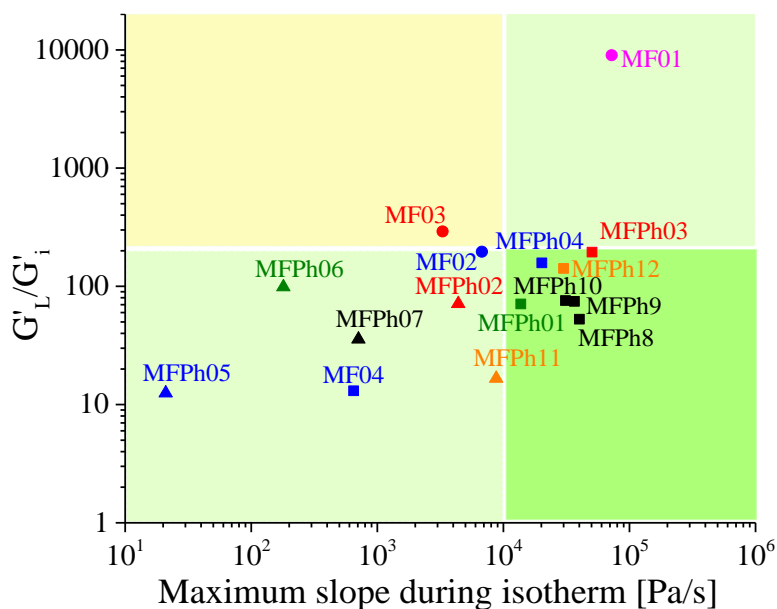


**Figure 3.26:** Curing efficiency chart for the melamine-based resins. The curing performances of a novolac HMTA free resin (sample Ph00) blended with 10% wt of HMTA, used as a benchmark, is not explicitly indicated. The color indicates the amount of melamine component in the resin: blue 10% wt, green 25% wt, black 25-40% wt, red 40% wt, orange 45-50% wt, and magenta 100% wt. The symbols indicate the type of melamine component: HMM without HMTA (▲), HMM with HMTA (■), MF resin (●).

### 3.4 Characterization of samples cured by compression molding

After curing by compression molding in a press, the samples show WAXS profiles characterized by the sole presence of a halo centered at  $2\theta \approx 19^\circ$ . The Bragg peaks of crystalline HMTA shown by the uncured samples disappear. As an example, the WAXS profiles of the PF resin Ph02 before and after curing are reported in Figure 3.27.

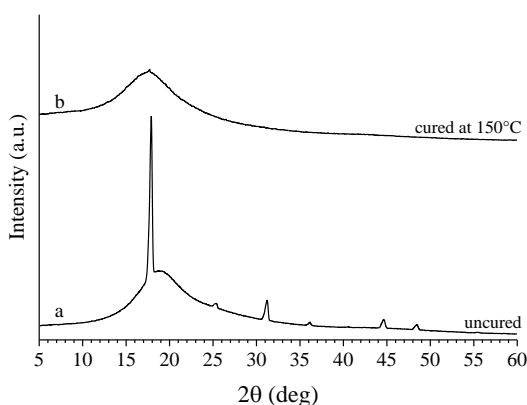


**Figure 3.27:** WAXS profiles of the resin Ph02 before (a) and after (b) curing by compression molding in a press. The curing temperature is 150 °C.

All the resins have been cured by compression molding at two different temperatures  $T_{cm}=T_{CL}$  and  $T_{cm}=T_{CL}+50^\circ\text{C}$  as described in chapter II for a time  $t_{cm}$  of 4 min and then have been characterized in order to obtain information about thermal stability and viscoelastic performances. These two properties are crucial for the final use of the thermoset.

#### 3.4.1 Thermal stability of the specimens

The thermal stability of the cured resins was evaluated by TGA. As an example, the TGA curves and the corresponding first derivate of PF resin Ph01 are reported in Figure 3.28. The samples were cured in a press at the temperatures  $T_{CL} = 150^\circ\text{C}$  and  $T_{CL}+50^\circ\text{C} = 200^\circ\text{C}$ . It is apparent that the thermal stability of the cured resins

increases with increasing the curing temperature. In particular, the value of  $T_{95\%}$  (that is the temperature at which the weight loss is 5%) increases from 250 to 416 °C, whereas the value of  $T_d$  (that is the temperature of maximum weight loss rate) increases from 552 to 630 °C.

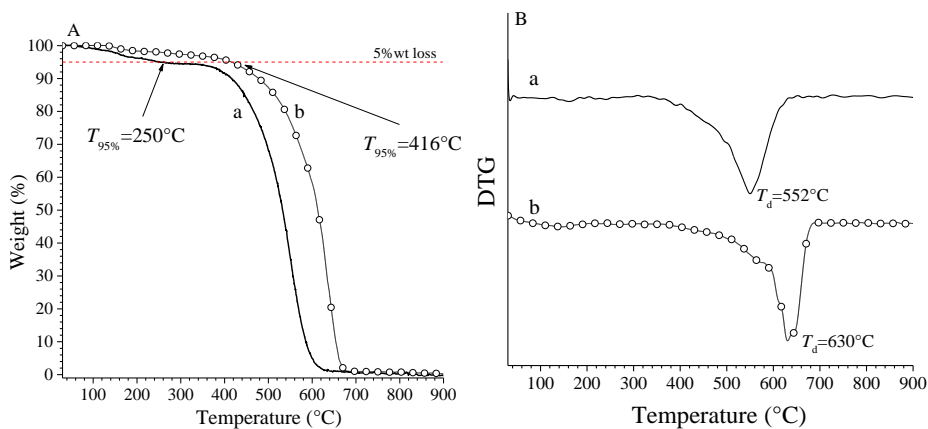


**Figure 3.28:** TGA curves (A) and corresponding first derivatives of the cured PF resin Ph01 obtained by compression molding at the cross-linking temperatures  $T_{cm}$  equal to  $T_{CL} = 150\text{ °C}$  (a) and  $T_{CL}+50\text{ °C} = 200\text{ °C}$  (b).

The values of  $T_{95\%}$  and  $T_d$  of the PF resins cured at  $T_{cm} = T_{CL}$  and  $T_{CL}+50\text{ °C}$  are reported in Figure 3.29. In general, the values of  $T_{95\%}$  and  $T_d$  of the PF resins cured at  $T_{cm} = T_{CL}+50\text{ °C}$  are higher than those of the resins cured at lower  $T_{cm} = T_{CL}$ . Furthermore, all PF resins show no significant weight loss up to  $\approx 350\text{ °C}$ . Exceptions occur for the samples Ph03 and Ph14 which are unmodified and boron-modified ortho-PF resins, respectively, and for the PhSi03 and Ph13 resins which are modified through the addition of a silicon derivate and graphite, respectively (Figure 3.29). The decrease of thermal resistance with increasing curing temperature is due to the fact that the mechanism of the crosslinking reactions depends on the temperature and composition. In particular, with increasing the curing temperature, the benzoxazine crosslinking mechanism tends to prevail over the benzylamine mechanism of crosslinking<sup>55,56</sup> causing subsequent changes in curing kinetic and in the stability of the final three-dimensional polymer network.

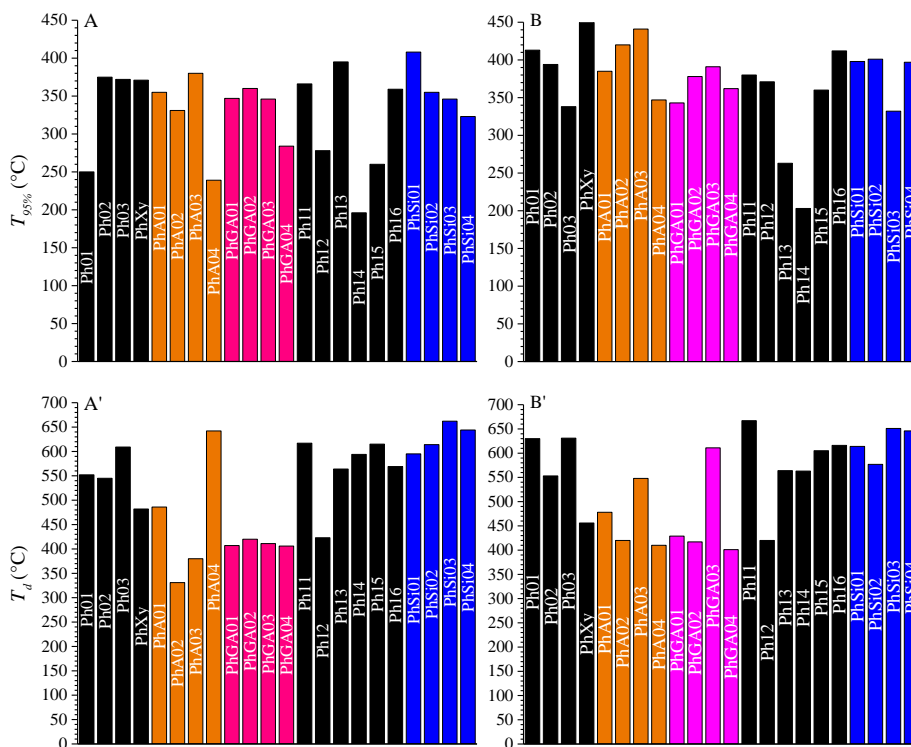


**Figure 3.29:** Values of  $T_{95\%}$  (A, B) and  $T_d$  (A',B') of the PF resins extracted from TGA analysis for specimens cured by compression-molding at different  $T_{cm}$  values equal to  $T_{CL}$  (A, B) and  $T_{CL}+50^\circ\text{C}$  (A',B'). The color indicates the type of modifier: black: unmodified resins; orange, aralkyl/aryl modified resins; blue, silicon modified resins; magenta, acrylic modified resins.

As an example, the TGA curves and the corresponding first derivative of the melamine modified sample MFPh02 cured at  $T_{cm} = T_{CL} = 150^\circ\text{C}$  and  $T_{CL} + 50^\circ\text{C} = 200^\circ\text{C}$  are reported in Figure 3.30. Unlike PF resins, for melamine modified PF resins the  $T_{95\%}$  value increases with increasing the curing temperature, whereas the value of  $T_d$  decreases. For instance, with increasing the curing temperature from  $T_{cm} = 150^\circ\text{C}$  to  $200^\circ\text{C}$ , the  $T_{95\%}$  value of the sample MFPh02 increases from 183 to  $327^\circ\text{C}$ . The temperature at which the thermal degradation reaches the maximum rate  $T_d$ , instead, decreases from  $\approx 640$  to  $\approx 625^\circ\text{C}$ .

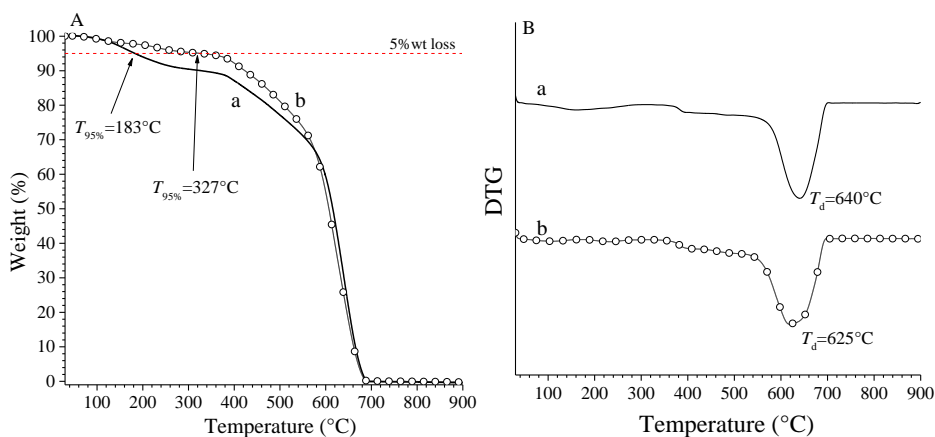


**Figure 3.30:** TGA curves (A) and corresponding first derivatives of the cured melamine resin MFPh02 obtained by compression molding at the cross-linking temperatures  $T_{cm}$  equal to  $T_{CL} = 150\text{ °C}$  (a) and  $T_{CL} + 50\text{ °C} = 200\text{ °C}$  (b).

The values of  $T_{95\%}$  of the melamine-based resins cured at  $T_{cm} = T_{CL}$  and  $T_{CL} + 50\text{ °C}$  are reported in Figure 3.31. In general, the higher the melamine amount, the lower the  $T_{95\%}$  value. For all melamine modified resins, the  $T_{95\%}$  values increase with increasing the curing temperature (Figure 3.31). Furthermore, except for the resins MFPh07, MFPh08, MFPh09, and MFPh10, the weight loss is not remarkable up to  $\approx 300\text{ °C}$ , especially for the resins cured at  $T_{cm} = T_{CL} + 50\text{ °C}$  ( $T_{95\%} > 300\text{ °C}$ ).

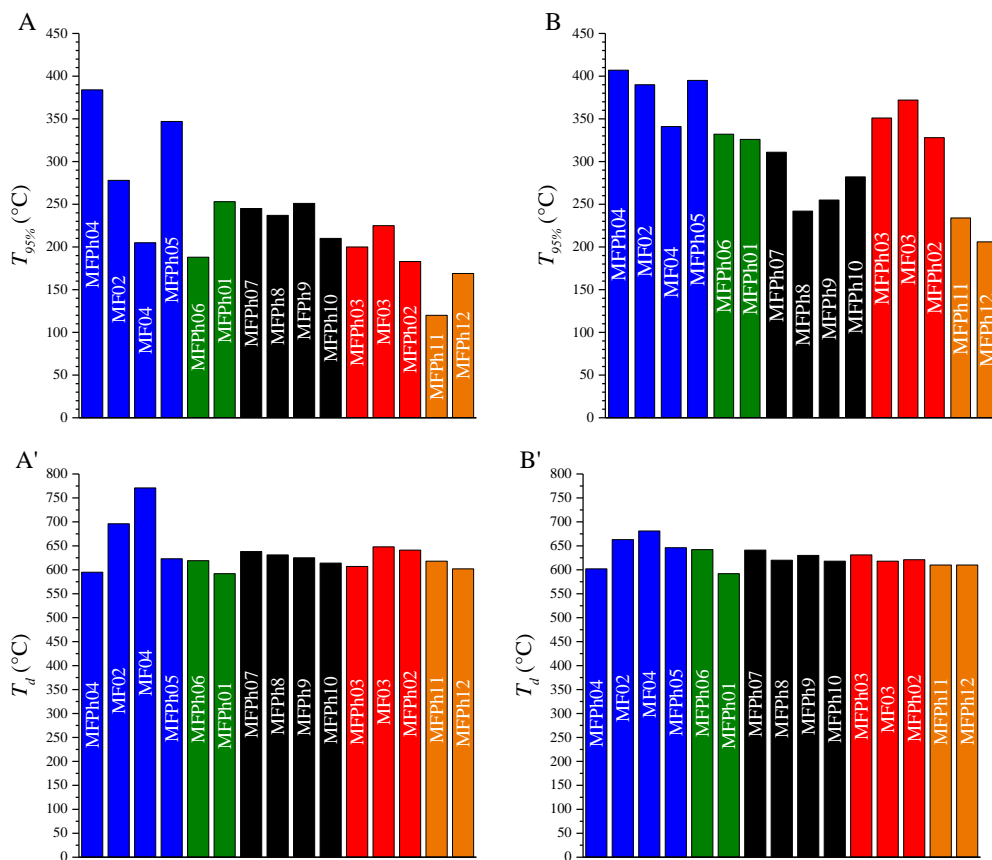


**Figure 3.31:** Values of  $T_{95\%}$  (A, B) and  $T_d$  (A', B') of the maleimide modified PF resins extracted from TGA analysis for specimens cured by compression molding at different  $T_{cm}$  values equal to  $T_{CL}$  (A) and  $T_{CL}+50^\circ\text{C}$  (B). The color indicates the amount of melamine component in the resin: blue 10% wt, green 25% wt, black 25-40% wt, red 40% wt, and orange 45-50% wt.

### 3.4.2 Viscoelastic properties of the specimens

The viscoelastic properties of the cured samples were investigated by performing DMTA measurements. Measurements were performed on samples cured for 4 min in a press at two different temperatures, that is  $T_{CM} = T_{CL}$  and  $T_{CM} = T_{CL} + 50$  or  $60^\circ\text{C}$ . It is worth noting that in the adopted curing conditions, the storage modulus is systematically higher than the loss modulus, in the whole temperature range. This indicates that a three-dimensional network structure is always formed.

As an example, the curves of storage and loss moduli and  $\tan \delta$  of two PF resins, namely the HAP resin Ph01 and the xylene modified resin PhXy are reported in Figure 3.32 as a function of temperature. The DMTA curves of all other PF resins are reported in the Appendix A3.3. For each sample, the DMTA curves were measured at two different curing temperatures,  $T_{cm} = 150$  and  $200$  °C for the sample Ph01 (Figure 3.32A) and  $160$  and  $210$ °C for the sample PhXy (Figure 3.32B), are compared.

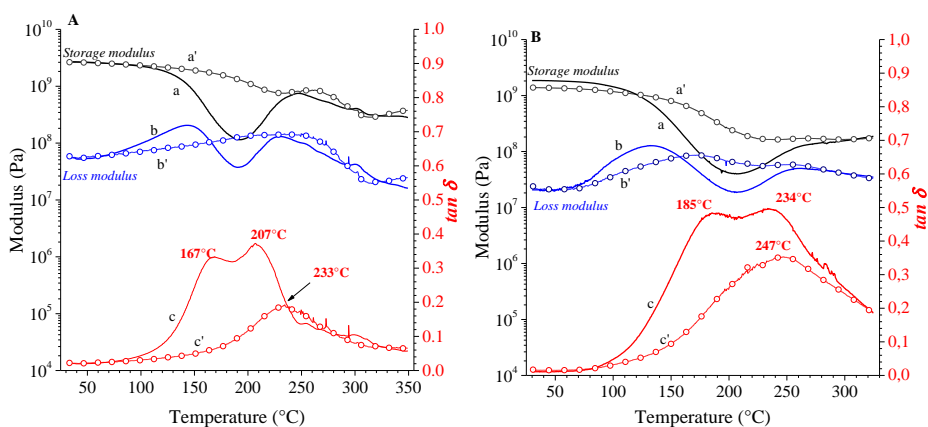


**Figure 3.32:** Storage modulus (a,a'), loss modulus (b,b'), and  $\tan \delta$  (c,c') as a function of temperature for the HAP resin Ph01 (A) cured at  $T_r = 150$  °C (a-c) and  $200$  °C (a'-c') and the Xylene modified PF resin PhXy (B) cured at  $T_r = 160$  °C (a-c) and  $210$  °C (a'-c'). In all cases, the curing time is fixed to 4 min.

For the HAP resin (sample Ph01) cured at  $150$  °C (Figure 3.31A), the storage (curve a, Figure 3.32A) and loss (curve b, Figure 3.32A) moduli are initially nearly constant. Then, with increasing temperature up to  $200$  °C, the storage modulus decreases by one order of magnitude accomplished by an increase of the loss modulus and development of a double-peaked  $\tan \delta$  maximum at  $168$  and  $207$  °C, due to the occurrence of complex relaxation phenomena pinned to the glass transition (curve c, Figure 3.32A). The decrease of storage modulus and the presence of the maximum in the  $\tan \delta$  indicates that the sample cured at  $150$  °C is only partially cross-linked and that the network formed at  $150$  °C is heterogeneous, being characterized by regions of different segmental mobility. At temperatures

higher than 200 °C, the values of storage and loss modulus approach a quasi plateau, indicating that no relevant further cross-linking reactions occur in the measurement conditions. For the HAP resin cured at 200 °C for 4 min, instead, the values of storage and loss modulus and  $\tan \delta$  (curves a'-c', Figure 3.32A) are almost constant throughout the entire explored temperature range. Only a slight decrease of the storage modulus (curve a', Figure 3.32A) and a slight increase of the loss modulus (curve b', Figure 3.32A) are, indeed, observed, associated with a faint and broad peak at 258 °C in the  $\tan \delta$  curve (curve c', Figure 3.32A), indicating that collective relaxation phenomena from mobile segments in the network still occur, even if these movements are highly damped and more damped than those occurring in the resin cured at 150 °C. This suggests that at 200 °C the cross-linking reactions occur almost completely using a curing time of 4 min.

Similar behavior is observed for the Xylene modified PF resin PhXy cured at 160 °C (Figure 3.32B). In particular, the storage modulus decreases (curve a, Figure 3.32B), and the loss modulus increases (curve b, Figure 3.32B) at temperatures higher than nearly 100 °C. Correspondingly, the  $\tan \delta$  curve shows a double-peaked maximum centered at 185 and 234 °C, (curve c, Figure 3.32B), indicating incomplete cross-linking and large heterogeneities of the formed network. Then, at temperatures higher than 250 °C, the storage modulus tends to increase, whereas the loss modulus tends to decrease with increasing temperature, due to the occurrence of additional cross-linking reactions (Figure 3.32B). For the resin PhXy cured at 210 °C, instead, the cross-linking reactions occur almost completely (curves a'-c', Figure 3.32B) as indicated by the weak decay of the storage modulus (curves a'), the small and broad maximum of the loss modulus (curve b'), and the broad and low-intensity maximum of the  $\tan \delta$  peak at 247 °C (curves c') that replace the strong maxima at lower temperatures of the resin cured at 160 °C (curves c). The presence of the  $\tan \delta$  maximum indicates that relaxation phenomena involving the phenol-formaldehyde main chain and/or constrained silicone segments included in the resin network are not completely suppressed.

The  $\tan \delta$  curve of the HAP resin Ph01 cured at 150°C is reported in Figure 3.33. The different viscoelastic behavior of the cured resins may be characterized using as parameters the position ( $T_g$ ), the height ( $I_{\max}$ ), and the half-width at half-height ( $w_{(1/2)}$ ) of the  $\tan \delta$  peaks, defined in Figure 3.33. Although the exact value of these viscoelastic parameters depends on a multiplicity of different factors, their values give information about the degree of cross-linking and efficiency of the curing. In particular, high values of  $I_{\max}$  indicate low cross-linking density as fully cross-linked resins should virtually present flat  $\tan \delta$  curves with no maxima. The temperature of the maximum in  $\tan \delta$  corresponds to the glass transition temperature  $T_g$ , due to the main relaxation of the mobile (generally long) segments comprised in between the nodes of the network. At temperatures higher than  $T_g$ , the global viscosity decrease, so that post-curing reactions may easily occur, provided that the mobility of the network strands bearing unreacted groups with complementary functionality is at least in part activated. Usually, high values of the glass transition temperature indicate a high degree of crosslinking associated with scarce segmental mobility at lower temperatures. Finally, the value of the half-width at mid-height  $w_{(1/2)}$  of a  $\tan \delta$  peak, represents a measure of the complexity of chain dynamics of the network. In particular, high values of  $w_{(1/2)}$ , indicate the formation of a heterogeneous network that includes regions of high and low segmental mobility due to a low or high cross-linking density, respectively. The size of these regions is rather big as the glass transition corresponds to collective dynamics of chains over domains of the order of 3-5 nm<sup>63,64</sup>. For the sake of simplicity, in the cases of samples that show double-peaked maxima in  $\tan \delta$ , the parameters  $T_g$ ,  $I_{\max}$ , and  $w_{(1/2)}$  are measured only for the first (low temperature) peak (Figure 3.33).

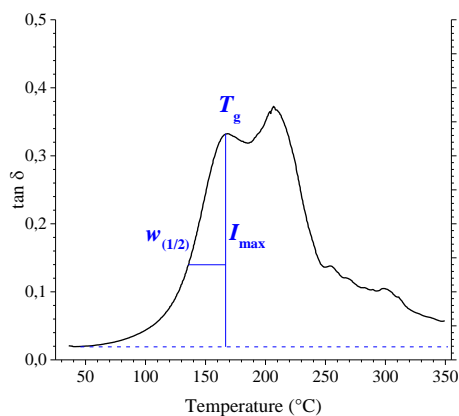


**Figure 3.33:** Definition of the parameters that measure the dynamic-mechanical behavior of a cross-linked resin, in correspondence of a  $\tan \delta$  peak, determined as a function of temperature in a DMTA experiment carried out at constant frequency and low strain amplitude. The parameters are the  $\tan \delta$  peak position, corresponding to the glass transition temperature  $T_g$ , the height of the maximum peak  $I_{\max}$  and the half-width at mid-height  $w_{(1/2)}$  of the peak. For a multiple peaked  $\tan \delta$  maximum such as the curve shown in the figure, only the low temperature peak is considered.

The so-determined values of the viscoelastic parameters deduced from the  $\tan \delta$  peaks of the PF resins of Table 3.1 are reported in Table 3.6. It is worth noting that almost all PF resins cured at  $T_{\text{cm}} = T_{\text{CL}}$  show double-peaked maxima in  $\tan \delta$ . The resins cured at  $T_{\text{cm}} = T_{\text{CL}} + 50\text{-}60$  °C, instead, show  $\tan \delta$  maxima peaked at a single temperature. Furthermore, the resin Ph14 cured at  $T_{\text{CL}}$  and the resin Ph12 cured at both temperatures give brittle specimens, so that the DMTA curves could not be measured.

It is apparent that, with increasing the curing temperature, all the samples exhibit a shift of  $T_g$  toward higher temperatures and a decrease of peak intensity  $I_{\max}$ . However, the changes in the values of the half-width at mid-height  $w_{(1/2)}$  of the  $\tan \delta$  peaks appear rather random. Since for the resins cured at  $T_{\text{CL}}$  only the first  $\tan \delta$  peak is considered, the reported values of  $w_{(1/2)}$  in Table 3.6 correspond to the half-width at mid-height of the first peak. Therefore, the effective values of the half-width at mid-height of the double-peaked  $\tan \delta$  maxima should be almost twice the reported values of  $w_{(1/2)}$ . This means that the values of the parameter  $w_{(1/2)}$  for the resins cured at higher temperature tend to decrease compared with twice the reported values of

$w_{(1/2)}$  of the resins cured at  $T_{CL}$  (Table 3.6), suggesting that at higher cross-linking temperature the cross-linking density increases, whereas the degree of heterogeneity in the cross-link distribution decreases.

**Table 3.6** – Values of the viscoelastic parameters, namely glass transition temperature  $T_g$ , height of the maximum  $I_{max}$  and half-width at mid-height  $w_{(1/2)}$  relative to the first  $\tan \delta$  peak, measured from DMTA analysis relative to the PF resins of Table 3.1.<sup>a</sup>

	$T_{cm} = T_{CL}$			$T_{cm} = T_{CL} + 50^\circ C$		
	$T_g$ ( $^\circ C$ )	$I_{max}$	$w_{(1/2)}$ ( $^\circ C$ )	$T_g$ ( $^\circ C$ )	$I_{max}$	$w_{(1/2)}$ ( $^\circ C$ )
<b>Ph01</b>	167, (207)	0.30	37	234	0,15	33
<b>Ph02</b>	162	0.26	33	171	0.17	42
<b>Ph03</b>	140	0.35	33	132	0,32	25
<b>PhXy</b>	185, (234)	0.47	41	247	0,34	68
<b>PhA01</b>	128, (233)	0.49	34	141	0,42	32
<b>PhA02</b>	225	0.56	56	254	0,49	59
<b>PhA03</b>	135, (202)	0.61	15	261	0,41	15
<b>PhA04</b>	213	0.37	63	217	0,31	72
<b>PhGA01</b>	202	0.13	43	238	0,06	25
<b>PhGA02</b>	193	0.42	25	246	0,09	39
<b>PhGA03</b>	200	0.21	34	276	0,05	32
<b>PhGA04</b>	198	0.06	30	234	0.03	40
<b>Ph11</b>	175, (208)	0.31	33	224	0,26	36
<b>Ph12</b>	n.a	n.a	n.a	n.a	n.a	n.a
<b>Ph13</b>	146, (215)	0.25	38	166	0,16	44
<b>Ph14</b>	n.a	n.a	n.a	147	0,32	45
<b>Ph15</b>	212	0.41	58	223	0,31	36
<b>Ph16</b>	214	0.22	57	253	0,18	37
<b>PhSi01</b>	202	0.32	54	217	0.24	43
<b>PhSi02</b>	205	0.37	73	218	0.30	55
<b>PhSi03</b>	143	0.49	34	163	0.26	41
<b>PhSi04</b>	168, (210)	0.27	52	215	0.17	nd

<sup>a</sup>Legenda: n.a. = not available; n.d. = not determined. Some PF resins cured at low temperatures show a double-peaked  $\tan \delta$  maximum. The high temperature  $T_g$  is indicated in parentheses. In these cases, the values  $I_{max}$  and  $w_{(1/2)}$  are relative to the sole  $T_g$  peak occurring at low temperature.

The DMTA curves of two melamine-based resins are reported in Figure 3.33, as an example. The DMTA curves of all other MF resins are reported in Appendix A3.3. Data in Figure 3.34 are relative resins MFPh02 containing 40%wt of HMM component and 0% HMTA and to the MF modified resin MF03 containing 40 %wt of PF resin and 3%wt of HMTA. Both samples are cured at  $T_{cm} = 150$  and  $200$  °C by compression molding in a press for 4 min. The viscoelastic behavior of these resins is different. The resin MFPh02 cured at  $T_{cm} = 150$  °C shows a weak  $\tan\delta$  peak at  $T_g = 160$  °C (curve c, Figure 3.34A). Furthermore, the specimen becomes brittle at high temperatures and breaks at  $250$  °C. The specimen cured at  $T_{cm} = 200$  °C, instead, shows higher thermal resistance (curve a', Figure 3.34A). At temperatures lower than  $150$  °C the conservative and loss moduli of the resin cured at  $T_{cm} = 200$  °C are higher than the corresponding values of the resin cured at  $T_{cm} = 150$  °C, and become lower at temperatures higher than  $150$ - $200$  °C. Furthermore, the specimens cured at  $200$  °C show a broad glass transition at  $\approx 213$  °C with a half-width at mid-height  $w_{(1/2)}$  of  $66$ °C.

The different behavior of the melamine resin MFPh02 containing 40%wt of HMM component and no HMTA at low and high curing temperatures can be explained by the influence of the temperature on reversible cross-linking reactions involving methylol group or by the occurrence of curing competitive reactions<sup>42</sup> (see Chapter 1). At low curing temperatures, e.g.  $150$ °C, the curing of a melamine resin mainly involves cross-linking reactions among the novolac functional groups and no significant HMM participation. During a DMTA measurement, the so-obtained network is subjected to additional, reversible reactions. These reactions involve cross-reactions at low temperatures through the formation of methylol groups, which lead to an increase in the cross-linking density. However, at high temperatures, the inverse reactions that lead to a gradual breaking of the chemical bonds become prevalent, up to induce complete rupture of the sample at  $250$  °C. At high curing temperatures such as  $200$  °C, instead, the active participation of the HMM species in the crosslinking reactions results in the formation of more stable networks, able to

resist reversible crosslinking reactions involving methylol groups, even at high temperatures.

For the resin MF03 cured at  $T_{cm} = 150$  °C, the conservative  $G'$  and loss  $G''$  shear moduli (curves a and b, Figure 3.34B) show broad undulations, due to superimposition of post-curing reactions among the residual functional groups that lead to an increase of moduli, and relaxation phenomena, that lead to a decrease of the moduli. This waviness corresponds to a  $\tan \delta$  curve (curves c, Figure 3.34B) that shows a first relaxation peak at 150 °C with  $I_{max} = 0.34$ , followed by two additional relaxation peaks at 192 °C and 273 °C. The presence of multiple peaks in the  $\tan \delta$  curve associated with undulations of the conservative and loss moduli indicates that the sample is only partially crosslinked at 150 °C and experiences complex and heterogeneous dynamics during the heating.

The conservative  $G'$  and loss  $G''$  shear moduli of the resin MF03 cured at  $T_{cm} = 200$  °C, instead, show a more regular behavior. With increasing the temperature the conservative shear modulus (curves a', Figure 3.34B) tends to decrease, whereas the loss modulus (curves b', Figure 3.34) tends to increase. Both curves show a small drop at around 287 °C. Simultaneously, the corresponding loss factor  $\tan \delta$  (curves c', Figure 3.34B) shows a complex and broad peak at  $T_g \approx 287$ °C, due to the relaxation of the residual mobile segments in the material, according to highly heterogeneous dynamics.

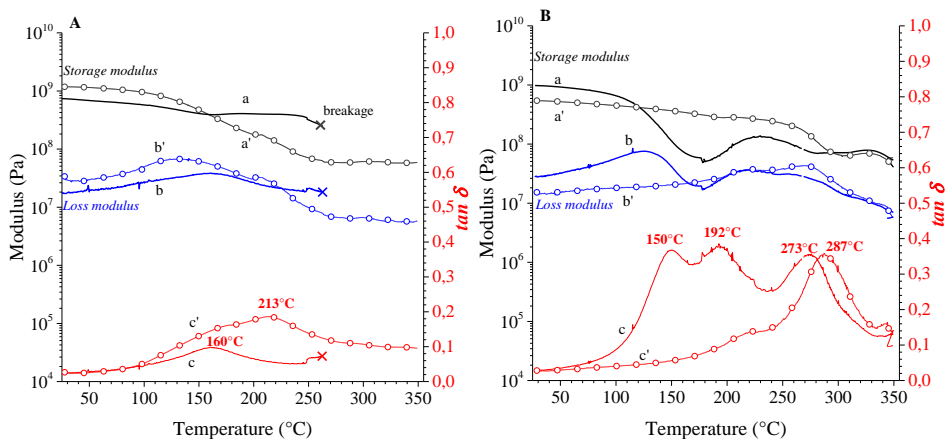


**Figure 3.34:** Storage modulus (a,a'), loss modulus (b,b'), and  $\tan \delta$  (c,c') as a function of temperature for the melamine resin MFPh02 with 40%wt of HMM and 0% HMTA (A) and MF03 with 40%wt of MF-resin and 3%wt of HMTA (B). The samples are cured 150 (a-c) and 200°C (a'-c'). In all cases, the curing time is fixed to 4 min.

The values of the viscoelastic parameters deduced from the  $\tan \delta$  peaks of the melamine resins of Table 3.2 are reported in Table 3.7. The resin MFPh06 cured at  $T_{CL}+50$  and the resin MF01 cured at both temperatures are brittle and produce a large emission of gas during heating. For this reason, DMTA measurements have not been performed. The resins MFPh07, and MFPh02 cured at  $T_{CL}$ , and the resins MFPh01, MFPh08, MFPh09, MFPh10, MFPh03, MFPh11, and MFPh12 cured at low and high temperature undergo breaking during the DMTA scan at temperatures higher than 250 °C.

Also for this set of samples, the values of  $T_g$  increase and those  $I_{max}$  decrease with increasing the curing temperature. Furthermore, also for these samples cured at high temperatures, the values of the parameter  $w_{(1/2)}$  tend to decrease with respect to the doubled values of  $w_{(1/2)}$  of the resins cured at  $T_{CL}$  (Table 3.7).

**Table 3.7** – Values of the viscoelastic parameters, namely glass transition temperature  $T_g$ , height of the maximum  $I_{\max}$  and half-width at mid-height  $w_{(1/2)}$  relative to the first  $\tan \delta$  peak, measured from DMTA analysis relative to the melamin resins of Table 3.2.<sup>a</sup>

	$T_{cm} = T_{CL}$			$T_{cm} = T_{CL} + 50^\circ\text{C}$		
	$T_g$ (°C)	$I_{\max}$	$w_{(1/2)}$ (°C)	$T_g$ (°C)	$I_{\max}$	$w_{(1/2)}$ (°C)
<b>MFPh04</b>	207	0.28	62	273	0.08	53
<b>MF02</b>	150, (198)	0.28	32	200	0.17	71
<b>MF04</b>	155, (193)	0.24	46	240	0.02	40
<b>MFPh05</b>	135	0.82	26	135	0.47	37
<b>MFPh06</b>	172	0.25	32	n.a	n.a	n.d.
<b>MFPh01</b>	183	0.22	33	n.a	n.a	n.a.
<b>MFPh07</b>	147	0.35	28	220	0.06	56
<b>MFPh08</b>	184	0.19	27	n.a	n.a	n.a.
<b>MFPh09</b>	200	0.15	31	n.a	n.a	n.a.
<b>MFPh10</b>	217	0.17	46	n.a	n.a	n.a.
<b>MFPh03</b>	199	0.08	67	250	0.08	14
<b>MF03</b>	150, (193)	0.34	26	287	0.33	30
<b>MFPh02</b>	162	0.07	40	200	0.16	66
<b>MFPh11</b>	125, (175)	0.39	24	269	0.04	47
<b>MFPh12</b>	124, (170)	0.45	22	265	0.04	35
<b>MF01</b>	n.d	n.d	n.d.	n.d	n.d	n.d.

<sup>a</sup>Legenda: n.a. not available; n.d. not determined. Some PF resins cured at low temperatures show multiple peaked  $\tan \delta$  maxima. The high-temperature  $T_g$  is indicated in parentheses. In these cases, the values  $I_{\max}$  and  $w_{(1/2)}$  are relative to the sole  $T_g$  peak occurring at low temperature.

## CHAPTER IV: SELF-HEALING SYSTEM

### 4.1 The self-healing system: PF resin/PA12 blends

The blending of PF resins with thermoplastic polymers is a simple, efficient, and economic way to modify the properties and the performance of the final material, and it could be used for achieving self-healing properties. The use of polyamides as additives in the thermosetting resin matrix is not new<sup>65-67</sup>, but they had not been used yet to obtain self-healing composites.

Among the PF resins described in Chapter III, the resin Ph01, which is the commercial-grade of Hexamine Adduct Phenolic (HAP) technology, has been selected to produce blends with a polyamide. In HAP resin, the cross-linking agent, hexamethylenetetramine (HMTA), is added into the melted polymer to ensure a good dispersion.

The self-healing system is obtained by mixing powders of the curable HAP resin with the polyamide 12 (PA12) in form of white powder finely ground. The powder blend is then compression-molded to obtain a composite cured material in the shape of bars (length, width, and thickness of 50, 10, and 1.5÷2 mm, respectively).

#### 4.1.1 Analysis of the PA12 sample

The used PA12 is a commercial-grade polyamide. PA12 crystallizes in four different forms, the principal ones being the  $\alpha$ - and  $\gamma$ -forms. The  $\gamma$ -form is obtained by crystallization from the melt in common condition,  $\alpha$ -form can be obtained by crystallization from the melt under pressure at 500MPa, by precipitation from phenol-ethanol solution, or by stretching at a temperature close to the melting temperature<sup>68</sup>.

PA12 exhibits properties intermediate between short-chain aliphatic nylons (e.g., nylon 6 and nylon 66) and polyolefins<sup>52</sup>, the melting temperature is the lowest among the important polyamides, and the mechanical properties, such as hardness,

tensile strength, and abrasion resistance, are similar to those of nylon 6 and nylon 66. Low water absorption and density, 1.01 g/mL, result from its relatively long hydrocarbon chain length in repeating unit (Figure 4.1), which also confers its dimensional stability and an almost paraffin-like structure<sup>52</sup>.

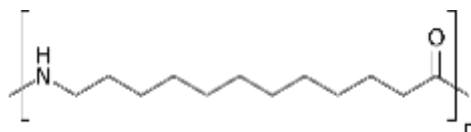
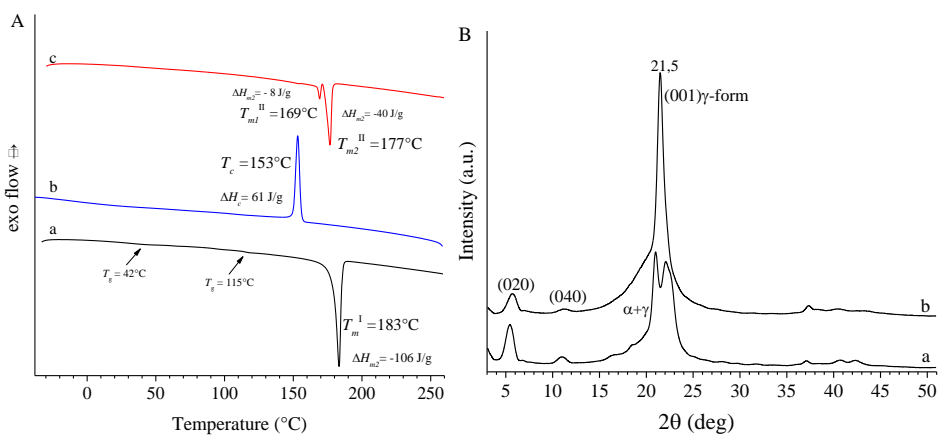


Figure 4.1. Repeating unit of PA12

The DSC curves of the PA12 sample recorded at scanning rate of 10 °C/min during heating, cooling from the melt and the second heating of the melt crystallized samples are reported in Figure 4.2A. The sample presents a melting temperature of 183 °C and crystallization temperature of 153°C. The melt-crystallized samples melt at 177°C.

The X-ray diffraction profiles of the as-prepared powder sample of PA12 and the sample crystallized from the melt by compression molding at 210 °C and cooling down to room temperature at ~20°C/min are shown in Figure 4.2B. The diffraction profile of the as-prepared sample (profile a, Figure 4.2B) shows the 040, 020, and 001 reflections at  $2\theta \approx 5.7$ , 11.1, and 21.5° of the  $\gamma$  form<sup>69</sup> and the 200 reflection at about  $2\theta \approx 20.5^\circ$  of the  $\alpha$  form<sup>70</sup> of PA12, indicating that the sample is crystallized in a mixture of  $\alpha$  and  $\gamma$  forms. The sample crystallizes from the melt in the pure  $\gamma$  form, as indicated by the diffraction profile of the compression-molded sample (profile b, Figure 4.2B) that presents only the 040, 020, and 001 reflections of the  $\gamma$  form<sup>69</sup> at  $2\theta \approx 5.7$ , 11.1, and 21.5°.



**Figure 4.2.** (A) DSC curves of the sample of PA12 recorded at  $10^\circ\text{C}/\text{min}$  during the 1<sup>st</sup> heating of the as-prepared sample (a), cooling from the melt (b) and 2<sup>nd</sup> heating (c). (B) WAXS profiles of the as-prepared sample of PA12 (a) and the sample crystallized from the melt after compression molding (b).

In order to better understand the performance of the PA12, the specimen obtained by compression molding has been also characterized by TGA and DMTA (Figure 4.3). The temperatures corresponding to 5% wt weight loss  $T_{95\% \text{wt}}$  corresponds to  $523^\circ\text{C}$ . The first derivative of the TGA curve shows two maxima, indicating that degradation occurs in two steps with maximum rate at  $T_{d1}$  and  $T_{d2}$  equal to  $561$  and  $582^\circ\text{C}$ , respectively. The high values of  $T_{95\% \text{wt}}$ ,  $T_{d1}$ , and  $T_{d2}$  confirm the high thermal stability of the sample (Figure 3A).

The DMTA scan (Figure 4.3B) performed in the range  $20$ - $140^\circ\text{C}$  (Figure 4.3B), shows a glass transition temperature of  $58^\circ\text{C}$ , evaluated as the  $\tan \delta$  peak maximum. Owing to the high crystallinity, this glass transition phenomenon is not very intense with  $\tan \delta$  peak intensity  $I_{\text{max}} = 0.07$  and width  $w_{(1/2)} = 17^\circ\text{C}$ .

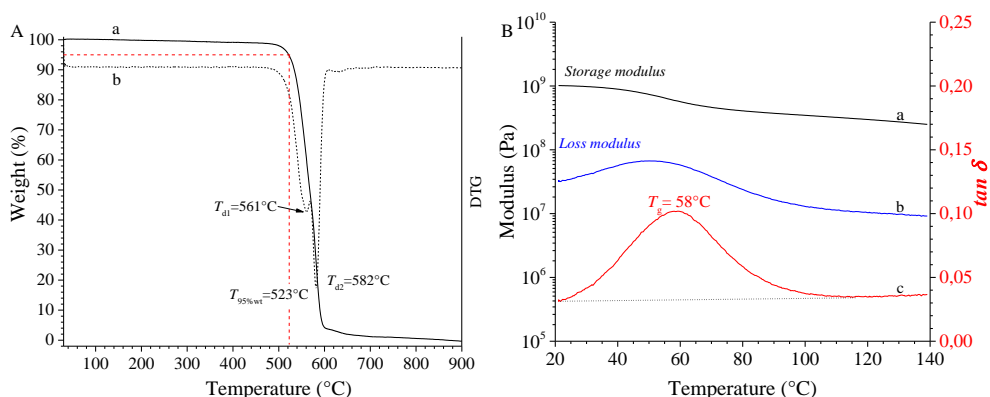


**Figure 4.3.** (A) TGA curve (a) and corresponding first derivate (b) and (B) DMTA curves showing storage(a) and loss (b) moduli and  $\tan\delta$  (c) of the compression molded sample of PA12.

#### 4.1.2 Analysis of the HAP resin/PA12 blends

The powders of the HAP resin and the PA12 have been mixed at various compositions and the obtained blends have been named “B1\_xy” where x and y indicate the relative amount of the resin and the PA12, respectively (e.g., B1\_8020 indicates the blend with 80wt% of HAP resin and 20wt% of PA12).

The DSC heating curves of the as-prepared powders of the blends B1\_xy with the amount of PA12 variable from y = 5 wt% to y = 50 wt%, and the neat components, are reported in Figure 4.4. As discussed in Chapter III the DSC of the pure HAP resin shows a softening endothermic peak at temperature  $T_s = 66$  °C and a cross-linking exothermic peak at temperature  $T_{CL} = 152$  °C (curve a, Figure 4.4 and Table 4.1). The softening phenomenon is visible also in the blends with PA12 even though it becomes less pronounced and the area of the softening peak decreases with increasing the content of PA12 in the DSC curves of the samples B1\_xy (curves b-g, Figure 4.4).

A remarkable effect of the presence of PA12 is instead observed in the DSC region of the curing temperature  $T_{CL}$ . In fact, the cross-linking temperature, indicated by the position of the exothermic peak  $T_{CL}$ , increases with increasing PA12 content from

$T_{CL} = 152$  °C of the neat resin to  $T_{CL} = 163$  °C of the sample with 50 wt% of PA12 (curve g, Figure 4.4), whereas the enthalpy of the curing reaction, indicated by the area of the exothermic peak, decreases with increasing the PA12 content (curves b-g, Figure 4.4). Furthermore, along with the increase of temperature and decrease of enthalpy of the curing reaction, a new endothermic peak at temperature  $T_1$  close to the curing temperature  $T_{CL}$  appears in the DSC curves of blends and is well visible in the samples with 40 and 50 wt% of PA12 (curves f and g, Figure 4.4).

Finally, the DSC curves of the blends B1\_xy of Figure 4.4 also show the melting endotherm of the PA12 that is visible starting from the sample B1\_8020 with 20 wt% of PA12 (curve d, Figure 4.4). The melting temperature of crystals of PA12 in the blends is lower than that of the pure PA12 and decreases with increasing PA12 content, from 183 °C of the pure PA12 (curve h, Figure 4.4) to 176 °C of the sample B1\_8020 (curves d-h, Figure 4.4 and Table 4.1).

The results of the thermal analysis performed on the blends B1\_xy with a clear increase of the softening and curing temperatures of the PF resin and decrease of the melting temperature of the PA12, indicate that some interactions between the PF resin and the PA12 occur. Possible miscibility between the two components may be also associated with the establishment of some chemical interactions of amorphous chains of PA12 and the PF resin. The development of an endothermic peak at temperature  $T_1$  just before the cross-linking at  $T_{CL}$  indicate that in the initial heating step of the unreacted powder blends, simultaneously or just before the curing reaction of the PF resin with HMTA, a second phenomenon may occur between the substituents of the aromatic rings of the PF resin and the nitrogen atom in the polyamide backbone, with the formation of hydrogen bonds between the amide groups and the hydroxyl groups of PF resin. The thermal behavior of the B1 blends suggests that PA12 has a non-innocent role in the cross-linking behavior of the HAP resin. Indeed, after the softening point, the uncured HAP species are liquid-like whereas the PA12 component is still solid, thus forming a sort of slurry. Probably, efficient hydrogen bond interactions are already established at this stage.

The good dispersion of PA12 in the blends is essentially due to the establishment of hydrogen bonds between the amide groups of PA12 chains and the hydroxyl groups of PF resin, even though, based on the work of Ravve et al.<sup>71</sup>, the formation of chemical bonds at amide/hydroxy groups interface may not be excluded. The values of the relevant temperatures extracted from the DSC thermograms of Figure 4.4 are reported in Table 4.1.

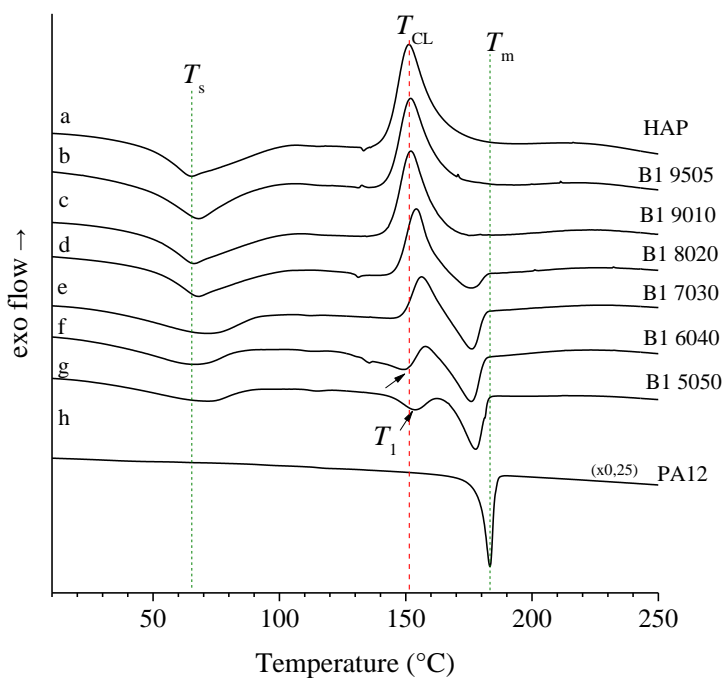


**Figure 4.4.** DSC heating thermograms of the as-prepared powder of the neat components and blends B1\_xy (HAP/PA12). The arrows indicate the new endothermic phenomenon at temperature  $T_1$ . a) pure resin HAP; b) B1-9505, c) B1-9010, d) B1-8020, e) B1-7030, f) B1-6040, g) B1-5050, h) pure PA12.

**Table 4.1.** Values of the softening ( $T_s$ ) and cross-linking ( $T_{CL}$ ) temperatures of the HAP resin, and melting temperature ( $T_m$ ) of PA12 extracted from DSC thermograms of Figure 4.4 relative to the neat components and the uncured blends B1.

Samples	$T_s$ (°C)	$T_{CL}$ (°C)	$T_m$ (°C)	$T_i$ (°C)
HAP	66	152	-	-
B1-9505	68	152	-	-
B1-9010	66	152	-	-
B1-8020	68	154	176	-
B1-7030	71	157	176	143
B1-6040	67	158	176	149
B1-5050	72	163	178	154
PA12	-	-	183	-

The X-ray diffraction profiles of the compression-molded cured samples of the blends B1\_xy are reported in Figure 4.5. The HAP resin, the PA12, and the blends B1\_xy have been cured at 200 °C for 10 min between the platens of a heating press. As already shown in Chapter III, the pure HAP resin is amorphous after curing and compression molding, the diffraction profile showing only a broad amorphous halo centered at  $2\theta = 18^\circ$  and no reflections of the hardener HMTA are visible (profile a, Figure 4.5). The diffraction profiles of the blends B1\_xy present the 020, 040, and 001 reflections of the  $\gamma$  form of PA12, whose intensities increase with increasing PA12 concentration (profiles b-h of Figure 4.5).

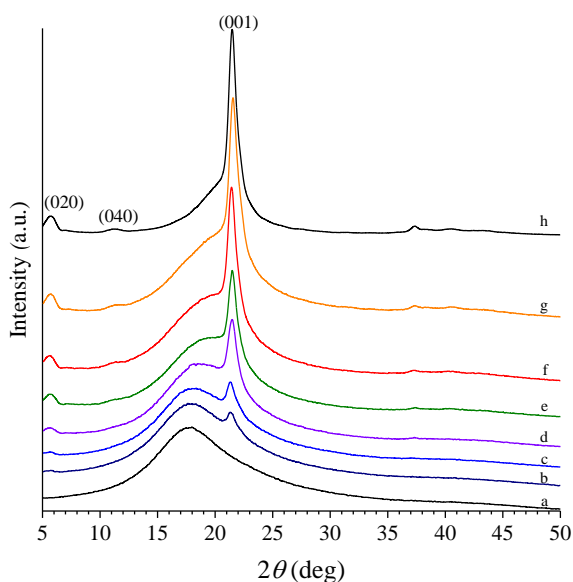


**Figure 4.5.** WAXS profiles of the compression-molded specimen of the blends HAP/PA12 reported in table 4.1. a) pure resin HAP; b) B1-9505, c) B1-9010, d) B1-8020, e) B1-7030, f) B1-6040, g) B1-5050, h) pure PA12.

The DSC curves of the cured compression molded samples of the blends B1\_xy recorded during first heating, cooling from the melt and second heating of the melt-crystallized samples are reported in Figure 4.6. According to the WAXS profiles of Figure 4.5, the pure HAP resin does not show endothermic or exothermic signals in the heating and cooling curves, whereas the blends show a weak inflection at about 50 °C due to the glass transition of the PA12 dispersed in the phenolic resin matrix and endothermic and exothermic peaks corresponding to the melting and crystallization of PA12 (curves b-f, Figure 4.6). The melting temperatures of the PA12 in the blends are lower than that of the pure PA12 ( $T_m = 179^\circ\text{C}$ , curve g, Figure 4.6A) and decrease with decreasing PA12 concentration (curves b-g, Figure 4.6A). The glass transition temperature seems to shift to lower temperatures with increasing PA12 amount. The melting and crystallization temperatures and enthalpies of compression-molded samples of the blends and pure components

evaluated from the DSC curves of Figure 4.6 are reported in Table 4.2 and Figure 4.7 as a function of the PA12 concentration.

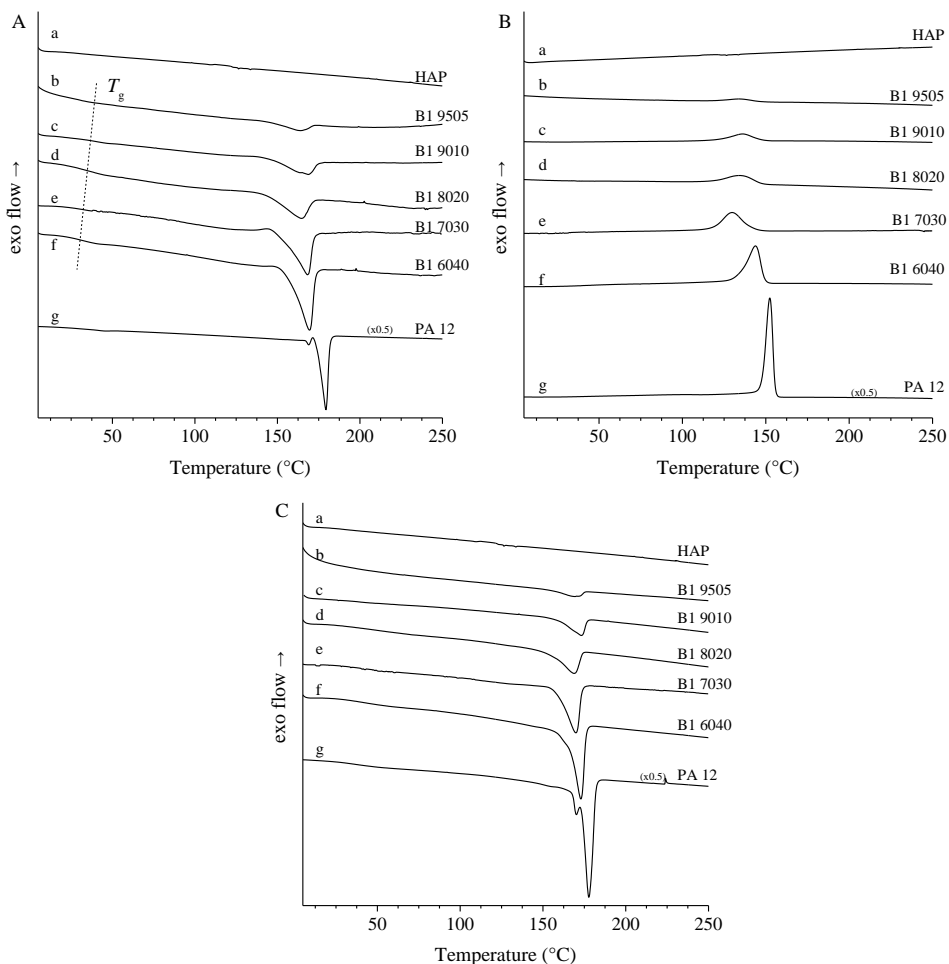


**Figure 4.6.** DSC curves of the compression-molded samples of the HAP/PA12 blends B1\_xy of Table 4.1 recorded during first heating (A), cooling from the melt (B) and second heating of the melt crystallized samples (C). a) pure HAP; b) B1-9505, c) B1-9010, d) B1-8020, e) B1-7030, f) B1-6040, g) pure PA12.

DSC data reported in Table 4.2 and Figure 4.7 indicate that the values of melting and crystallization enthalpies are arranged on straight lines. The melting temperatures recorded during the first ( $T_m^I$ ) and the second ( $T_m^{II}$ ) heating scan and the crystallization temperatures ( $T_c$ ) of the compression-molded specimens increase linearly with the PA12 amount (Figure 4.7A). The values of the glass transition

temperature of the blends, first decrease with increasing PA12 content and then increase, showing deviation from linearity as a function of the PA12 concentration.

**Table 4.2.** Values of the glass transition temperature ( $T_g$ ), melting ( $T_m^I$ ,  $T_m^{II}$ , 1<sup>st</sup> and 2<sup>nd</sup> heating) and crystallization ( $T_c$ ) temperatures and of the corresponding enthalpy ( $\Delta H_m^I$ ,  $\Delta H_m^{II}$ ,  $\Delta H_c$ ) of HAP, PA12, and their blends

Samples	$T_g$ (°C)	$T_m^I$ (°C)	$\Delta H_m^I$ (J g <sup>-1</sup> )	$T_c$ (°C)	$\Delta H_c$ (J g <sup>-1</sup> )	$T_m^{II}$ (°C)	$\Delta H_m^{II}$ (J g <sup>-1</sup> )
HAP	0	0	0	0	0	0	0
B1_9505	n.d.	163	-3,5	134	2,5	169	-3,0
B1_9010	40	169	-7,5	136	7,0	173	-6,0
B1_8020	33	165	-11	135	9,5	169	-9,5
B1_6040	31	169	-20,5	144	21,5	173	-20,5
PA12	45	179	-52	152	55,5	179	-52

n.d. = not determinable.

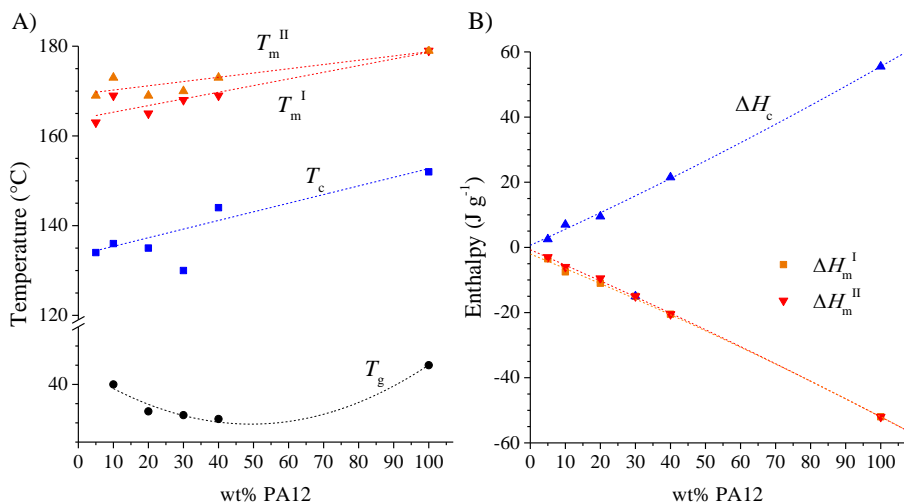


**Figure 4.7.** DSC data of the compression-molded specimens of the blends HAP/PA12 reported in Table 4.2. (A) First  $T_m^I$  and second  $T_m^{II}$  melting temperatures, crystallization temperature  $T_c$  and glass transition temperature  $T_g$ ; (B) melting and crystallization enthalpies ( $\Delta H_m^I$ ,  $\Delta H_m^{II}$ ,  $\Delta H_c$ ).

The Thermogravimetric analysis is used to evaluate the thermal stability of the obtained materials, the temperature observed at 5% weight loss is used as the criterion for the onset of polymer decomposition. The compression-molded specimens of the HAP/PA12 blends are thermally stable up to 350°C.

TGA curves of the blends B1\_xy are shown in Figure 4.8. The TGA data of an additional sample with 60 wt% of PA12 (B1\_4060) are included in Figure 4.8 to better understand the degradation behavior. The TGA curves exhibit two main mass loss steps (2 and 3 in Figure 4.8), probably due to the two different components of the system, the resin and the thermoplastic PA12, anticipated by a lower mass loss at a lower temperature (1 in Figure 4.8).

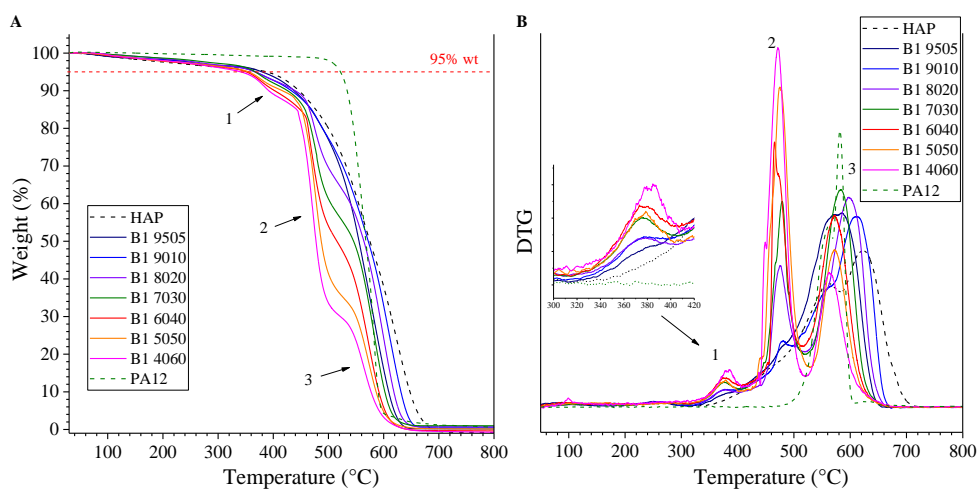


**Figure 4.8:** Thermogravimetric curves (A) and first the derivate (B) recorded at scanning rate of 10°C/min in airflow, of samples of cured blends B1\_xy of Table 2 compression molded for 10 minutes at 200°C. The three weight loss phenomena  $T_{d1}$ ,  $T_{d2}$ , and  $T_{d3}$  have been indicated by the numbers 1, 2, and 3 respectively.

More in detail, the initial mass loss below 150 °C is due to the gradual evaporation of absorbed moisture and the releasing of the volatile products typical of the PF resins as formaldehyde, methanol, and/or ammonia<sup>72</sup>. The higher the PA12 amount, the lower is this the mass drop in this temperature range. At higher temperatures the cured blends B1\_xy show three degradation phenomena (1, 2, and 3 in Figure 4.8) instead of two as expected for the degradation of physical blends of two components.

From the analysis of the first derivative of the TGA curves of the B1 blends (Figure 4.8B), it is apparent that the intensity of the first two peaks at  $T_{d1} \sim 370$  °C and  $T_{d2} \sim 475$  °C increases with the increase of the PA12 content (Figure 4.8B). They could be

due to the temperature-induced rupture of new bonds formed between the two components that lead to the release of volatile species and/or to a decrease of the thermal stability of the PA12 component, triggered by the strong (non-bonded) interactions established at PF interface. The third degradation step of the cured B1 samples, instead, is centered at the same temperature of the neat components ( $T_{d3} \sim 580$  °C). It is due to the thermal degradation of PF resin and the residual PA12 chains not directly involved in the strong interactions with the cross-linked matrix. The multiple degradation steps of the B1\_xy blends suggest that the thermal stability of PA12 is impaired by the formation of strong interactions with the PF matrix. Whether these interactions imply the formation of covalent bonds between the amide groups of PA12 and the unreacted hydroxyl groups of the PF resin can be only indirectly inferred from TGA data.

DMTA measurements of the fresh cured unbroken compression-molded specimens of the blends B1\_xy with 20, 30, and 40 %wt of PA12 are shown in Figure 4.9. The storage and loss moduli are influenced by the presence of the PA12. In particular, two drops in storage modulus occur in the range 30÷50°C, due to the glass transition of the compatible mixture PA12-PF resin, and in the range 160÷180°C due to the melting of the PA12. In general, higher amount of PA12 in the mixture gives lower values of the storage and loss moduli. The intensities of the glass transition peak in loss modulus and loss factor increase with the PA12 amount.

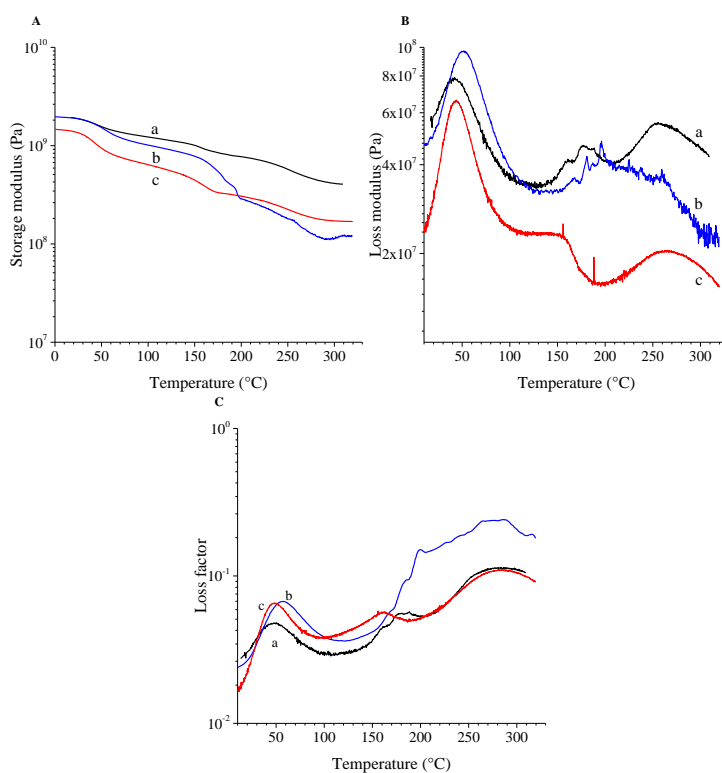


**Figure 4.9:** DMTA curves of compression-molded specimen of the blends B1\_8020 (a), B1\_7030 (b), and B1\_6040 (c), recorded at scanning rate of 5°C/min. Storage modulus (A) loss modulus (B), and loss factor(C).

## 4.2 Self-healing tests

### 4.2.1 DMTA and SEM analysis

The self-healing performance has been studied for the cured system HAP/PA12 (cured blends B1\_xy) with different compositions as reported in Table 4.3, the efficiency of the healing was qualitatively assessed visually. To demonstrate the self-healing phenomenon, the cured compression-molded specimens are broken in liquid nitrogen, the two pieces are then brought together, locked in a clamp, and heated in an oven at 200 °C and kept at 200 °C for 45 min. After this heat treatment, the specimens with PA12 content higher than 20 wt% appear fully repaired<sup>73</sup> (Figure 4.10). Instead, the cured HAP resin and the blend B1\_xy with 5 wt% of PA12 do not

experience any welding, whereas the welding of the blend B1\_xy with 10 wt% of PA12 results unstable and fragile.

**Table 4.3.** Results of the breaking/healing tests performed on the cured HAP resin and the cured B1 blends having PA12 content in the range 5-50 % wt.

Sample	HAP resin		PA12 (% wt)	Efficiency of healing
	PF resin (wt%)	HMTA(wt%)		
HAP	90	10	0	No
B1-9505	85.5	9.5	5	No
B1-9010	81	9	10	Poor, fragile
B1-8020	72	8	20	Good
B1-7030	63	7	30	Good
B1-6040	54	6	40	Good
B1-5050	45	5	50	Good

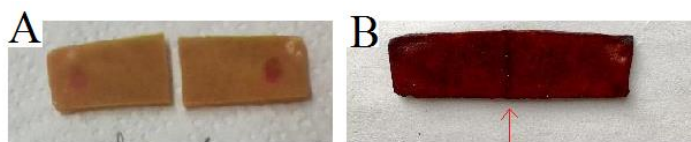


**Figure 4.10.** Specimen of cured blend B1\_8020.

A) Broken specimen; B) Specimen welded at 200°C for 45 min. The arrow indicates the welding line between the two pieces.

The temperature and the long time are necessary to obtain the polymer-polymer welding, which occurs after melting of PA12 at the interface through surface rearrangement and chain diffusion<sup>74</sup>.

The performances of the welded specimens have been tested by performing DMTA measurements. In particular, the DMTA curves of the freshly cured samples are compared with those of the corresponding repaired specimens, measured in two consecutive heating runs, in Figure 4.11. In particular, in Figure 4.11 the storage modulus  $G'$ , the loss modulus  $G''$ , and the loss factor ( $\tan \delta$ ) of specimens of the samples B1\_8020, B1\_7030, and B1\_6040 are reported.

Regardless of the blend composition, the storage modulus of the freshly cured samples shows an inflection at about 65-80 °C and a broad peak at about 160 °C,

associated with the glass transition and the melting point of PA12, respectively. In correspondence of these discontinuities in  $G'$ , the loss modulus and the loss factor show broad maxima (Figure 4.11). The broken specimens, after welding, show a similar behavior during the first heating DMTA scans, indicating that the heating treatment at 200 °C for 45 min leads to the formation of a stable network at the fracture interface, equivalent to the pristine, unbroken samples. However, in the second heating scans, the melting peaks become less pronounced or completely absent.

The results of Figure 4.11 suggests that PA12 acts as a reservoir in the breaking/healing process. During the heat treatment of the broken specimens, indeed, the melted thermoplastic polymer flows throughout the interface of the fracture. Welding is generated by the strong interactions occurring between complementary groups of the two components and by the successive crystallization of PA12 during the cooling. Furthermore, the cross-linking reactions occurring during the curing of the pristine sample and in the successive welding at 200 °C for 45 min are not complete. Therefore, for the welded specimens, further reactions occur during the first DMTA scan, resulting in a further stabilization, and consequent damping of the relaxation phenomena of the network in correspondence of the melting of PA12 crystals during the successive heating.

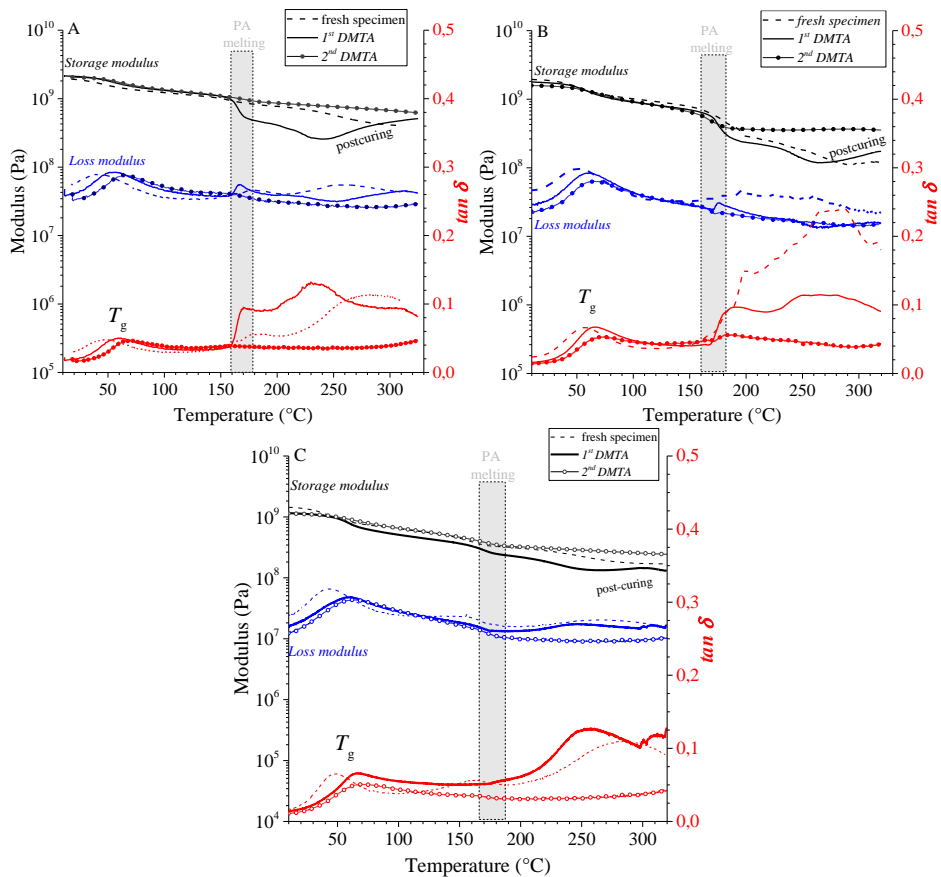


**Figure 4.11.** DMTA data of specimens of blends B1\_8020 (A), B1\_7030 (B) and B1\_6040 (C) compression molded at 200 °C for 10 minutes (dashed lines), broken and healed at 200 °C for 45 minutes (continuous lines) and second scan on the same healed specimen successive to the first scan after cooling to room temperature (circle lines).

SEM micrographs confirm the mechanism and the efficiency of the welding process. SEM images of the compression-molded cured blend B1\_6040 after breaking in liquid nitrogen are shown in Figure 4.12A. The crystalline polyamide is well-dispersed in the HAP resin matrix in the form of crystalline domains of variable sizes between 10 to 200 microns (Figure 4.12A). The dispersion is favored by the presence of the in-situ formation of tightly bound layers at the interface with PF resin (double arrow in figure 4.12B), whereas the formation of huge PA12 domains is due to the crosslinking PA reaction, which does not allow the dispersion of the PA12.

The SEM image of the fracture surface of the blend B1\_6040, after removal of the PA12 component using phenol at 100 °C for 6 h is shown in Appendix A4.0. The regions occupied by the spherical entities are replaced by holes, confirming that PA12 is well dispersed in the PF network.

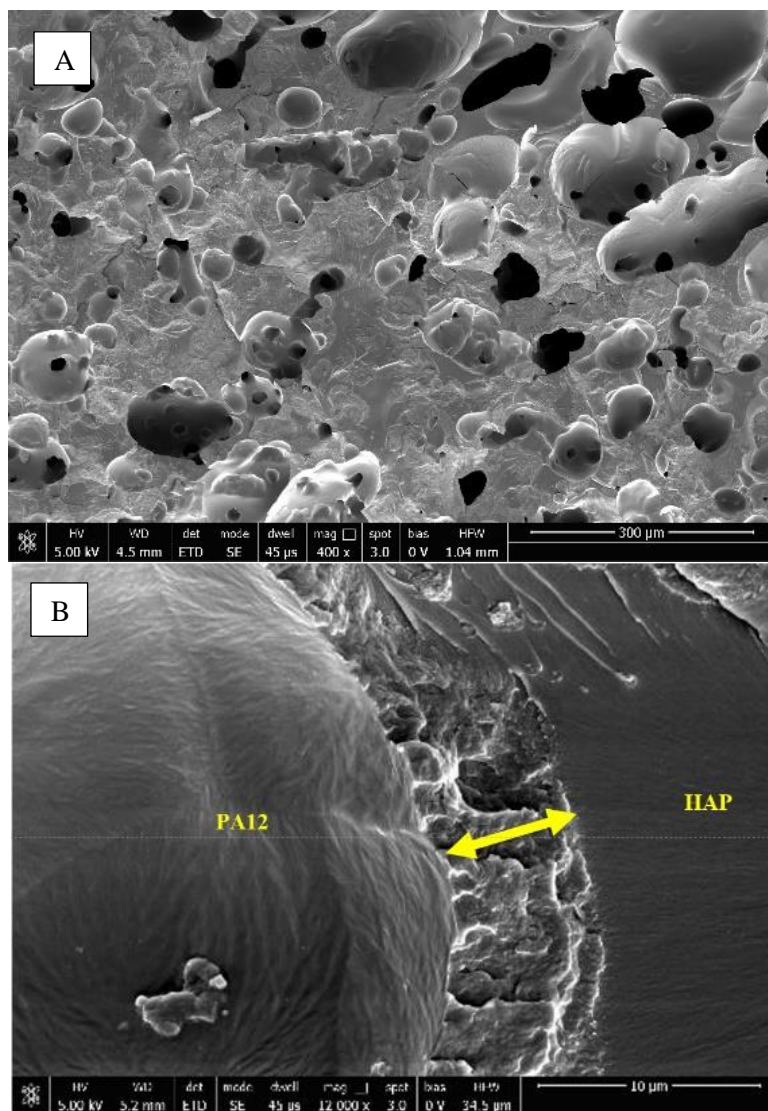


**Figure 4.12.** SEM micrographs of the inner surface of the specimen of the blend B1\_6040 cured at 200 °C for 10 min after breaking in liquid nitrogen. (A) magnification 400x, (B) magnification 12000x. The double-headed arrow shows an interface layer of PA12 chemically and/or physically bound to the surrounding HAP resins.

When the broken specimen is brought at a temperature higher than 170°C, the PA12 melt can flow in the matrix and fill the cavities, cracks, and fractures. In our test the fracture is macroscopic, a deliberately extreme case that involves the entire specimen, although the possible final applications of PF resins do not involve such breakages. The main difficulty is to match perfectly the two pieces to be repaired, however, the imperfect arrangement allows us to define the welding area which could be almost indistinguishable from the bulk of the specimen. The SEM microphotographs relative to the inner area of the samples B1\_6040 and B1\_7030 that have been first broken, then welded, and successively cut perpendicularly to the welding surface are shown in Figure 4.13 and 4.14, respectively. The welding line is evident in the dashed rectangle and appears straight with some regions which are undistinguishable from bulk. The SEM microphotographs of the specimen B1\_6040 perfectly welded are shown in Figure 4.15.

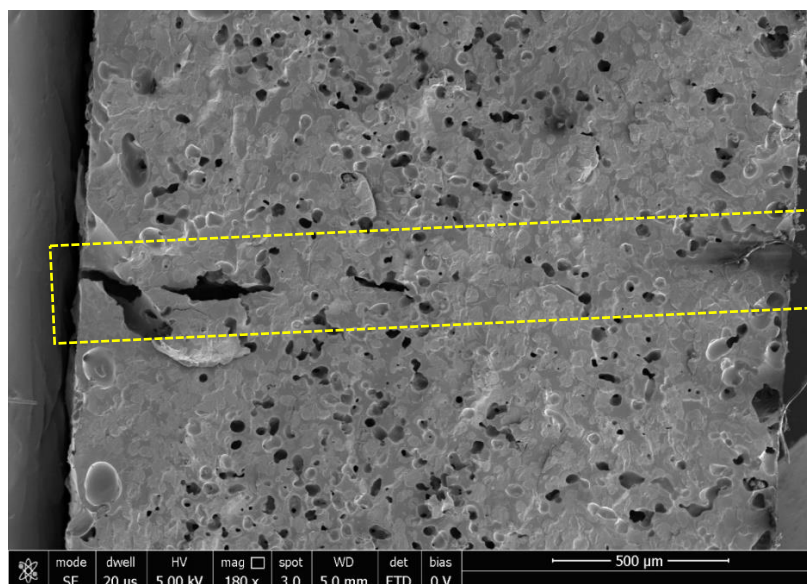


**Figure 4.13.** SEM micrographs of a specimen of the blend B1\_6040 cured at 200°C for 10 min after breaking, successive healing, and successively cut perpendicularly to the welding surface. The whole welded fracture has indicated by dashed rectangle.

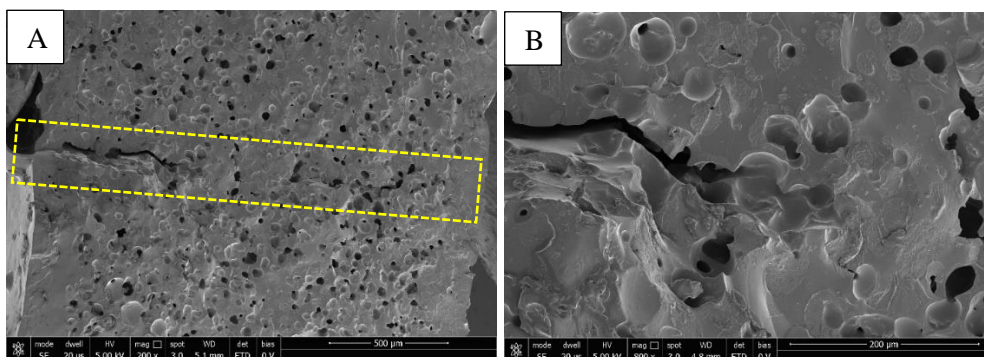


**Figure 4.14.** SEM micrographs of a specimen of the blend B1\_7030 cured at 200°C for 10 min after breaking, successive healing, and successively cut perpendicularly to the welding surface. A) The whole welded fracture has indicated by a dashed rectangle. B) Detail of the repaired fracture.

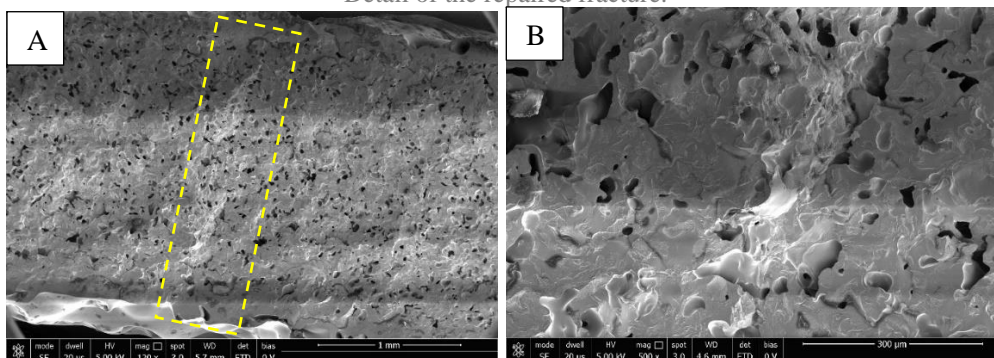


**Figure 4.15.** SEM micrographs of a specimen of the blend B1\_6040 cured at 200°C for 10 min after breaking, successive healing, and successively cut perpendicularly to the welding surface. The two pieces are perfectly welded. A) The whole welded fracture is indicated by a dashed rectangle. B) Detail of the repaired fracture.

#### 4.2.2 Curing temperature

As described in the previous chapters, the curing temperature affects the mechanism of the cross-linking reactions, through the formation of different types of intermediates such as benzylamines and/or benzoxazines, and the final performances of the PF resins.

The influence of the temperature at which the compression molding is performed and at which the curing reaction occurs ( $T_{cm}$ ) on the behavior of the final specimen and the behavior of the self-healed (welded) specimen has been studied for the blend

B1\_6040. This parameter could be crucial for the final properties of the material. In particular, the temperatures have been chosen considering the different phenomena which occur in this system, the endothermic phenomenon at temperatures higher than 140°C, the curing at about 150°C, the melting of polyamide at about 180°C, and post-curing phenomena for temperature higher than 220°C. The unreacted powders of the blends have been compression molded at the same condition described in the previous paragraph but using different curing temperature  $T_{cm}$  (150°C, 170°C, 190°C, 200°C, 220°C).

X-ray diffraction profiles of the so obtained specimen compared to the blend between ground cured HAP and PA12 powder are reported in Figure 4.16.

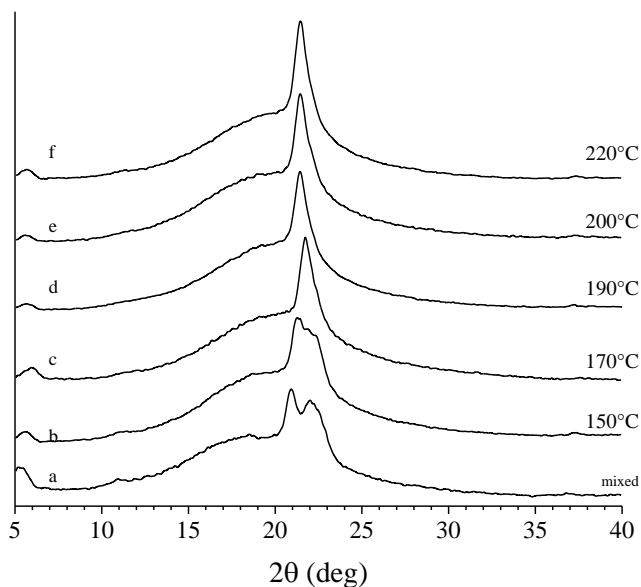


**Figure 4.16.** WAXS profiles of the mixed PA12 powder with ground HAP cured resin (a) and of samples of the blend B1\_6040 compression molded at different temperatures  $T_{cm}$  of 150 (b), 170°C (c), 190°C (d), 200°C (e) and 220°C (f).

All the specimens show PA12 crystalline  $\gamma$  form, except for the B1\_6040 compression molded at 150°C which shows still the mixing between the two different crystalline forms indicating that during the compression molding the PA12 has been not totally melted.

The DMTA curves showing the storage modulus, loss modulus, and loss factor of the fresh unbroken specimens of the blends cured at the different temperatures are shown in Figure 4.17. It is apparent that higher  $T_{cm}$  give lower loss factor curve, higher loss modulus curve, and less drop in the storage modulus in the PA12 melting range temperature.

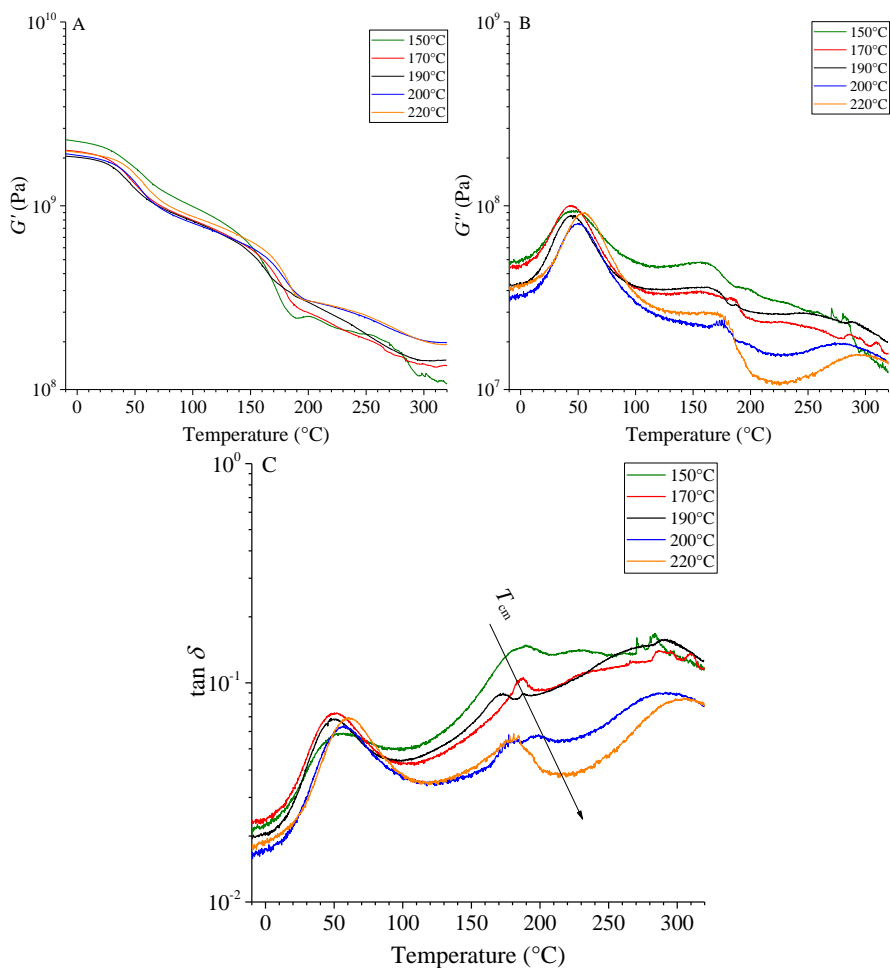


**Figure 4.17.** DMTA data of fresh samples of the blend B1\_6040 (unbroken) obtained by compression molding for 10 minutes at curing temperatures of 150°C (green), 170°C (red), 190°C (black), 200°C (blue), and 220°C (orange). A) Storage modulus, B) Loss modulus, C) Loss factor.

A comparison between storage modulus, loss modulus, and loss factor of the samples of the blend B1\_6040 cured at different temperatures, broken, and then

welded (at 200°C for 45mins) are shown in Figure 4.18. In this case, the performances seem to increase with compression molding temperatures and then worsen beyond 200 °C. Similar behavior has been observed during the second scans performed on the same welded sample after the DMTA scan and cooling to room temperature (second DMTA scan of the welded specimen) (Figure 4.19).

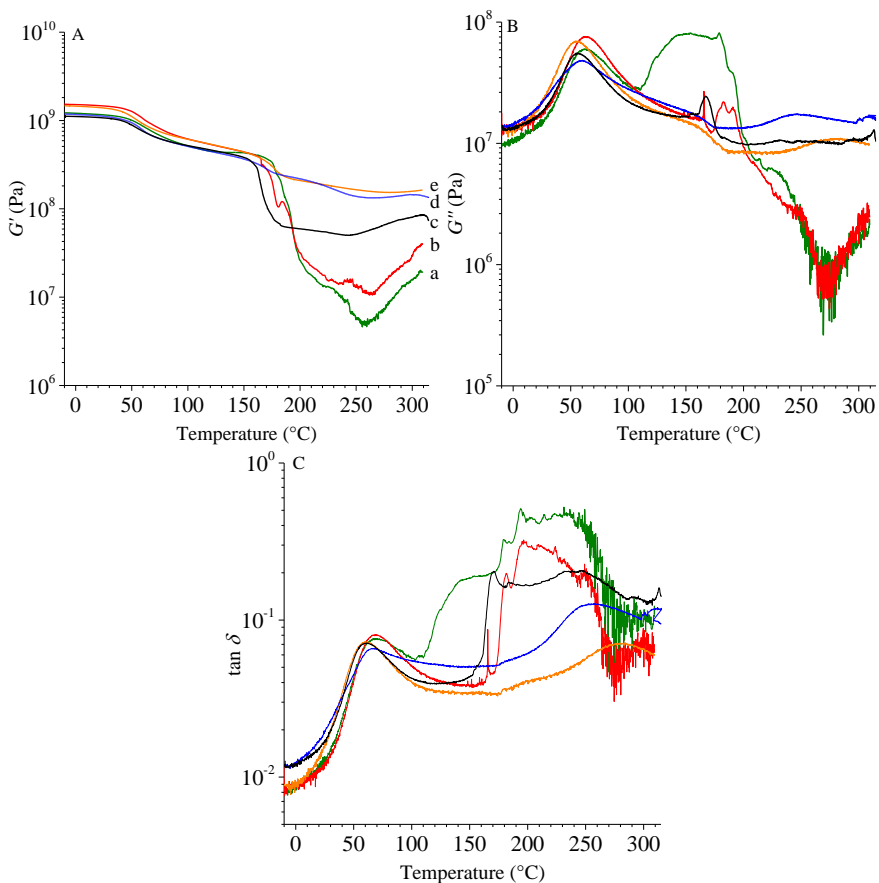


**Figure 4.18.** DMTA curves of specimens of the blend B1\_6040 that are obtained by breaking in liquid N<sub>2</sub> and successive heating at 200 °C for 45 min, the powders cured for 10 min at  $T_{cm}$  equal to 150 (green), 170 (red), 190°C (black), 200 (blue), and 220 °C (orange). A) Storage modulus, B) Loss modulus, C) Loss factor.

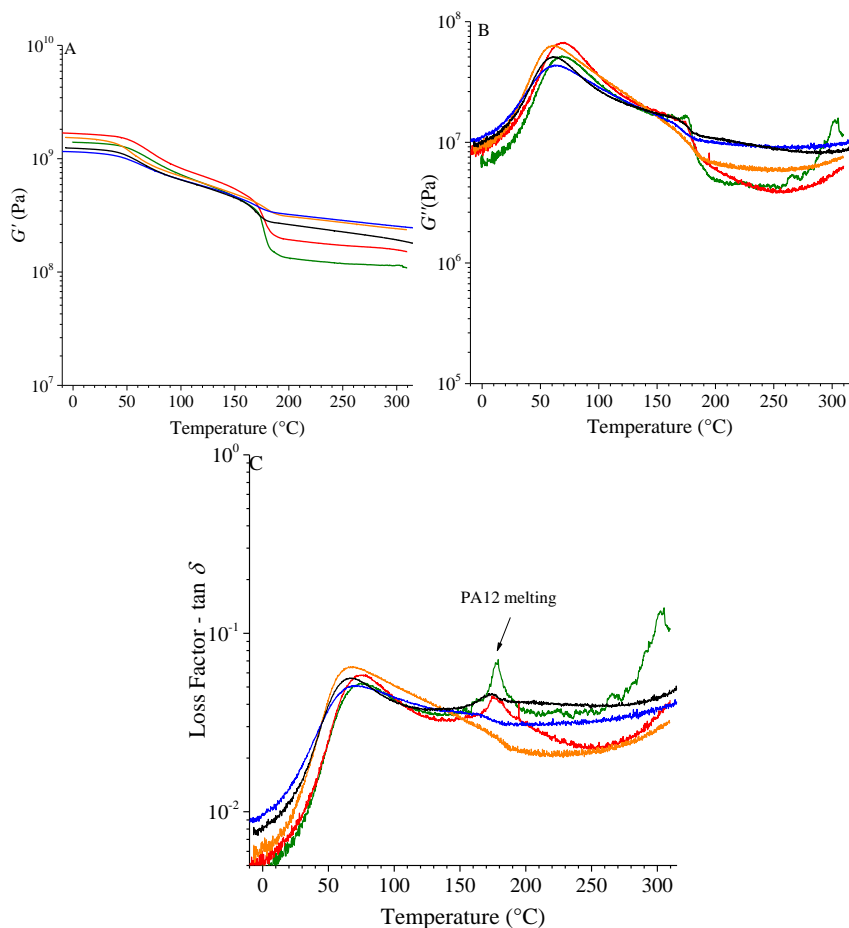


**Figure 4.19.** DMTA curves recorded in the II heating scan of the same specimens of Figure 4.18. The samples are obtained by subjecting to first DMTA scan specimens of the sample B1\_6040 broken in liquid N<sub>2</sub> and successively welded at 200 °C for 45 min, starting from powders cured for 10 min at  $T_{cm}$  of 150 (green), 170 (red), 190°C (black), 200 (blue), and 220 °C (orange). A) Storage modulus, B) Loss modulus, C) Loss factor.

As discussed above (Figure 4.11), the intact samples as well as those subjected to welding show double inflections in the storage modulus and double maxima for the loss factor, regardless of the curing temperature  $T_{cm}$ . They correspond to the glass transition of PA12, in the range 65÷80°C, and the melting of PA12 at about 160÷107°C.

The melting of the PA12 component in the fresh (unbroken) specimens (Figure 4.17) is less pronounced than that observed for the samples subjected to welding

(Figure 4.18). The results of the thermomechanical analysis of Figures 4.17 and 4.18 suggest that for the freshly cured specimens, the crosslinking reactions are not complete, even adopting high curing temperatures. The samples, indeed, regardless of the curing temperature, show the same relaxation phenomena, with only minor differences in the relative intensity. However, after breaking and successive welding, through annealing at 200 °C for 45 min, the heat treatment leads to the formation of a network that is less prone to relaxation, in the case of the samples that are early cured at 200 and 220 °C. For the pristine samples early cured at lower temperatures, 150 and 170 °C, instead, the curing efficiency is not so high, so that, after breaking and successive welding (Figure 4.18), the annealing is not so effective, leading to welded specimens exhibiting relaxation phenomena more pronounced than those shown by the corresponding unbroken specimens (Figure 4.17).

The thermomechanical behavior of the welded specimens in Figure 4.18 is probed also by recording DMTA curves in a successive heating scan (second heating run). The results are shown in Figure 4.19. There are no huge differences in the DMTA curves of the samples subjected to second heating scans, regardless of the curing temperature adopted for the corresponding pristine samples  $T_{cm}$ .

In particular, for the samples obtained by early curing the pristine powders at  $T_{cm} = 150$  and  $170$  °C, the relaxation phenomena of the network associated with the melting of the PA12 component corresponds to a weak and narrow peak in the loss moduli and  $\tan \delta$  curves in the second heating scan of the broken and successively welded specimens, in the other temperature regions the DMTA curves being very similar.

### 4.2.3 Study of other resin/PA12 systems

The welding capability of HAP resins achieved resorting to the addition of PA12 was tested also for other PF resins and also for the MF-based and BMI resins. Six commercial grades of PF resins characterized in Chapter III are selected for these

tests, through the use of the *curing efficiency chart*<sup>62</sup>. Grades belonging to the quadrants of fast curing resins, with high (Quadrant 1) and low curing efficiency (Quadrant 4), and resins belonging to the quadrants of slow curing resins with high (Quadrant 2) and low curing efficiency (Quadrant 3) were selected.

The three MF-based resin has been selected considering the different amount of HMM (25wt% and 40wt%) and the absence or presence of HMTA (0wt% and 3wt%).

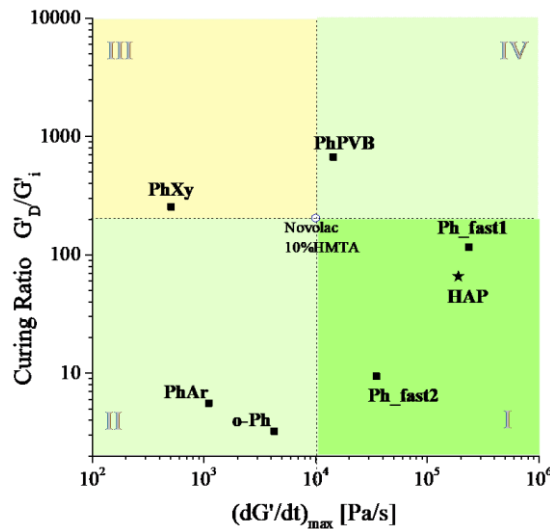


**Figure 4.20:** Correlation diagram of the curing efficiency of phenolic resins, denominated “curing efficiency chart”. Parameters indicative of the curing rate and curing efficiency are reported on the *x*- and *y*-axis, respectively (see Chapter III for details). The position of the selected PF resins is indicated. The position of the HAP resin is also indicated for comparison.

All the blends between the resin and the PA12 have 40% wt of PA12, with the aim to maximize the compatibilization and the subsequent healing mechanism, and have been compression molded, broken, and healed with the same procedure used for the blends B1\_xy. The DMTA curves of the PF resins are shown in Figures 4.21-4.23 and those of a BMI resin are shown in Figure 4.24. A summary of the results is reported in Table 4.4. The welding occurs for all the samples except for the MF-based resin. As reported in Table 4.4, all the studied systems show self-healing

properties, regardless of the curing kinetics of the phenolic resin and some resins having only the ortho- structure have shown brittle behavior after welding. Probably, the brittle welding behavior observed using the ortho-PF resin is directly related to the ortho-substitution that makes the reactivity of the amide groups toward the phenol substituents of the resins more hampered and/or energetically less favorable.

**Table 4.4.** Commercial thermosetting resins blended with PA12 40wt%

Sample	Components (wt%)	Type of resin	HMTA (wt%) <sup>a</sup>	Welding capability
HAP	PF resin (80-90%) – <i>Ph01</i>	PF	10	Yes
o-Ph	Ortho-PF resin – <i>Ph03</i>	PF	6-7	Yes, brittle
Ph_fast1	PF resin with secret additive 5% - <i>Ph17</i>	PF	10-20	Yes, brittle
Ph_fast2	PF resin with secret additive – <i>Ph18</i>	PF	10-20	Yes
PhAr	PF resin modified with 1,4-bis(methoxymethyl)benzene/phenol copolymer (>80%) – <i>Ph07</i>	PF	≤ 10	Yes
PhXy	PF resin copolymer 1,3-dimethylbenzene (≥89.5%)	PF	< 9	Yes
PhPVB	PF Resin modified with PVB – <i>PhA04</i>	PF	8.5-9.5	Yes
MFPh01	PF resin with 25% HMM	MF	-	NO
MFPh02	PF resin with 40% HMM	MF	-	NO
MFPh03	PF resin with 40% HMM	MF	3	NO
BMI	Bismaleimide resin – <i>BM-24</i>	BMI	-	Yes

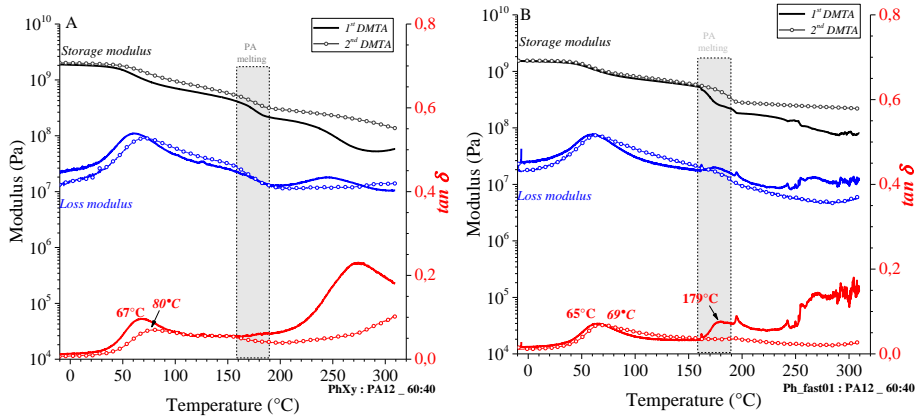


**Figure 4.21.** DMTA data of the cured compression-molded specimen broken and healed of PF resin blended with 40wt% of PA12. A) Xylene-PF resin (PhXy), B) HAP resin fast curable (Ph\_fast1)

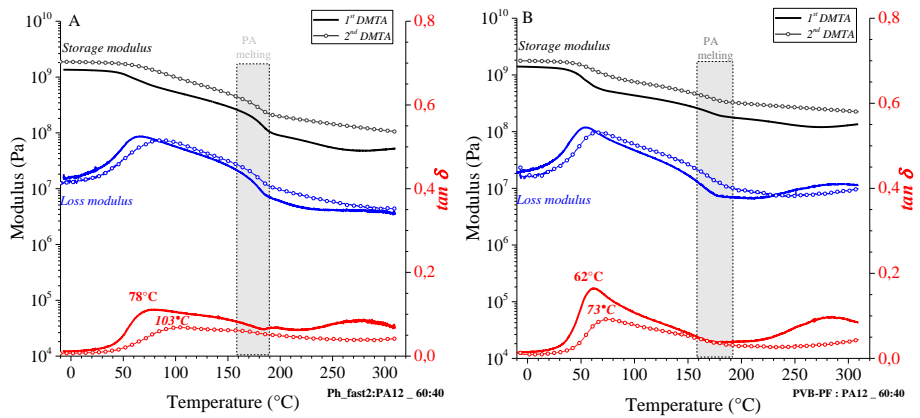


**Figure 4.22.** DMTA data of the cured compression-molding specimen broken and healed of PF resin blended with 40wt% of PA12. A) PF resin fast curable (Ph\_fast2), B) PVB-PF resin (PhPVB).

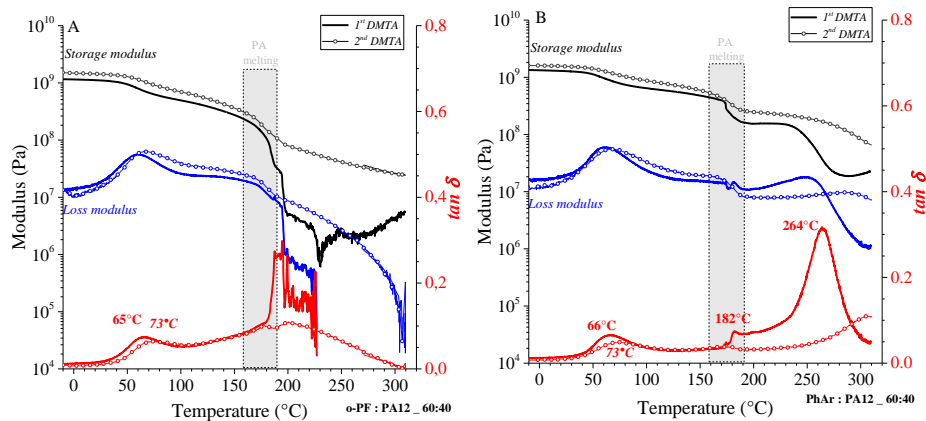


**Figure 4.23.** DMTA data of the compression molding specimen broken and healed of PF resin blended with 40wt% of PA12. A) ortho-PF resin, B) methoxymethylbenzene copolymer.

In the case of BMI resin mixed with 40wt% PA12 longer curing time  $t_{cm}$  is needed to obtain a specimen suitable for DMTA measurements. The compression-molded specimen, cured at  $T_{cm}=200^{\circ}\text{C}$  and  $t_{cm} =10$  mins, melts during the measurements probably also due to poor crosslinking, for this reason, the specimen has been obtained with  $t_{cm} =20$  mins.

In figure 4.24A two consecutive DMTA scans performed on the same intact unbroken specimen are reported. During the first scan, two drops in storage modulus have been detected. The first one occurs in the temperature range of  $40\div 70^{\circ}\text{C}$  and it is due to the PA12 glass transition, the second deeper drop occurs in the temperature range between 150 and  $250^{\circ}\text{C}$  and is due to the melting of PA12 and a glass transition of the BMI resin not fully cured. Above  $230^{\circ}\text{C}$  the storage modulus starts increasing which means post-curing reaction occurs. During the second scan, the glass transition temperature is higher than the first scan of  $\sim 10^{\circ}\text{C}$ , and the second drop in storage modulus is less deep.

In figure 4.24B two consecutive DMTA scans performed on the same specimen after the breakage and the subsequent healing at  $200^{\circ}\text{C}$  for 45mins have been reported. It is worth noting that storage modulus, loss modulus, and loss factor

follow similar behavior during the first and the second scan in both intact and broken and healed samples.

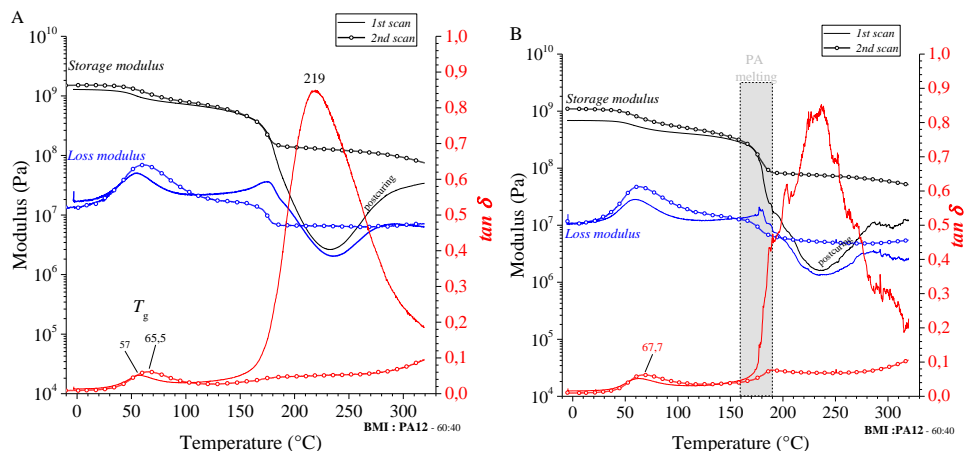


**Figure 4.24.** DMTA curves of samples of the blend BMI resin:PA12 60:40 compression molded at 200°C for 20 minutes. Unbroken samples scanned twice (A); broken/healed samples scanned twice (B).

### 4.3 Novolac (HMTA free)-polyamide blends: the study of the compatibilization

Blends between the o/p novolac resin not containing the hardener HMTA and polyamide 12 with different compositions. The composition and properties of the blends are reported in Table 4.5. It is worth noting that whereas HMTA is involved in the reactions with the PF resins, it does not react at all with PA12 (see Appendix A4.1). The powders of the HMTA free PF resin (Ph00) and the PA12 have been mixed at various compositions and the obtained blends have been named “B0\_xy” where x and y indicate the relative amount of the resin and the PA12, respectively. (e.g. B0\_8020 indicates the blend with 80wt% of PF resin and 20wt% of PA12).

The simplicity of this approach lies in the fact that there is no need to add any external agent since the compatibilization of the resin and PA12 occurs through interactions between functional groups already present in the phenolic resin or functional groups that are formed during its heating. Furthermore, being a compatible physical blend, polyamide and PF-resin could act as a reactive blend and

during heating, a new covalent bond between ortho or para free position of the aromatic phenolic ring of uncured PF resin and the amide group of the polyamide could be probably generated (Figure 4.25). The reaction is not well described but should take place between a methylol group and the nitrogen of the amide group<sup>71</sup>. Anyway, the new bond is not easy to detect, so only indirect clues have been obtained (see Appendix A.4.2).

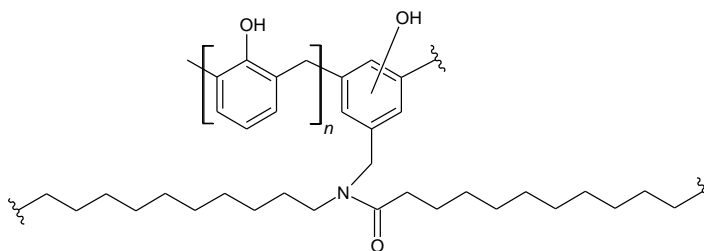


**Figure 4.25.** The newly formed bond between an aromatic ring of PF resin and a nitrogen atom of PA12 occurs by reactive blending triggered by heating.

The DSC curves of the B0<sub>xy</sub> blends recorded during heating of the as-prepared blends, cooling from the melt and successive second heating of the melt-crystallized samples are reported in Figure 4.26. As already discussed in Chapter III for the neat PF resins, the DSC heating curve of the as-prepared neat Ph resin shows a softening endothermic peak at temperature  $T_s = 50\text{-}60\text{ }^\circ\text{C}$  and an endothermic peak at nearly  $160\text{ }^\circ\text{C}$  corresponding to partial cross-linking without hardener and/or gas releasing (Figure 4.26A). The DSC heating curves of the blends B0<sub>xy</sub> with PA12 show an endothermic peak at temperature  $T_1$  variable between  $134\text{ }^\circ\text{C}$  of the sample B0<sub>9010</sub> with low PA12 content and nearly  $150\text{ }^\circ\text{C}$  of the samples with higher PA12 content, and an endothermic peak at higher temperatures corresponding to the melting of PA12 (Figure 4.26A). The temperature of the endothermic peak  $T_1$  increases with increasing PA12 content up to merge into the melting endotherm of PA12. The melting temperature of PA12 decreases with decreasing PA12 content, from  $184\text{ }^\circ\text{C}$  of the pure PA12 to  $150\text{-}160\text{ }^\circ\text{C}$  of the samples with  $50\text{-}60\text{ wt\%}$  of PA12 (Figure 4.26A).

The DSC cooling curves of Figure 4.26B indicate that PA12 does not crystallize from the melt in the blends with PA12 concentration lower than 65 wt% and only the glass transition of the blends is observed in the cooling thermograms. Crystallization of PA12 is clearly visible for samples with PA12 content higher than 60 wt% and the crystallization temperature increases with increasing PA12 content from 107 °C of the sample B0\_3565 to 153 °C of the pure PA12 (curves l-o of Figure 4.26B). The glass transition temperature instead decreases with increasing PA12 content (Figure 4.26B).

The DSC curves recorded during the second heating of the amorphous pure Ph resin and amorphous blends with PA12 content lower than 65 wt% of Figure 4.26C (curves a-l) show only the glass transition at a temperature that decreases with increasing PA12 content. For blends with higher PA12 concentration, the DSC heating curves also show the melting endotherm of PA12 with melting temperature that increases with increasing PA12 content (curves h-o of Figure 4.26C). Blends that crystallize only in part during the cooling step from the melt of Figure 4.26B, as the samples B0\_4060 and B0\_3565 with 60 and 65 wt% of PA12 (curves i and l of Figure 4.26B), crystallize during the heating scan giving the cold-crystallization exothermic peaks at 120 and 108 °C, respectively (curves i and l of Figure 4.26C).

The absence of crystallization and melting of the PA12 component on the blends with low PA12 content up to nearly 60 wt% suggests that that PA12 is almost completely dispersed in the novolac matrix (Figure 4.26 B and C). The dispersion is probably favored by the establishment of chemical interaction (hydrogen bonds) between chains of the novolac resin and PA12 occurring during the first heating of the as-prepared blends, as indicated by the presence of the endothermic peak at  $T_1=134-150^{\circ}\text{C}$  which increase with the polyamide amount and by the absence of the melting peak at  $T_m\approx 175^{\circ}\text{C}$  of PA12 (Figure 4.26A). With PA12 concentration higher or equal to 60%, the excess of PA12 crystallizes and melts at temperatures close to those of the neat component, as shown by the DSC curve in Figure 4.26A-C.

The presence of a single glass transition clearly visible in the cooling and second heating DSC curves of Figure 4.26B,C also gives evidence of dispersion of the PA12 within the PF resin.

The values of the glass transition temperature evaluated from the DSC second heating curves (figure 4.26C) are reported in Table 4.2 and in Figure 4.26D as a function of PA12 concentration and compared with the theoretical values calculated for blends or copolymers with the Fox-Flory equation. All amorphous blends exhibit negative deviation  $\Delta T_g$  (equation 1) from the theoretical model. These kinds of deviations usually are due to prevailing conformational entropic effects<sup>75</sup>.

$$\Delta T_g = T_g - \frac{1}{\frac{\omega_{PF}}{T_{gPF}} + \frac{\omega_{PA12}}{T_{gPA12}}} \quad (1)$$

**Table 4.5.** DSC data of the blend between PFresin without hardener (Ph) and PA12.

Sample	Ph (%wt)	PA12 (%wt)	$T_1$ (°C) <sup>a</sup>	$T_m^I$ (°C) <sup>b</sup>	$T_c$ (°C) <sup>c</sup>	$T_m^{II}$ (°C) <sup>d</sup>	$T_g$ (°C) <sup>e</sup>	$\Delta T_g$ (°C)
Ph00	100	0	-	-	-	-	98	0
B0_9010	90	10	134	-	No	No	86	-2,0
B0_7822	78	22	139	-	No	No	77	-1,8
B0_6832	68	32	141	-	No	No	63	-8,5
B0_6040	60	40	143	-	No	No	59	-6,9
B0_5050	50	50	146	-	No	No	54	-5,2
B0_4456	44	56	147	-	CC	146	49	-6,2
B0_4258	42	58	149	-	CC	146	47	-6,9
B0_4060	40	60	152	-	CC	149	45	-7,7
B0_3565	35	65	-	163	107	156	43	-6,5
B0_3070	30	70	-	173	126	160	48	1,6
B0_2080	20	80	-	179	134	168	47	6,6
PA12	0	100	-	183	157	177	29	0

<sup>a</sup> endothermic phenomenon recorded during the 1<sup>st</sup> heating scan; <sup>b,d</sup> melting temperatures of PA12 recorded during the 1<sup>st</sup> and 2<sup>nd</sup> heating scan; <sup>c</sup> crystallization temperatures of PA12 recorded during the cooling scan; <sup>e</sup> glass transition recorded during the 2<sup>nd</sup> heating scan.

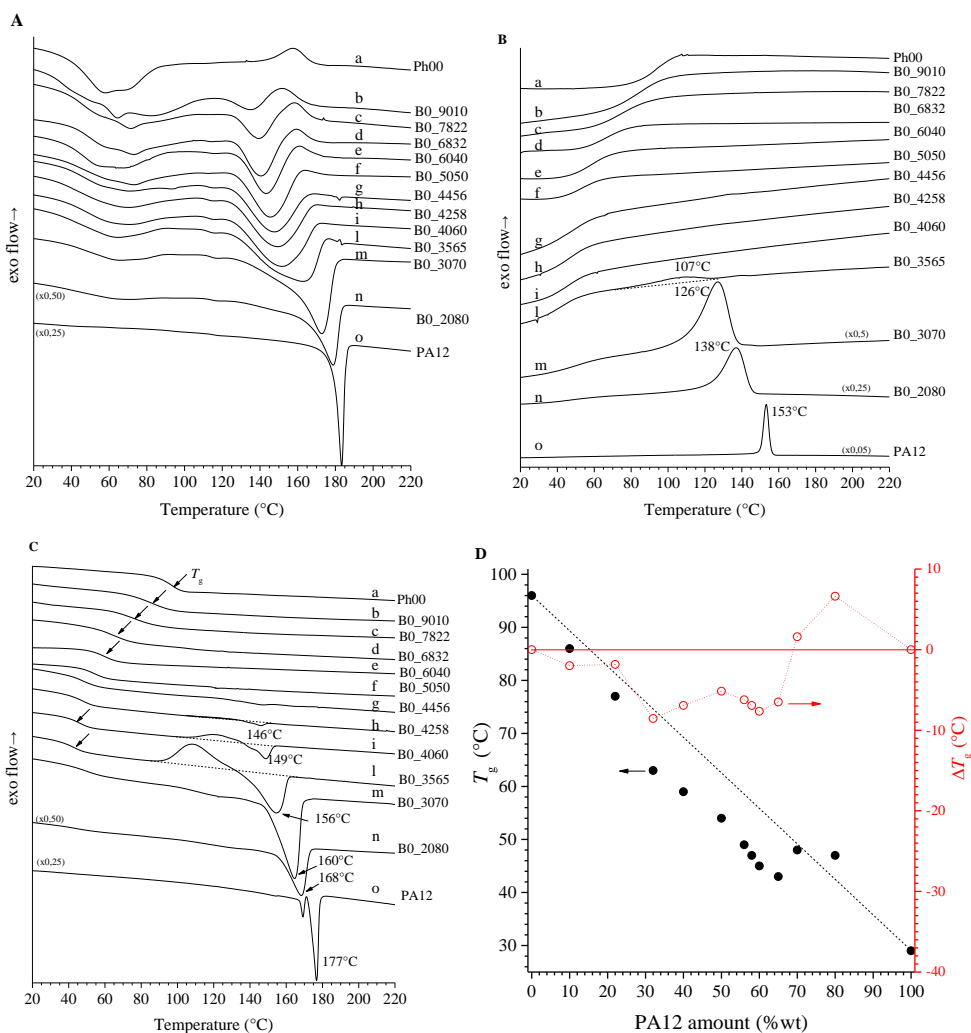


**Figure 4.26.** (A-C) DSC curves recorded at 10 C/min during 1<sup>st</sup> heating of as-prepared samples (A), cooling from the melt (B), and successive 2<sup>nd</sup> heating of the melt-crystallized samples (C) of blends B0\_xy of table 2, not containing HMTA. (D) Values of the glass transition temperature of blends evaluated from the DSC 2<sup>nd</sup> heating curves as a function of the PA12 concentration (filled circles) compared to the theoretical values calculated with the Fox-Flory equation (dashed line) and deviation  $\Delta T_g$  from the model (open circles) (D).

Figure 4.27 shows the WAXS profiles of the blend B0\_6040 recorded at different temperatures of 25°C, 60°C, 80°C, 100°C, 130°C, 180°C with a heating ramp of 10°C/min between each step, and at 25 °C after cooling. The temperatures have been selected from the DSC first heating of the sample (curve e, Figure 4.26A). The

WAXS profiles present Bragg reflections at  $2\theta \approx 5.7^\circ$ ,  $11.1^\circ$ , and  $20.5^\circ$  due to the presence of crystals of the  $\alpha$  and  $\gamma$  forms of PA12 in the as-prepared sample of the blend. These peaks are still visible at  $100^\circ\text{C}$  (curve d, Figure 4.27) but with lower intensity and at  $130^\circ\text{C}$  disappear indicating melting of PA12. This corresponds to the endothermic peak that appears at the temperature  $T_1$  in the DSC curve of the as-prepared sample of the blend B0\_6040 (curve e of Figure 4.26A), which has been associated to the establishment of the chemical interaction between chains of PA12 and the PF resin. This interaction probably favors the melting of PA12 crystals. When the sample is cooled to room temperature after melting, the PA12 does not crystallize (curve g of Figure 4.27).

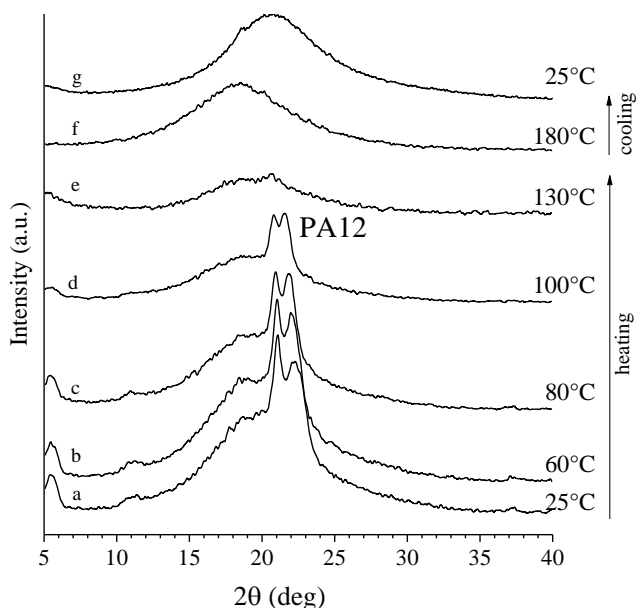


**Figure 4.27.** WAXS profiles of the blend B0\_6040 recorded at different temperatures during heating (a-f) and at  $25^\circ\text{C}$  after cooling (g). The endothermic phenomenon observed in the DSC heating curve at  $T_1 = 134^\circ\text{C}$  favors the melting of the PA12 (profile e).

The results of Figures 4.26 and 4.27 indicate that the strong interactions established in the B0\_xy mixtures between the two components, induce a strong influence on the crystallization properties of PA12. In particular, the increase of PF resin in the B0\_xy blends induces a strong decrease of the crystallization rate of PA12, as

indicated by the strong decrease of the crystallization temperature for the samples with PF content lower than 35%wt, cold crystallization for the blends B0\_3565 and B0\_4060, up to prevent any crystallization, not only from the melt in the cooling step but also during the successive heating scans. Whether PA12 in the B0 blends with PF content higher or equal to 60%wt crystallizes by aging at temperatures higher than the glass transitions has not been checked in depth. The most interesting result of DSC and diffraction analysis consists in having evidenced that in absence of HMTA the interactions established at PF/PA12 interface are really strong.

The strong interaction and the reaction between the nitrogen of PA12 and phenolic rings of PF resin are directly visualized using Infrared spectroscopy. ATR has been used for the powder samples with a low amount of polyamide for which films cannot be prepared, and FTIR for samples with a high amount of PA12 for which it is possible to prepare films with the right thickness by compression molding.

The IR spectrum of the as-prepared sample of the blend B0\_6040 (unreacted) is compared with the spectrum of the blends B0\_6040 compression molded at 200 °C for 10 minutes and with the spectrum of PA12 in Figure 4.28. The band at  $\nu = 3290 \text{ cm}^{-1}$  relative to the N-H stretching of the PA12 (curve a of Figure 4.28A) disappears in the compression-molded sample (curve c of Figure 4.28A). Moreover, the band relative to the vibration of the amide group at  $\nu = 1635 \text{ cm}^{-1}$  of PA12 (curve a of Figure 4.28B), is shifted to lower wavenumber in the compression molded sample (curve c of Figure 4.28B). This confirms the establishment of hydrogen bonds between the nitrogen of the amide group of PA12 and the hydroxyl group of the PF resin.

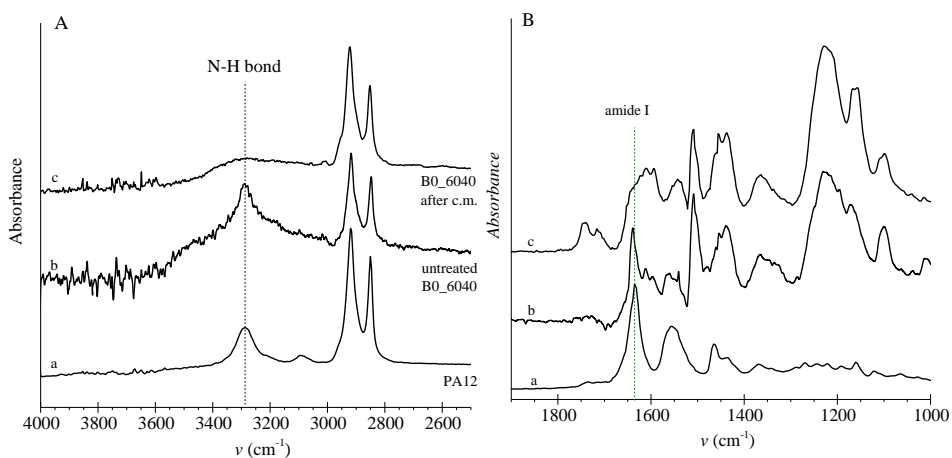


**Figure 4.28.** ATR spectra in the range 4000-2600  $\text{cm}^{-1}$  (A) and 2000-1000  $\text{cm}^{-1}$  (B) of PA12 (a), as-prepared blend B0\_6040 (b) and blend B0\_6040 after compression molding at 200 °C (c).

Figure 4.29 shows the FTIR (figure 4.29A) and ATR (Figure 4.29B) spectra of samples of the blends B0\_7030, B0\_5050, B0\_4060, and of PA12 obtained as films after compression molding at 200°C for 10 minutes and of the uncured HMTA free novolac (Ph). The band at  $\nu = 3290\text{cm}^{-1}$  relative to the N-H stretching of the PA12 is not visible in blends with low amounts of PA12, less than 50%, and becomes barely visible in the sample B0\_4060 (curves b-d of Figure 4.29A). Moreover, the band relative to the vibration of the amide group at  $\nu = 1635\text{cm}^{-1}$  is shifted to lower wavenumber in the blends with low PA12 content and returns visible for PA12 amount higher than 50% (Figure 4.29). This confirms the formation of chemical interaction involving the amide group of the PA12 and the aromatic ring of the resin.

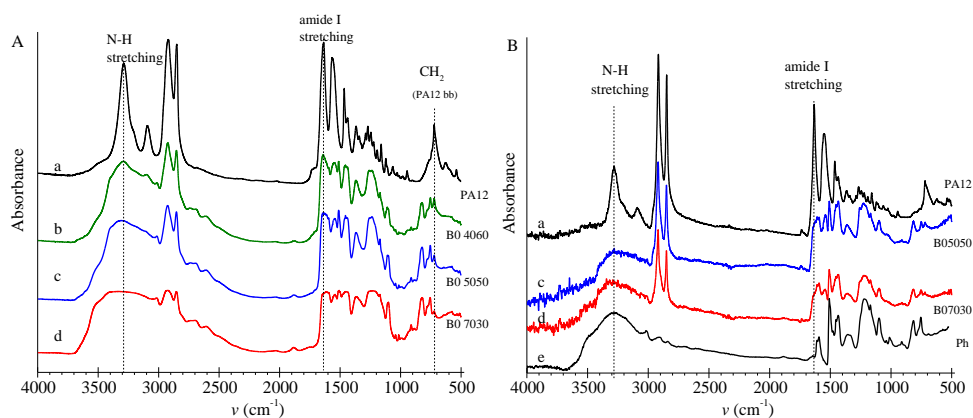


Figure 4.29. FT-IR (A) and ATR (B) spectra of compression-molded films of PA12 (a) and blends B0\_4060 (b), B0\_5050 (c), and B0\_7030 (d) and uncured HMTA-free PF Resin (e). The dashed lines indicate the N-H stretching and the amide I stretching peaks respectively.

#### 4.4 Novolac-polyamide blend as masterbatch

Masterbatch is a concentrated mixture of an additive into a carrier resin, generally added in a small amount to a given polymer during the processing, to modify the properties in a controlled manner. In this paragraph, it is explored the possibility to use PA12 in a masterbatch, in order to prepare cross-linked resins with self-healing properties using a lower amount of PA12.

The masterbatch, which is a PA12 rich blend, has been prepared in two steps. In the first step, a mixture containing 70 %wt of PA12 and 30% of an HMTA free PF resin, has been subjected to intensive mixing with a vibration mixer and successive compression molding at 180°C for 20 min, to obtain the sample coded B0\_3070 in a preceding paragraph. Then the so obtained material has been finely ground in a mechanical miller. The so-prepared powders are coded as B0\_3070C. In the second step, the B0\_3070C powders are used as masterbatch, in mixture with the HAP resin in various proportions and then cured at 200 °C for 10 min in a press. The preparation scheme is summarized in Figure 4.30.

The obtained blends have been defined “B2\_xy” where the two numbers x and y indicate the ratio between the two components, the resin HAP and the masterbatch B0\_7030C (for example, B2\_72 indicates the blend HAP:B03070C with ratio 7:2). The obtained blends have been named “B2\_” followed by two numbers which indicate the ratio between the two components (e.g. B2\_72 indicates the blend HAP:B03070C with ratio 7:2). The blends with masterbatch, their final composition, and the qualitative occurrence of the healing after breaking are reported in Table 4.6. Notice that the blends B2\_xy contain from  $\approx 12$  to  $\approx 23$  %wt of PA12. They are obtained by mixing for 1 part of masterbatch, 2, 2.5, 3.5, and 5 parts of the HAP resin.



**Figure 4.30:** The schematic process used to obtain the masterbatch B0\_3070C and then the cured specimen by compression molding.

**Table 4.6.** Composition of blends composed of the HAP resin and the masterbatch B0\_3070C as a self-healing agent

Sample	HAP:B0_3070C	HMTA <sup>a</sup> (wt%)	PF resin (wt%)	PA12 (wt%)	Self-healing with B0_3070C
B2_21	2:1	6.7%	70.0%	23.3%	Yes
B2_52	5:2 (2.5:1) <sup>b</sup>	7.1%	72.8%	20.0%	Yes
B2_72	7:2 (3.5:1) <sup>b</sup>	7.8%	76.6%	15.6%	Yes
B2_51	5:1	8.3%	80.0%	11.7%	Yes, brittle

<sup>a</sup>Calculated considering that the HAP resin contain about 10 %wt of HMTA.

<sup>b</sup>Codes are given using exclusively integer numbers.

The WAXS profiles of the cured compression molded samples of blends B2\_21, B2\_52, B2\_72, and B2\_51 (curing temperature 200 °C, curing time 10 min) are reported in Figure 4.31. All samples show crystalline PA12 which is fundamental for the occurrence of the self-healing mechanism. The total contents of PA12 in the

resultant blends are 23.3wt%, 20.0wt%, 15.6wt%, and 11.7wt% respectively (Table 4.6).

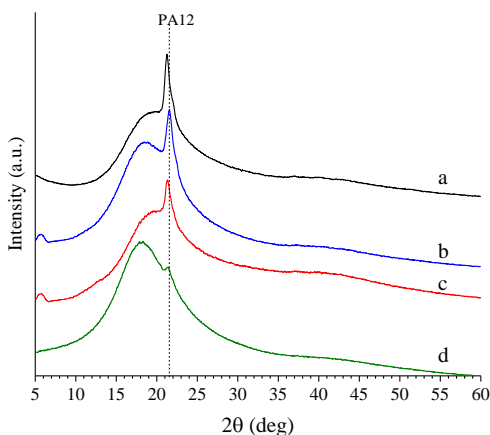


**Figure 4.31:** WAXS profiles of the cured compression molded samples of the blends B2\_21(a), B2\_52(b), B2\_72(c), and B2\_51(d). The PA12 content corresponds to 11.7, 15.6, 20.0 and 23.3 %wt, respectively.

Two consecutive DMTA measurements have been performed on the compression molded cured samples of the blends B2\_21, B2\_52, B2\_72, and B2\_51 (curing temperature 200 °C, curing time 10 min). The DMTA curves are reported in Figures 4.32A, 4.33A, 4.34A, and 4.35A, respectively. Two consecutive DMTA measurements of the same specimen after breaking and successive welding are also reported in Figures 4.32B-4.35B.

For the welded samples with PA12 content lower than 16wt%, B2\_72 and B2\_51, a remarkable drop in storage modulus occurs in the melting temperature range of PA12 (160-180°C). For all the compositions except for the sample B2\_51 which has the lowest PA12 content, during the DMTA scan, the samples do not break, but post-curing reactions occur giving rise to a fully stable material. This is confirmed in the second DMTA scan, performed on the same specimens which show similar viscoelastic behavior of the unbroken specimen tested twice. Compared to the specimens B1\_8020 (Figure 4.11A) which has 20%wt of PA12 content, all the specimens prepared by addition of the masterbatch shows a more pronounced loss

factor peak in the glass transition range (45-65°C), a higher drop in storage modulus, and the start of post-curing phenomena at a temperature of about 30°C lower. In general, even if it is a secondary effect, the effect on the  $\tan \delta$  curve is seen positively as a more damped material is also obtained. This is the direct consequence of the higher amount of amorphous PA12 in this system.

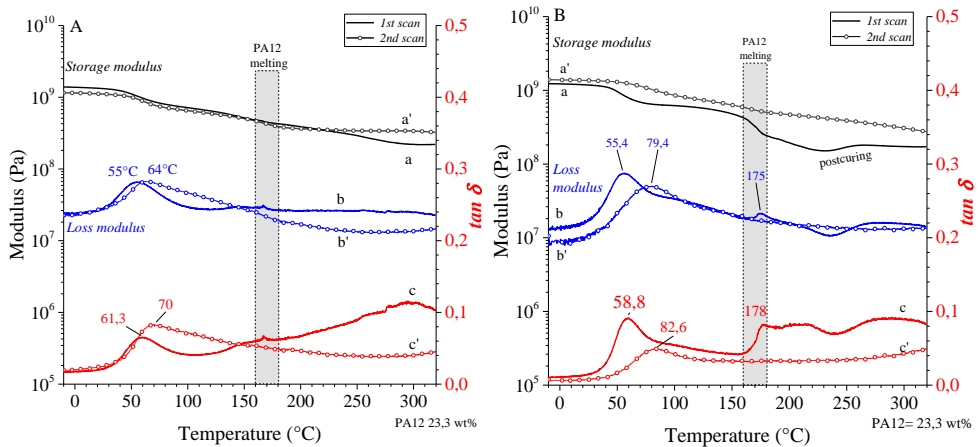


**Figure 4.32.** Storage modulus (a,a'), loss modulus (b,b'), and  $\tan \delta$  (c,c') as a function of temperature of the sample B2\_21 cured at  $T_{cm} = 200^\circ\text{C}$ . The first scan (a-c) and the second scan on the same specimen (a'-c') performed on the intact sample (A) and the sample after breakage and healing (B).

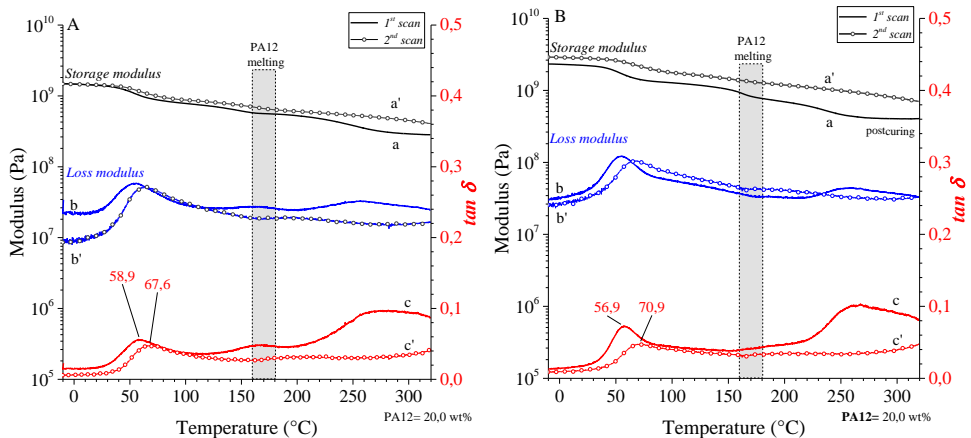


**Figure 4.33.** Storage modulus (a,a'), loss modulus (b,b'), and  $\tan \delta$  (c,c') as a function of temperature of the sample B2\_52 cured at  $T_{cm} = 200^\circ\text{C}$ . The first scan (a-c) and the second scan on the same specimen (a'-c') performed on the intact sample (A) and the sample after breakage and healing (B).

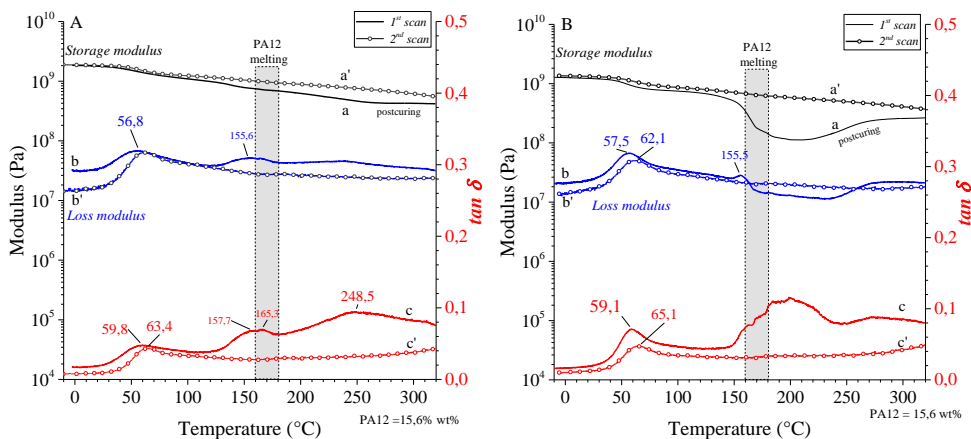


**Figure 4.34.** Storage modulus (a,a'), loss modulus (b,b'), and  $\tan \delta$  (c,c') as a function of temperature of the sample B2\_72 cured at  $T_{cm} = 200^\circ\text{C}$ . The first scan (a-c) and the second scan on the same specimen (a'-c') performed on the intact sample (A) and the sample after breakage and healing (B).

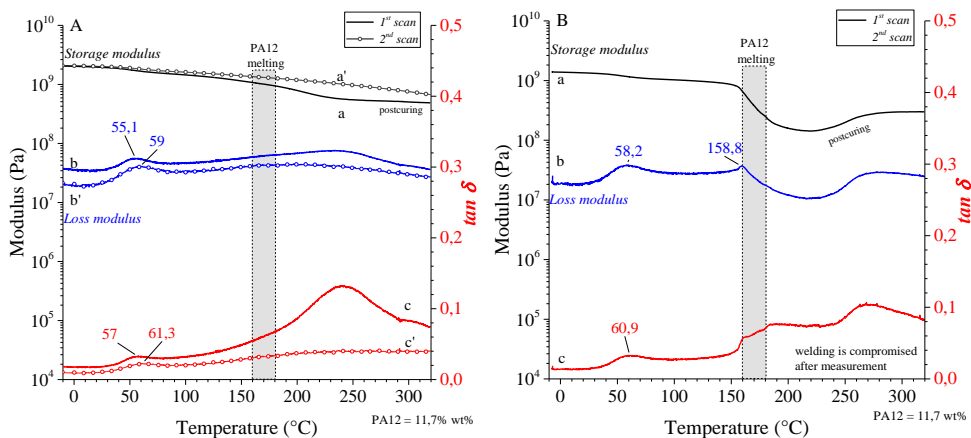


**Figure 4.35.** Storage modulus (a,a'), loss modulus (b,b'), and  $\tan \delta$  (c,c') as a function of temperature of the sample B2\_51 cured at  $T_{cm} = 200^\circ\text{C}$ . The first scan (a-c) and the second scan on the same specimen (a'-c') performed on the intact sample (A) and the sample after breakage and healing (B). The second scan has not been performed because of the detaching of the two pieces.

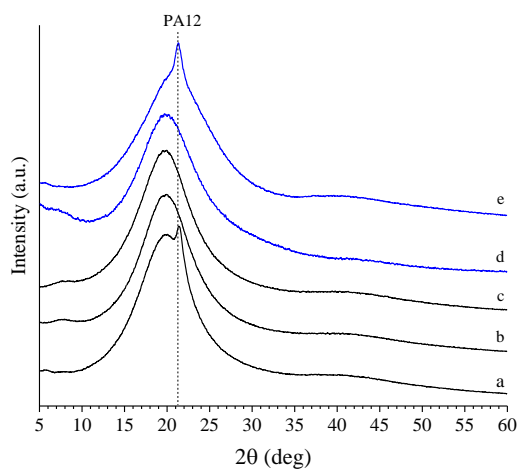
The use of the masterbatch has been extended also to melamine-based resins. The efficiency of the self-healing has been tested on 5 different resins, three of which have different amounts of HMM species, and two of which have different amounts of MF oligomer. They contain a variable amount of PF resin, and HMTA content from 0 to 5wt%. The exact composition of the selected BF resins is specified in

Table 4.7. They are mixed with 50 % of the masterbatch B0\_3070C, so that the final content of PA12 results of 35 %wt. The so obtained blends have been cured at 200°C for 10 mins. Self-healing tests were carried out using the same protocol adopted for the blends B2, annealing the broken specimens at 200 °C for 45min. As indicated in Table 4.7, all the samples show good self-healing properties.

**Table 4.7.** MF-based resin blended with 50% wt B0\_3070C as a self-healing agent (35% wt PA12)

Sample	Novolac (%wt)	HMM (%wt)	MF oligomer (%wt)	HMTA (%wt)	Self-healing with B0_3070C
MF01	-	-	100	-	Yes
MF03	55	-	40	5	Yes
MFPh01	70	25	-	5	Yes
MFPh02	60	40	-	-	Yes
MFPh03	57	40	-	3	Yes

The WAXS profiles and the DSC curves of the cured blends of the MF resins with 50 wt% of the masterbatch B0\_3070C are reported in Figures 4.36 and 4.37, respectively. Only the cured samples with resins MF01 and MFPh01 show Bragg peaks of crystalline PA12 (profiles a and e of Figure 4.36), whereas the DSC heating curves (Figure 4.37A) of all samples show melting peaks of PA12, even though the enthalpy of the blends with resins MF03, MFPh02, and MFPh03 is very small compared with those of the blends with the resins MF01 or MFPh01. All the DSC data obtained from the first heating, cooling, and second heating of the cured blends (Figure 4.37A-C) are reported in Table 4.8.



**Figure 4.36.** WAXS profiles of the cured blends obtained by mixing 50% of B0\_7030C with 50% wt of the melamine-based resin MFPh01(a), MFPh02(b), MFPh03(c), MF03(d), and MF01(e).

Samples	$T_m^I$ (°C)	$\Delta H_m^I$ (J g <sup>-1</sup> )	$T_c$ (°C)	$\Delta H_c$ (J g <sup>-1</sup> )	$T_m^{II}$ (°C)	$\Delta H_m^{II}$ (J g <sup>-1</sup> )
MF01	163	-19	116	11	163	-12
MF03	143	-2	n.d	n.d	n.d	n.d.
MFPh03	154	-9	65 ; 150	3 ; 0,25	161 ; 176	-10 ; -0,25
MFPh02	144	-1	n.d	n.d	158	-1
MFPh01	157	-14	62	2	162	-12

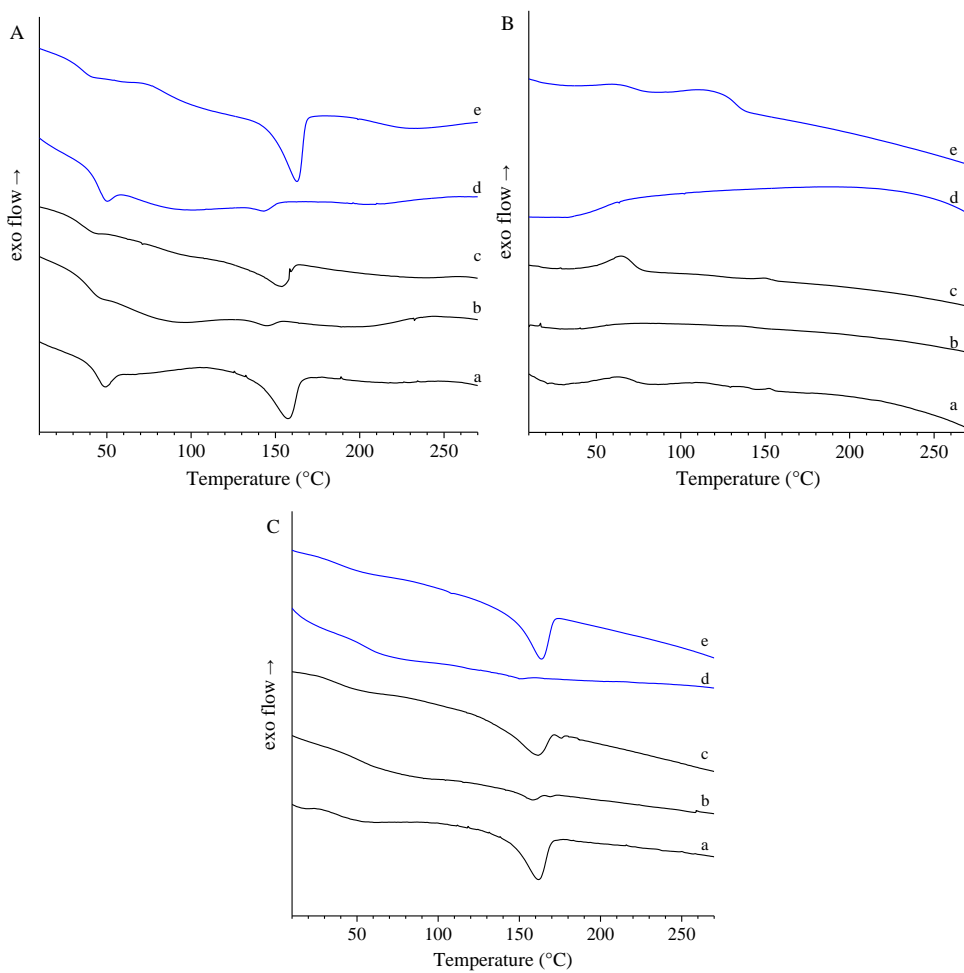


**Figure 4.37.** DSC curves recorded at 10 °C/min during first heating (A), cooling from the melt (B), and successive second heating (C) of the cured blends obtained by mixing 50% of B0\_7030C with 50%wt of the melamine-based resin MFPh01(a), MFPh02(b), MFPh03(c), MF03(d), and MF01(e).

The DMTA curves of the blends containing the melamine-based resins with MF-oligomer content of 40 and 100% (MF03 and MF01) are shown in Figure 4., whereas those relative to the blends 38 containing the melamine-based resins with initial HMM content of 25 and 40 %wt (MFPh01, MFPh02, and MFPh03) are shown in Figure 4.39. In particular, the DMTA measurements have been performed on specimens that have been firstly broken and then welded, during two consecutive heating runs.

Similar to the blends with the PF resins (Figure 4.32-4.35), in the first DMTA scan, all the blends show two principal relaxations, at 40-70 °C, and above 250 °C, due to the collective dynamics at glass transition of the PA12 chains and the long segments of the cured resin segments. These relaxations are followed by a small increase of the storage modulus at high temperatures, due to the occurrence of posturing reactions. As a matter of fact, in the second DMTA scans the segmental dynamics becomes more hindered due to the formation of a more stable network, characterized by a slightly greater cross-linking density. It is worth noting that for samples prepared by directly mixing MF resin with PA12, even using 50 %wt, welding does not occur at all.

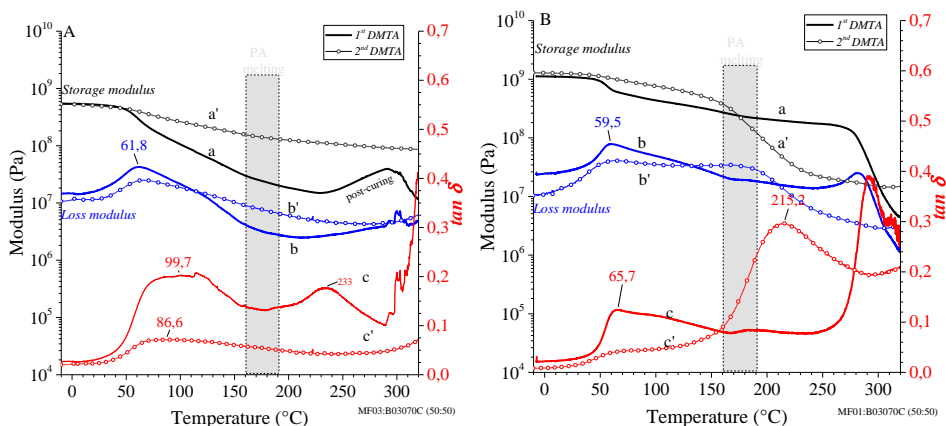


**Figure 4.38.** Storage modulus (a,a'), loss modulus (b,b'), and tan  $\delta$  (c,c') as a function of temperature of the cured samples of blends obtained by mixing 50 wt% of masterbatch BO\_7030C with 50 wt% of the melamine based resin MF03 (A), MF01 (B). The specimen after breakage and healing (a-c) and the second scan on the same specimen (a'-c').

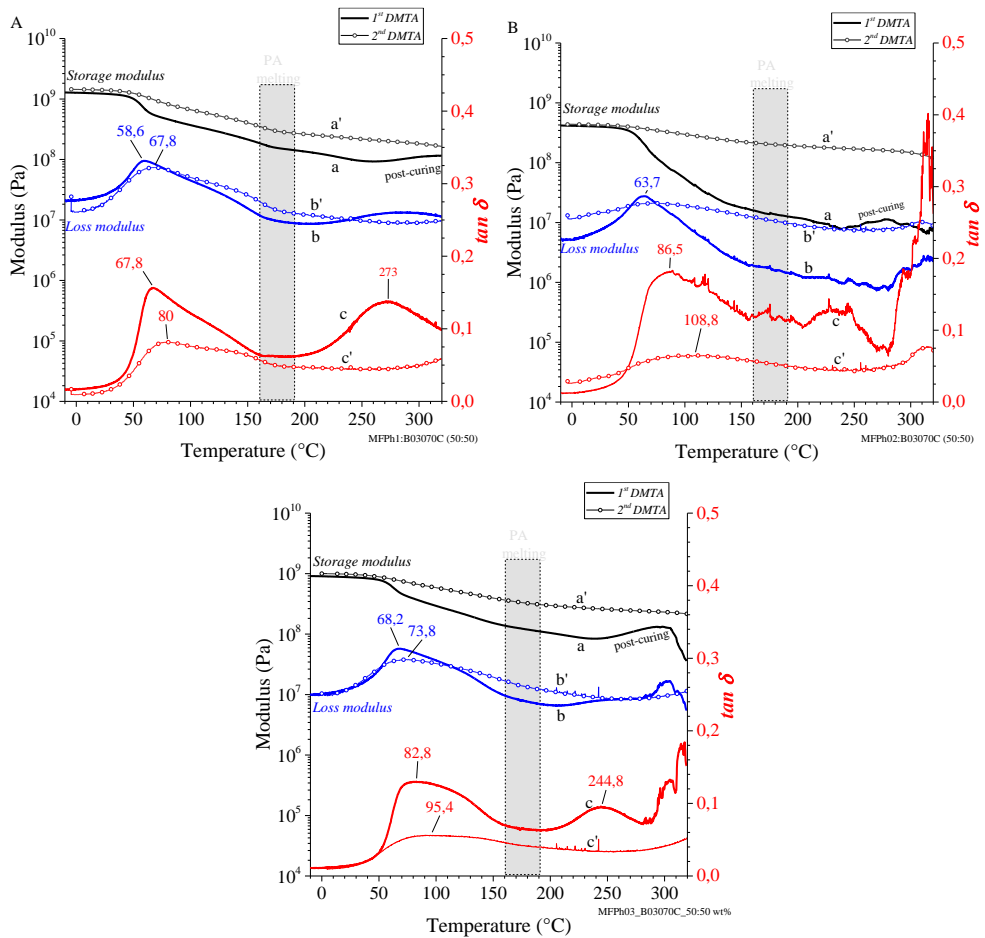


**Figure 4.39.** Storage modulus (a,a'), loss modulus (b,b'), and  $\tan \delta$  (c,c') as a function of temperature of the cured samples of blends obtained by mixing 50 wt% of masterbatch B0\_3070C with 50%wt of the melamine based resin MFPh01(A), MFPh02(B), and MFPh03(C). The specimen after breakage and healing (a-c) and the second scan on the same specimen (a'-c').

## CHAPTER V: SELF-HEALING COMPOSITES

### 5.1 Composite material

A composite material, as known as composite, is a material that is produced from two or more constituent materials, wherein the individual elements remain separate and distinct. Usually, the constituent materials are selected with different chemical or physical properties in order to create a material with merged properties. There are various reasons for designing composite materials, typical examples include materials that are less expensive, lighter, stronger, or more durable when compared with common materials.

Composite materials are generally used for buildings, bridges, and structures such as boat hulls, swimming pool panels, racing car bodies, shower stalls, bathtubs, storage tanks, imitation granite, cultured marble sinks, and countertops.<sup>49,76,77</sup> They are also being increasingly used in general automotive applications.<sup>78</sup>

In general, the constituents of a composite consist of a matrix (binder) and the fillers and/or reinforcement agents. The addition of reinforcement is aimed at improving the properties of the matrix, through the synergistic effect occurring at the interface between the two phases. Typical engineering composites include ceramic, metal, or polymer binder. In this thesis, the used binders for fabrication of composites the HAP thermoset resin studied in the Chapter III and IV.

In particular, the selected **binder** is mixed with polyamide 12 (PA12) to obtain composites with self-healing properties. The prominent advantageous features of the HAP resin and PF resins, in general, are the very high binding properties for a variety of materials such as wood, glass, metals, cellulosic and lignocellulosic fibers, and various type of rubbers<sup>6,79</sup>. The favorable cost/performance characteristics surpass those of most other polymeric resin systems<sup>6</sup>. The fillers adopted for the composites under study are some commercial samples rubbers and PAN fibers.

The importance of using **fibers** in the composite material lies in the fact that applied loads are transferred into the fibers, establishing the principle of load-bearing

component through the matrix. This enables the composite to withstand compression, shear forces, flexural and tensile loads. The matrix should be able to protect the fibers from mechanical damage such as abrasion and environmental attack. The matrix gives the compressive strength to the composite and it is typically a thermoplastic or thermoset polymer. In particular, ductile materials will slow down or stop the cracks at broken fibers, while in brittle materials the fibers will act as stoppers of matrix cracks<sup>80-82</sup>.

Rubbers are characterized by a cross-linked network that provides very durable properties and high resistance to environmental agents. These materials are widely used in many applications such as household, healthcare, industrial, military, automotive, civil, and aerospace. They are characterized by better-wet grip, relatively resistance to gas and water permeability, and reduced swelling in hydrocarbon oils<sup>83,84</sup>. Rubbers features also other valuable characteristics such as the property of being able to dampen or reduce vibrations<sup>85-87</sup>.

Therefore, the use of **rubbers** in composites allows resolving problems like noise and vibrations in the resultant material. The design and fabrication of materials with high damping performances become of increasing demand. Nowadays, rubber damping materials are widely used in shock absorption areas, mainly in automotive, locomotives, railway pads, brake pads, bridges, architecture, and so on<sup>88</sup>. In particular, in automotive applications, the annual demand for rubber shock absorbers has reached several hundred million, and the number is rising year by year.

Therefore, the aim of this chapter is the study of HAP-based composites containing PA12 to elicit self-healing, that incorporate fibers as reinforcement and rubbers as damping fillers in order to obtain good mechanical properties and good dissipative properties while preserving self-healing properties. All composites were prepared by mechanical mixing in a cryogenic grinder miller mixer and the thermo-mechanical and damping properties of the resultant cured materials were investigated by dynamic mechanical thermal analysis.

The next paragraphs describe a characterization study of the materials (rubber and fiber) that were used as fillers to obtain the composites.

## 5.2 Characterization of the Rubber Samples

Different types of vulcanized rubbers were considered. All the samples were supplied as blocks that were cut in slices for the analyses. The main characteristics of the rubber samples used for the preparation of the PF-based nanocomposites are reported in Table 5.1. In particular, the sample Rb01 is a nitrile butadiene rubber (NBR), the samples Rb02, Rb03, and Rb04 are ethylene-propylene-diene rubbers (EPDM), with different diene (namely ethylidene norbornene, ENB) content, the sample Rb05 is an acrylic rubber (ACR), the samples Rb06, Rb07, and Rb08 are chlorinated isobutylene-isoprene rubbers (C-IIR), whereas the sample Rb09 is polyisobutylene (PIB). Finally, the sample Rb10 is an ethylene-propene-diene-rubber, with low diene (ENB) content, grafted with maleic anhydride (EPDM-mA). All the rubbers were characterized through IR, WAXS, DSC, TGA, and DMTA analysis. Solution  $^1\text{H}$  and  $^{13}\text{C}$  NMR spectra were also collected for some selected samples (*vide infra*) in order to gather information about the chain microstructures. The results of these preliminary studies are summarized in Table 5.1.

Table 5.1: the main characteristics of the rubbers							
Sample	material	polymer identification	Substitution/ comonomer	Glass transition	Glass transition	Degradation $T_{95\%}$	other information
		(by ATR-FTIR) <sup>a</sup>	(by NMR)	(by DSC)	(by DMTA)	(by TGA)	by WAXS and/or TGA
Rb01	NBR	poly (butadiene: acrylonitrile) (match 93%)	Acrylonitrile ~35% mol	-29°C	-5°C	407°C	amorphous
Rb02	EPDM	ethylene propylene diene rubber (match 70%)	diene = ENB 4,5% wt ethylene 79% wt	-43°C	-22°C	336°C	amorphous with low polyethylene crystallinity and crystalline fillers - 3% wt of Calcite
Rb03	EPDM	ethylene propylene diene rubber (match 80%)	diene = ENB 4,4% wt ethylene 83% mol	-43°C	-21°C	281°C	amorphous with low polyethylene crystallinity and very low crystalline fillers (Talc)
Rb04	EPDM	ethylene propylene diene rubber (match 83%)		-55°C	-31°C	381°C	amorphous with 32% wt of fillers; Talc and Kaolin
Rb05	ACR	poly acrylate (match 80%)		-16°C	8°C	335°C	amorphous
Rb06	C-IIR	poly (isobutylene: isoprene)	1,4 % halogen 1,9% unsaturation	-65°C	-22°C	315°C	amorphous with low amount of crystallizable material
Rb07	C-IIR	poly (isobutylene: isoprene)	1,1 % halogen 2,0% unsaturation	-65°C	-23°C	315°C	amorphous
Rb08	C-IIR	poly (isobutylene: isoprene)	2,1% halogen 3,0% unsaturation	-65°C	-25°C	287°C	amorphous
Rb09	PIB	poly isobutylene (match 85%)		-67°C	-38/-17°C	358°C	amorphous with 32% wt of fillers; Talc and Kaolin
Rb10	EPDM-mA	ethylene-propene (match 97%)	ethylene 60% mol low content of ENB	-57°C	-40°C	292°C	low PE crystallinity (~2%)

<sup>a</sup> The percentage of FTIR bands corresponding to the specific polymer species is indicated.

### 5.2.1 Infrared spectroscopy

Infrared spectroscopy was used to confirm the polymer nature of the rubber samples by comparing the spectra with those contained in a library of data. The ATR-FTIR spectra of the rubber samples are reported in Figure 5.1 - 5.3.

The ATR-FTIR spectrum of the sample Rb01 (Figure 5.1A) is matched by that of a poly (butadiene-acrylonitrile) sample of the database to 93% agreement. In Figure 5.1A the typical peak of the nitrile group at  $\nu=2237\text{ cm}^{-1}$  is indicated.

The ATR-FTIR spectra of the samples Rb04, Rb02, and Rb03 of Figure 5.1B are matched by that of a database ethylene-propylene-diene rubber with an agreement of 83%, 70%, and 80% respectively. The main differences between the spectra of the three EPDM samples are in the relative intensity of the peaks at  $\nu=1539\text{ cm}^{-1}$  assigned to the C=S and/or CS<sub>2</sub> group<sup>89</sup> and the presence of a broad peak in the range 1300-1000  $\text{cm}^{-1}$  for the sample Rb04 (curve a, Figure 5.1B) typical of kaolin. The presence of C=S and/or CS<sub>2</sub> bands indicate the samples are partially vulcanized. The ATR-FTIR spectrum of the sample Rb05, Figure 5.2A, is matched to 80% agreement by the database spectrum of a polyacrylate, as confirmed by the presence of the characteristic carbonyl, ether, and  $\alpha$ -methyl bands at  $\nu=1724, 1153, \text{ and } 1379\text{-}758\text{ cm}^{-1}$  respectively<sup>90</sup>. Acrylic rubbers (ACR) are obtained by copolymerization of ethyl acrylate with other acrylates such as *n*-butyl acrylate.

The ATR-FTIR spectra of the samples Rb06, Rb07, and Rb08, Figure 5.2B, are matched by the database spectrum of a poly (isobutylene-isoprene) rubber. Differences occur for the relative intensity of the bands due to carbon double bonds and halogenated substituent falling in the range  $\nu=1800\text{-}1500\text{ cm}^{-1}$ , indicating that the samples are characterized by differences in unsaturation and halogen content.

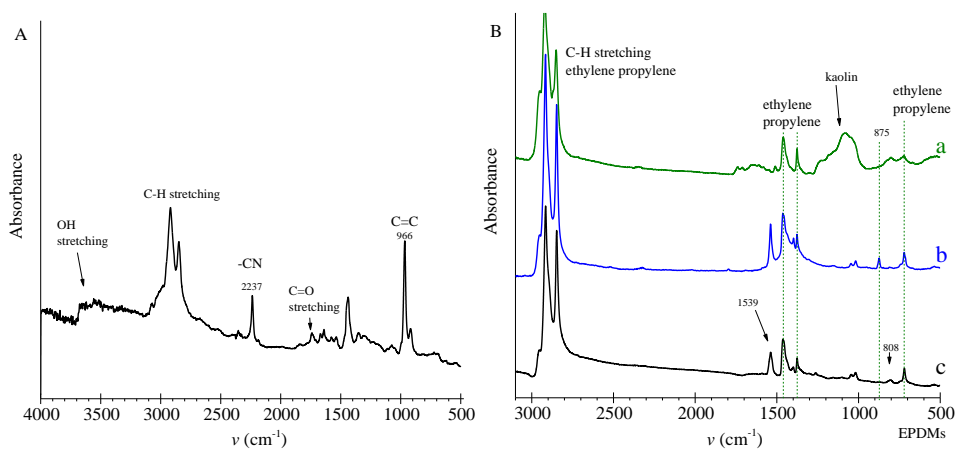


Figure 5.1: ATR-FTIR spectra of the A) sample Rb01, and B) the EPDMs samples Rb04 (a), Rb02 (b), and Rb03 (c).

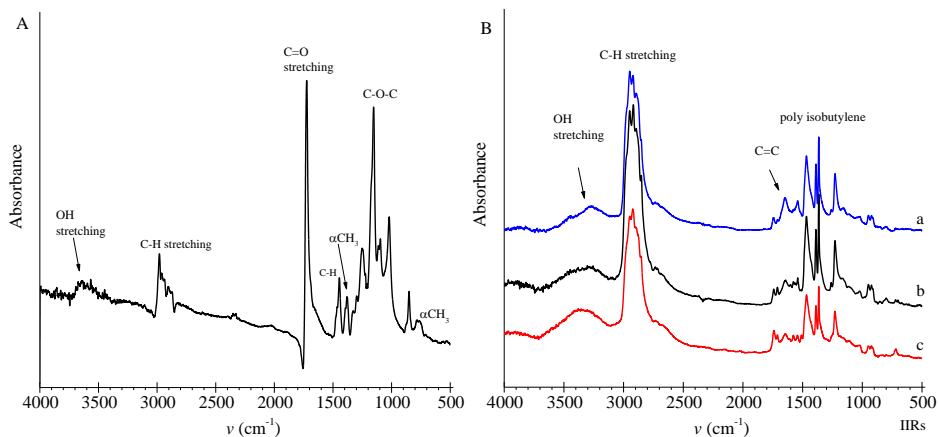


Figure 5.2: ATR-FTIR spectra of the A) sample Rb05, and B) the IIR samples Rb08 (a), Rb07 (b), Rb06 (c).

The FTIR spectrum of the sample Rb09, Figure 5.3A, is matched with 85% agreement by the database spectrum of polyisobutylene (PIB), as indicated by the presence of the bands at  $\nu=2965-2875$ , 1467, and  $1365\text{ cm}^{-1}$  due to the stretching and bending vibration of the C-H bonds. The broad peak in the range  $1300-1000\text{ cm}^{-1}$  is due to the presence of kaolin.

Finally, the FTIR spectrum of the sample Rb10, Figure 5.3B, is matched with an agreement of 97% by the spectrum of ethylene-propylene rubber, as indicated by the presence of the bands at  $\nu=2965-2875$ , 1468, 1375, and  $721\text{ cm}^{-1}$  due to the stretching

and bending vibrations of the C-H bonds. In addition to these peaks, there are two peaks at  $\nu=1789$  and  $1710\text{ cm}^{-1}$  due to the carbonyl group of the grafted maleic anhydride.<sup>91</sup>

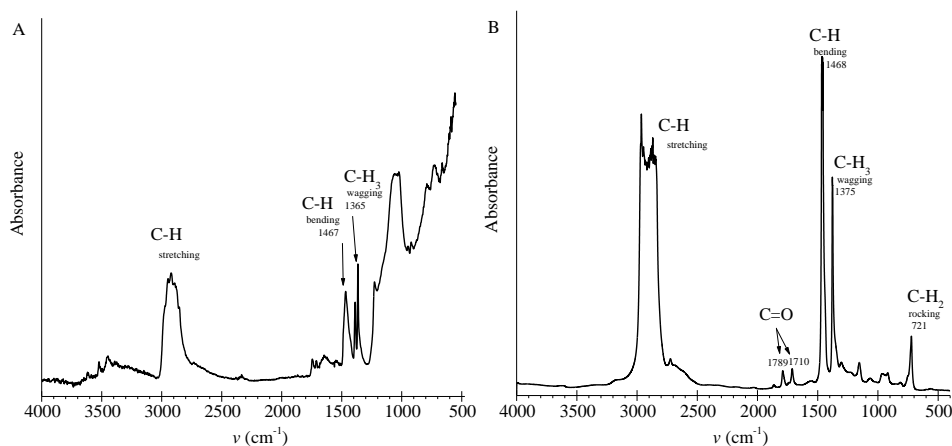
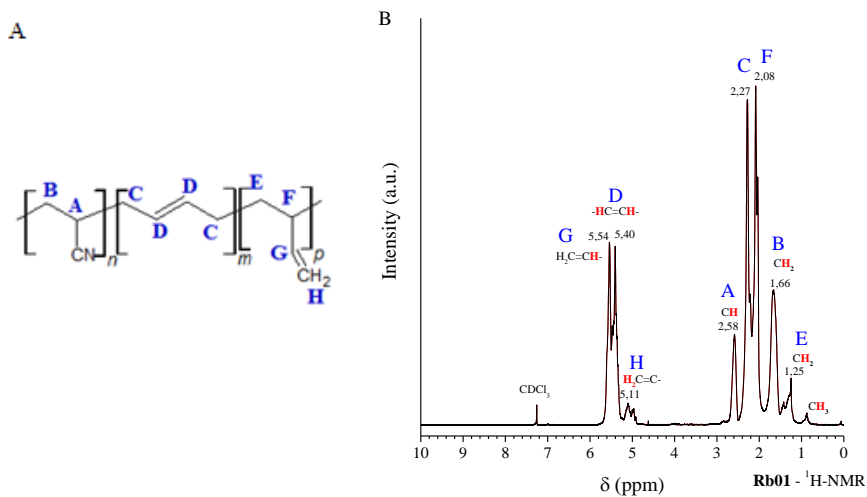


Figure 5.3: FTIR spectra of the A) sample Rb09 matching with an agreement of 85% the database spectrum of PIB, and B) the sample Rb10 matching with 97% agreement the spectrum of an EPR sample.

### 5.2.2 Solution Nuclear Magnetic Resonance analysis

The solution NMR spectra of selected rubber samples are reported in Figure 5.4-5.8. Spectra were recorded at 25°C in deuterated chloroform (see Chapter 2).

In particular, the  $^1\text{H}$ -NMR spectrum of the sample Rb01 reported in Figure 5.4 is used to evaluate the content of acrylonitrile units and the relative amount of 1,2- and 1,4-butadiene unit<sup>86</sup>. Data analyses indicate that the amount of acrylonitrile units is about 35% mol, whereas the relative amount of 1,2- and 1,4-butadiene units are 21 and 79% mol, respectively<sup>92,93</sup>.



**Figure 5.4.** Chemical structure (A) and solution <sup>1</sup>H-NMR spectrum of the NBR sample Rb01 (B).

The solution <sup>1</sup>H-NMR spectra of the samples Rb02 and Rb03 of Figure 5.5, have allowed to identify the diene unit and calculate the its relative amount, following the resonance assignment of Kolbert and Didier.<sup>94</sup> In particular the characteristic peaks of ethylidene-norbornene (ENB) are observed at  $\delta = 5.01$ - $5.04$  and  $5.23$ - $5.24$  ppm for both the samples (Figure 5.5). The relative amount of ENB in the polymer chain is 4.5% wt and 4.4% wt respectively.

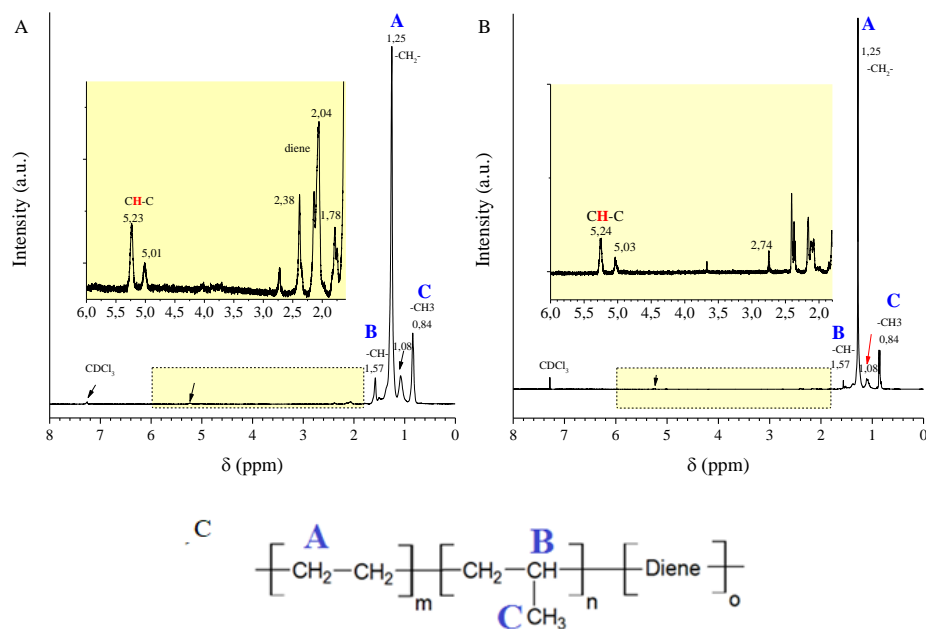


**Figure 5.5:** <sup>1</sup>H-NMR spectra of A) Rb02, ENB (wt%) =4,5%; B) Rb03, ENB (wt%) =4,4%; C) polymer structure of EPDM.

In order to calculate the relative amount of ethylene and propylene units in the EPDM chains for the samples Rb02, Rb03, solution <sup>13</sup>C-NMR spectra have been collected (Figure 5.6). The peak attribution and the integration value are shown in Table 5.2<sup>95–98</sup>.

<b>Table 5.2</b> – Relative intensity of the <sup>13</sup> C-NMR peaks of the EPDM samples.				
resonances		Chemical shift [ppm]	Rb02 integration (relative)	Rb03 integration (relative)
Primary	P	19.7	1.00	1.00
Secondary	S	32.8; 29.7; 27.1	8.55	10.56
Tertiary	T	32.8	0.70	0.88

Indicating with P, S, and T the primary, secondary, and tertiary carbon atoms, the amount of ethylene units (C<sub>2</sub>) in the polymer backbone calculated with the equation (1)<sup>97</sup>:

$$\%molC_2 = \frac{E'}{E' + P'} = \frac{S - P}{S + P} = \frac{S - T}{S + T} \quad (1)$$

corresponds to 79 and 83 for the samples Rb02 and Rb03, respectively.

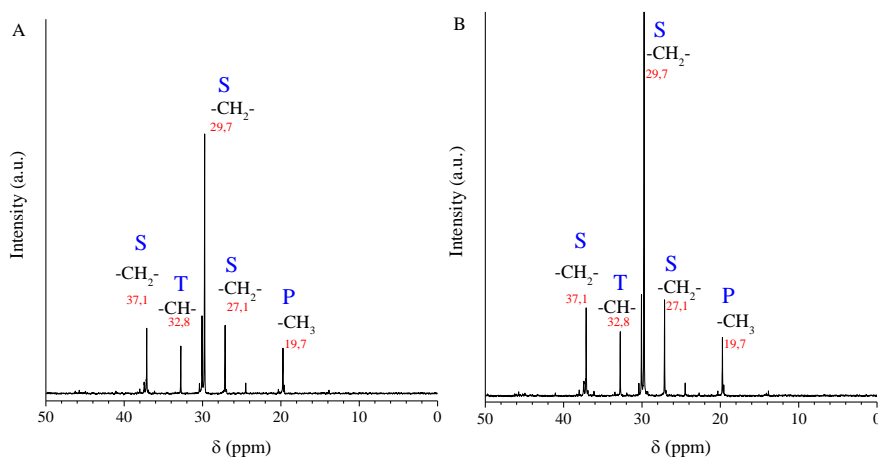
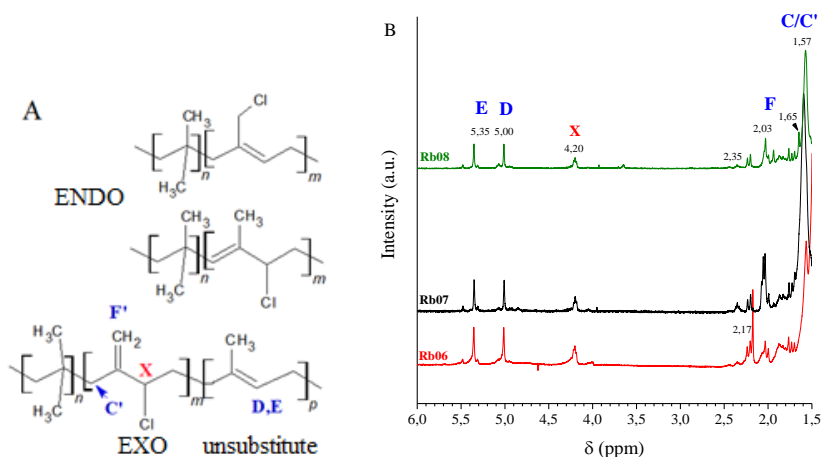


Figure 5.6: Solution  $^{13}\text{C}$ -NMR spectra of the EPDM samples A) Rb02, and B) Rb03.

The solution  $^1\text{H}$ -NMR of the samples Rb06, Rb07, and Rb08 (Figure 5.7A) allowed evaluating the degree of unsaturation and halogen substitution of the isoprene units and the relative amount of exo-methylene allyl (EXO) and endo-chloromethyl olefin (ENDO) microstructures. In particular, the position of the peaks marked with the letter X in the Figure 5.7B indicate also the nature of the halogen, since the protons vicinal to chlorine and bromine substituents show chemical shift above (in the range 4,10 - 4,20 ppm) and below 4,00 ppm, respectively<sup>99</sup>. As reported in Table 5.3, the three samples are chlorinated isobutylene-isoprene rubbers (C-IIR) with chlorine content in the range 1.1-2.1 % mol.

<b>Table 5.3 – <math>^1\text{H}</math>-NMR data of the C-IIR samples</b>			
<b>content of (%mol)</b>	<b>Rb07</b>	<b>Rb06</b>	<b>BRb08</b>
<b>Total Isoprene</b>	2,0%	1,9%	3,0%
<b>Chlorine</b>	1,1%	1,4%	2,1%
<b>Exo form</b>	0,9%	1,4%	1,7%
<b>Unsubstitute isoprene<sup>a</sup></b>	0,5%	0,3%	0,8%

<sup>a</sup>The sum of Unsubstituted isoprene units and chlorine content experimentally determined by proton NMR spectra does not perfectly match the total content of isoprene units.



**Figure 5.7:** A) Chemical structure of C-IIR rubbers and substitution scheme of chlorine atoms. B) Solution  $^1\text{H}$ -NMR spectra of the C-IIR samples in the resonance region of isoprene proton atoms, from 6.0 to 1.5 ppm. The peaks C and C' are attributed at H  $\alpha$ -C=C; D is =CH of isoprene (E isomer); E is =CH of isoprene (Z isomer); X: Peaks at 4,00 - 4,20 ppm are due to H-C-Cl.

The solution  $^1\text{H}$ -NMR spectrum of sample Rb10 is typical of ethylene-propylene-diene rubbers. In particular, the magnification on the 6-2 ppm range relative to the diene ENB and maleic anhydride grafting protons, shows that the ENB content is less than 1 wt% (Figure 5.8A). The ethylene content, calculated from the solution  $^{13}\text{C}$ -NMR spectrum results of 60% mol (Figure 5.8B).

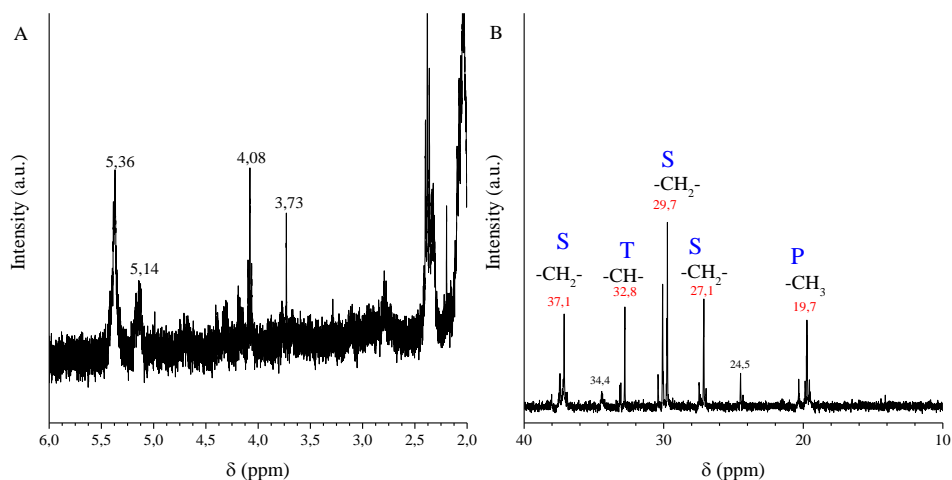


**Figure 5.8:** A) Solution  $^1\text{H-NMR}$  spectrum in the ppm range of ENB and maleic anhydride protons and B) solution  $^{13}\text{C-NMR}$  spectrum in the ppm range of the backbone carbon atoms of the EPDM sample Rb10.

### 5.2.3 DSC and WAXS

All the rubber samples were characterized by DSC and WAXS in order to evaluate the thermal properties and to identify the crystalline phases, the possible presence of inorganic crystalline fillers, and measure the glass transition temperature.

The DSC thermograms and the WAXS profiles of the rubber samples are reported in Figure 5.9-5.15.

The NBR sample Rb01 (Figure 5.9A) shows a faint melting peak at  $93^\circ\text{C}$  in the first heating scan. The sample does not show any tendency to crystallize neither from the melt nor from the amorphous phase (cold crystallization) in the successive cooling and second heating scans, respectively. However, the sample does crystallize by aging at room temperature, as indicated by the DSC scan recorded after the melt cooled sample after 5 days. The WAXS profile of this sample shows an amorphous halo centered at  $2\theta \approx 19^\circ$ . Low-intensity peaks at  $2\theta \approx 6$  and  $20^\circ$  are also observed, due to the presence of additives (Figure 5.9B).

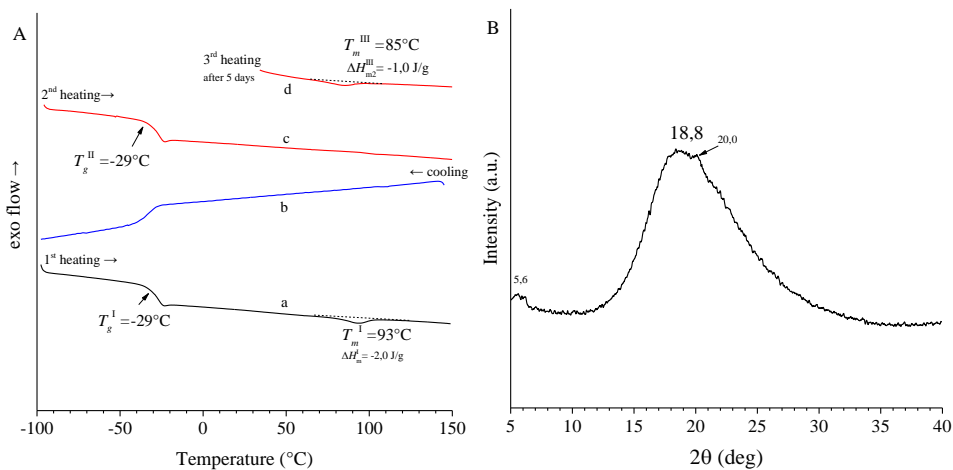


**Figure 5.9:** (A) DSC thermograms recorded at 10 °C/min during the 1<sup>st</sup> heating (a), cooling from the melt (b), 2<sup>nd</sup> heating (c) of the as-prepared sample Rb01, and the melt cooled samples aged for 5 days(d). (B) WAXS profiles of the as-prepared sample Rb01.

As shown by Severe et al<sup>100</sup>, the **glass transition** temperature of the NBR systems increases almost linearly with the increase of acrylonitrile content. The plot of the glass transition temperatures extracted from Ref. 100 is reported in Figure 5.10B as a function of acrylonitrile content. Since these data were obtained from the DSC thermograms of NBR samples recorded at the heating rate of 20 °C/min, the value of -27 °C of the glass transition temperature of the sample Rb01 extracted from the DSC thermogram recorded at the same heating rate (Figure 5.10A) may be used to deduce that the corresponding acrylonitrile content amounts to  $\approx 29$  % mol (Figure 5.2.10A). The ACN content determined by proton NMR analysis results in 35 % mol.

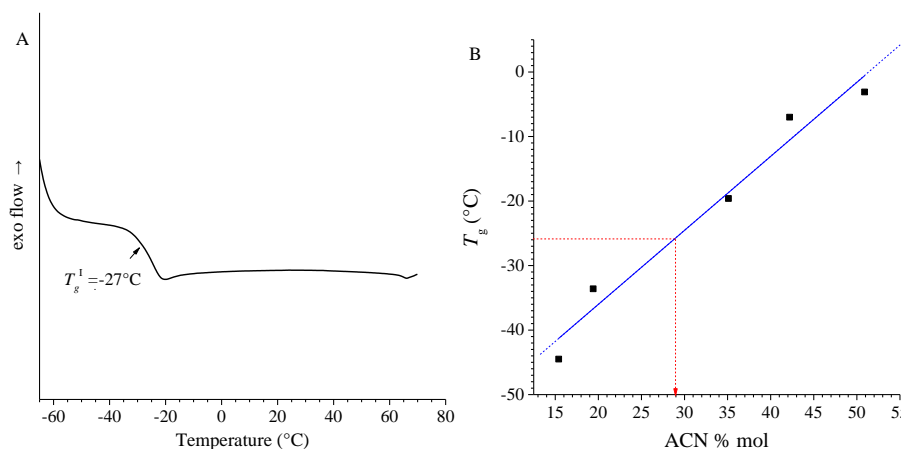


**Figure 5.10:** A) DSC thermogram recorded at 20°C/min of the NBR sample Rb01; B) Glass transition temperature vs. acrylonitrile content of NBR samples extracted from Ref. 26. From the interpolation of the  $T_g$  value of the sample Rb01 an ACN content of ~29% mol may be deduced.

The DSC thermograms relative to the EPDM rubber Rb03 are reported in Figure 5.11A. The sample shows three melting endotherms at 44, 107, and 122°C in the first heating scan, three crystallization peaks at 107, 94, and 24°C, in the successive cooling, followed by three melting peaks at 38, 107, and 122°C in the second heating. These peaks reflect the fractionated crystallization/melting of ethylene sequences of different lengths. The glass transition temperature corresponds to  $\approx -43^\circ\text{C}$ . The WAXS profiles of the sample Rb03 show peaks at  $2\theta \approx 21$  and  $24^\circ$  corresponding to the 110 and 200 reflections, respectively, of the orthorhombic form of PE. Additional peaks are also present due to a low amount of calcite (Figure 5.11B).

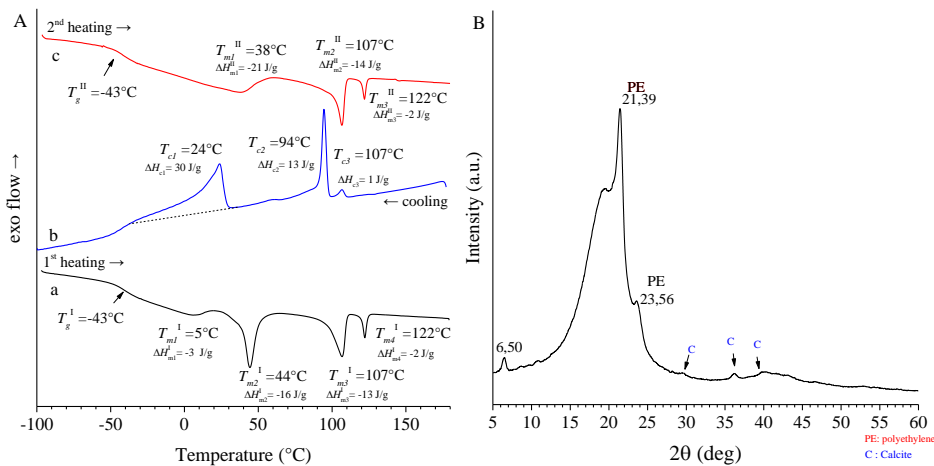


**Figure 5.11:** A) DSC thermograms recorded at 10 °C/min during the 1st heating (a), successive cooling (b), and 2nd heating (c) of the as-prepared sample Rb03 and (B) corresponding WAXS profile. Polyethylene peaks are indicated with PE.

Also, the DSC thermograms of the EPDM rubber Rb02, reported in Figure 5.12A, show multiple melting/crystallization peaks. In particular, the curve recorded in the first heating shows melting peaks at 44 and 123°C, the curve recorded in the cooling step shows crystallization peaks at 106 and 17 °C, whereas the curve recorded in the second heating scan show peaks at 29 and 122°C. Therefore, also this sample is characterized by the separate and distinct melting/crystallization of ethylene sequences of different lengths. The glass transition temperature corresponds to  $T_g = -43^\circ\text{C}$ . The crystallization of PE in the orthorhombic form is confirmed by the WAXS profile that shows the 110 and 200 reflections  $2\theta \approx 21$  and  $24^\circ$ , typical of this form (Figure 5.12B). Additional reflections are also apparent in the diffraction profile of Figure 5.12B, due to the presence of calcite.

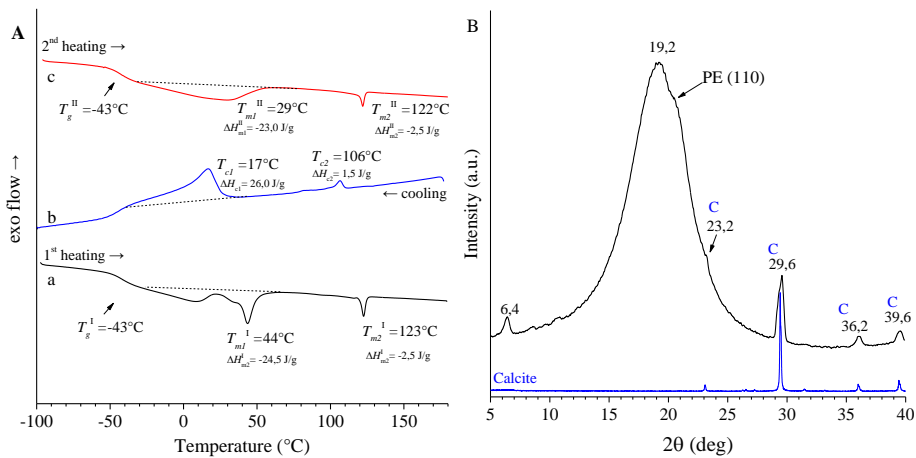


**Figure 5.12:** (A) DSC curves of the sample of Rb02 recorded at  $10^\circ\text{C}/\text{min}$  during the 1st heating of the as-prepared sample (a), successive cooling (b), and 2nd heating (c) scans and (B) corresponding WAXS profiles. The reflections of PE and calcite (C) are indicated. The diffraction profile of calcite (ICCD database, PDF 5-586) is also reported.

The DSC thermograms and the WAXS profile of the EPDM sample Rb04, reported in Figure 5.13, reveal that it is amorphous. The glass transition is  $\approx -55^\circ\text{C}$ . The sample includes talc, calcite, and silicate species (namely kaolinite) as fillers, as indicated by the narrow diffraction peaks overlaying the amorphous halo centered at  $2\theta \approx 19^\circ$  (Figure 5.13B).

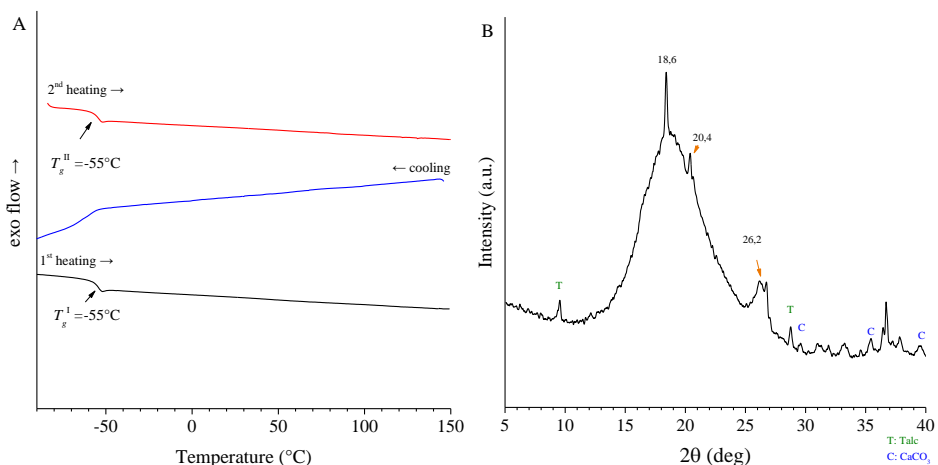


**Figure 5.13:** (A) DSC thermograms of the sample of Rb04 recorded at  $10^\circ\text{C}/\text{min}$  during the 1st heating (a), successive cooling (b), and 2nd heating (c) scans and (B) corresponding WAXS profile. The reflections due to talc and calcite are indicated with the letters T and C, respectively.

The DSC thermograms and the WAXS profiles of the PIB sample Rb09 reported in Figure 5.14 reveal that the sample is amorphous. The glass transition of this rubber is  $T_g = -67^\circ\text{C}$ . The presence of inorganic fillers such as talc, calcite, and silicate species (kaolinite) is indicated by the narrow diffraction peaks overlaying the amorphous halo centered at  $2\theta \approx 14.7$  (Figure 5.14B).

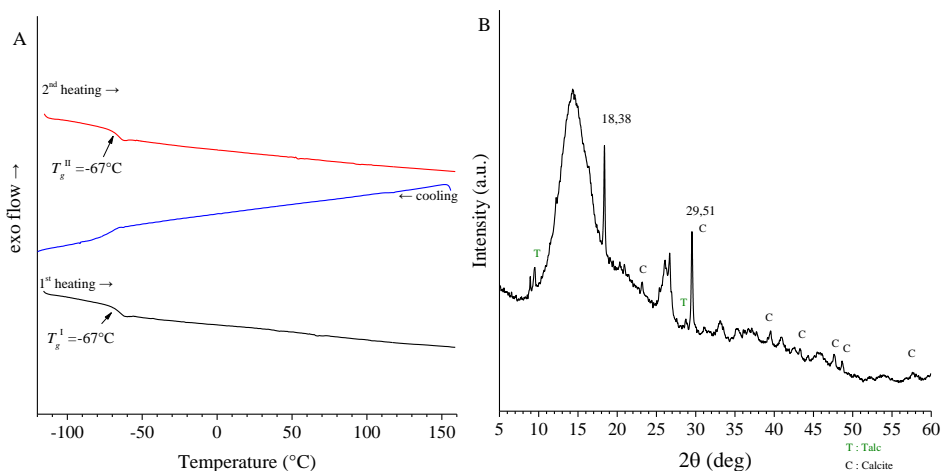
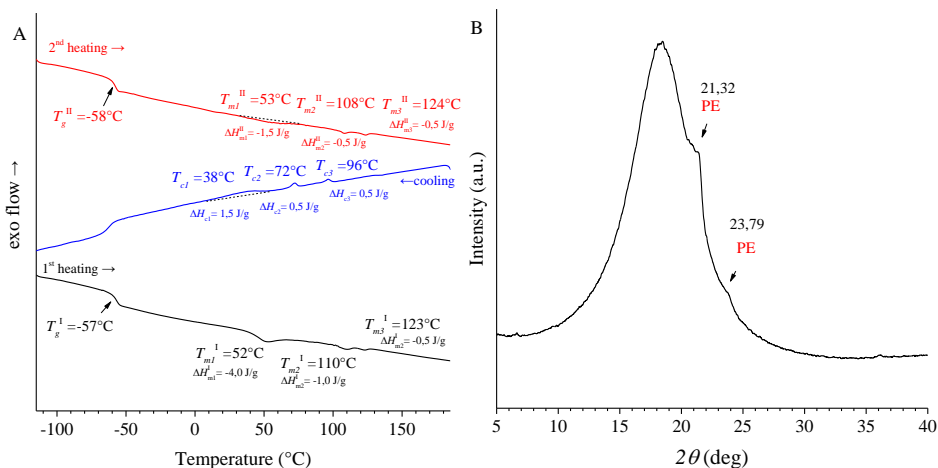


Figure 5.14: (A) DSC thermograms of the PIB sample Rb09 recorded at  $10^\circ\text{C}/\text{min}$  during the 1<sup>st</sup> heating (a), cooling (b), and 2<sup>nd</sup> heating (c) and (B) corresponding WAXS profiles. The reflections of talc and calcite are indicated with the letters T and C, respectively.

The DSC thermograms of the maleic anhydride grafted EPDM sample Rb10, reported in Figure 5.15A, reveal three weak melting peaks at  $\approx 52$ - $53$ ,  $108$ - $110$ , and  $123$ - $124^\circ\text{C}$  during the first and second heating, and three small crystallization peaks at  $96$ ,  $72$  and  $38^\circ\text{C}$  during the cooling. Also, in this case, the multiplicity of melting/crystallization peaks indicate the separate and distinct melting/crystallization of ethylene sequences of different lengths. The glass transition temperature is  $-58^\circ\text{C}$ . The WAXS profile confirms the presence of PE crystals in the orthorhombic form, as indicated by the occurrence of the 110 and 200 reflections of low intensity at  $2\theta \approx 21$  and  $24^\circ$ , respectively typical of this form (Figure 5.15B).

The presence of multiple melting and crystallization peaks in the DSC thermograms of the EPDM samples, probably indicates that these copolymers are synthesized by heterogeneous Ziegler Natta catalysis.



**Figure 5.15:** (A) DSC thermograms of the sample of Rb10 recorded at  $10^\circ\text{C}/\text{min}$  during the 1<sup>st</sup> heating (a), cooling (b), and 2<sup>nd</sup> heating (c) and (B) corresponding WAXS profile. The reflections of PE in the orthorhombic form are indicated by the letters PE.

## 5.2.4 Thermogravimetric Analysis

The thermogravimetric analysis (TGA) has been used to verify if the thermal stability of the rubber samples is suitable for the use of them as fillers in the PF-based composites, considering the temperature at which the composites need to be cured and the temperature of the final operating conditions. The parameter used for this evaluation is the temperature where the sample reaches 5wt% loss, that is the temperature at which the sample is reduced to 95% of its initial weight  $T_{95\%}$ . This technique has been also used to evaluate the amount of inorganic fillers present in the samples.

The TGA thermograms of EPDM samples Rb02, Rb03, and Rb04 are shown in Figure 5.16. The temperatures at which the sample is reduced to 95% of its initial weight are  $T_{95\%} = 336, 281,$  and  $381^\circ\text{C}$  respectively. Furthermore, the samples Rb02,

Rb03, and Rb04 contain <1.0% wt, 3.0% wt, and 32.5% wt of inorganic fillers, respectively (Figure 5.16).

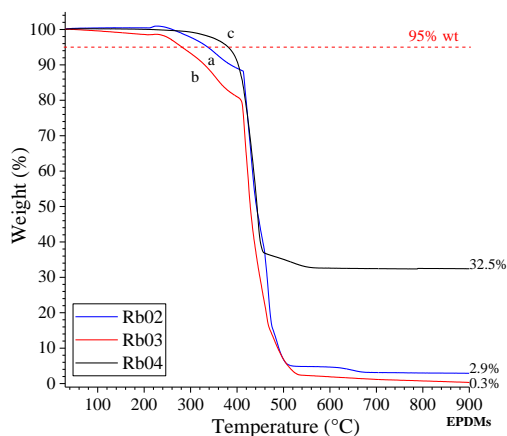


Figure 5.16: TGA thermograms recorded at 10°C/min in air of the EPDM samples Rb02 (a), Rb03 (b), and Rb04 (c).

The TGA thermograms of C-IIR samples Rb07, Rb08, and Rb09 are shown in Figure 5.17. All the samples show similar thermal stability with a single degradation phenomenon at about 350°C. The values of the parameter  $T_{95\%}$  are 315, 315, and 287°C respectively. These samples do not show any relevant content of inorganic additives.

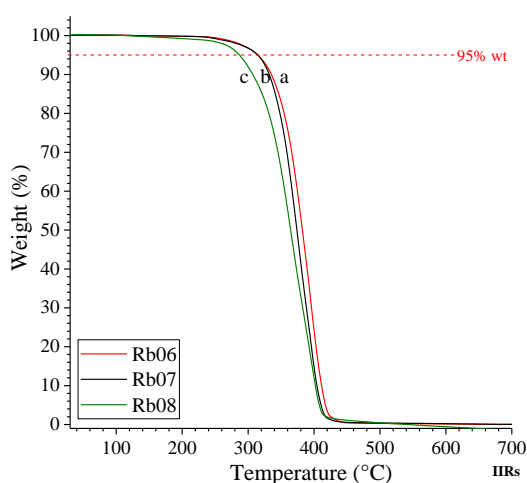
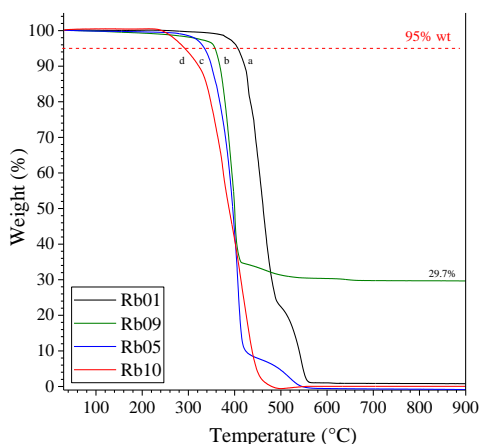


Figure 5.17: TGA thermograms recorded at 10°C/min in air of the C-IIR samples Rb06 (a), Rb07 (b), and Rb08 (c).

The TGA thermograms of the rubber samples Rb01, Rb05, Rb09, and Rb10 are shown in Figure 5.18. The values of the parameter  $T_{95\%}$  correspond to 407, 335, 358, and 292 °C respectively. These samples do not show any relevant content of inorganic additive, except for the sample Rb09 which contains 29.7%wt of inorganic fillers (Figure 5.18, curve b).



**Figure 5.18:** TGA thermogram recorded at 10°C/min of the samples Rb01 (a), Rb09 (b), Rb05 (c), and Rb10(d).

### 5.2.5 Dynamical Mechanical Thermal Analysis of the Rubber Samples

The rubber samples were shaped as rectangular specimens in a press by heating at 180°C, holding them at this temperature for 10 min and successive cooling to room temperature in the press platens while fluxing cold water in the refrigerating system. The resultant specimens were subjected to DMTA measurements in order to gather information about the dissipative properties.

The storage and loss modulus and the loss factor ( $\tan \delta$ ) of the three EPDM rubber samples Rb02, Rb03, and Rb04 are reported in Figure 5.19. It is apparent that the DMTA curves of the kaolinite-rich rubber sample Rb04 (32 wt%) show a remarkable difference with respect to the DMTA curves of the other samples. In particular, the kaolinite-rich EPDM sample shows both moduli one order of magnitude lower and a higher loss factor compared with those of the other EPDM

samples. The glass transition temperature for the samples Rb02, Rb03, and Rb04 are -22, -21, and -31°C, respectively.

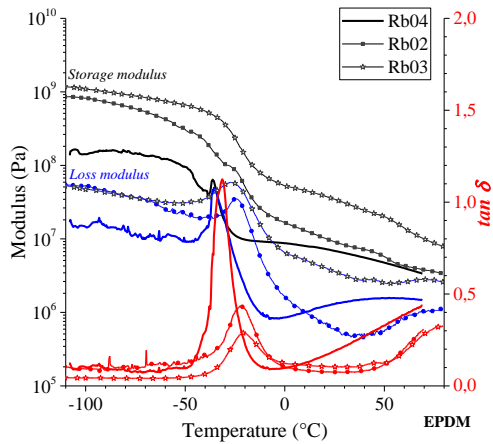


**Figure 5.19:** DMTA curves of specimens obtained by compression molding of the EPDM samples Rb04 (straight lines), Rb02 (circle lines), and Rb03 (star lines). The colors indicate the storage modulus (black), loss modulus (blue), and loss factor (red).

The DMTA curves of the three C-IIR rubbers are reported in Figure 5.20. All the samples show similar thermomechanical behavior and comparable glass transition temperature of -22, -23, and -25°C for the samples Rb06, Rb07, and Rb08 respectively.

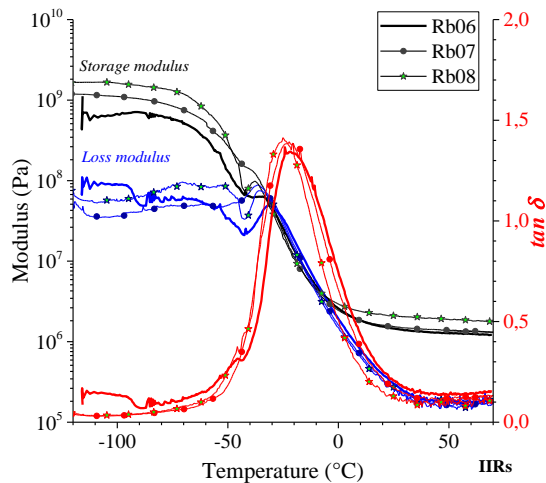


**Figure 5.20:** DMTA curves of specimens obtained by compression molding of the EPDM samples Rb06 (straight lines), Rb07 (circle lines), and Rb08 (star lines). The colors indicate the storage modulus (black), loss modulus (blue), and loss factor (red).

The DMTA curves of the rubber samples Rb01, Rb05, Rb09, and Rb10 are reported in Figure 5.21. The rubber sample Rb10 shows the lowest values of storage and loss moduli and the lowest values of the loss factor, whereas the rubbers sample Rb05 shows the highest values of storage and loss moduli and the highest values of the loss factor. The double high and broad loss factor peak of the rubber Rb09 is influenced by the presence of kaolin.

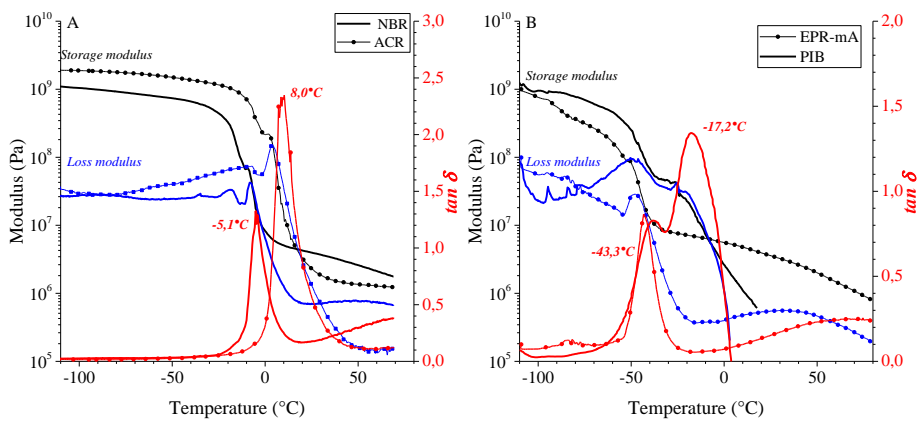


**Figure 5.21:** DMTA curves of specimens obtained by compression molding of the NBR sample Rb01 (straight lines), the acrylic rubber Rb05 (circle lines) (A), the PIB sample Rb09 (straight lines), and the maleic Rb10 (circle lines). Storage modulus (black), loss modulus (blue), and loss factor (red).

The selection of the most suitable rubber samples to be used for the preparation of PF-based composites with relevant dissipative properties was carried out by comparing the values of the loss factor as a function of the temperature in the relevant temperature range (Figure 5.22). In general, to obtain good damping, it is possible to choose an elastomer with a high value of the loss factor and a broad peak. Of course, the final choice depends on the chemistry of the rubber, the interactions with the polymer matrix, and the working temperature of the final product too. The rubber samples containing a high filler content such as Rb09 and Rb04 have not been selected, because the presence of the filler induces also a remarkable decrease of storage modulus. The rubber Rb05 has not been selected because of the high glass transition temperature. Instead, the selected rubber samples

are the EPDM-mA Rb10 sample, because of the presence of the functional maleic anhydride groups, the NBR Rb01, the EPDM Rb03, and the C-IIR Rb06 samples as examples of nitrile, ethylene/propylene/diene, and chloro-butyl rubbers. Additional DMTA analyses were carried out on composite mixtures of the neat HAP resin with 20% wt of the rubber samples, that were cured at 200 °C for 10 min (see Appendix 5). These data suggest that the thermomechanical properties of the cured HAP resins are not greatly altered in the high-temperature region by the presence of the rubber, and only the behavior at sub-zero temperature are influenced, because of the glass transition of the rubber.

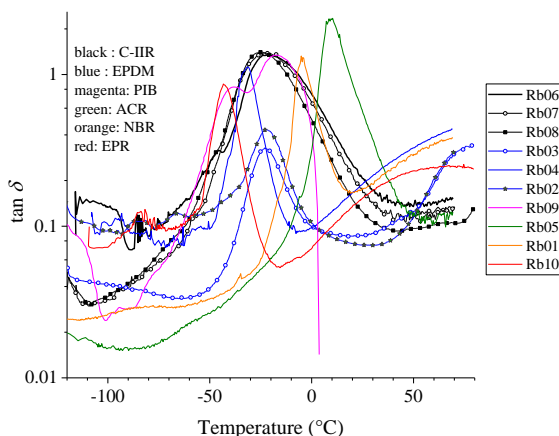


**Figure 5.22:** loss factor comparison of all the rubber samples of Table 5.1.  
Characterization of PAN fibers and their mixture with the HAP Resin

### 5.3.1 Characterization of PAN fibers

The fibers selected for the preparation of HAP-based composites are constituted by polyacrylonitrile (PAN). PAN is a very interesting polymer for its outstanding mechanical strength, even though the thermal resistance is much inferior to that of Kevlar. However, compared with Kevlar, PAN is by far cheaper. Indeed, PAN is a semicrystalline polymer that undergoes degradation at about 300°C, before melting<sup>101</sup>.

The DSC curves of PAN fiber recorded at scanning rate of 10 °C/min during heating, cooling, and the second heating are reported in Figure 5.23A. The X-ray

diffraction profiles of the PAN fiber profile show the 100 reflection at  $2\theta = 16,6^\circ$  of crystalline PAN<sup>102</sup>.

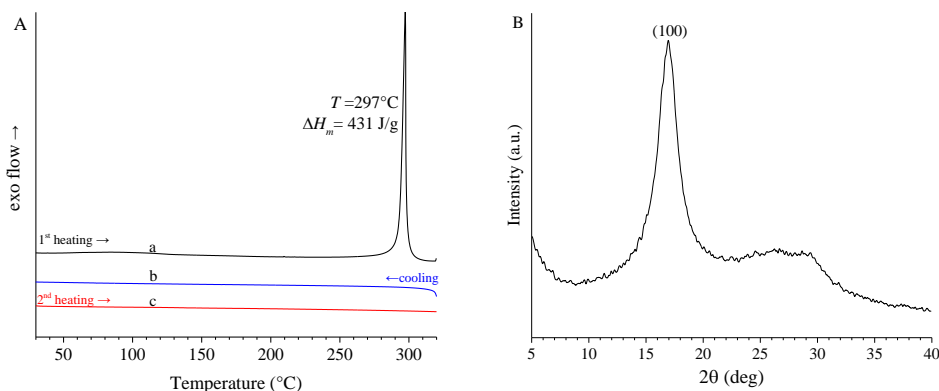


**Figure 5.23:** DSC thermograms of the PAN fibers recorded at 10 °C/min during the 1<sup>st</sup> heating (a), cooling (b), and 2<sup>nd</sup> heating (c) and (B) corresponding WAXS profile.

The exothermic peak recorded during the first heating scan of PAN fiber at 297°C is due to the activation of reactions of cyclization as shown in Figure 5.24. The reaction mechanism is different if it occurs in air or in absence of oxygen and could give rise to different products.<sup>103,104</sup> After the first heating, the sample becomes amorphous, as indicated by the flat thermograms recorded in the cooling and second heating scans (Figure 5.23A).

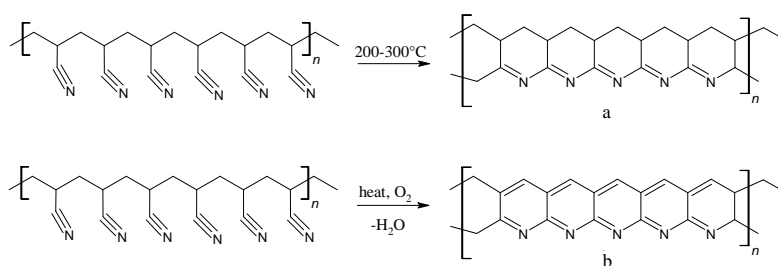


**Figure 5.24:** Cyclization reaction of PAN in absence (a) and presence of oxygen (b). Both lead to an increase in thermal stability and amorphization.

The thermal resistance of the PAN fibers is probed by recording the TGA curve in air (Figure 5.25). At the beginning of the heating scan about 5wt% of the initial weight is lost before 100°C, probably due to moisture evaporation. At about 300°C there is a weight loss of about 10wt% due to the reactions described in Figure 3.24a.

The first derivative of the TGA curve shows two maxima, indicating that degradation occurs in two steps with maximum rate at  $T_{d1}$  and  $T_{d2}$  equal to 329 and 633°C, respectively. This indicates that upon cyclization the thermal resistance of PAN is greatly increased.

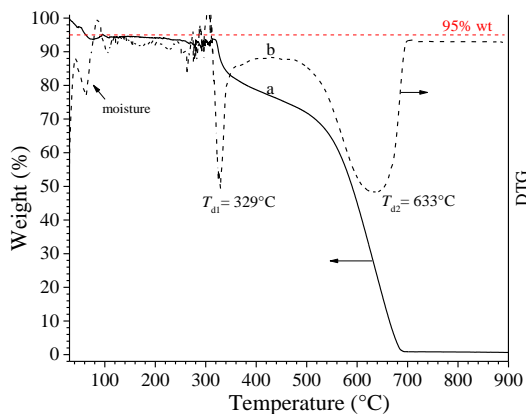


Figure 5.24: TGA curve (a) and corresponding first derivate (b) of PAN fiber.

### 5.3.2 HAP-based composites with PAN

In order to evaluate the behavior of the PAN fibers as a reinforcement agent in composites with the HAP resin, mixtures of the HAP resin with various amounts (from 5 to 20wt%) of PAN were prepared by mechanical mixing.

The thermal properties of the composite mixtures have been evaluated by DSC using the sequent program temperature: 1<sup>st</sup> heating from 30°C to 260°C, cooling to 30°C, and 2<sup>nd</sup> heating from 0°C to 320°C (Figure 5.26). In this way, the curing reaction occurs during the first heating ( $T_{CL} \sim 152^\circ\text{C}$ ), whereas the chemical reactions involving PAN occur during the second heating scan at about 280°C. It is worth noting that in presence of the HAP resin, the cyclization reactions of PAN occur at lower temperatures with respect to the neat sample (curves c of Figure 5.26A, B, C).

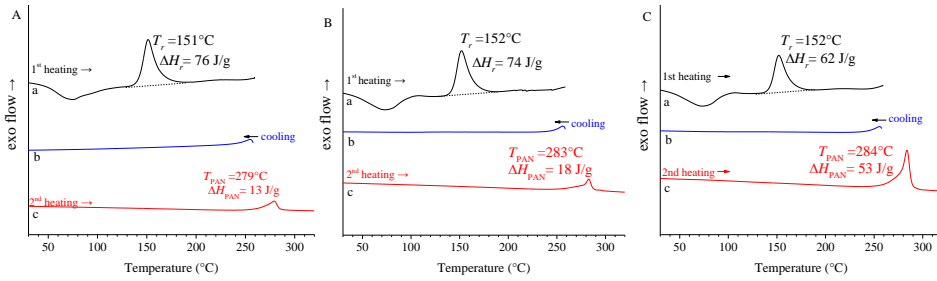


Figure 5.26: DSC thermograms of HAP-PAN composite mixtures recorded during the 1<sup>st</sup> heating (a), cooling (b), and 2<sup>nd</sup> heating (c) with PAN content of A) 5, B) 10 and C) 20% wt.

The HAP-PAN composite mixtures were hence cured by compression molding at  $T_{cm} = 150\text{ }^{\circ}\text{C}$  for  $t_{cm} = 10\text{ min}$ . The curing temperature of  $150\text{ }^{\circ}\text{C}$  prevents the cyclization reaction of PAN.

The TGA curves of the cured HAP-PAN composites with various PAN content (5, 7.5, 10, 20wt%) are compared with those of the neat HAP resin cured in the same conditions ( $150\text{ }^{\circ}\text{C}$ , 10 min) and the neat PAN in Figure 5.27. All the composites show a degradation temperature slightly lower than that of the neat HAP resin.

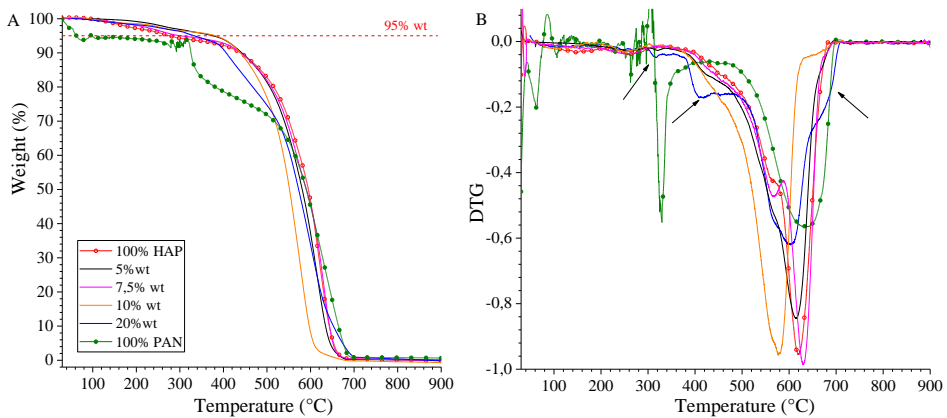


Figure 5.27: Thermogravimetric analysis of the cured HAP resin and the cured HAP-PAN composite mixtures with 5, 7.5, 10, and 20wt% of PAN. A) TGA curves and B) the first derivative. The TGA curves of the neat PAN fibers are also reported for comparison.

The DMTA curves of the cured HAP-PAN composites recorded in the first and successive heating scans are compared with those of the cured HAP resin in Figure 5.28. In the first heating scan (Figure 5.28A) the storage and loss moduli show a

small but significant drop around 150-200 °C, followed by a neat increase at higher temperatures, due to the occurrence of post-curing reactions. Simultaneously, the loss factor of the HAP-PAN composites, show a double peak in the temperature range 150-250 °C. In the second heating scan, instead, the DMTA curves show a monotonous behavior with the temperature and the peaks in the loss modulus and loss factor appear greatly damped. The composite with PAN content of 5wt%, in particular, shows the highest values of the storage and loss moduli (lines with circles of Figure 5.28B), indicating the reinforcement effect exerted by PAN fibers in the mixtures.

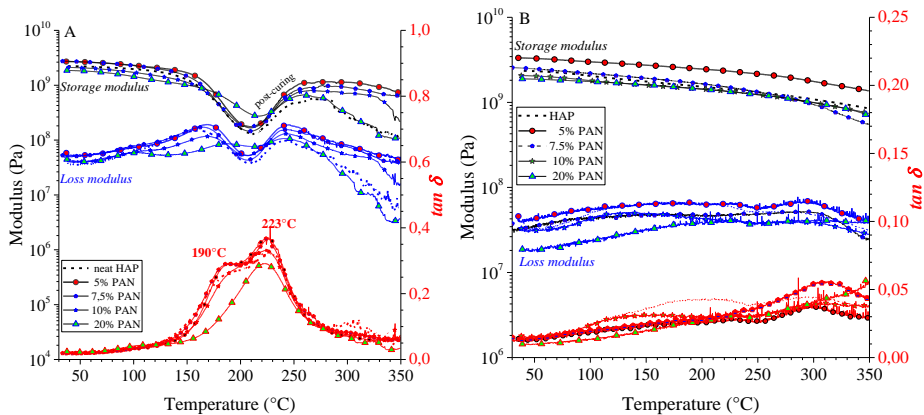


Figure 5.28: DMTA curves of the cured HAP resin and the cured HAP-PAN composite mixtures with 5, 7.5, 10, and 20wt% of PAN measured in a first (A) and a second heating scan (B).

In order to reduce to minimum degradation phenomena up to 500 °C and reach good reinforcement, only composites with PAN content lower than 10wt% (namely  $\approx 6$  % wt) were successively considered.

#### 5.4 HAP/PA12/PAN/Rubbers Composites

Two series of composites with potential self-healing properties were prepared by mixing the HAP resin with PAN fibers and selected rubber samples, either through the addition of PA12 or of the PA12 containing masterbatch B03070C, as self-healing components.

The resultant composites are coded with 10 characters that contain information on the composition. In particular, the code consists of a first letter followed by nine numbers, which indicates the composition of the mixture (e.g. in Figure 5.29):

- The first letter indicates the healing component, “D” standing for PA12 and “C” for B03070C;
- The successive number indicates the type of rubber, namely “1” stands for the EPDM-mA rubber sample Rb10, “2” stands for the NBR rubber sample Rb01, “3” stands for the EPDM rubber sample Rb03 and “4” stands for the C-IIR rubber sample Rb06.
- The successive four numbers, separated by a dash indicate the relative amount of the HAP resin, the healing component, PAN fiber, and rubber, respectively.

#### 5.4.1 Composite with PA12 as a healing agent

The “D” type composites are made by mixing the HAP resin as a binder, PA12 as a healing agent, PAN as fiber, and different kinds of rubber samples. The selected rubbers are the samples EPDM-mA Rb10, NBR Rb01, EPDM Rb03, and C-IIR Rb06 (Table 5.2). All the analyzed samples have the same relative amount of the components (Table 5.4) and they have been named as described in Figure 5.29. As an example, code D1-47-35-06-12 indicates a composite obtained by mixing 47 %wt of the HAP resin, 35 %wt of PA12, 6 %wt of PAN fibers, and 12%wt of the rubber sample EPDM-mA Rb10 (Figure 5.29).

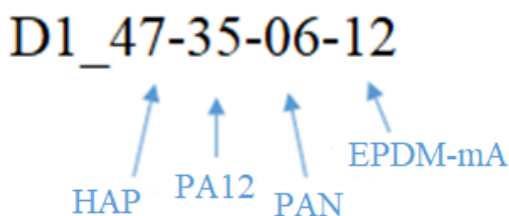


**Figure 5.29:** Code adopted to address the type and content of the different components used to prepare a typical composite.

<b>Table 5.4:</b> relative amount of the components of the “D” compounds		
binder	HAP	47,0%wt
Self-Healing agent	PA12	35,3% wt
rubber	EPDM-mA (Rb01, code 1); NBR (Rb01, code 2); EPDM (Rb03, code 3); C-IIR (Rb06, code 4)	11,8%wt
fiber	PAN	5,9%wt
Code	D1-47-35-06-12; D2-47-35-06-12; D3-47-35-06-12; D4-47-35-06-12	

#### 5.4.2 Differential Scanning Calorimetry

DSC measurements have been performed on the four uncured mixtures (Figure 5.30). As discussed in Chapter IV, the presence of the PA12 in the mixture produces a shift in the softening and crosslinking temperature compared to the pure HAP resin ( $T_s = 66\text{ °C}$  and  $T_{CL} = 152\text{ °C}$ ). In fact, the softening phenomenon occurs at about  $80\text{ °C}$  for all the uncured mixtures (curves a, Figure 5.30), and the exothermic crosslinking peak is barely visible between the two endothermic phenomena which occur at  $T_1 = 151\text{-}152\text{ °C}$  and  $T_m^1 = 177\text{-}178\text{ °C}$ . These two phenomena are due to the interaction of PA12 with the PF resin and the melting of PA12, respectively, as described in Chapter IV. The PAN reactions are activated at the same temperature observed for the neat PAN fibers, of  $\approx 295\text{ °C}$ . In the successive cooling and second heating scans only the exothermic peak at  $141\text{-}144\text{ °C}$  (curves b of Figure 5.30) and the endothermic peak at  $173\text{-}176\text{ °C}$  (curves c of Figure 5.30), respectively, are observed, due to crystallization and melting of the PA12 component, respectively.

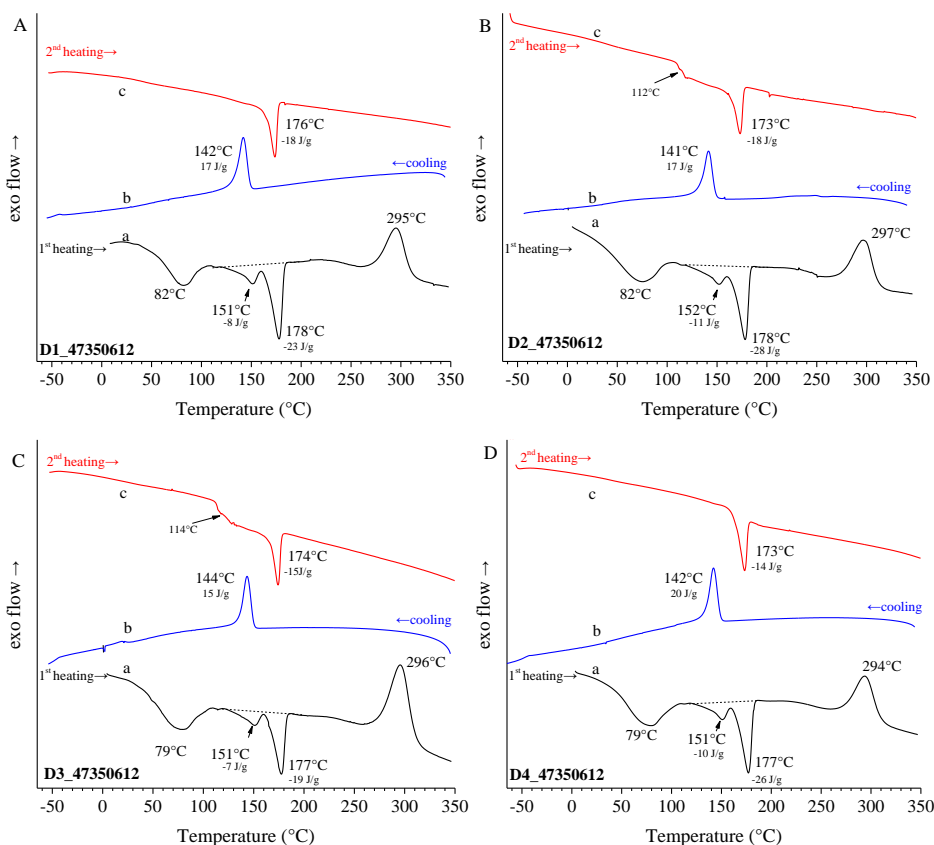


**Figure 5.30:** DSC thermograms of the uncured mixtures D1-D4 recorded at 10 °C/min during the 1<sup>st</sup> heating (a), cooling from the melt (b), and 2<sup>nd</sup> heating (c). The composites contain 11.8wt% of the rubber samples EPDM-mA Rb10 (A, D1), NBR Rb01 (B, D2), EPDM Rb03(C, D3), and C-IIR Rb06 (D, D4).

### 5.4.3 Thermogravimetric Analysis

All the mixtures have been cured by compression molding at  $T_{cm}=200^{\circ}\text{C}$ , for  $t_{cm}=10$  min, using the same conditions adopted for the self-healing systems HAP/PA12 described in the Chapter IV.

The TGA curves of the cured composites D1-D4 are shown in Figure 4.31. All of them are similar to the TGA curves of the B1 series shown in Chapter IV. The TGA curves, indeed, exhibit two main mass loss steps at  $T_{d2}$  and  $T_{d3}$  of about 470 and 590 °C (Figure 5.31), due to the thermal degradation of the two leading components in the composites, namely the PA12 resin (35%wt) and HAP (47 %wt), respectively.

Moreover, similar to the samples B1, the degradation steps occurring at  $T_{d2}$  and  $T_{d3}$  are preceded by a smaller mass loss at  $T_{d1}$  of about 370 °C (Figure 5.31), due to degradation of PA12/PF interacting segments. This indicates that the presence of rubber (12% wt) does not interfere with the interaction scheme occurring at PF/PA12 interfaces. The values of the temperature marking the maximum degradation of the HAP resin, PA12, and the rubber components depend on the type of the latter. In particular, the temperature of maximum degradation rate for the three leading components ( $T_{d1}$ ,  $T_{d2}$ , and  $T_{d3}$ ), in the case of the composite including EPDM-mA, are slightly lower than those observed for the other composites. This behavior is probably due to the fact that the maleic anhydride-modified EPDM somehow prevents the formation of an efficient PF resin network.

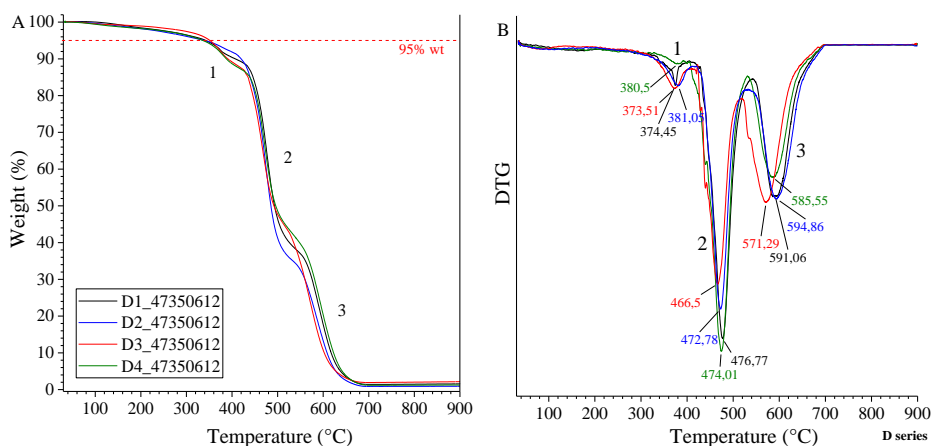


**Figure 5.31:** Thermogravimetric curves (A) and first the derivate (B) recorded at scanning rate of 10°C/min in air, for the composites D1-D4 cured by compression molding for 10 min at 200°C. The temperatures marking the maximum degradation rate of the PA12 and the HAP resin are indicated with  $T_{d1}$ ,  $T_{d2}$ , and  $T_{d3}$  respectively.

The cured composites were subjected to two consecutive DMTA scans (curing temperature 200 °C, curing time 10 min). The DMTA curves are reported in Figures 5.32A-5.35A respectively. DMTA measurements were also extended to the D1-D4 cured composites after breaking them and successive welding. Welding is performed at 200 °C, for 45 min, as detailed in Chapter IV. The DMTA curves recorded in two consecutive steps for the welded composites are reported in Figures 5.32B-5.35B. It

is apparent that the presence of PA12 induces efficient welding even in the composites, regardless of the nature of the rubber. The unbroken and the broken and successively repaired composites show three relaxation phenomena in the temperature range  $-60\div 10$ ,  $55\div 80$ , and around  $160$  °C, as indicated by the three-step drops of storage modulus and the three peaks in the loss modulus and loss factor. These relaxations correspond, in order, to the glass transition of the rubber component, and the glass transition and melting of PA12, respectively. It is worth noting that for the broken and successively repaired specimens, the storage modulus recorded in the first heating scan at temperatures higher than  $250$ °C tends to increase, owing to the occurrence of post-curing reactions.

The exact temperature of the first relaxation depends on the specific rubber sample used in the composites. In particular, the DMTA curves of unbroken specimens of the composite D1 (Figure 5.32) indicate that the glass transition of the EPDM-mA rubber (Rb10) occurs at  $\approx -52$ °C and does not greatly change in the scans successive the first one, neither after breaking and successive welding.

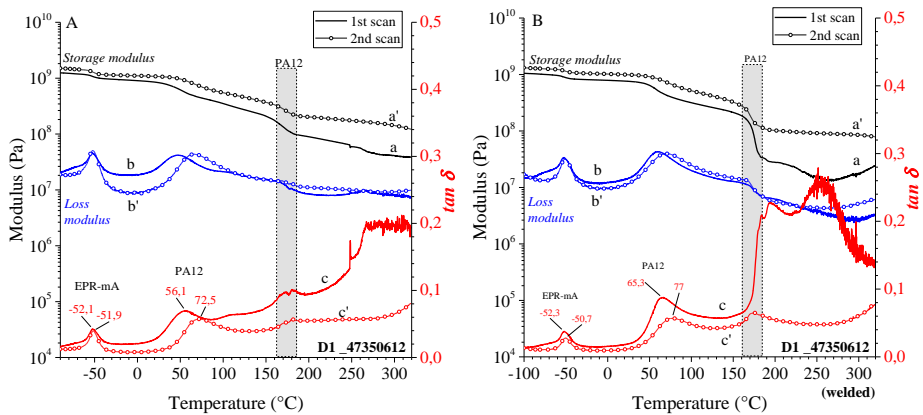


**Figure 5.32:** Storage modulus (a,a'), loss modulus (b,b'), and  $\tan \delta$  (c,c') as a function of the temperature of the composite D1-47-35-06-12, containing the EPDM-mA rubber sample Rb10, cured at  $T_{cm} = 200$ °C for 10 min, recorded during a first (a-c) and a second heating scan (a'-c'), relative to an unbroken specimen (A) and a broken and successively welded specimen (B). The welding is performed at  $200$  °C for 45min as detailed in Chapter IV.

The DMTA curves of unbroken and broken and then welded specimens of the composite D2 (Figure 5.33) indicate that the glass transition of the NBR rubber occurs at  $\approx -13^\circ\text{C}$  during the first heating scans and at  $\approx 3^\circ\text{C}$  during the second heating scan. The shift of the glass transition temperature may be ascribed to the occurrence of rather strong interactions between the NBR chains and PF resin segments<sup>105</sup>,

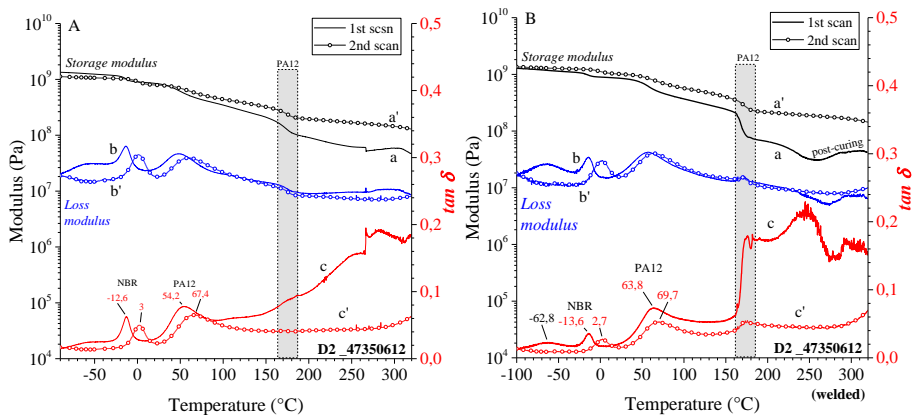


**Figure 5.33:** Storage modulus (a,a'), loss modulus (b,b'), and  $\tan \delta$  (c,c') as a function of temperature of the sample D2\_40300510 cured at  $T_{\text{cm}} = 200^\circ\text{C}$ . The first scan (a-c) and the second scan on the same specimen (a'-c') performed on the intact sample (A) and the sample after breakage and healing (B).

The DMTA curves of unbroken and of broken and then welded specimens of the composite D3 (Figure 5.34) indicate that the glass transition temperature of the EPDM rubber occurs at  $\approx -34^\circ\text{C}$  during the first heating and does not greatly change in the scans successive the first one, neither after breaking and successive welding.

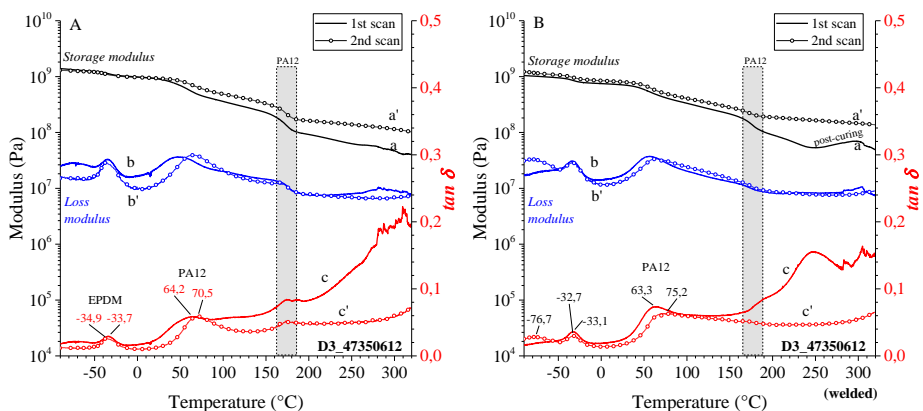


**Figure 5.34:** Storage modulus (a,a'), loss modulus (b,b'), and  $\tan \delta$  (c,c') as a function of the temperature of the composite D3-47-35-06-12, containing the EPDM rubber sample Rb03, cured at  $T_{cm} = 200^\circ\text{C}$  for 10 min, recorded during a first (a-c) and a second heating scan (a'-c') relative to an unbroken specimen (A) and a broken and successively welded specimen (B). The welding is performed at  $200^\circ\text{C}$  for 45 min as detailed in Chapter IV.

The DMTA curves of unbroken and broken and then welded specimens of the composite D4 (Figure 5.35) indicate that the glass transition of the IIR rubber occurs at  $\approx -60^\circ\text{C}$  during the first heating scans and at  $\approx -50^\circ\text{C}$  during the second heating scan. The decrease of the glass transition may be ascribed to the occurrence of rather strong interactions between the C-IIR chains and PF resin segments.

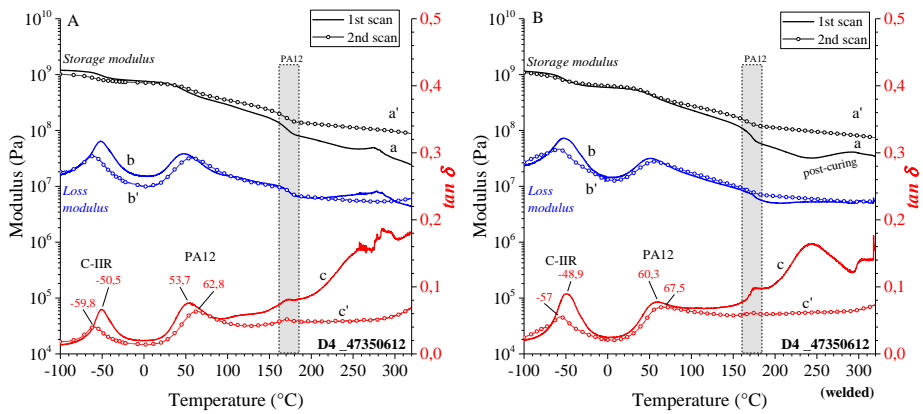


**Figure 5.35:** Storage modulus (a,a'), loss modulus (b,b'), and  $\tan \delta$  (c,c') as a function of the temperature of the composite D4-47-35-06-12, containing the C-IIR rubber sample Rb06, cured at  $T_{cm} = 200^\circ\text{C}$  for 10 min, recorded during a first (a-c) and a second heating scan (a'-c') relative to an unbroken specimen (A) and a broken and successively welded specimen (B). The welding is performed at  $200^\circ\text{C}$  for 45 min as detailed in Chapter IV.

The results of Figures 5.32-5.35 indicate that all the composites give good welding after breaking under nitrogen and healing into an oven at  $200^\circ\text{C}$  for 45 minutes. The rubber and the fibers seem not to interfere with the healing process, at least for the selected composition. The different nature of the rubbers influences the final mechanical properties essentially at lower temperatures, that is in the temperature range corresponding to their glass transition.

The comparison between storage modulus, loss modulus, and loss factor of the samples D1-D4 cured at  $200^\circ\text{C}$  for 10 min are shown in Figure 5.36. It is apparent that the NBR containing composite D2 shows somehow enhanced dissipative properties, as indicated by the fact that it shows the highest value of loss modulus, especially at high temperatures (blue lines).

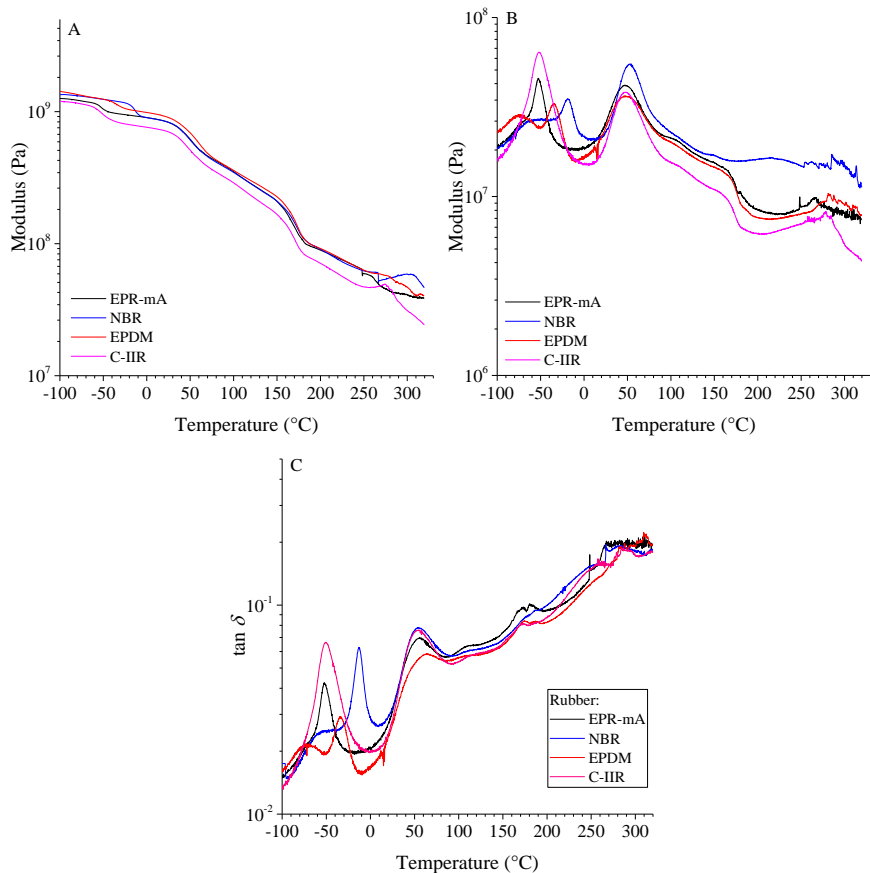


Figure 5.36: Comparison of the DMTA curves of specimens of the composites D1-47-35-06-12 (black), D2-47-35-06-12 (blue), D3-47-35-06-12 (red), and D4-47-35-06-12 (magenta) cured at 200 °C for 10 min, recorded at scanning rate of 5°C/min. Storage modulus (A), loss modulus (B), and loss factor(C).

#### 5.4.4 Composite prepared using the masterbatch B03070C as a healing agent

The “C” composites are made by the HAP resin as binder, the sample B03070C containing PA12 as healing agent and used as masterbatch, PAN as fiber, and different kinds of rubbers.

The selected rubbers are the samples EPDM-mA Rb10 and NBR Rb01 (Table 5.1).

All the analyzed samples have the same relative amount of the components (Table 5.5) and they have been coded adopting the scheme of Figure 5.29, replacing the letter “D” with “C”. As an example, the code C1-50-33-06-11, indicate a composite obtained by mixing 50 %wt of the HAP resin, 33 % wt of the masterbatch B03070C, 6 %wt of PAN fibers and 11%wt of the rubbers sample EPDM-mA Rb01.

binder	HAP	50.0%wt
SH agent	B03070C	33.3% wt (23.3wt%PA12)
rubber	EPDM-mA (Rb01, code 1); NBR (Rb01, code 2);	11.1%wt
fiber	PAN	5.6%wt
Code	C1-50-33-06-11; C2-50-33-06-11;	

#### 5.4.5 Thermogravimetric Analysis of “C” composites

The TGA curves of the “C” composite cured by compression molding at 200°C for 10 min, are shown in Figure 4.37. Relevant mass drops occur at  $T_{d1} \approx 463^\circ\text{C}$  and  $T_{d2} \approx 546$  and  $592^\circ\text{C}$  (double peak), for the C2 composite containing NBR (curve b, Figure 5.37), and  $T_{d1} \approx 470^\circ\text{C}$  and  $T_{d2} \approx 631^\circ\text{C}$  for the C1 composite containing EPDM-mA (curve a, Figure 5.37), due to the degradation of PA12 and the HAP resin, respectively. Similar of the B2 samples (HAP/B03070C) of Chapter IV, the low-temperature degradation peak, expected to occur at temperatures lower than  $460^\circ\text{C}$ , is faintly observed.

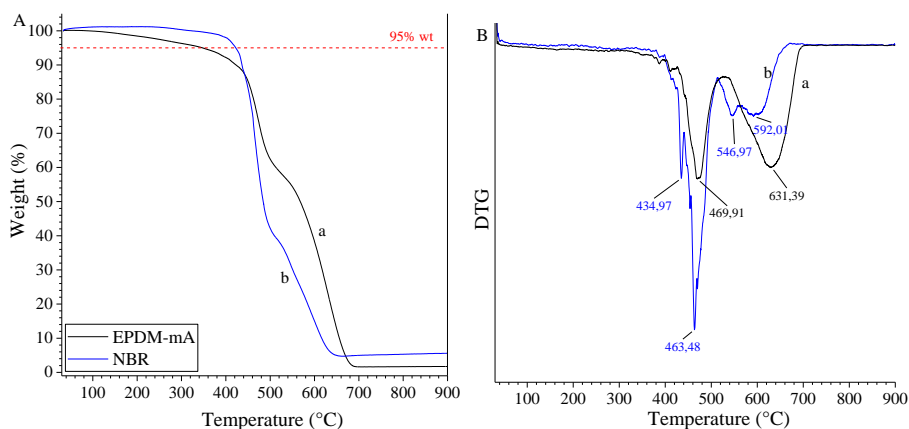


**Figure 5.37:** Thermogravimetric curves (A) and first the derivative (B) recorded at scanning rate of 10°C/min in air, for the composites C1 and C2 containing EPDM-mA (sample Rb10) (a) and NBR (sample Rb01) (b), cured by compression molding at 200°C for 10 min. The temperatures marking the maximum degradation rate of PA12 and the HAP resin are indicated with  $T_{d1}$  and  $T_{d2}$ , respectively.

The DMTA curves recorded in two consecutive scans of the “C” composites are shown in Figures 5.38 and 5.39. DMTA analysis was carried out on unbroken specimens and on specimens that were broken and then welded at 200°C for 45 min, as detailed in Chapter IV. It is apparent that the welding behavior of the “C” composites containing the masterbatch is excellent, regardless of the kind of rubber sample included in the material. This is also demonstrated by the welding line observed in the SEM micrograph of the composite C1 (see Appendix 5).

Similar to the composites “D”, the DMTA curves of the composites “C” are similar, and show three relaxation phenomena in correspondence of the glass transition temperature of the rubber component in the temperature range  $-60 \div 10^\circ\text{C}$ , and in correspondence of the glass transition and melting of PA12, in the range  $55 \div 80^\circ\text{C}$  and at about  $160^\circ\text{C}$ , respectively. Post-curing reactions also occur to a small extent, as indicated by the slight increase of the storage modulus in the first heating scan of the unbroken specimens (curves a of Figures 5.38 and 5.39).

Furthermore, as in the case of the composites “D”, the DMTA curves of unbroken and broken and then welded specimens of the composite C1 (Figure 5.38) indicate that the glass transition of the EPDM-mA rubber occurs at  $\approx -52^\circ\text{C}$  and does not

greatly change in the scans successive the first one, neither after breaking and successive welding.

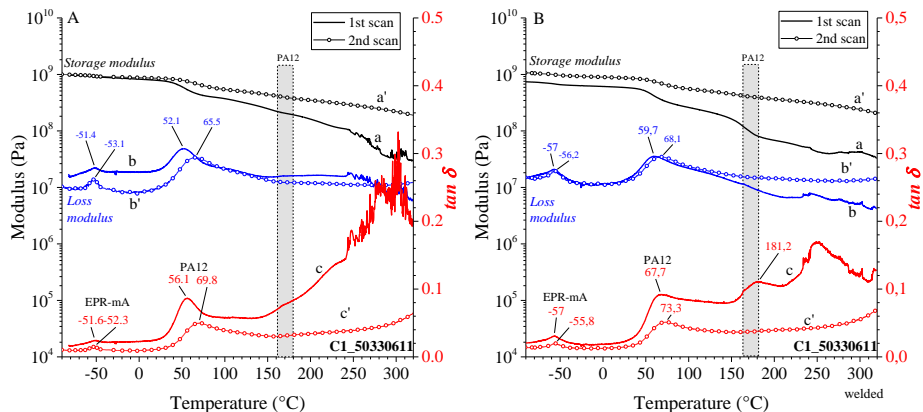


**Figure 5.38:** Storage modulus (a,a'), loss modulus (b,b'), and  $\tan \delta$  (c,c') as a function of the temperature of the composite C1-50-33-06-11 containing the EPDM-mA rubber sample Rb10, cured at  $T_{cm} = 200^\circ\text{C}$  for 10 min, recorded during a first (a-c) and a second heating scan (a'-c') relative to an unbroken specimen (A) and a broken and successively welded specimen (B). The welding is performed at  $200^\circ\text{C}$  for 45 min as detailed in Chapter IV.

Similarly, the DMTA curves of unbroken and broken and then welded specimens of the composite C2 (Figure 5.39) indicate that the glass transition of the NBR rubber occurs at  $\approx -13^\circ\text{C}$  during the first heating scans and at  $\approx 3^\circ\text{C}$  during the second heating scan. The shift of the glass transition may be ascribed to the occurrence of rather strong interactions between the NBR chains and PF resin segments.

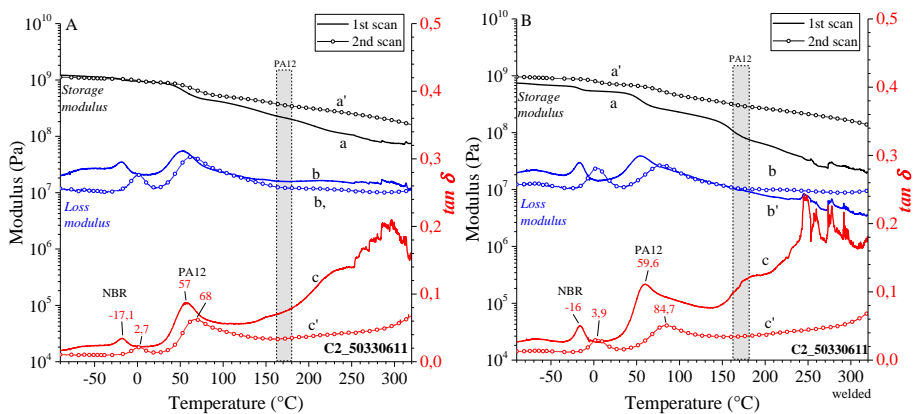


**Figure 5.39:** Storage modulus (a,a'), loss modulus (b,b'), and tan  $\delta$  (c,c') as a function of the temperature of the composite C2-50-33-06-11 containing the NBR rubber sample Rb01, cured at  $T_{cm} = 200^\circ\text{C}$  for 10 min, recorded during a first (a-c) and a second heating scan (a'-c') relative to an unbroken specimen (A) and a broken and successively welded specimen (B). The welding is performed at  $200^\circ\text{C}$  for 45 min as detailed in Chapter IV.

#### 5.4.6 Comparison of the thermomechanical behavior of “D” and “C” composites

The loss factor curves measured through DMTA of the unbroken composites having similar HAP, PAN, and rubber content and including EPDM-mA (sample Rb10) and NBR (sample Rb01), but obtained by addition of PA12 (“D” samples) and the masterbatch B03070C (“C” samples) are compared in Figure 5.40.

The loss factor in the temperature region of the glass transition temperature of the rubber component dispersed in the thermoset matrix for the “C” composites is lower than that exhibited by the “D” composites, regardless of the nature of the rubber. In the glass transition region of PA12, instead, the values of the loss factor of the “C” composites are higher than those of the “D” composites, even though the PA12 content in the “C” samples is lower (23 %wt) than the PA12 content in the “D” samples (35 %wt).

This indicates that the addition of neat PA12 or of a PA12 masterbatch induces good self-healing properties without impairing the damping not only to the cured PF resins but also to the composites of the PF resins including other components such

as PAN fibers and rubbers. Furthermore, it is demonstrated that composites with tailored damping properties in different temperature regions may be obtained, depending on the chemical nature of the rubber.

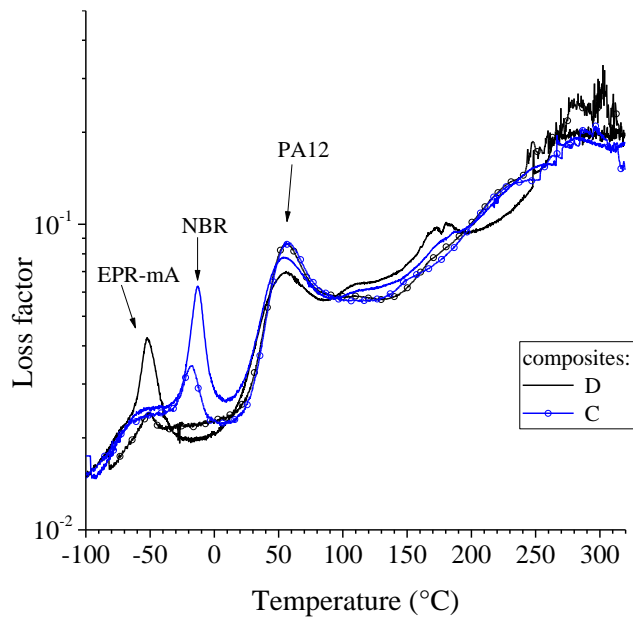


**Figure 5.40:** Comparison of the loss factor curves of specimens of the “C” and “D” composites cured at 200°C for 10 min, relative to the samples D1-47-35-06-12 and D2-47-35-06-12 containing PA12 (straight lines) and the samples C1-50-33-06-11 and C1-50-33-06-11 containing the masterbatch B03070C (circle lines). C1 and D1 indicate composites containing the rubber sample EPDM-mA Rb10 (black lines) and C2 and D2 indicate the composites containing the rubber sample NBR Rb01(blue lines).

## CONCLUSIONS

In this Ph.D. thesis, commercial grades of thermoset resin have been used to design materials that exhibit self-healing properties. A total of 41 resins have been selected in the available portfolio of thermosets conventionally used in the automotive and construction industries, namely Phenol-Formaldehyde (PF), Melamine-Formaldehyde (MF) resins containing hexamethylenetetramine (HMTA) as a hardener, and a Bismaleimide (BMI) resin.

The synthesis and the curing of thermoset resins are characterized by complex mechanism reactions that engrave on the kinetics and the final properties of the material, depending on composition, chemistry, curing condition, presence of hardener, and additives.

To address the complexity of these curable systems, research activities were first focused on the basic characterization of the resins. The chemical composition of the resins, the nature of the additive, the crosslinking temperature ( $T_{CL}$ ) of the initial resins, and the thermomechanical behavior of the cured specimens have been determined. The  $T_{CL}$  value has been used to study the viscoelastic behavior during the isothermal curing of the resin in rheological experiments, and to select the compression molding temperature ( $T_{cm}$ ) used for the curing.

A method based on numerical descriptors extracted from the rheological data has been proposed in order to tag the different types of resins on the basis of the curing kinetics. The values of these parameters, the *maximum curing rate* in the first 500 s of isotherm at the curing temperature  $(dG'/dt)_{max}$ , and the *curing ratio* between the conservative modulus at the end of the fixed time and at the beginning of the curing process  $(G'_L/G'_i)$  have been used to construct a diagram named “curing efficiency chart”. Four sectors are identified depending on the combination of the values of the curing ratio  $G'_L/G'_i$  and of the maximum curing rate  $(dG'/dt)_{max}$  in comparison with those of a novolac HMTA free resin blended ad hoc with 10%wt of HMTA, which has been arbitrarily selected as the benchmark. Compared with the benchmark,

resins that are already well cured at the beginning of the isotherm and quickly become stiffer during isotherm fall in the region I; resins that are already well cured at the beginning of the isotherm and slowly become stiffer during isotherm fall in the region II; resins that are not well cured at the beginning of the isotherm and slowly become stiffer during isotherm fall in the region III; resins that are not well cured at the beginning of the isotherm and quickly become stiffer during isotherm would fall in the region IV.

TGA measurements performed on the cured resin specimens, allowed to discriminate the different thermal stability of the material for the resin cured for 5 min at two different  $T_{cm}$  set equal to  $T_{CL}$  and  $T_{CL} + 50$ . It is shown that the thermal stability of the cured resins increases with increasing the curing temperature, with some exceptions.

The viscoelastic properties of the samples cured for 5 min at two different temperatures have been investigated by performing DMTA measurements. The different viscoelastic behavior of the cured resins has been characterized using as parameters the position ( $T_g$ ), the height ( $I_{max}$ ), and the half-width at half-height ( $w_{(1/2)}$ ) of the  $\tan \delta$  peaks. It has been shown that the values of these parameters depend strictly on the type of the thermoset resin. PF resins cured at  $T_{cm}=T_{CL}$  show large relaxation phenomena due to partial and heterogeneous cross-linking. In fact, during the measurements, additional cross-linking reactions (post-curing) occur. PF resins cured at  $T_{cm}=T_{CL}+50$ , instead, do not show these phenomena which indicates that the cross-linking reactions are almost complete. It is apparent that, with increasing the curing temperature, all the samples exhibit a shift of  $T_g$  toward higher temperatures and a decrease of peak intensity  $I_{max}$ . The cured MF resins, instead, show different behavior. Regardless of the curing temperature ( $T_{cm}=T_{CL}$  or  $T_{CL}+50$ ) the melamine-based resins are generally brittle and could give breakage during the measurements when temperatures higher than 250°C are reached. Crucial for this set of resins is the composition and the relative amount of the melamine component.

Considering the thermal stability, composition, curing behavior, and viscoelastic

properties evaluated by DMTA, the HAP resin, that is a resin in which the cross-linking agent (HMTA) is added to the molten polymer to ensure a good dispersion, according to the Hexamine Adduct Phenolic (HAP) technology, is selected as a suitable matrix to be used for testing self-healing properties, through the addition of polyamide 12 (PA12).

The self-healing properties of HAP resin mixed with various PA12 content have been investigated. To this aim, the PF/PA12 mixtures have been firstly cured in a press. Successively, viscoelastic and morphological studies have been carried out on these samples after breaking and successive restoration, in order to evaluate the efficiency of the self-healing process. In particular, thermomechanical analysis has revealed that the mixtures with PA12 content higher than 20 %wt are inherently able to restore their integrity. These data suggest that the self-healing efficiency of these systems can be ascribed to the good dispersion of PA12 in the PF matrix.

The effect of other parameters has been also explored as for instance the effect of the curing temperature used during the compression molding ( $T_{cm}=150, 170, 190, 200,$  and  $220^{\circ}\text{C}$ ) of the pristine mixtures of the HAP resin with PA12 as well as the effect of the use of other types of resin as matrix instead of the HAP. The tested resins have been selected considering the composition and the curing behavior evaluated through the *curing efficiency chart*. In general, it is shown that the final viscoelastic properties of the material depend on compression molding temperature ( $T_{cm}$ ), PA12 content, and type of resin matrix. In particular, melamine-based resins are not suitable as matrices for self-healing materials with PA12. Considering that melamine-based resins are specifically formulated to contain at least 57 wt% of a PF resin, the fragility of their mixtures with PA12 indicates that the melamine component, either HMM or MF oligomer, counteracts the compatibilization mechanism.

Since PA12 keeps crystallizing in the cured samples before and after healing, it is suggested that the healing process is triggered by heating at temperatures higher than the melting temperature of the PA12 component through the diffusion of the melt

towards the fracture and the establishment of new interactions of the amide groups with the hydroxyl groups of PF resin, followed by successive crystallization of PA12 upon cooling. It has been shown that this mechanism is general as it allows achieving efficient welding regardless of the temperature adopted for curing the mixtures and also for other types of PF resins having different curing behavior.

In order to investigate the nature of the interactions at PF/PA12 interface, model mixtures of PF resin and PA12 in absence of the hardener have been also studied. For these systems, the competitive curing reactions of the PF resin with HMTA are prevented, so that the possible set up of direct interaction of PF resin with PA12 can be better evidenced. In independent experiments, indeed, it is demonstrated that HMTA does not establish relevant interactions with PA12. Whereas investigation of the structure and thermal properties of the model mixtures confirm the good compatibility at PF/PA12 interface, FTIR analysis provides direct evidence of the formation of hydrogen bonds even though the possible formation of covalent bonds could not be unambiguously discarded. In general, the presence of PA12 in the mixtures shows negative deviations of the glass transition of the blends from the predicted values of the Fox-Flory equation, resulting in an increase of the damping properties of the final cured material at high temperatures.

Finally, a simple procedure is set up, that allows using PF/PA12 blends with high PA12 content as masterbatch, to obtain efficient self-healing materials by mixing with the HAP resin or other types of PF resins. Interestingly, it has been shown that the use of the masterbatch allows to obtain cross-linked materials with self-healing properties even in the case of melamine-based resins, regardless of the composition or type of melamine component (MF or HMM) or the HMTA content as a hardener in the pristine samples. In all cases, it is demonstrated that with the use of the masterbatch, the desired self-healing performances may be achieved using a lower amount of PA12 component.

## BIBLIOGRAPHY

- (1) Goodman, S. H. *Handbook of Thermoset*; Jaico Publishing House, 2005.
- (2) Pizzi, A.; Mittal, K. L. *Handbook of Adhesive Technology*; Marcel Dekker, INC, 2017. <https://doi.org/10.1201/9781315120942>.
- (3) Jamir, M. R. M.; Majid, M. S. A.; Khasri, A. Natural Lightweight Hybrid Composites for Aircraft Structural Applications. *Sustain. Compos. Aerosp. Appl.* **2018**, 155–170. <https://doi.org/10.1016/B978-0-08-102131-6.00008-6>.
- (4) Chung, D. *Carbon Fiber Composites*, 1st Editio.; Butterworth-Heinemann, 1994.
- (5) Pilato, L. Phenolic Resins: 100Years and Still Going Strong. *React. Funct. Polym.* **2013**, 73 (2), 270–277. <https://doi.org/10.1016/j.reactfunctpolym.2012.07.008>.
- (6) Knop, A.; Pilato, L. A. *Phenolic Resins. Chemistry, Applications and Performance*; 1985; Vol. 51.
- (7) Ribeiro, M. C. S.; Meira-Castro, A. C.; Silva, F. G.; Santos, J.; Meixedo, J. P.; Fiúza, A.; Dinis, M. L.; Alvim, M. R. Re-Use Assessment of Thermoset Composite Wastes as Aggregate and Filler Replacement for Concrete-Polymer Composite Materials: A Case Study Regarding GFRP Pultrusion Wastes. *Resour. Conserv. Recycl.* **2015**, 104, 417–426. <https://doi.org/10.1016/J.RESCONREC.2013.10.001>.
- (8) Pickering, S. J. Recycling Technologies for Thermoset Composite Materials—Current Status. *Compos. Part A Appl. Sci. Manuf.* **2006**, 37 (8), 1206–1215. <https://doi.org/https://doi.org/10.1016/j.compositesa.2005.05.030>.
- (9) Koo, B.; Subramanian, N.; Chattopadhyay, A. Molecular Dynamics Study of Brittle Fracture in Epoxy-Based Thermoset Polymer. *Compos. Part B Eng.* **2016**, 95, 433–439. <https://doi.org/10.1016/J.COMPOSITESB.2016.04.012>.

- (10) van der Sanden, M. C. M.; Meijer, H. E. H. Deformation and Toughness of Polymeric Systems: 3. Influence of Crosslink Density. *Polymer (Guildf)*. **1993**, *34* (24), 5063–5072. [https://doi.org/10.1016/0032-3861\(93\)90249-A](https://doi.org/10.1016/0032-3861(93)90249-A).
- (11) Vengatesan, M. R.; Varghese, A. M.; Mittal, V. Chapter 3 - Thermal Properties of Thermoset Polymers. In *Thermosets (Second Edition)*; Guo, Q., Ed.; Elsevier, 2018; pp 69–114. <https://doi.org/https://doi.org/10.1016/B978-0-08-101021-1.00003-4>.
- (12) Folkes, M. J.; Hope, P. S. *Polymer Blends and Alloys*; Springer, Dordrecht, 1993. <https://doi.org/https://doi.org/10.1007/978-94-011-2162-0>.
- (13) Osswald, T.; Menges, G. Failure and Damage of Polymers. In *Materials Science of Polymers for Engineers*; 2012; pp 423–487. <https://doi.org/10.3139/9781569905241.010>.
- (14) Wu, D. Y.; Meure, S.; Solomon, D. Self-Healing Polymeric Materials: A Review of Recent Developments. *Prog. Polym. Sci.* **2008**, *33* (5), 479–522. <https://doi.org/10.1016/j.progpolymsci.2008.02.001>.
- (15) Wang, S.; Urban, M. W. Self-Healing Polymers. *Nat. Rev. Mater.* <https://doi.org/10.1038/s41578-020-0202-4>.
- (16) Dhanasekaran, R.; Reddy, S. S.; Kumar, A. S. *Application of Self-Healing Polymers to Overcome Impact, Fatigue and Erosion Damages*; 2018; Vol. 5.
- (17) Bosch, T. C. G. Why Polyps Regenerate and We Don't: Towards a Cellular and Molecular Framework for Hydra Regeneration. *Dev. Biol.* **2007**, *303* (2), 421–433. <https://doi.org/https://doi.org/10.1016/j.ydbio.2006.12.012>.
- (18) Garcia, S. J. Effect of Polymer Architecture on the Intrinsic Self-Healing Character of Polymers. *Eur. Polym. J.* **2014**, *53* (1), 118–125. <https://doi.org/10.1016/j.eurpolymj.2014.01.026>.
- (19) Holstein, T. W.; Hobmayer, E.; Technau, U. Cnidarians: An Evolutionarily Conserved Model System for Regeneration? *Dev. Dyn.* **2003**, *226* (2), 257–267. <https://doi.org/https://doi.org/10.1002/dvdy.10227>.
- (20) Speck, T.; Mülhaupt, R.; Speck, O. Self-Healing in Plants as Bio-Inspiration

- for Self-Repairing Polymers. In *Self-Healing Polymers*; John Wiley & Sons, Ltd, 2013; pp 61–89. <https://doi.org/https://doi.org/10.1002/9783527670185.ch2>.
- (21) Zhang, P.; Li, G. Advances in Healing-on-Demand Polymers and Polymer Composites. *Prog. Polym. Sci.* **2016**, *57*, 32–63. <https://doi.org/10.1016/j.progpolymsci.2015.11.005>.
- (22) Baekeland, L. H. Method of Making Insoluble Products of Phenol and Formaldehyde, 1909. <https://doi.org/10.1145/178951.178972>.
- (23) Baekeland, L. H. The Synthesis, Constitution, and Uses of Bakelite. *J. Ind. & Eng. Chem.* **1909**, *1* (3), 149–161. <https://doi.org/10.1021/ie50003a004>.
- (24) Ibeh, C. C. 2 - Phenol-Formaldehyde Resins. In *Handbook of Thermoset Plastics (Second Edition)*; Goodman, S. H., Ed.; William Andrew Publishing: Westwood, NJ, 1998; pp 23–71. <https://doi.org/https://doi.org/10.1016/B978-081551421-3.50005-9>.
- (25) Trinowski, D. M. *Phenolic Resins: A Century of Progress*; 2010. [https://doi.org/10.1007/978-3-642-04714-5\\_18](https://doi.org/10.1007/978-3-642-04714-5_18).
- (26) Bijwe, J.; Nidhi; Majumdar, N.; Satapathy, B. K. Influence of Modified Phenolic Resins on the Fade and Recovery Behavior of Friction Materials. *Wear* **2005**, *259* (7–12), 1068–1078. <https://doi.org/10.1016/j.wear.2005.01.011>.
- (27) Hesse, W.; Lang, J. Phenolic Resins. In *Ullmann's Encyclopedia of Industrial Chemistry*; American Cancer Society, 2011. [https://doi.org/https://doi.org/10.1002/14356007.a19\\_371.pub2](https://doi.org/https://doi.org/10.1002/14356007.a19_371.pub2).
- (28) Artmann, A.; Bianchi, O.; Soares, M. R.; Nunes, R. C. R. Rheokinetic Investigations on the Thermal Cure of Phenol-Formaldehyde Novolac Resins. *Mater. Sci. Eng. C* **2010**, *30*, 1245–1251.
- (29) Kopf, P. W.; Wagner, E. R. Formation and Cure of Novolacs: NMR Study of Transient Molecules. *J. Polym. Sci. Polym. Chem. Ed.* **1973**, *11* (5), 939–960. <https://doi.org/https://doi.org/10.1002/pol.1973.170110503>.

- (30) Wan, J.; Wang, S.; Li, C.; Zhou, D.; Chen, J.; Liu, Z.; Yu, L.; Fan, H.; Li, B. G. Effect of Molecular Weight and Molecular Weight Distribution on Cure Reaction of Novolac with Hexamethylenetetramine and Properties of Related Composites. *Thermochim. Acta* **2012**, *530*, 32–41. <https://doi.org/10.1016/j.tca.2011.11.032>.
- (31) Lim, A. S. C.; Solomon, D. H.; Zhang, X. Chemistry of Novolac Resins. x. Polymerization Studies of Hmta and Strategically Synthesized Model Compounds. *J. Polym. Sci. Part A Polym. Chem.* **1999**, *37* (9), 1347–1355. [https://doi.org/10.1002/\(sici\)1099-0518\(19990501\)37:9<1347::aid-pola15>3.0.co;2-1](https://doi.org/10.1002/(sici)1099-0518(19990501)37:9<1347::aid-pola15>3.0.co;2-1).
- (32) Zhang, X.; Potter, A. C.; Solomon, D. H. The Chemistry of Novolac Resins: Part 8. Reactions of Para-Hydroxybenzylamines with Model Phenols. *Polymer (Guildf)*. **1998**, *39* (10), 1967–1975. [https://doi.org/10.1016/S0032-3861\(97\)00581-8](https://doi.org/10.1016/S0032-3861(97)00581-8).
- (33) Dannels, B.; Shepard, A. Inorganic Esters of Novolacs. *J. Polym. Sci. Part A-1 Polym. Chem.* **1968**, *6*. <https://doi.org/10.1002/pol.1968.150060802>.
- (34) Bu, Z.; Hu, J.; Li, B. Novel Silicon-Modified Phenolic Novolac Resins: Non-Isothermal Curing Kinetics, and Mechanical and Thermal Properties of Their Biofiber-Reinforced Composites. *Thermochim. Acta* **2014**, *575*, 244–253. <https://doi.org/https://doi.org/10.1016/j.tca.2013.11.003>.
- (35) Li, C.; Ma, Z.; Zhang, X.; Fan, H.; Wan, J. Silicone-Modified Phenolic Resin: Relationships between Molecular Structure and Curing Behavior. *Thermochim. Acta* **2016**, *639*, 53–65. <https://doi.org/https://doi.org/10.1016/j.tca.2016.07.011>.
- (36) Takahashi, A.; Yamamoto, H. Polycondensation in Monomolecular Layers of Poly(p-Vinylphenol), Formaldehyde, and Hexamethylenetetramine. *Polym. J.* **1980**, *12* (2), 79–85. <https://doi.org/10.1295/polymj.12.79>.
- (37) Ito, H.; Willson, C. G.; Frechet, J. M. J.; Farrall, M. J.; Eichler, E. Synthesis of Poly(p-Hydroxy- $\alpha$ -Methylstyrene) by Cationic Polymerization and

- Chemical Modification. *Macromolecules* **1983**, *16* (4), 510–517.  
<https://doi.org/10.1021/ma00238a004>.
- (38) Nair, C. P. R. Advances in Addition-Cure Phenolic Resins. *Prog. Polym. Sci.* **2004**, *29* (5), 401–498. <https://doi.org/10.1016/j.progpolymsci.2004.01.004>.
- (39) Fan, Z.; Lederer, A.; Voit, B. Synthesis and Characterization of A<sub>2</sub>+B<sub>3</sub>-Type Hyperbranched Aromatic Polyesters with Phenolic End Groups. *Polymer (Guildf)*. **2009**, *50* (15), 3431–3439.  
<https://doi.org/https://doi.org/10.1016/j.polymer.2009.05.039>.
- (40) Marra, A. A. *Technology of Wood Bonding : Principles in Practice / Alan A. Marra*; Van Nostrand Reinhold New York, 1992.
- (41) Talbot, W.; Mass, F. United States Patent n. 2260239, 1953.
- (42) Merline, D. J.; Vukusic, S.; Abdala, A. A. Melamine Formaldehyde: Curing Studies and Reaction Mechanism. *Polym. J.* **2013**, *45* (4), 413–419.  
<https://doi.org/10.1038/pj.2012.162>.
- (43) Bajia, S.; Sharma, R.; Bajia, B. Solid-State Microwave Synthesis of Melamine-Formaldehyde Resin. *E-Journal Chem.* **2009**, *6* (1), 120–124.  
<https://doi.org/10.1155/2009/807851>.
- (44) Diem, H.; Matthias, G.; Wagner, R. A. Amino Resins. In *Ullmann's Encyclopedia of Industrial Chemistry*; American Cancer Society, 2010.  
[https://doi.org/https://doi.org/10.1002/14356007.a02\\_115.pub2](https://doi.org/https://doi.org/10.1002/14356007.a02_115.pub2).
- (45) Okano, M.; Ogata, Y. Kinetics of the Condensation of Melamine with Formaldehyde. *J. Am. Chem. Soc.* **1952**, *74* (22), 5728–5731.  
<https://doi.org/10.1021/ja01142a047>.
- (46) Kumar, A.; Katiyar, V. Modeling and Experimental Investigation of Melamine-Formaldehyde Polymerization. *Macromolecules* **1990**, *23* (16), 3729–3736. <https://doi.org/10.1021/ma00218a003>.
- (47) Nastke, R.; Dietrich, K.; Reinisch, G.; Rafler, G.; Gajewski, H. The Initial Stage of the Reaction of Melamine with Formaldehyde. *J. Macromol. Sci. Part A - Chem.* **1986**, *23* (5), 579–596.

<https://doi.org/10.1080/00222338608058497>.

- (48) Raval, D. K.; Patel, A. J.; Narola, B. N. A Study on Composites from Casein Modified Melamine-Formaldehyde Resin. *Polym. Plast. Technol. Eng.* **2006**, *45* (3), 293–299. <https://doi.org/10.1080/03602550500371562>.
- (49) Hse, C.-Y.; Branham, S. J.; Chou, C. Adhesive Technology and Bonded Tropical Wood Products. *Adhes. Technol. Trop. Woods Symp. (1993 Taipei, Taiwan)* **1998**.
- (50) Satheesh Chandran, M.; Reghunadhan Nair, C. P. 12 - Maleimide-Based Alder-Enes. In *Handbook of Thermoset Plastics (Third Edition)*; Dodiuk, H., Goodman, S. H., Eds.; William Andrew Publishing: Boston, 2014; pp 459–510. <https://doi.org/https://doi.org/10.1016/B978-1-4557-3107-7.00012-9>.
- (51) Iredale, R. J.; Ward, C.; Hamerton, I. Modern Advances in Bismaleimide Resin Technology: A 21st Century Perspective on the Chemistry of Addition Polyimides. *Prog. Polym. Sci.* **2017**, *69*, 1–21. <https://doi.org/10.1016/J.PROGPOLYMSCI.2016.12.002>.
- (52) Marck, J. E. *Polymer Data Handbook*; Oxford University Press, 1999.
- (53) Ninan, K. N.; Krishnan, K.; Mathew, J. Addition Polyimides. I. Kinetics of Cure Reaction and Thermal Decomposition of Bismaleimides. *J. Appl. Polym. Sci.* **1986**, *32* (7), 6033–6042. <https://doi.org/10.1002/app.1986.070320731>.
- (54) Tungare, A. V.; Martin, G. C. Analysis of the Curing Behavior of Bismaleimide Resins. *J. Appl. Polym. Sci.* **1992**, *46* (7), 1125–1135. <https://doi.org/https://doi.org/10.1002/app.1992.070460701>.
- (55) Liu, X.; Yu, Y.; Li, S. Viscoelastic Phase Separation in Polyethersulfone Modified Bismaleimide Resin. *Eur. Polym. J.* **2006**, *42* (4), 835–842. <https://doi.org/10.1016/J.EURPOLYMJ.2005.10.004>.
- (56) BAOYAN, Z.; PING, L. I.; XIANGBAO, C. Studies of Modified Bismaleimide Resins Part I The Influence of Resin Composition on Thermal and Impact Properties. *J. Mater. Sci.* **1998**, *33* (23), 5683–5687.

<https://doi.org/10.1023/A:1004492921996>.

- (57) Macosko, C. W. *Rheology: Principles, Measurements, and Applications*; Wiley, 1996.
- (58) Carfagni, M.; Lenzi, E.; Pierini, M. Loss Factor as a Measure of Mechanical Damping. *Proc. Int. Modal Anal. Conf. - IMAC 1998*, *1*, 580–584.
- (59) Rasa, A. Applying Dynamic Mechanical Analysis to Research & Development for Viscoelastic Damping Materials. *INTERNOISE 2014 - 43rd Int. Congr. Noise Control Eng. Improv. World Through Noise Control 2014*, 1–10.
- (60) Holopainen, T.; Alvila, L.; Rainio, J.; Pakkanen, T. T. *IR Spectroscopy as a Quantitative and Predictive Analysis Method of Phenol-Formaldehyde Resol Resins*; John Wiley & Sons, Inc, 1998; Vol. 69.
- (61) Liu, R.; Zhang, X.; Gao, S.; Liu, X.; Wang, Z.; Yan, J. Bio-Based Epoxy-Anhydride Thermosets from Six-Armed Linoleic Acid-Derived Epoxy Resin †. **2016**. <https://doi.org/10.1039/c6ra09077j>.
- (62) Milazzo, M.; Amoresano, A.; Pasquino, R.; Grizzuti, N.; Auriemma, F.; De Stefano, F.; Sin Xicola, A.; Iodice, V.; De Rosa, C. Curing Efficiency of Novolac-Type Phenol-Formaldehyde Resins from Viscoelastic Properties. *Macromolecules* **2021**. <https://doi.org/10.1021/acs.macromol.1c01598>.
- (63) Merabia, S.; Long, D. Heterogeneous Dynamics at the Glass Transition in van Der Waals Liquids: Determination of the Characteristic Scale. *Eur. Phys. J. E* **2002**, *9* (2), 195–206. <https://doi.org/10.1140/epje/i2002-10084-2>.
- (64) Long, D. R.; Conca, L.; Sotta, P. Dynamics in Glassy Polymers: The Eyring Model Revisited. *Phys. Rev. Mater.* **2018**, *2* (10), 1–6. <https://doi.org/10.1103/PhysRevMaterials.2.105601>.
- (65) Wang, F. Y.; Ma, C. C. M.; Wu, H. Der. Hydrogen Bonding in Polyamide Toughened Novolac Type Phenolic Resin. *J. Appl. Polym. Sci.* **1999**, *74* (9), 2283–2289. [https://doi.org/10.1002/\(SICI\)1097-4628\(19991128\)74:9<2283::AID-APP18>3.0.CO;2-X](https://doi.org/10.1002/(SICI)1097-4628(19991128)74:9<2283::AID-APP18>3.0.CO;2-X).

- (66) Hartikainen, J.; Lehtonen, O.; Harmia, T.; Lindner, M.; Valkama, S.; Ruokolainen, J.; Friedrich, K. Structure and Morphology of Polyamide 66 and Oligomeric Phenolic Resin Blends: Molecular Modeling and Experimental Investigations. *Chem. Mater.* **2004**, *16* (16), 3032–3039. <https://doi.org/10.1021/cm0401591>.
- (67) Hung, A. Y. C.; Wang, F. Y.; Ma, C. C. M.; Wu, H. Der. Thermodynamic Properties Affect the Molecular Motion of Novolac Type Phenolic Resin Blended with Polyamide. *Eur. Polym. J.* **2003**, *39* (2), 225–231. [https://doi.org/10.1016/S0014-3057\(02\)00230-6](https://doi.org/10.1016/S0014-3057(02)00230-6).
- (68) Rhee, S.; White, J. L. Crystal Structure and Morphology of Biaxially Oriented Polyamide 12 Films. *J. Polym. Sci. Part B Polym. Phys.* **2002**, *40* (12), 1189–1200. <https://doi.org/10.1002/polb.10181>.
- (69) Ramesh, C. Crystalline Transitions in Nylon 12. *Macromolecules* **1999**, *32* (17), 5704–5706. <https://doi.org/10.1021/ma990494o>.
- (70) Ma, N.; Liu, W.; Ma, L.; He, S.; Liu, H.; Zhang, Z.; Sun, A.; Huang, M.; Zhu, C. Crystal Transition and Thermal Behavior of Nylon 12. *E-Polymers* **2020**, *20* (1), 346–352. <https://doi.org/10.1515/epoly-2020-0039>.
- (71) Ravve, A.; Fitko, C. W. Graft Copolymers of Phenolic Novolacs on Polyamide Backbones. *J. Polym. Sci. Part A-1 Polym. Chem.* **1966**, *4* (10), 2533–2541. <https://doi.org/10.1002/pol.1966.150041017>.
- (72) Rosu, D.; Varganici, C.-D.; Rosu, L.; Mocanu, O. M. *Thermal Degradation of Thermosetting Blends*; 2015. [https://doi.org/10.1007/978-3-319-03464-5\\_2](https://doi.org/10.1007/978-3-319-03464-5_2).
- (73) Sin, N.; Milazzo, M.; Iodice, V.; De Rosa, C.; Auriemma, F. Italian Patent n. A-AIT-1903, 2020.
- (74) Kim, Y. H.; Wool, R. P. A Theory of Healing at a Polymer Polymer Interface. *Macromolecules* **1983**, *16* (7), 1115–1120. <https://doi.org/10.1021/ma00241a013>.
- (75) Kalogeras, I. M.; Brostow, W. Glass Transition Temperatures in Binary

- Polymer Blends. *J. Polym. Sci. Part B Polym. Phys.* **2009**, *47* (1), 80–95. <https://doi.org/10.1002/POLB.21616>.
- (76) Kim, S.; Kim, H. S.; Kim, H. J.; Yang, H. S. Fast Curing PF Resin Mixed with Various Resins and Accelerators for Building Composite Materials. *Constr. Build. Mater.* **2008**, *22* (10), 2141–2146. <https://doi.org/10.1016/j.conbuildmat.2007.07.007>.
- (77) Schmidt, R. G.; Frazier, C. E. Network Characterization of Phenol-Formaldehyde Thermosetting Wood Adhesive. *Int. J. Adhes. Adhes.* **1998**, *18* (2), 139–146. [https://doi.org/10.1016/S0143-7496\(97\)00042-0](https://doi.org/10.1016/S0143-7496(97)00042-0).
- (78) Beardmore, P.; Johnson, C. F. The Potential for Composites in Structural Automotive Applications. *Compos. Sci. Technol.* **1986**, *26* (4), 251–281. [https://doi.org/10.1016/0266-3538\(86\)90002-3](https://doi.org/10.1016/0266-3538(86)90002-3).
- (79) Tang, K.; Zhang, A.; Ge, T.; Liu, X.; Tang, X.; Li, Y. Research Progress on Modification of Phenolic Resin. *Mater. Today Commun.* **2021**, *26* (June 2020), 101879. <https://doi.org/10.1016/j.mtcomm.2020.101879>.
- (80) Haeri, H.; Sarfarazi, V.; Marji, M. F.; Hedayat, A.; Zhu, Z. Experimental and Numerical Study of Shear Fracture in Brittle Materials with Interference of Initial Double Cracks. *Acta Mech. Solida Sin.* **2016**, *29* (5), 555–566. [https://doi.org/10.1016/S0894-9166\(16\)30273-7](https://doi.org/10.1016/S0894-9166(16)30273-7).
- (81) Grellmann, W.; Seidler, S. *Deformation and Fracture Behaviour of Polymers*; Springer, 2001.
- (82) Bao, Y.; Wierzbicki, T. A Comparative Study on Various Ductile Crack Formation Criteria. *J. Eng. Mater. Technol. Trans. ASME* **2004**, *126* (3), 314–324. <https://doi.org/10.1115/1.1755244>.
- (83) Benazzouk, A.; Douzane, O.; Mezreb, K.; Laidoudi, B.; Quéneudec, M. Thermal Conductivity of Cement Composites Containing Rubber Waste Particles: Experimental Study and Modelling. *Constr. Build. Mater.* **2008**, *22* (4), 573–579. <https://doi.org/10.1016/j.conbuildmat.2006.11.011>.
- (84) Nuzaimah, M.; Sapuan, S. M.; Nadlene, R.; Jawaid, M. Recycling of Waste

- Rubber as Fillers: A Review. *IOP Conf. Ser. Mater. Sci. Eng.* **2018**, 368 (1). <https://doi.org/10.1088/1757-899X/368/1/012016>.
- (85) Samsuri, A. Degradation of Natural Rubber and Synthetic Elastomers. In *Shreir's Corrosion*; 2010; Vol. 3, pp 2407–2438. <https://doi.org/10.1016/B978-044452787-5.00117-7>.
- (86) Samantarai, S.; Nag, A.; Singh, N.; Dash, D.; Basak, A.; Nando, G. B.; Das, N. C. Chemical Modification of Nitrile Rubber in the Latex Stage by Functionalizing Phosphorylated Cardanol Prepolymer: A Bio-Based Plasticizer and a Renewable Resource. *J. Elastomers Plast.* **2019**, 51 (2), 99–129. <https://doi.org/10.1177/0095244318768644>.
- (87) Kruzelač, J.; Hudec, I. Vulcanization Systems for Rubber Compounds Based on IIR and Halogenated IIR: An Overview. *Rubber Chem. Technol.* **2018**, 91 (1), 167–183. <https://doi.org/10.5254/rct-18-82609>.
- (88) Kelly, J. M.; Konstantinidis, D. A. *Mechanics of Rubber Bearings for Seismic and Vibration Isolation*; 2011. <https://doi.org/10.1002/9781119971870>.
- (89) Sanches, N. B.; Cassu, S. N.; De Cássia Lazzarini Dutra, R. TG/FT-IR Characterization of Additives Typically Employed in EPDM Formulations. *Polimeros* **2015**, 25 (3), 247–255. <https://doi.org/10.1590/0104-1428.1819>.
- (90) Duan, G.; Zhang, C.; Li, A.; Yang, X.; Lu, L.; Wang, X. Preparation and Characterization of Mesoporous Zirconia Made by Using a Poly (Methyl Methacrylate) Template. *Nanoscale Res. Lett.* **2008**, 3 (3), 118–122. <https://doi.org/10.1007/s11671-008-9123-7>.
- (91) Wu, C. H.; Su, A. C. Functionalization of Ethylene-propylene Rubber via Melt Mixing. *Polym. Eng. Sci.* **1991**, 31 (23), 1629–1636. <https://doi.org/10.1002/pen.760312302>.
- (92) Liang, L.; Dong, J.; Yue, D. Branched EHNBR and Its Properties with Enhanced Low-Temperature Performance and Oil Resistance. *RSC Adv.* **2019**, 9 (55), 32130–32136. <https://doi.org/10.1039/c9ra03656c>.

- (93) Liu, J.; Sun, J.; Zhang, Z.; Yang, H.; Nie, X. One-Step Synthesis of End-Functionalized Hydrogenated Nitrile-Butadiene Rubber by Combining the Functional Metathesis with Hydrogenation. *ChemistryOpen* **2020**, *9* (3), 374–380. <https://doi.org/10.1002/open.201900369>.
- (94) Kolbert, A. C.; Didier, J. G. Determination of Monomer Sequence Distribution in EPDM by <sup>13</sup>C-NMR: Third Monomer Effects. *J. Appl. Polym. Sci.* **1999**, *71* (4), 523–530. [https://doi.org/10.1002/\(SICI\)1097-4628\(19990124\)71:4<523::AID-APP1>3.0.CO;2-G](https://doi.org/10.1002/(SICI)1097-4628(19990124)71:4<523::AID-APP1>3.0.CO;2-G).
- (95) Brandolini, A. J.; Hills, D. D. *NMR Spectra of Polymers and Polymer Additives*; 2000. <https://doi.org/10.1201/9781482293425>.
- (96) Cheng, H. N.; Lee, G. H. Two-Dimensional NMR Spectroscopy and Automated <sup>1</sup>H NMR Analysis of Ethylene-Propylene Copolymers. *Polym. Bull.* **1980**, *440*, 437–440.
- (97) Kakugo, M.; Naito, Y.; Mizunuma, K.; Miyatake, T. <sup>13</sup>C NMR Determination of Monomer Sequence Distribution in Ethylene-Propylene Copolymers Prepared with  $\delta$ -TiCl<sub>3</sub>-Al(C<sub>2</sub>H<sub>5</sub>)<sub>2</sub>Cl. *Macromolecules* **1982**, *15* (4), 1150–1152. <https://doi.org/10.1021/ma00232a037>.
- (98) Randall, J. C. Journal of Macromolecular Science , Part C : Polymer Reviews PHOTOPOLYMERIZATION : A REVIEW. *Jounral Macromol. Sci. Part C Polym. Rev.* **1989**, *C42* (4), 201–317.
- (99) Smolentseva, I. I.; Mashukov, V. I.; Korotkova, E. I. Determination of Unsaturation Level, Halogen Content, and Main Forms of Isoprene Units in Halogenated Butyl Rubbers by <sup>1</sup>H NMR Spectroscopy. *J. Appl. Spectrosc.* **2015**, *82* (3), 465–469. <https://doi.org/10.1007/s10812-015-0131-y>.
- (100) Severe, G.; White, J. L. Transition Behavior of Hydrogenated Acrylonitrile-Butadiene Rubber. *KGK-Kautschuk und Gummi Kunststoffe* **2002**, *55* (4), 144–148.
- (101) Qin, Y. A Brief Description of Textile Fibers. *Med. Text. Mater.* **2016**, 23–42. <https://doi.org/10.1016/B978-0-08-100618-4.00003-0>.

- (102) Yu, M.; Wang, C.; Bai, Y. Microstructural Evolution in Polyacrylonitrile Fibers During Oxidative Stabilization. *Wiley Intersci.* **2008**, 759–765. <https://doi.org/10.1002/polb>.
- (103) Dalton, S.; Heatley, F.; Budd, P. M. Thermal Stabilization of Polyacrylonitrile Fibres. *Polymer (Guildf)*. **1999**, 40 (20), 5531–5543. [https://doi.org/10.1016/S0032-3861\(98\)00778-2](https://doi.org/10.1016/S0032-3861(98)00778-2).
- (104) Rahaman, M. S. A.; Ismail, A. F.; Mustafa, A. A Review of Heat Treatment on Polyacrylonitrile Fiber. *Polym. Degrad. Stab.* **2007**, 92 (8), 1421–1432. <https://doi.org/10.1016/j.polymdegradstab.2007.03.023>.
- (105) Derakhshandeh, B.; Shojaei, A.; Faghihi, M. Effects of Rubber Curing Ingredients and Phenolic Resin on Mechanical, Thermal, and Morphological Characteristics of Rubber/Phenolic-Resin Blends. *J. Appl. Polym. Sci.* **2008**, 108 (6), 3808–3821. <https://doi.org/10.1002/app.28034>.

## APPENDIX A3.0

The ATR performed on samples Ph14, Boron modified PF resin, confirms the predominance of the ortho-methylene linkages in the backbone, the Xylene modified PF resin PhXy shows random ortho/para linkages.

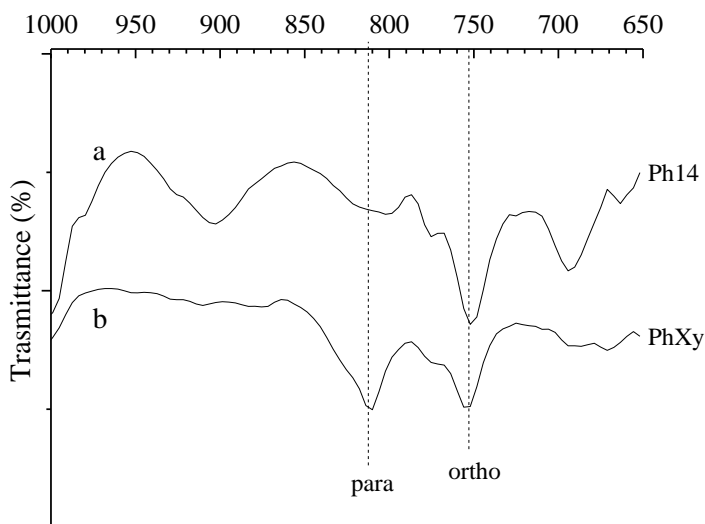
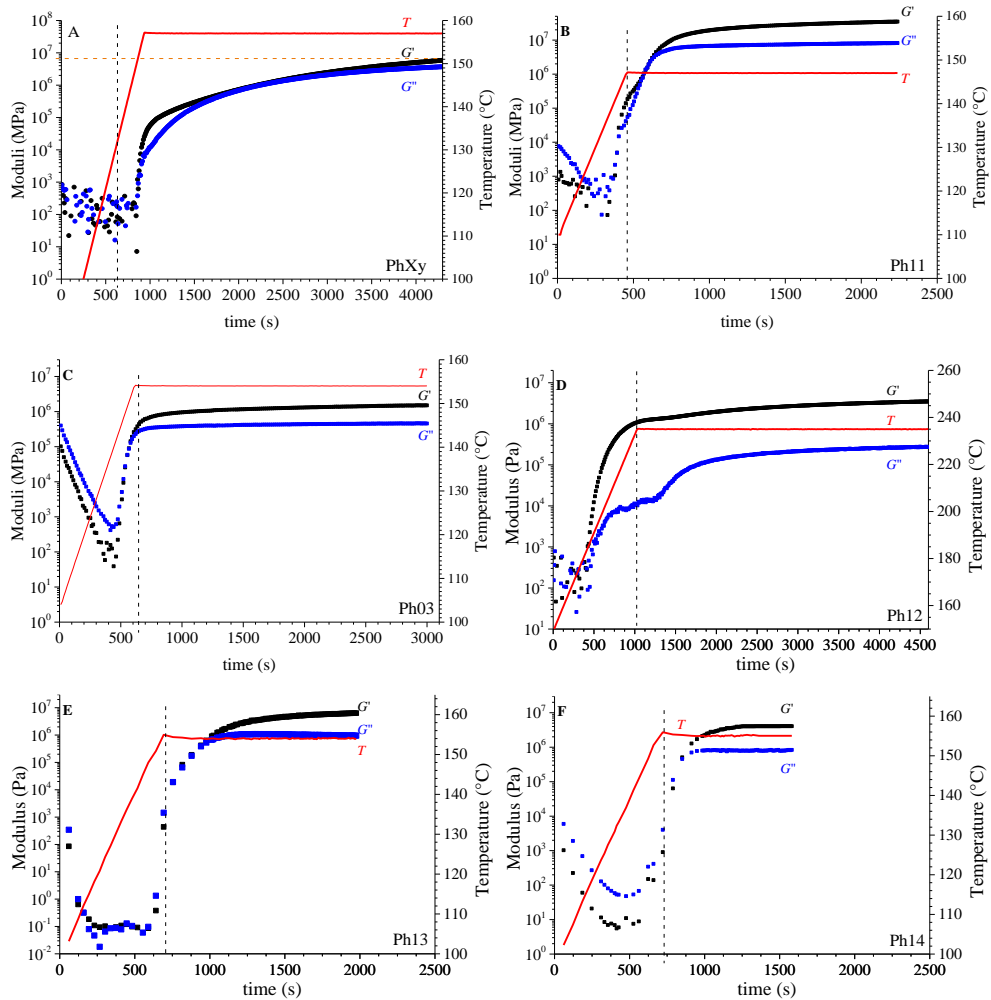


Figure A3.0: ATR-FTIR spectra in the region of the ortho/para linkage of the PF resins Ph14 (a) and PhXy (b)

## APPENDIX A3.1

Rheological measurements were performed on the PF and MF resin powders. From the measurements have been extracted the numerical descriptors  $G'_{L}/G'_{i}$  and  $(dG')/dt)_{\max}$  used for the curing efficiency chart.



**Figure A3.1.1:** Storage ( $G'$ ) and loss ( $G''$ ) moduli of the PF resins PhXy (A), Ph11 (B), Ph03 (C), Ph12 (D), Ph13 (E), and Ph14 (F) measured during the rheological measurements as a function of time. The samples are heated (at 5 °C/min) from 100-110 °C up to the cross-linking temperature  $T_r = T_{CL}$ .

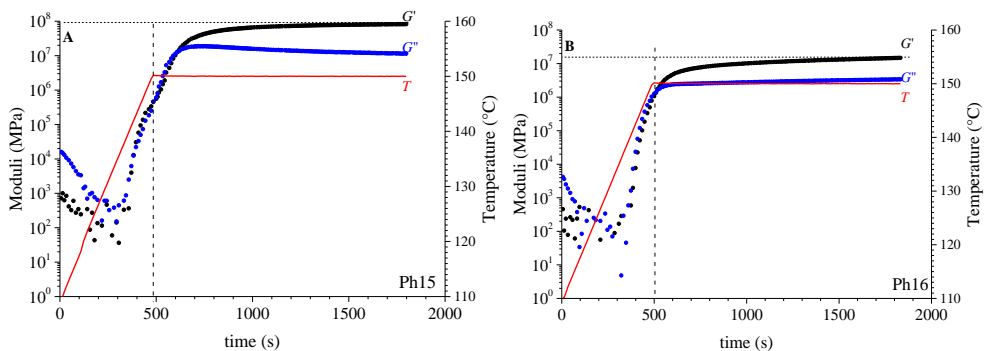


**Figure A3.1.2:** Storage ( $G'$ ) and loss ( $G''$ ) moduli of the fast curable PF resins Ph15 (A) and Ph16 (B) measured during the rheological measurements as a function of time. The samples are heated (at 5 °C/min) from 100 °C up to the cross-linking temperature  $T_r$  of 150°C.

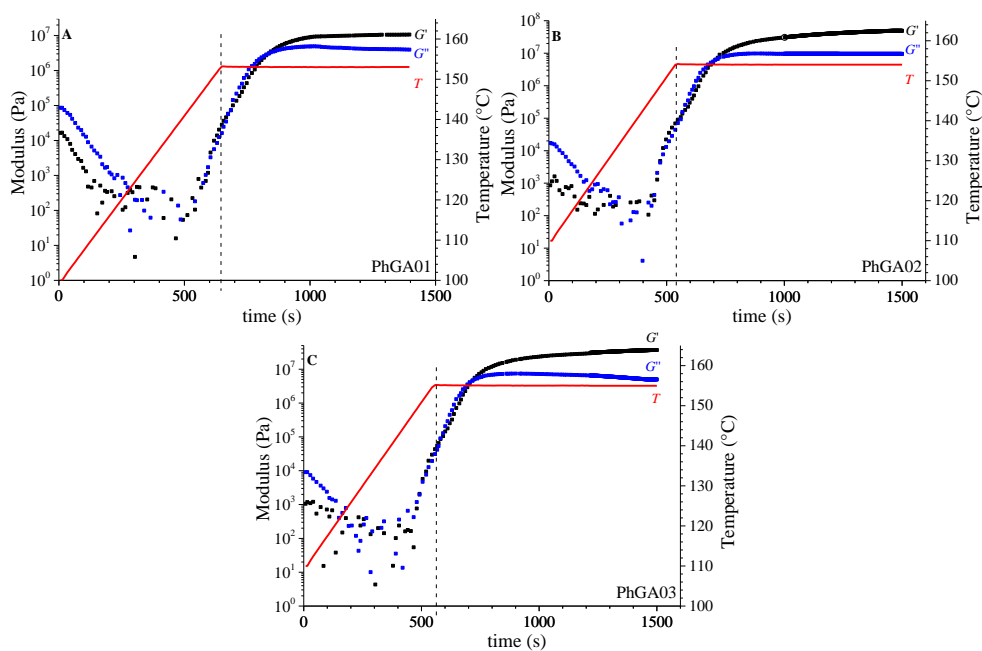


**Figure A3.1.3:** Storage ( $G'$ ) and loss ( $G''$ ) moduli of the Acrylic modified PF resins PhGA01(A), PhGA02 (B), PhGA03 (C) measured during the rheological measurements as a function of time. The samples are heated (at 5 °C/min) from 100 °C up to the cross-linking temperature  $T_r$  of 152.

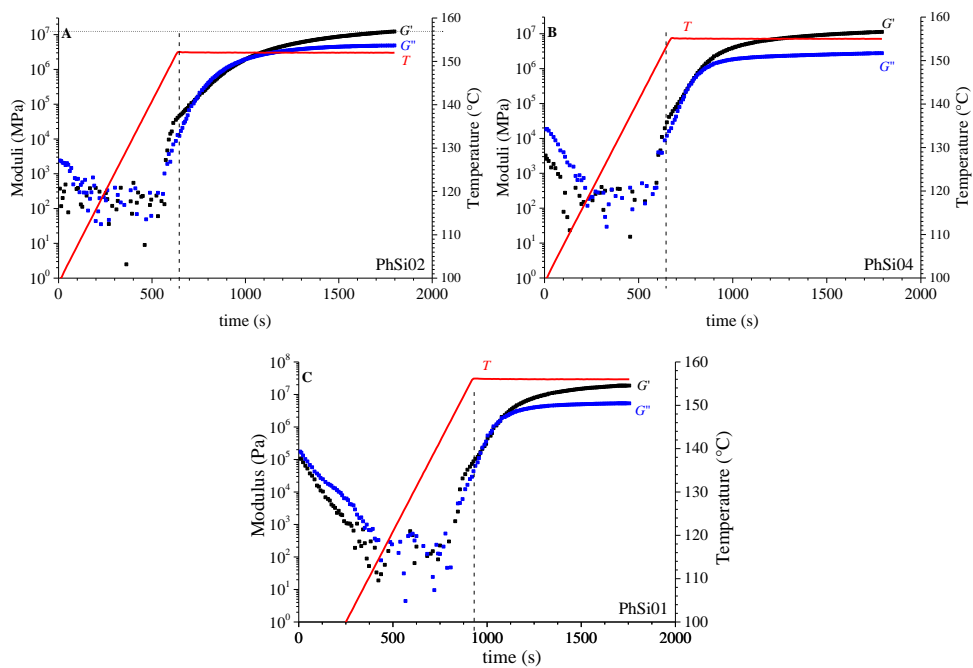


**Figure A3.1.4:** Storage ( $G'$ ) and loss ( $G''$ ) moduli of the Silicon modified PF resins PhSi02 (A), PhSi04 (B), and PhSi01 (C) measured during the rheological measurements as a function of time. The samples are heated (at  $5^{\circ}\text{C}/\text{min}$ ) from  $100^{\circ}\text{C}$  up to the cross-linking temperature  $T_r = T_{CL}$ .

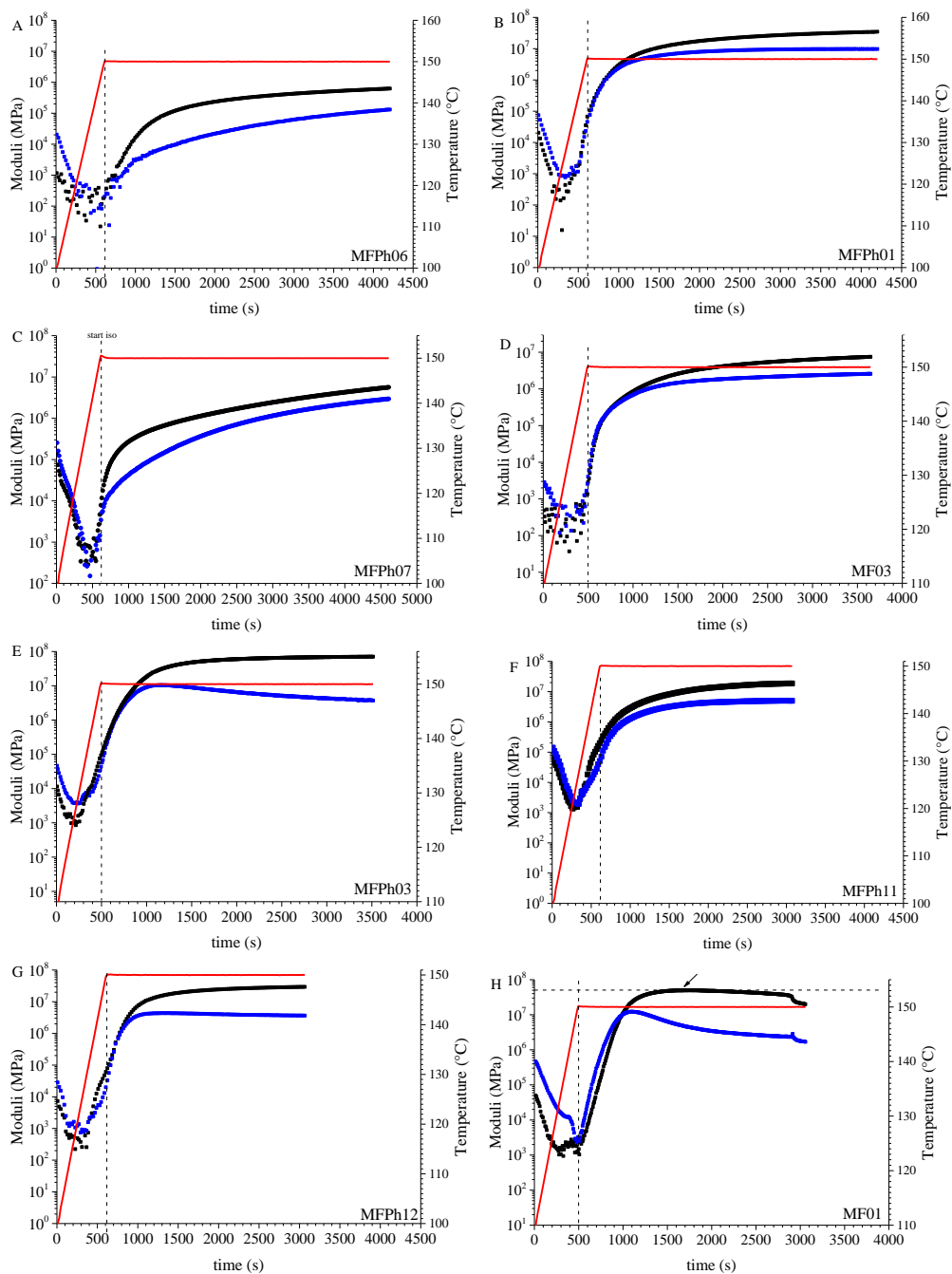


**Figure A3.1.5** Storage ( $G'$ ) and loss ( $G''$ ) moduli of the melamine-based resins MFPh06 (A), MFPh01 (B), MFPh07 (C), MF03 (D), MFPh03 (E), MFPh11 (F), MFPh12 (G) and MF01 (H) measured during the rheological measurements as a function of time. The samples are heated (at 5  $^{\circ}\text{C}/\text{min}$ ) from 100  $^{\circ}\text{C}$  up to the cross-linking temperature  $T_r = T_{CL}$ .

## APPENDIX A3.2

Thermogravimetric Analysis (TGA) was performed on the cured resin at two different compression molding temperatures  $T_{cm} = T_{CL}$  and  $T_{CL} + 50$ .

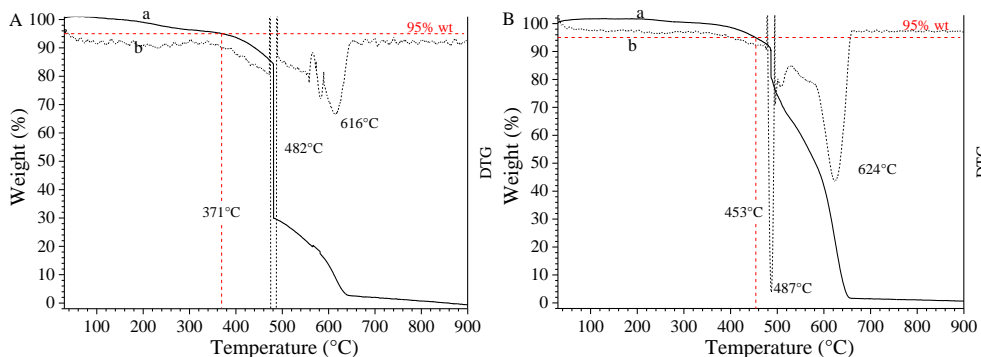


**Figure A3.2.1:** TGA curves (a) and corresponding first derivatives (b) of the cured resin PhXy obtained by compression molding at the cross-linking temperatures  $T_{cm} = T_{CL}$  (A) and  $T_{cm} = T_{CL} + 50$  (B).

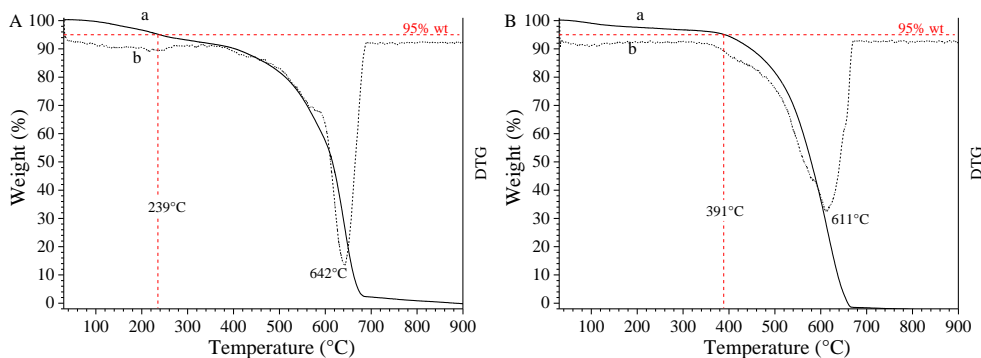


**Figure A3.2.2:** TGA curves (a) and corresponding first derivatives (b) of the cured resin PhA04 obtained by compression molding at the cross-linking temperatures  $T_{cm} = T_{CL}$  (A) and  $T_{cm} = T_{CL} + 50$  (B).

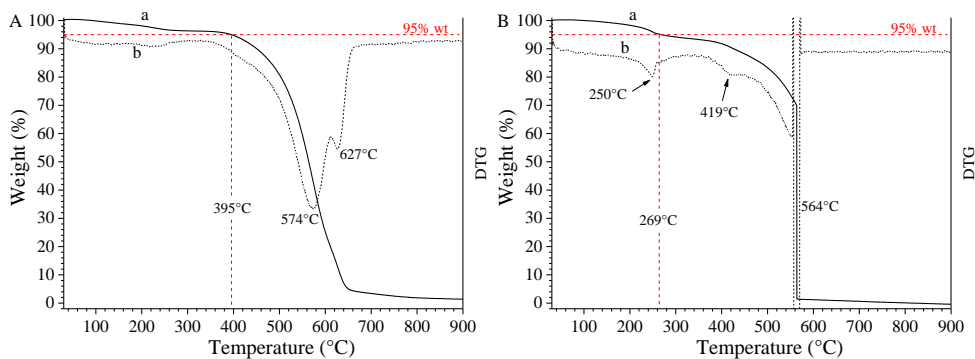


**Figure A3.2.3:** TGA curves (a) and corresponding first derivatives (b) of the cured resin Ph13 obtained by compression molding at the cross-linking temperatures  $T_{cm} = T_{CL}$  (A) and  $T_{cm} = T_{CL}$  (B).

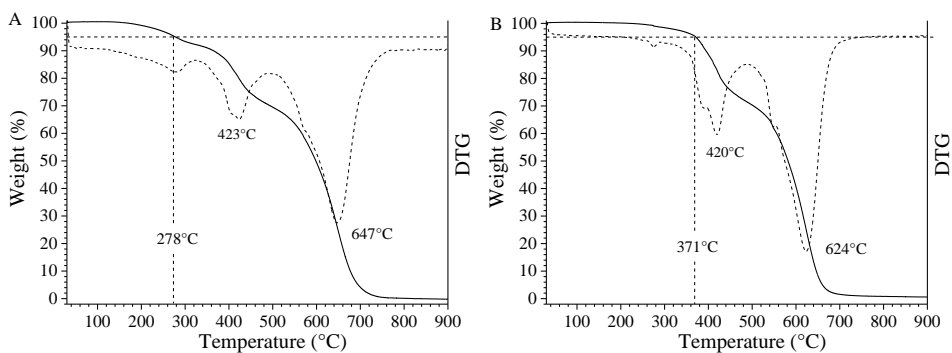


**Figure A3.2.4:** TGA curves (a) and corresponding first derivatives (b) of the cured resin Ph12 obtained by compression molding at the cross-linking temperatures  $T_{cm} = T_{CL}$  (A) and  $T_{cm} = T_{CL}$  (B).

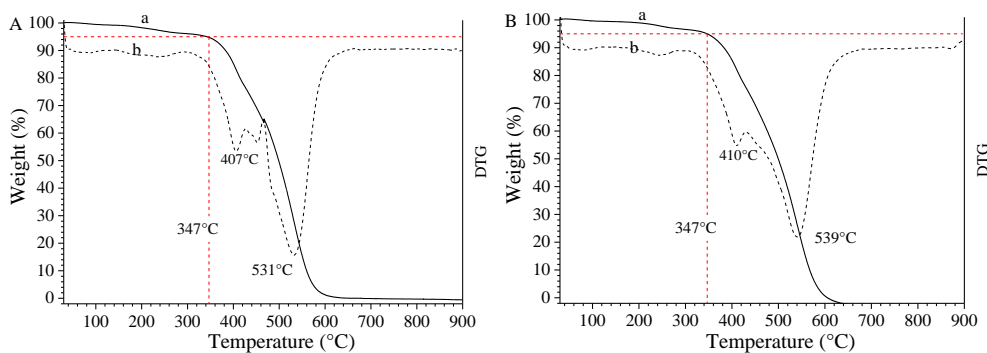


**Figure A3.2.5:** TGA curves (a) and corresponding first derivatives (b) of the cured resin PhGA01 obtained by compression molding at the cross-linking temperatures  $T_{cm} = T_{CL}$  (A) and  $T_{cm} = T_{CL}$  (B).

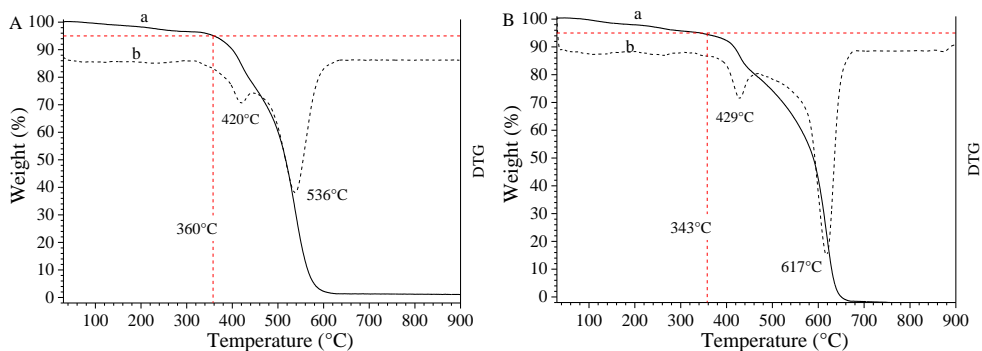


**Figure A3.2.6** TGA curves (a) and corresponding first derivatives (b) of the cured resin PhGA02 obtained by compression molding at the cross-linking temperatures  $T_{cm} = T_{CL}$  (A) and  $T_{cm} = T_{CL}$ (B).

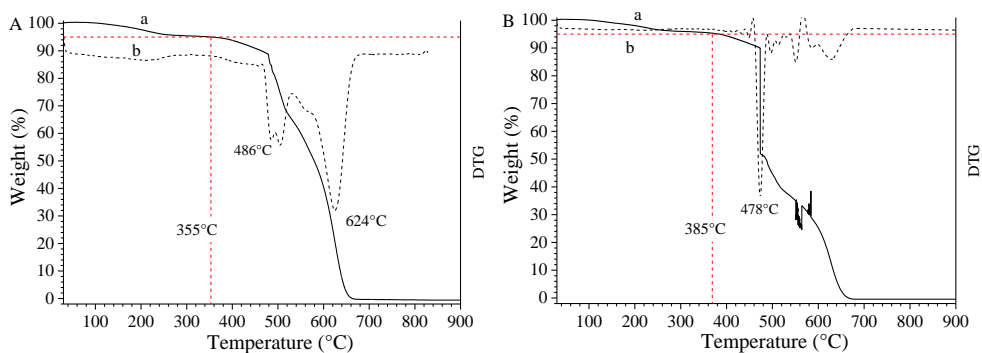


**Figure A3.2.7:** TGA curves (a) and corresponding first derivatives (b) of the cured resin PhA01 obtained by compression molding at the cross-linking temperatures  $T_{cm} = T_{CL}$  (A) and  $T_{cm} = T_{CL}$ (B).

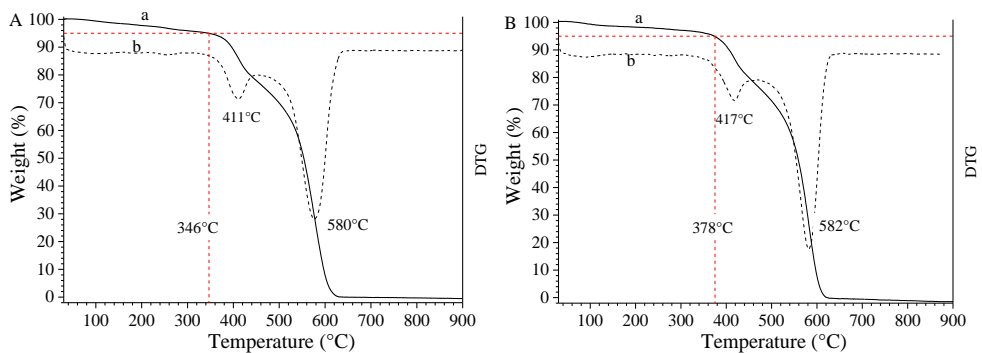


**Figure A3.2.8:** TGA curves (a) and corresponding first derivatives (b) of the cured resin PhGA03 obtained by compression molding at the cross-linking temperatures  $T_{cm} = T_{CL}$  (A) and  $T_{cm} = T_{CL}$ (B).

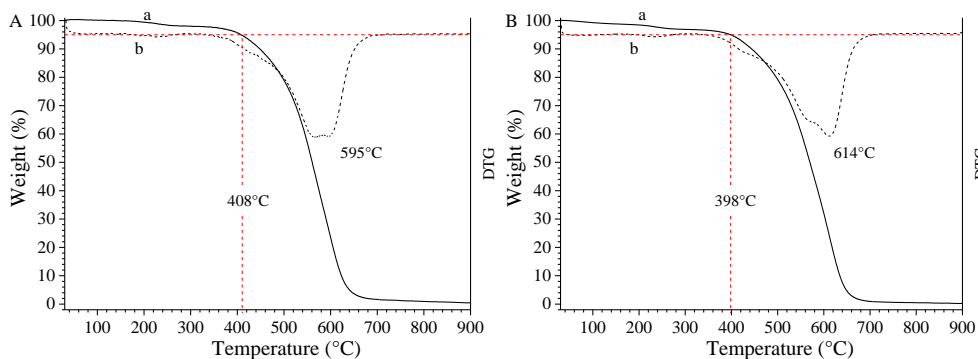


**Figure A3.2.9:** TGA curves (a) and corresponding first derivatives (b) of the cured resin PhSi01 obtained by compression molding at the cross-linking temperatures  $T_{cm} = T_{CL}$  (A) and  $T_{cm} = T_{CL}$ (B).

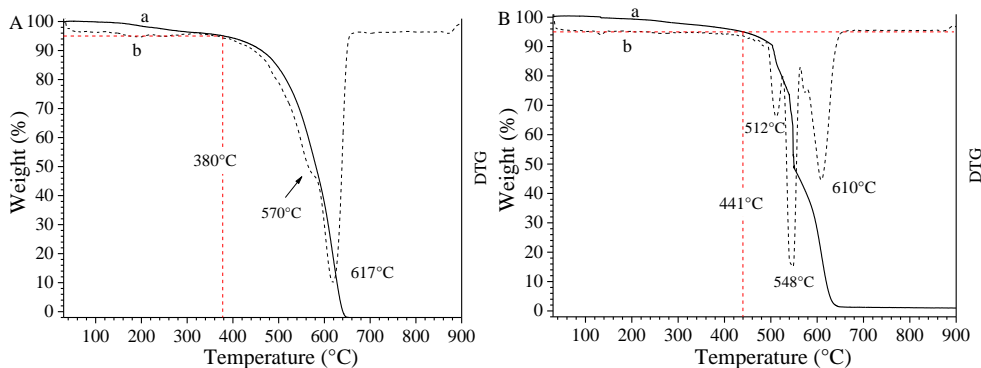


**Figure A3.2.10:** TGA curves (a) and corresponding first derivatives (b) of the cured resin PhA03 obtained by compression molding at the cross-linking temperatures  $T_{cm} = T_{CL}$  (A) and  $T_{cm} = T_{CL}$ (B).

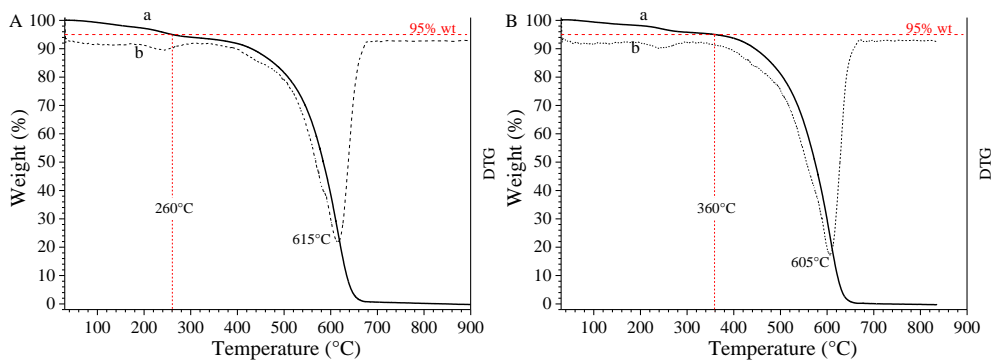


**Figure A3.2.11:** TGA curves (a) and corresponding first derivatives (b) of the cured resin Ph15 obtained by compression molding at the cross-linking temperatures  $T_{cm} = T_{CL}$  (A) and  $T_{cm} = T_{CL}$ (B).

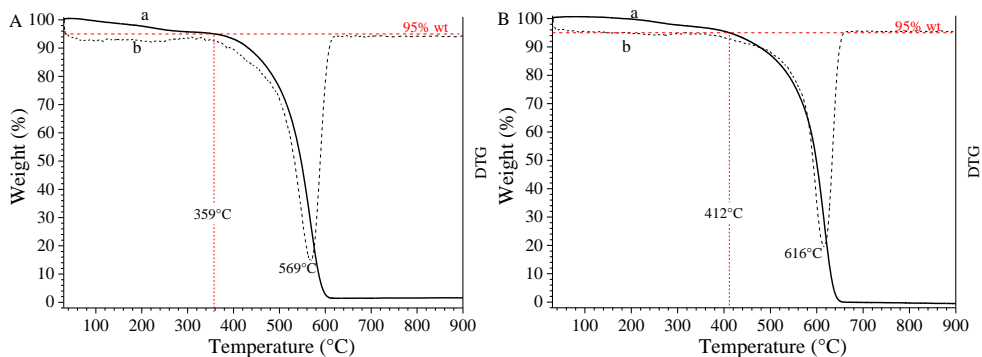


**Figure A3.2.12:** TGA curves (a) and corresponding first derivatives (b) of the cured resin Ph16 obtained by compression molding at the cross-linking temperatures  $T_{cm} = T_{CL}$  (A) and  $T_{cm} = T_{CL}$ (B).

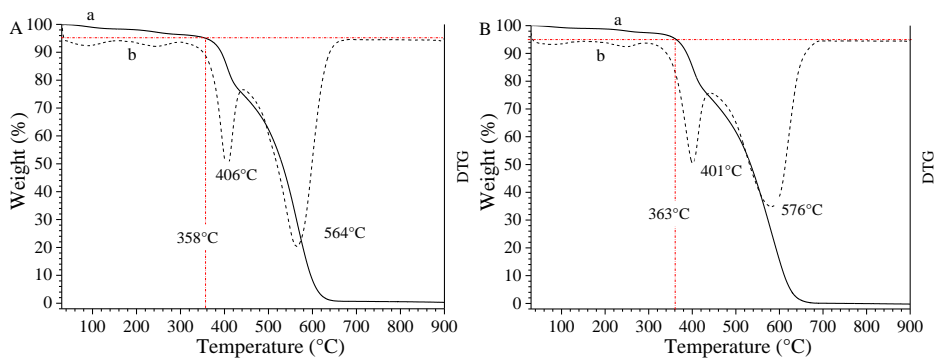


**Figure A3.2.13:** TGA curves (a) and corresponding first derivatives (b) of the cured resin PhGA04 obtained by compression molding at the cross-linking temperatures  $T_{cm} = T_{CL}$  (A) and  $T_{cm} = T_{CL}$ (B).

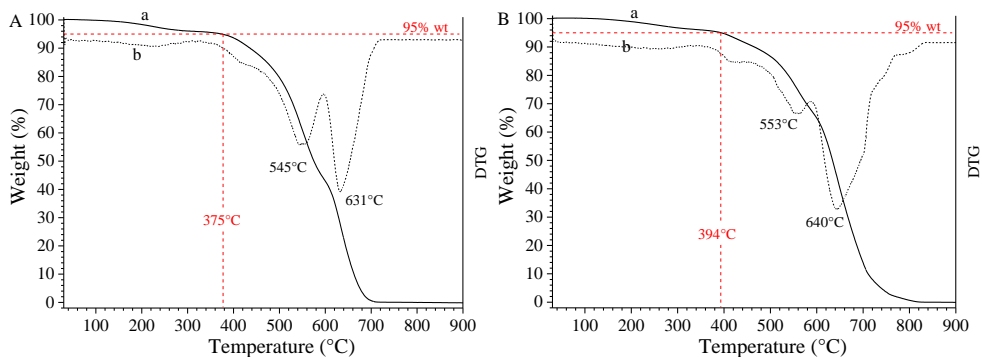


**Figure A3.2.14:** TGA curves (a) and corresponding first derivatives (b) of the cured resin Ph02 obtained by compression molding at the cross-linking temperatures  $T_{cm} = T_{CL}$  (A) and  $T_{cm} = T_{CL}$ (B).

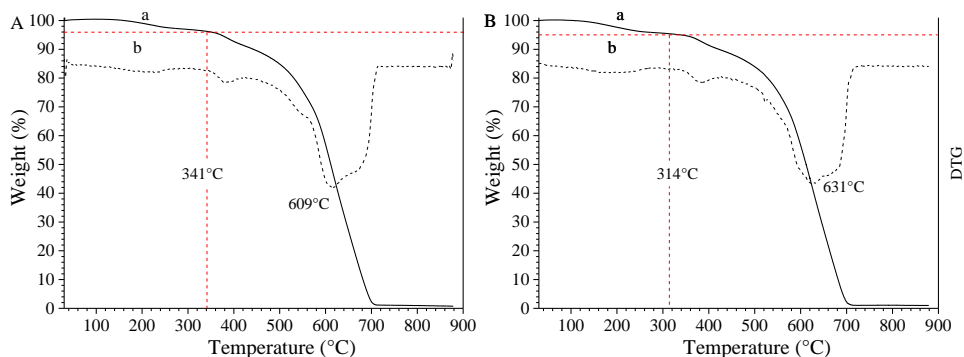


**Figure A3.2.15:** TGA curves (a) and corresponding first derivatives (b) of the cured resin Ph03 obtained by compression molding at the cross-linking temperatures  $T_{cm} = T_{CL}$  (A) and  $T_{cm} = T_{CL}$ (B).

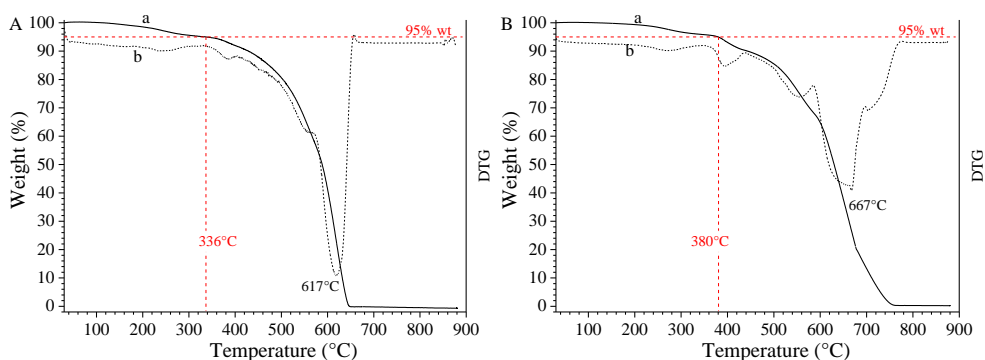


**Figure A3.2.16:** TGA curves (a) and corresponding first derivatives (b) of the cured resin Ph11 obtained by compression molding at the cross-linking temperatures  $T_{cm} = T_{CL}$  (A) and  $T_{cm} = T_{CL}$ (B).

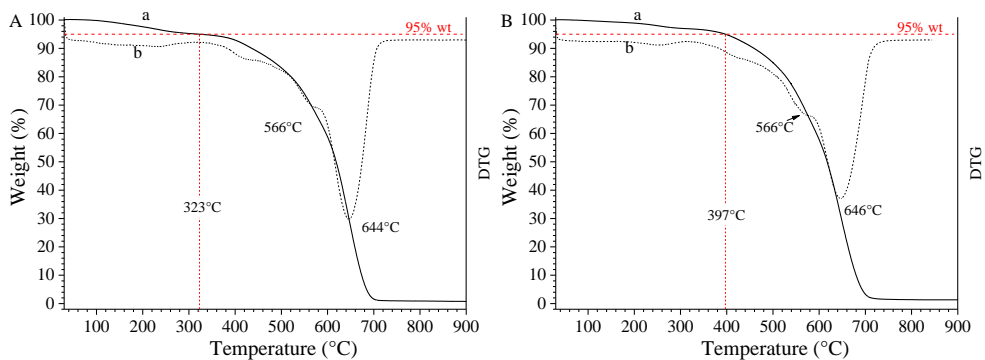


**Figure A3.2.17:** TGA curves (a) and corresponding first derivatives (b) of the cured resin PhSi04 obtained by compression molding at the cross-linking temperatures  $T_{cm} = T_{CL}$  (A) and  $T_{cm} = T_{CL}$ (B).

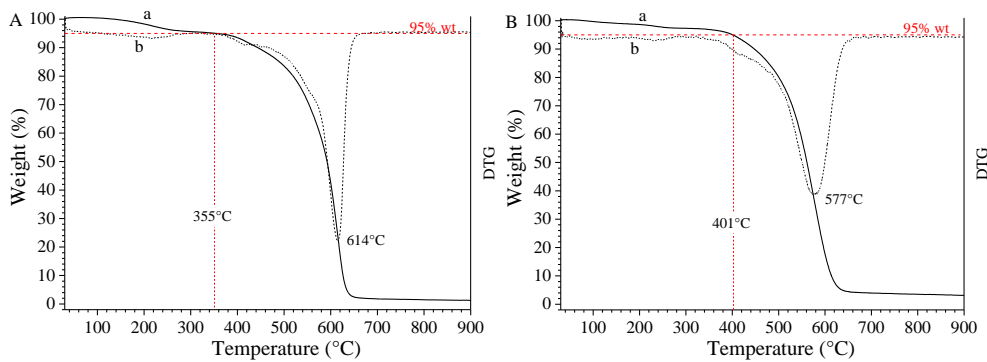


**Figure A3.2.18:** TGA curves (a) and corresponding first derivatives (b) of the cured resin PhSi02 obtained by compression molding at the cross-linking temperatures  $T_{cm} = T_{CL}$  (A) and  $T_{cm} = T_{CL}$ (B).

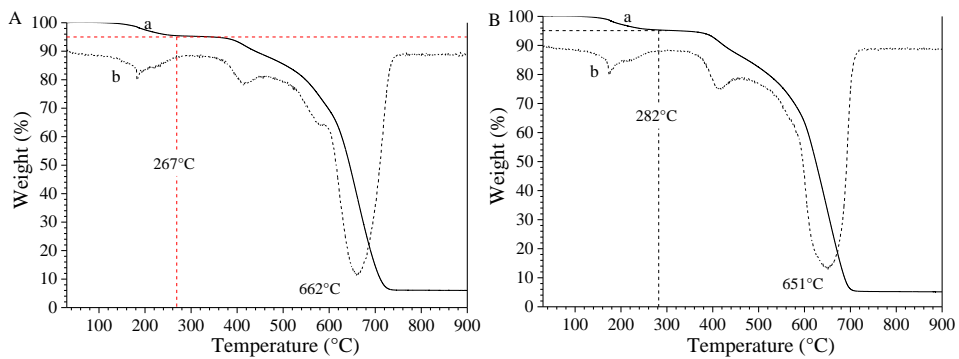


**Figure A3.1.19:** TGA curves (a) and corresponding first derivatives (b) of the cured resin PhSi03 obtained by compression molding at the cross-linking temperatures  $T_{cm} = T_{CL}$  (A) and  $T_{cm} = T_{CL}$ (B).

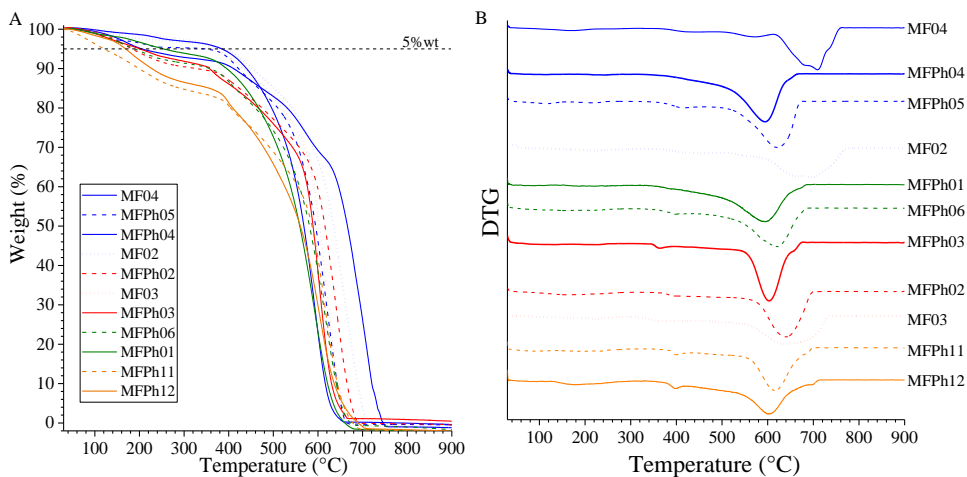


**Figure A3.2.20:** TGA curves (A) and corresponding first derivatives (B) of the cured melamine based resin obtained by compression molding at the cross-linking temperatures  $T_{cm}$  equal to  $T_{CL} = 150$  °C.

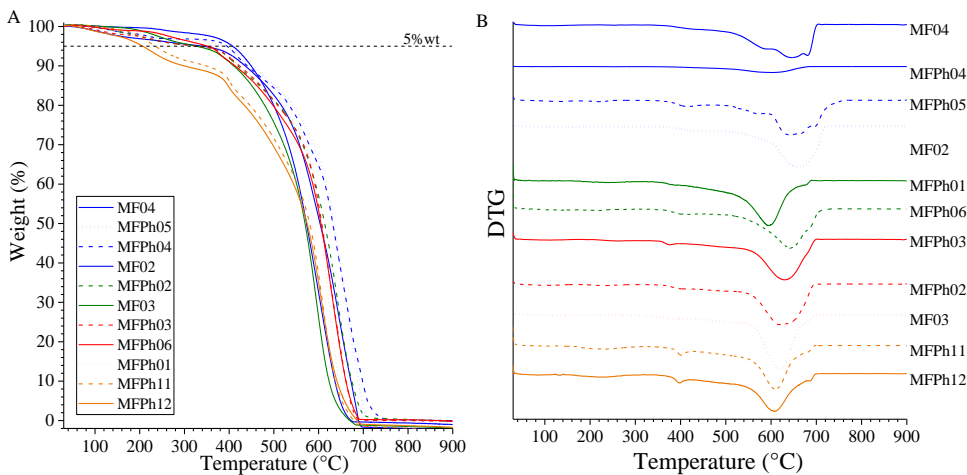


**Figure A3.2.21:** TGA curves (A) and corresponding first derivatives (B) of the cured melamine based resin obtained by compression molding at the cross-linking temperatures  $T_{cm}$  equal to  $T_{CL} + 50$  °C = 200 °C.

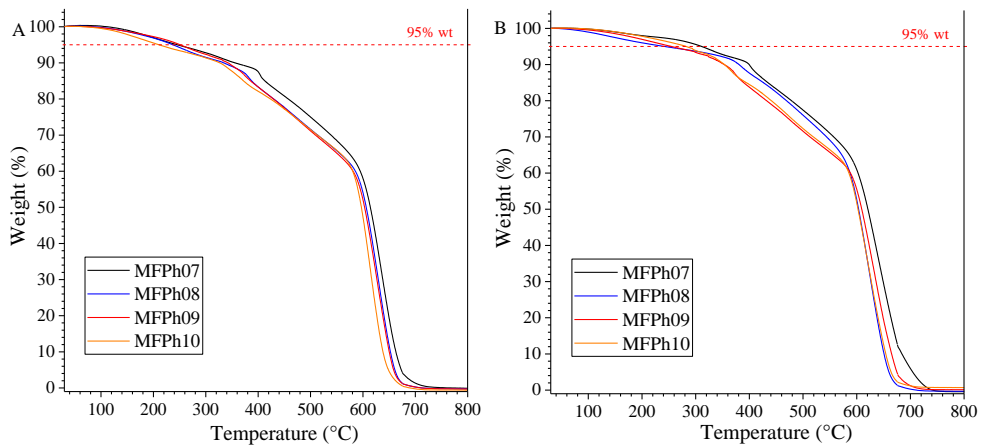
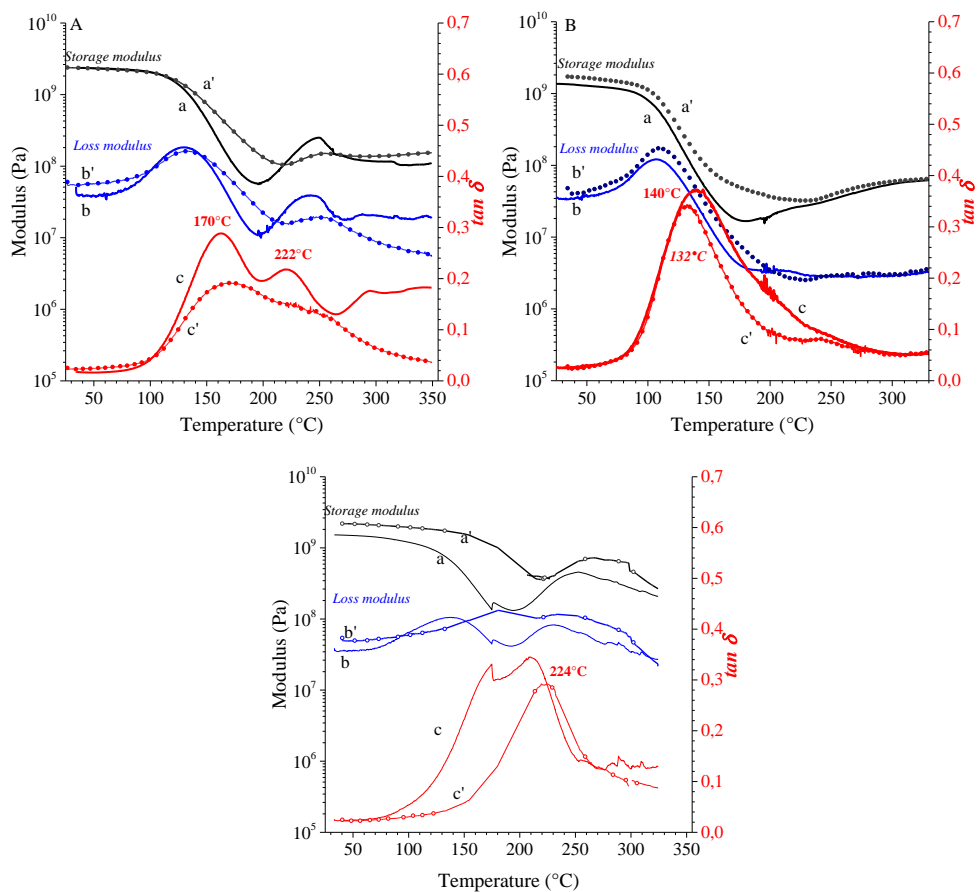


**Figure A3.2.22:** TGA curves of the cured melamine based resin with HMM content 25-40% wt obtained by compression molding at the cross-linking temperatures  $T_{cm} = 150^{\circ}\text{C}$  (A) and  $T_{cm} = 200^{\circ}\text{C}$  (B).

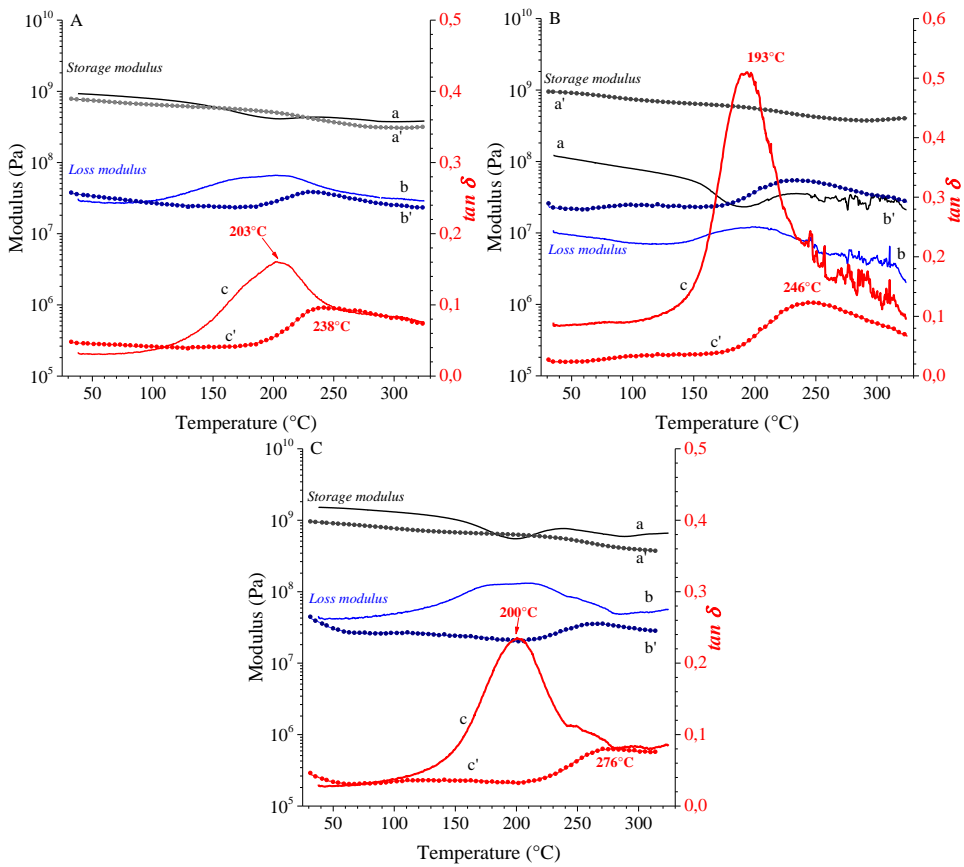
## APPENDIX A3.3

The cured PF resin DMTA data are reported in Figures A3.3.1-A3.3.5.

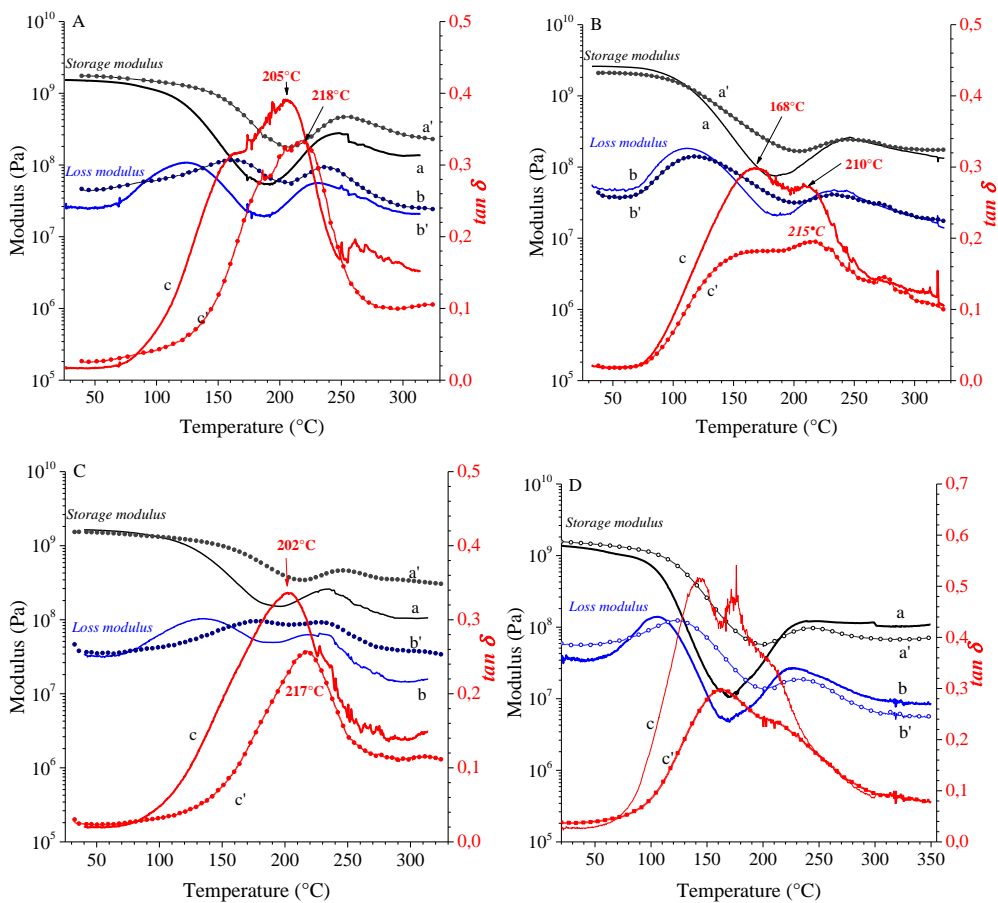
In the same graph are reported the storage and the loss moduli, and the loss factor of specimen cured for 4 min at two different compression-molding temperatures.



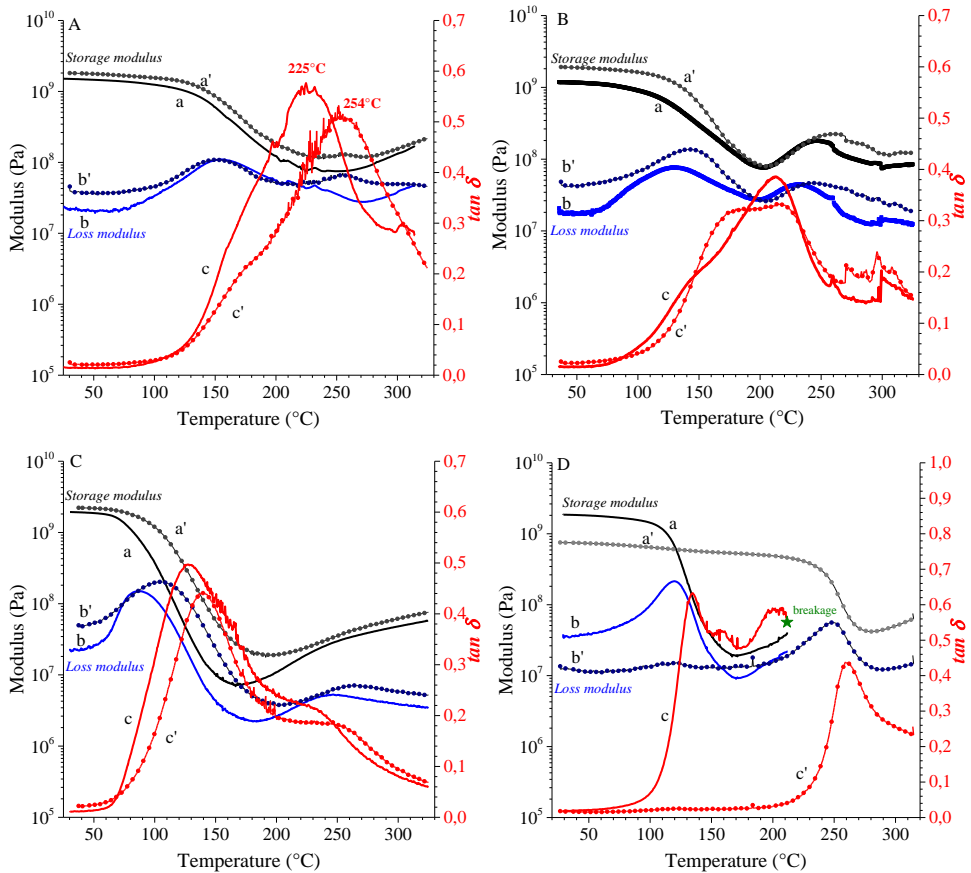
**Figure A3.3.1:** Storage modulus (a,a'), loss modulus (b,b'), and  $\tan \delta$  (c,c') as a function of temperature for the PF resin cured at  $T_r = T_{CL}$  (a-c) and  $T_r = T_{CL}+50$  (a'-c'). Ph02 (A), Ph03 (B), Ph11(C). In all cases, the curing time is fixed to 4 min.



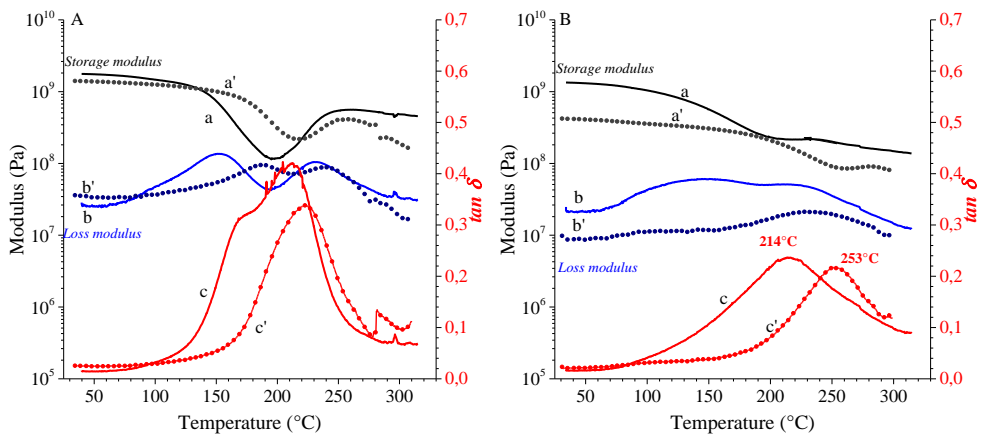
**Figure A3.3.2:** Storage modulus (a,a'), loss modulus (b,b'), and  $\tan \delta$  (c,c') as a function of temperature for the Acrylic codified PF resin cured at  $T_r = 150$   $^{\circ}\text{C}$  (a-c) and  $200$   $^{\circ}\text{C}$  (a'-c'). PhGA01 (A), PhGA02 (B), PhGA03 (C). In all cases, the curing time is fixed to 4 min.

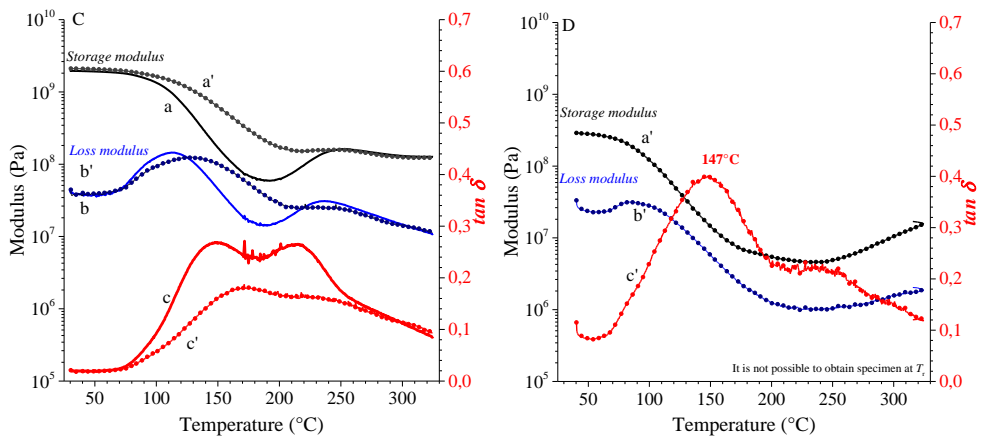


**Figure A3.3.3:** Storage modulus (a,a'), loss modulus (b,b'), and  $\tan \delta$  (c,c') as a function of temperature for the Silicon modified PF resin cured at  $T_r = T_{CL}$  (a-c) and  $T_r = T_{CL}+50$  (a'-c'). PhSi02 (A), PhSi04 (B), PhSi01(C), and PhSi03 (D). In all cases, the curing time is fixed to 4 min.



**Figure A3.3.4:** Storage modulus (a,a'), loss modulus (b,b'), and tan  $\delta$  (c,c') as a function of temperature for the Aralkyl modified PF resin cured at  $T_r = T_{CL}$  (a-c) and  $T_r = T_{CL}+50$  (a'-c'). PhA02(A), PhA04 (B), PhA01(C), and PhA03. In all cases, the curing time is fixed to 4 min.

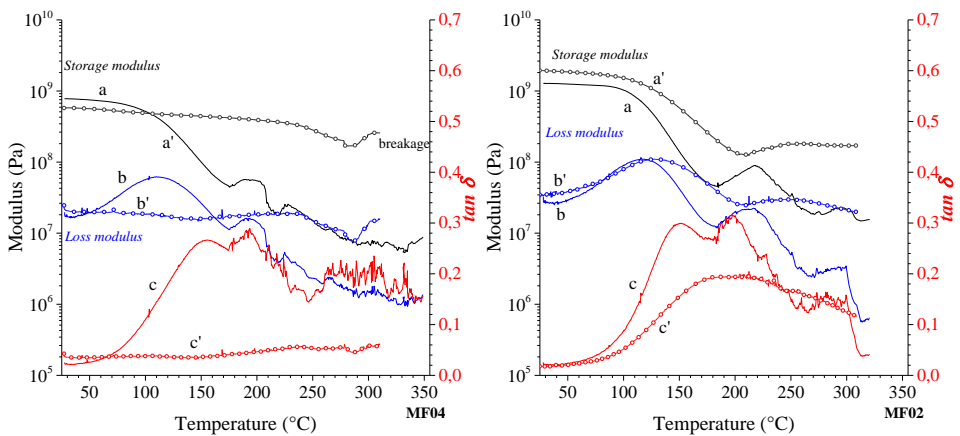


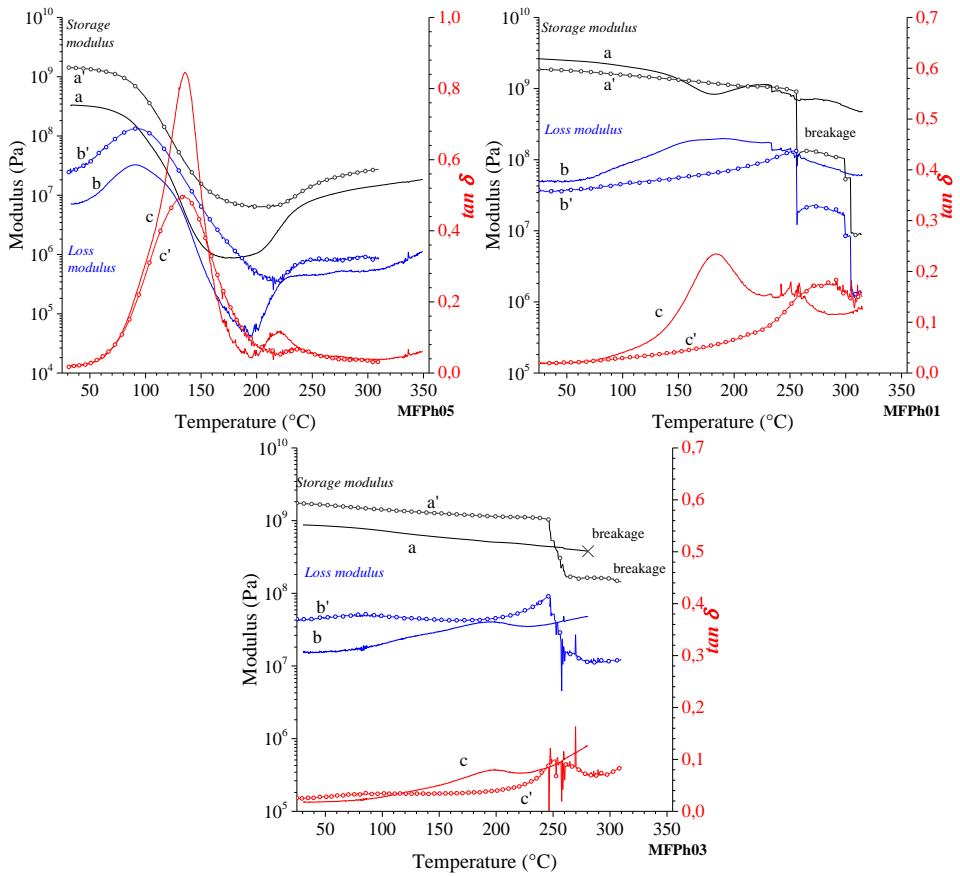


**Figure A3.3.5:** Storage modulus (a,a'), loss modulus (b,b'), and  $\tan \delta$  (c,c') as a function of temperature for the PF resin cured at  $T_r = T_{CL}$  (a-c) and  $T_r = T_{CL}+50$  (a'-c'). Ph15(A), Ph16 (B), Ph13 (C), and Ph14. In all cases, the curing time is fixed to 4 min. The specimen of the resin Ph14 cured at  $T_r = T_{CL}$  is too brittle to perform the measurement.

The melamine-based resin DMTA data are reported in Figure A3.3.6.

In the same graph are reported the storage and the loss moduli, and the loss factor of specimen cured for 4 min at two different compression-molding temperatures.





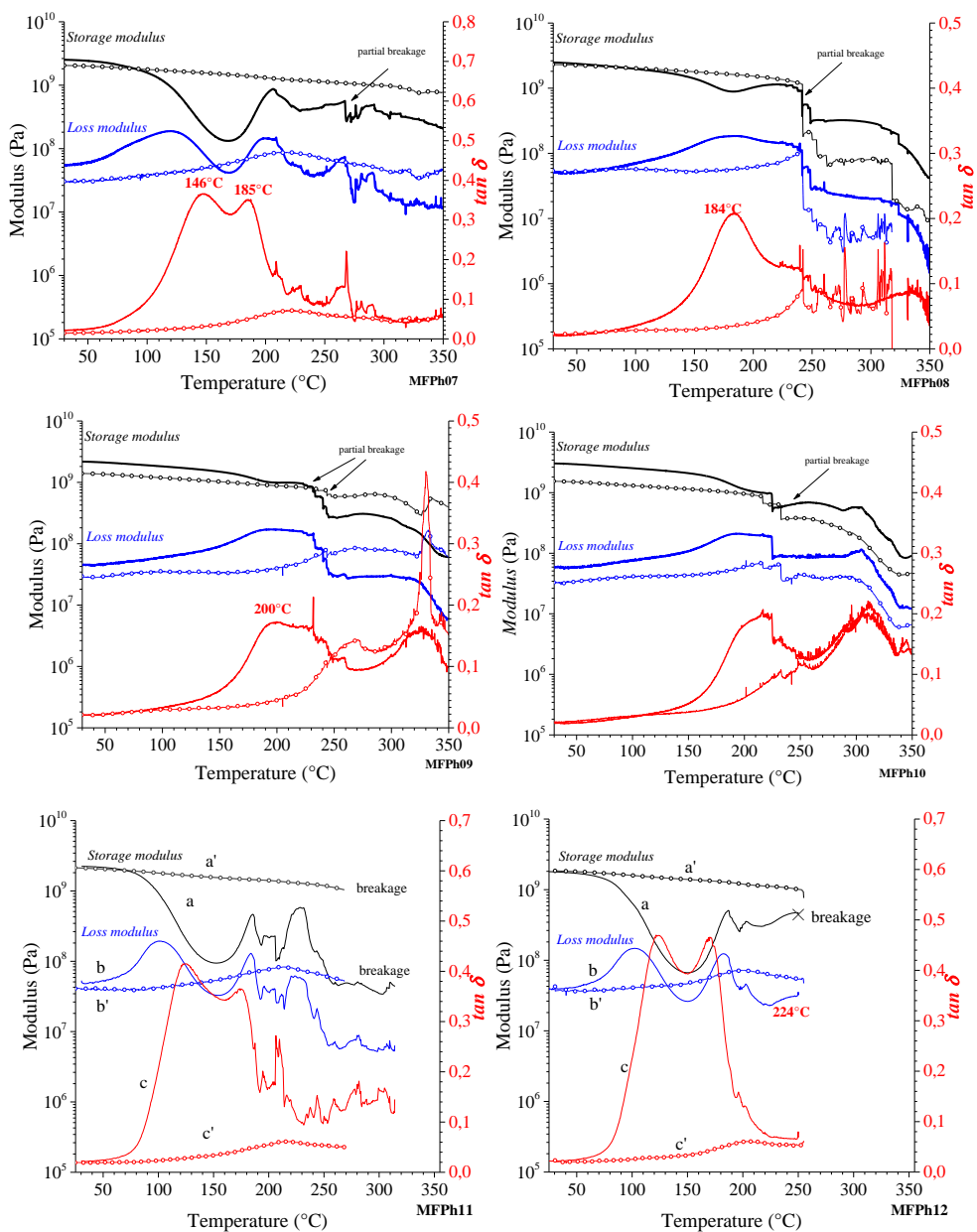


**Figure A3.3.6:** Storage modulus (a,a'), loss modulus (b,b'), and tan  $\delta$  (c,c') as a function of temperature for the melamine based resin cured at  $T_r = 150^\circ\text{C}$  (a-c) and  $200^\circ\text{C}$  (a'-c'). In all cases, the curing time is fixed to 4 min. The sample name is indicated on the graph.

## APPENDIX A4.0

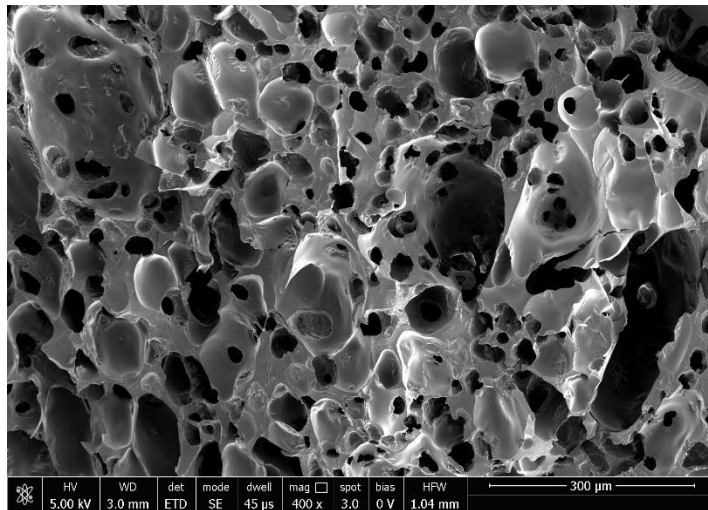


**Figure A4.0.1:** SEM micrographs magnification 400x of the inner surface of the specimen of the blend B1\_6040 cured at 200 °C for 10 min after breaking in liquid nitrogen and then etched with Phenol. PA12 domains. The holes indicate the region occupied by the dispersed PA12.

## APPENDIX A4.1

The system HMTA-PA12 has been studied by DSC analysis. No phenomena occur between the two mixed components with a ratio of 50:50.

After the measurements, the weight loss is about 50wt% and it is due to the degradation of the HMTA component at 243°C recorded during the 1<sup>st</sup> heating scan.

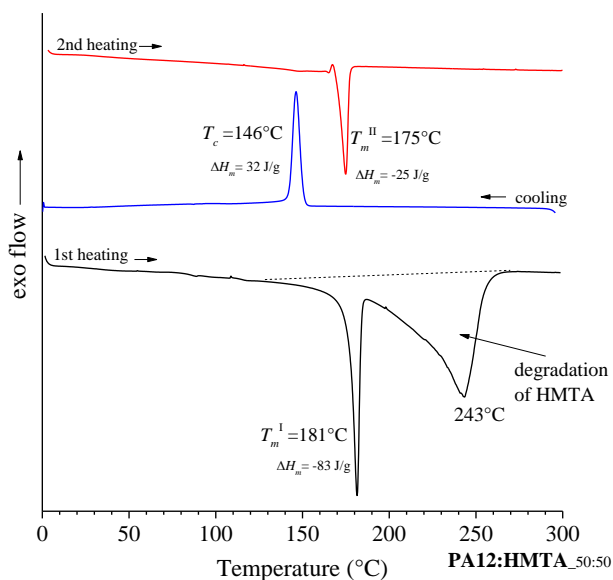


**Figure A4.1.1:** DSC thermograms of the mixed PA12:HMTA with ratio 50:50. The degradation of the HMTA occurs at  $243^\circ\text{C}$ .

## APPENDIX A4.2

In order to evaluate the formation of the covalent bonds between PA12 and HMTA-free novolac (Ph00) extractions with Soxhlet technique have been performed using acetone as a selective solvent for the unreacted novolac, for 24 hours.

The novolac HMTA resin has been washed in distilled water and dried in the oven at 80°C under vacuum in order to remove any traces of reactive components (e.g. HMTA).

The mixture B0\_6040 which contains 60wt% of HMTA-free novolac and 40wt% of PA12 has been obtained as described in Chapter IV.

A sample of 100% novolac and a sample of the blend B0\_6040 have been heated at 180°C for 20 min. The heated samples are named B0\_6040C and PhC, respectively.

The analyzed samples are the uncured mixed powder, the heated mixed powders, and the heated novolac alone. The results are reported in Table A.4.2

The evaluation of the Acetone soluble fraction (As) and Acetone insoluble fraction (Ai) could give information about the occurrence of reactions.

	<b>Unreacted B0_6040</b>	<b>B0_6040C</b>	<b>PhC</b>
Insoluble fraction ( <b>Ai</b> ) %	39.8 ±0.2	45.0 ±0.2	3.6 ±0.2
Soluble fraction ( <b>As</b> ) %	60.2 ±0.2	55.0 ±0.2	96.4 ±0.2

Considering the complete solubility of the HMTA-free novolac in acetone, the As fraction is attributed to the novolac soluble oligomers.

The insoluble fraction recorded for the PhC ( $A_i = 3.6 \pm 0.2$  %) is due to the condensation reaction occurring with some methylol group present in the uncured novolac or thanks formaldehyde-releasing after the rearrangements of ether bridges in methylene bridges. The presence of this group has been confirmed by MALDI-TOF spectra of the unreacted HMTA-free PF resin (Figure A.4.2) compatible with a structure containing one  $-CH_2O-$  group (Figure A.4.3).

The  $A_i$  of the B0\_6040C is about 45% which means that contains 10% of insoluble PF resin. Considering that the  $A_i$  fraction of the PhC is 3.6%, in the case of condensation of the novolac oligomers the contribution of the PF resin should be  $A_i=42.2\%$ . The higher value of the insoluble fraction, therefore, suggests that the oligomers can be directly bound to the PA12. It is worth noticing that the unreacted B0\_6040 gives the initial amount of the components as expected. The reaction between polyamide, formaldehyde, and phenol has been investigated by Ravve et al. but the mechanism has not been explained whether the reaction involves the direct reaction N atom of the amide group to a methylol group, or it occurs through the reaction of the amide group and formaldehyde, in the first step.

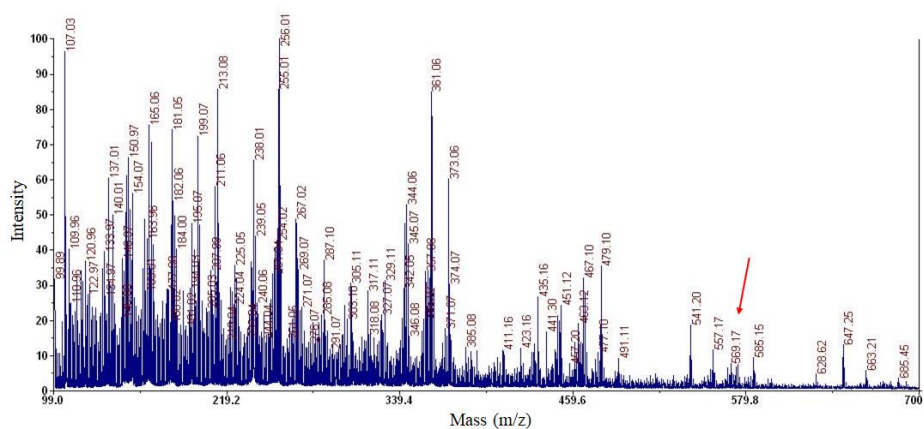


Figure A.4.2: MALDI-TOF spectrum of the sample Ph00. The arrow indicates a signal of an oligomer of 546 Da, considering the contribution of the Na ion (23 Da) the oligomer molecular weight is 546 Da.

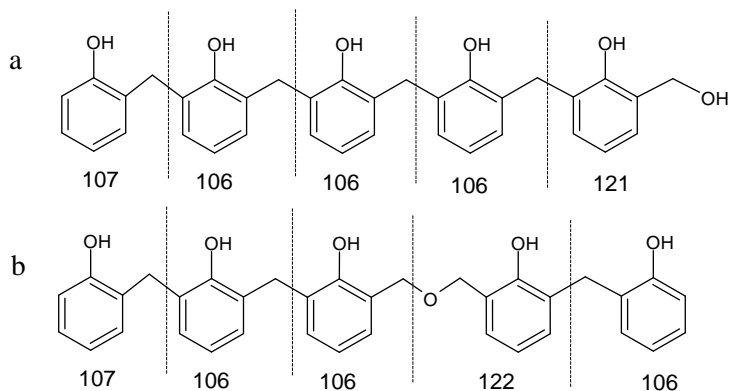


Figure A.4.3: Possible structures compatible with a molecular weight of 546 Da indicated in Figure A.4.2 considering the contribution of the  $\text{Na}^+$  (~23 Da) with methylol moiety (a) or ether bridge (b).

The formation of chemical bonds between PA12 and PF resin interface could not be probed directly, due to the scarce solubility of the insoluble fraction obtained.

## APPENDIX A5.0

In order to evaluate the behavior of a rubber as damper in composites with the HAP resin, mixtures of the HAP resin with 20wt% of rubber selected from Table 5.1 were prepared by mechanical mixing.

The composite between HAP resin as binder and EPDM-mA gives the highest value in loss factor in the range 0-100°C. For this reason, this rubber has been also selected in the composite described in the Chapter V.

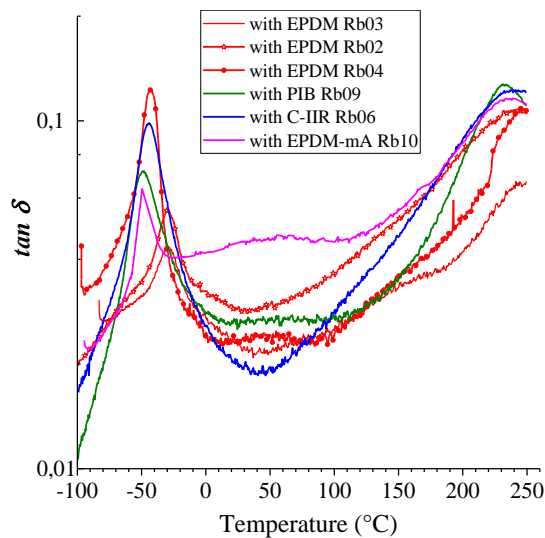


**Figure A5.0.1:** Comparison of the loss factor of the composite between HAP resin and rubber samples (20wt%). The composites have been cured at 200°C for 10 min. The composite containing EPDM-mA show the higher loss factor value in the range 0-100°C.

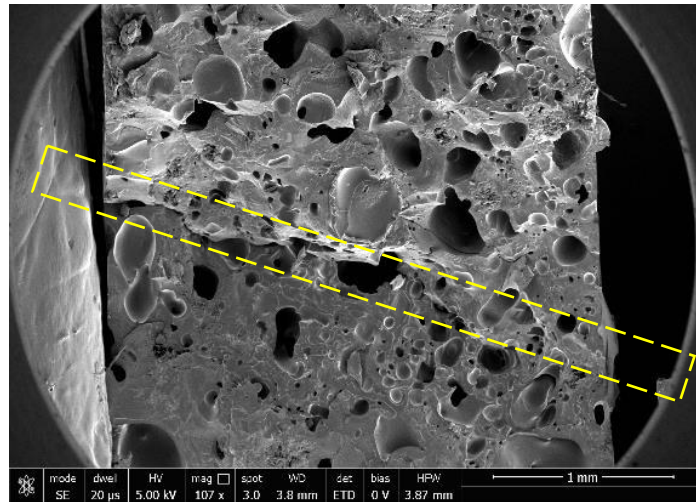


**Figure A5.0.2:** SEM micrographs magnification 107x of the inner surface of the specimen of the composite C1\_50330612 cured at 200 °C for 10 min, successive healing, and successively cut perpendicularly to the welding surface. The whole welded fracture has indicated by dashed rectangle.

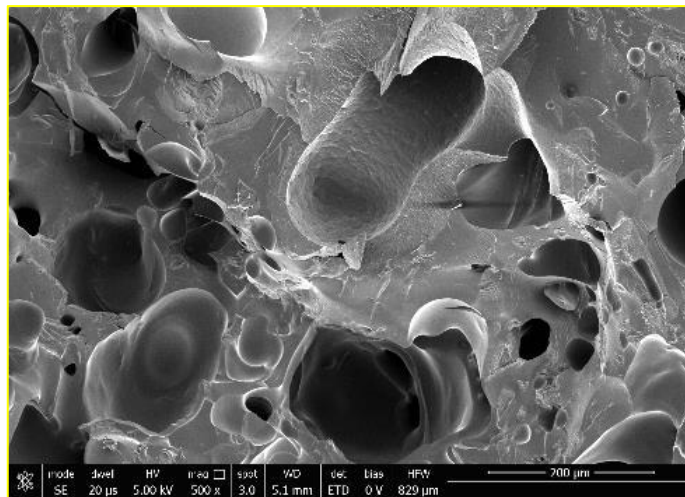


**Figure A5.0.3:** SEM micrographs magnification 500x of the inner surface of the specimen of the composite C1\_50330612 cured at 200 °C for 10 min, successive healing, and successively cut perpendicularly to the welding surface. Detail of the welding area